TU/e EINDHOVEN UNIVERSITY OF TECHNOLOGY

Performance-driven control of nano-motion systems

Citation for published version (APA):
Merry, R. J. E. (2009). *Performance-driven control of nano-motion systems*. [Phd Thesis 1 (Research TU/e / Graduation TU/e), Mechanical Engineering]. Technische Universiteit Eindhoven.
https://doi.org/10.6100/IR653237

DOI:
10.6100/IR653237

Document status and date:
Published: 01/01/2009

Document Version:
Publisher's PDF, also known as Version of Record (includes final page, issue and volume numbers)

Please check the document version of this publication:

• A submitted manuscript is the version of the article upon submission and before peer-review. There can be important differences between the submitted version and the official published version of record. People interested in the research are advised to contact the author for the final version of the publication, or visit the DOI to the publisher's website.
• The final author version and the galley proof are versions of the publication after peer review.
• The final published version features the final layout of the paper including the volume, issue and page numbers.

Link to publication

General rights
Copyright and moral rights for the publications made accessible in the public portal are retained by the authors and/or other copyright owners and it is a condition of accessing publications that users recognise and abide by the legal requirements associated with these rights.

• Users may download and print one copy of any publication from the public portal for the purpose of private study or research.
• You may not further distribute the material or use it for any profit-making activity or commercial gain
• You may freely distribute the URL identifying the publication in the public portal.

If the publication is distributed under the terms of Article 25fa of the Dutch Copyright Act, indicated by the "Taverne" license above, please follow below link for the End User Agreement:

www.tue.nl/taverne

Take down policy
If you believe that this document breaches copyright please contact us at:

openaccess@tue.nl

providing details and we will investigate your claim.

Download date: 16. Nov. 2023

Performance-driven control of nano-motion systems

PROEFSCHRIFT

ter verkrijging van de graad van doctor aan de
Technische Universiteit Eindhoven, op gezag van de
rector magnificus, prof.dr.ir. C.J. van Duijn, voor een
commissie aangewezen door het College voor
Promoties in het openbaar te verdedigen
op woensdag 25 november 2009 om 16.00 uur

door

Roel Johannes Elisabeth Merry

geboren te Sittard

Dit proefschrift is goedgekeurd door de promotor:

prof.dr.ir. M. Steinbuch

Copromotor:
dr.ir. M.J.G. van de Molengraft

This dissertation has been completed in partial fulfillment of the requirements of the Dutch Institute of Systems and Control (DISC) for graduate study.

This research was partially supported by SenterNovem/Point One as part of the Micro- and Nano-Motion project and partially by NanoNed, a national nanotechnology program coordinated by the Dutch Ministry of Economic Affairs.

A catalogue record is available from the library of the Eindhoven University of Technology.

Performance-driven control of nano-motion systems / by Roel J.E. Merry.
Eindhoven University of Technology, 2009.
Proefschrift. – ISBN: 978-90-386-2059-6

Copyright © 2009 by R.J.E. Merry. All rights reserved.

Typeset by the author with the pdfLaTeX documentation system.
Cover design: Esther van Hinsberg.
Reproduction: Ipskamp Drukkers B.V., Enschede, The Netherlands.

Contents

I Motivation **1**

1 Introduction **3**
1.1 Nano-motion systems 3
1.2 Performance limiting factors 5
1.3 Thesis goals 9
1.4 Case descriptions 11
1.5 Outline 15

II The walking piezo actuator **17**

2 Drive principle and feedback control **19**
2.1 Introduction 21
2.2 The piezo motor 23
2.3 System description and modeling 26
2.4 Control design 32
2.5 Results 37
2.6 Conclusions 41

3 Modeling of a walking piezo actuator **43**
3.1 Introduction 45
3.2 The piezo motor 47
3.3 Modeling 48
3.4 Model identification 57
3.5 Results 59
3.6 Conclusions 66

4 Waveform optimization **69**
4.1 Introduction . . . 71
4.2 The experimental setup . . . 73
4.3 Modeling . . . 75
4.4 Experimental validation . . . 83
4.5 Waveform optimization . . . 88
4.6 Conclusions . . . 96

5 Delay-varying repetitive control **97**
5.1 Introduction . . . 99
5.2 Repetitive control . . . 101
5.3 Delay-varying repetitive control . . . 103
5.4 Stability analysis . . . 106
5.5 Application and controller design . . . 113
5.6 Results . . . 121
5.7 Conclusions . . . 125

III The metrological AFM **127**

6 Control and hysteresis compensation **129**
6.1 Introduction . . . 131
6.2 The metrological AFM . . . 133
6.3 Identification . . . 136
6.4 Controller design . . . 141
6.5 Results . . . 145
6.6 Conclusions . . . 151

7 MIMO and repetitive control **153**
7.1 Introduction . . . 155
7.2 The metrological AFM . . . 157
7.3 Control design . . . 162
7.4 Directional repetitive control . . . 169
7.5 Experimental results . . . 175
7.6 Conclusions . . . 180

IV Optical incremental encoders **181**

8 Encoder velocity and acceleration **183**
8.1 Introduction . . . 185
8.2 Time-stamping concept . . . 187
8.3 Position reconstruction . . . 188

8.4 Skip option 190
8.5 Experimental results 192
8.6 Conclusions 198

9 Optimal higher-order time-stamping 199
9.1 Introduction 201
9.2 Higher-order time-stamping 204
9.3 Optimal parameter settings 210
9.4 Encoder errors 212
9.5 The experimental setup 213
9.6 Calibration results 215
9.7 HOTS results 216
9.8 Conclusions 223

V Closing 225

10 Conclusions and recommendations 227
10.1 Concluding remarks 227
10.2 Recommendations for future development 233

Bibliography 235

A Position-dependent dynamics 255
A.1 FRF measurements 255
A.2 Gain variations 258

B List of symbols 261

Summary 271

Samenvatting 273

Dankwoord 275

Curriculum Vitae 277

Part I

Motivation

Chapter 1

Introduction

Abstract - This chapter introduces the research objective of this thesis, which focusses on high-precision mechatronic systems, especially on nano-motion systems with piezo actuators and/or encoder sensors. To improve the performance of such systems, different performance limiting factors in nano-motion systems are modeled and compensation methods are developed in the form of new actuator driver software, encoder signal processing and control algorithms. Three representative cases of nano-motion systems are selected of which the performance will be improved using a performance-driven control procedure. Finally, the outline of this thesis is given.

1.1 Nano-motion systems

Both industrial and commercial high-tech mechatronic systems improved significantly during the past decades in terms of both speed and accuracy. It is expected that this trend will continue in the future. For example, state-of-the-art wafer scanners that currently produce 175 300 mm wafers per hour with features as small as 32 nm are expected to increase their throughput (>300) with larger wafers (450 mm) that contain even smaller features (<15 nm). Electron microscopes, which are currently able of magnifications up to sub-Angström level, are expected to increase their speed and accuracy of sample positioning and scanning. Commercial printers, nowadays capable of 65 pages per minute at a resolution of 600 - 1800 dpi, are expected to increase their throughput (>120 ppm) with an increased resolution (>5000 dpi).

The demand for an increase in accuracy and throughput of high-tech mechatronic systems enforces strict requirements on the motion-stages in these systems. The class of motion systems that require a movement with velocities ranging from nanometers per second to millimeters per second with (sub)nanometer resolution are referred to as nano-motion systems. Typical motion profiles for nano-motion systems encountered in industrial applications are constant velocity setpoints and point-to-point movements.

Nano-motion systems can be roughly divided into systems with short- and long-stroke drives. For both types, different actuators and sensors are available. In this thesis, we focus on nano-motion systems that are driven by piezo actuators and/or use encoder sensors. Piezo actuators are often used because of their attractive properties such as high reproducibility, high stiffness, fast response and good displacement resolution. For a detailed description on piezoelectricity, piezo actuators and their properties see [140,169,200,201]. Optical incremental encoders are often used since they provide a good resolution for a relatively low cost price. The length of the encoder rulers is scalable, such that optical incremental encoders can be used for both short- and long-stroke stages.

The increasing demands regarding speed and accuracy also hold for nano-motion systems. This thesis assumes that the mechanical and electrical design of the nano-motion system is fixed, which leaves the control design as the main degree of freedom to further improve performance. More specifically, the design freedom to be explored in this thesis is the actuator driver software, the sensor signal processing and the control algorithms. So, this thesis aims at improving the performance of nano-motion systems in terms of disturbance attenuation, accuracy and speed by improving the control design.

In parallel to the technological innovations in industry, scientific research has been performed to improve the performance of high-precision motion systems. Research areas include among others the development of new actuators, actuator drivers, mechanical designs, materials, sensor systems and control algorithms. The translation of state-of-the-art theoretical results to usable technology could open the way to significantly improve the performance of nano-motion systems. The desired performance is generally formulated on a system level, whereas the developed scientific formalisms mostly act on a component level. This makes the translation of theoretical results to usable technology non-trivial. Identification of the relevant system boundaries, inputs and outputs on a system level allows the performance limiting factor (PLF) to be identified and the appropriate scientific result to be selected on a component level. For industry, keeping an overview of all developed methods is often difficult or even impossible. On the other hand, in science, applications and their challenges are often not considered.

In this thesis, we focus on the modeling and compensation of several selected performance limiting factors (PLFs), which are believed to be commonly encountered in piezo-driven nano-motion systems with encoders. The identification of the main PLF itself is not explicitly considered. A set of PLFs is selected on the basis of experimentally obtained data from various nano-motion systems. In the next section, the selected PLFs are described.

1.2 Performance limiting factors

In nano-motion systems with piezo actuators and/or encoder sensors the following performance limiting factors (PLFs) are commonly encountered:

1. actuator driver software,
2. hysteresis,
3. stick-slip and contact dynamics,
4. repetitive disturbances,
5. coupling,
6. geometric nonlinearities,
7. quantization.

The above PLFs can be divided into sources that are related to the actuator driver, the sensor system and/or the system dynamics. The modeling and compensation techniques available in literature for the different PLFs will be discussed next.

1.2.1 Actuator driver software

Currently, piezo-driven nano-motion systems employ different types of piezo actuators. For short-stroke scanners, piezo tube actuators [40] or piezo stack actuators in different configurations [8,17,99,172] are commonly used. For applications that require a larger traveling length often stepping piezo motors are applied. Examples of stepping piezo motors are inchworm actuators [167, 200], ultrasonic motors [9, 201] and elliptical piezo motors in which one or more actuators cooperate to drive the nano-motion stage [12, 209]. The drive properties of piezo actuators are largely influenced by the driver software design.

The drive optimization techniques in literature can be split into optimization techniques that improve the properties for a given shape of the electric drive waveform to the piezo actuator [90, 101, 118] or techniques that optimize the shape itself [61, 152]. Currently available industrial drivers for stepping piezo motors

make use of basic driving waveforms, such as sinusoidal, triangular or trapezoidal waveforms, which do not exploit additional knowledge of the system to be driven.

Combining developed modeling techniques of system dynamics, piezoelectricity and several types of disturbances, e.g. friction, allows accurate models to be derived of nano-motion systems, which in turn can be used to develop accurate model-based actuator driver software that reduces this PLF in nano-motion systems.

1.2.2 Hysteresis

Piezo actuators are known to exhibit hysteresis. The application of linear control techniques to piezo-driven nano-motion systems with voltage steering does not fully compensate for the hysteresis. If the performance of a piezo-driven system is limited by the presence of hysteresis, several approaches can be followed. For a fixed hardware, a model-based feedforward or feedback controller can be employed.

Although hysteresis can be reduced by feedback control techniques [35, 130], always some amount of hysteresis remains since the feedback controller will have a finite attenuation of disturbances. Feedforward compensation techniques can be either data-based [105, 112, 220] or model-based using phenomenological operators [6,70,83,180], e.g., Maxwell slip, Preisach or Prandtl-Ishlinskii models, or using differential equations [50, 182, 190], e.g., Duhem, Bouc-Wen or Coleman-Hodgdon models.

In literature, a lot of research on hysteresis in various applications and on the modeling of this hysteresis is performed. However, the hysteresis effects are influenced by the design of the piezo actuator itself and by the way the actuator is incorporated in the nano-motion system. So, the reduction of the hysteresis PLF for every specific nano-motion system asks for a customized approach for which dedicated models have to be derived, e.g. by extending or altering existing hysteresis models available in literature.

1.2.3 Stick-slip and contact dynamics

Stepping piezo actuators rely on friction to drive the nano-motion stages. Slip between the actuator and the drive surface of the stage reduces the efficiency and results in wear of the actuator. Furthermore, the contact between the actuator and drive surface cannot be regarded as rigid. The contact dynamics influence the driving performance of the stepping piezo actuators.

To maximize efficiency and minimize actuator wear, stick-slip behavior and contact dynamics should be taken into account in the driver software design. In literature, several models have been proposed to model the stick-slip effects and their transition regions at a nanometer scale [7,146] and also to model the contact dynamics [16,145] between the actuator and the drive surface. However, the available models of stick-slip effects in literature are not commonly taken into account in the actuator driver software design to reduce the effect of these PLFs.

1.2.4 Repetitive disturbances

Systems that perform repetitive tasks or have repetitive components are subject to repetitive disturbances. For such systems, various techniques exist to improve the performance, e.g., mapping the disturbance in a look-up table [20], iterative learning control (ILC) [117,133,142] or repetitive control (RC) [34,77,81].

Standard RC assumes repetitive disturbances with a constant period-time. However, the repetitive disturbances can also be repetitive with respect to another variable than time, possibly resulting in repetitive disturbances with a non-constant period-time. This is especially the case for piezo-driven nano-motion systems since the piezo actuators act as position actuators and are often driven by harmonic waveforms. Fluctuations in the harmonic waveforms directly influence the period-time of the repetitive disturbances. In literature, methods have been described to cope with repetitive disturbances with a varying period-time, such as a adaptive RC [27,30,199], RC with a coordinate transformation to a fully repetitive domain [33,191] and higher order RC [157,185].

However, most existing methods do not employ knowledge of the period-varying disturbance. If the nature of the variation can be modeled and taken into account in the design of the learning controller, this PLF is expected to be compensated more accurately.

1.2.5 Coupling

Nano-motion systems that contain several degrees-of-freedom (DOFs) and multiple actuators and sensors are generally designed such that each actuator-sensor pair ideally only influences only a single DOF. However, always a certain amount of coupling between the different DOFs is present, especially at a nanometer scale. The use of decentralized controllers will therefore often not leave enough room for improvement to reduce the coupling PLF.

In the control design of multi-DOF nano-motion systems, such as atomic force microscopes (AFMs), the coupling between the different DOFs is often assumed to be negligible small [149] and separate single-input single-output (SISO) controllers are used for the different axes. Multiple-input multiple-output (MIMO) controllers are not commonly used, although they could improve the performance of AFMs [26]. Combining existing techniques in literature on the modeling, analysis and control synthesis of MIMO systems allows for a systematic assessment of the coupling between the different axes and a control synthesis that guarantees both stability and performance of the controlled MIMO nano-motion system.

1.2.6 Geometric nonlinearities

Geometric nonlinearities in systems can be introduced by the actuator choice, the actuator driver (software), or the mechanical design of the stages. This can result in operating point dependent system dynamics, e.g., a position-dependent actuator or system gain. The inclusion of the geometric nonlinearities in the control synthesis model is expected to guarantee stability and improve the performance of nano-motion systems with geometric nonlinearities.

The nature of the geometric nonlinearities can be analyzed using the existing methods in literature on system identification in combination with linearization techniques. Using the identified characteristics of the geometric nonlinearities, an appropriate control synthesis method can be selected, e.g., $\mathcal{H}_\infty$ control, gain scheduling or linear-parameter-varying (LPV) control.

1.2.7 Quantization

The use of optical incremental encoders for the position measurements in nano-motion systems introduces quantization errors in the measurements, which limit the accuracy of the position measurements. A cost-effective way to reduce the effect of quantization is to add signal processing algorithms to the encoder sensor. Existing signal processing techniques of encoder measurements can be divided into postfiltering techniques [88, 115, 202], observer based techniques [14, 100, 196], or indirect measurement techniques [15, 23, 106].

Recent technological advances allow capturing and storage of the time and position information of encoder transitions in hardware, which is referred to as encoder time-stamping. Integration of encoder time-stamping with signal analysis techniques and modeling of the encoder errors is expected to facilitate compensation of the quantization errors.

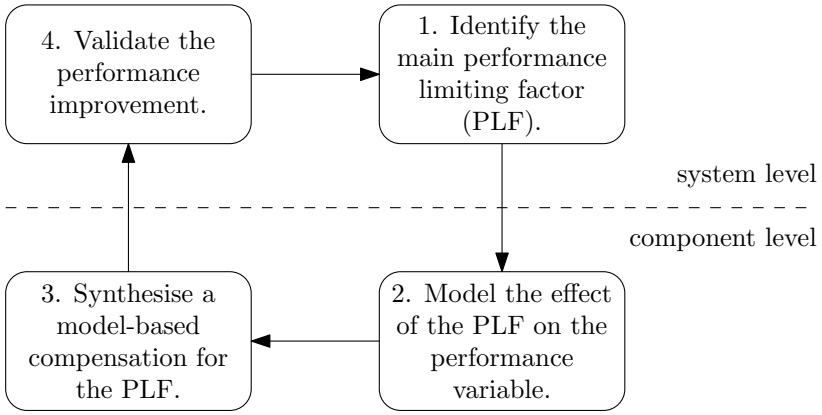

Figure 1.1: Flowchart of the adopted procedure of selecting, modeling and compensating the performance limiting factors (PLFs) in nano-motion systems.

1.3 Thesis goals

The goal of this thesis is to systematically explore the opportunities to improve the performance of nano-motion systems with piezo actuators and/or encoder sensors by developing new actuator driver software, sensor signal processing and/or control algorithms. The mechanical and electrical hardware design is considered to be fixed. The hypothesis is that the performance of many existing nano-motion systems can be improved by incorporating model-based technology from recent theoretical results. Therefore, this thesis aims to bridge the gap between science and technology in translating developed theoretical methods to usable technology.

To systematically improve the performance of nano-motion systems, we adopt the procedure as depicted in Fig. 1.1. Firstly, the performance of the nano-motion system is evaluated from a system point-of-view. The component that limits the performance is identified from the measured performance. This component is referred to as the performance limiting factor (PLF). Secondly, the influence of the identified PLF on the performance is modeled. Thirdly, a model-based compensation method for the PLF is derived and implemented in the nano-motion system. Finally, the obtained performance improvement is evaluated. Iterative application of this procedure enables different PLFs to be compensated successively.

The procedure of Fig. 1.1 starts on a system level in the first step, zooms in to the component level for the modeling and compensation in steps two and three and returns to system level for the performance evaluation in step four. In order to

obtain an overall performance improvement, identification of the correct PLF is crucial. Obviously, the identification is strongly problem-dependent, hence, providing a general identification procedure is difficult. Generally, engineering knowledge and/or experience with the system under consideration is required in this step. During the design phase of high-precision motion systems, error budgeting and decomposition techniques [86,144] from systems engineering are already widely used and give a structured analysis procedure for determining relevant PLFs. For a given electro-mechanical design and a realized hardware setup, a careful time and frequency domain analysis of the tracking error will be performed as a starting point to identify the main PLF [87,186].

In this thesis, we focus on the second, third and fourth step in the procedure of Fig. 1.1, i.e., the identification step is not explicitly considered. For the compensation of a specific PLF, existing state-of-the-art control theory is mostly not directly applicable. The synthesis of a suitable compensation method can require an adjustment, extension, or combination of one or multiple methods or new methods to be developed in order to compensate the PLF and improve the performance of the nano-motion system.

To meet the thesis goal, the following objectives are formulated:

1. **Nano-motion piezo actuation**
   Investigate the different types of piezo actuators for driving nano-motion systems with short and long strokes. Derive appropriate models that can be used for design optimization and/or control design purposes.

2. **Piezo driver software design**
   Develop actuator driver software to drive a long-stroke nano-motion system with a stepping piezo motor employing multiple actuators.

3. **Control of nano-motion systems**
   Develop appropriate feedback and feedforward control algorithms for short- and long-stroke piezo-driven nano-motion systems.

4. **Signal processing for incremental encoders**
   Investigate the available techniques in literature and develop an appropriate signal processing technique to suppress the quantization errors and imperfections in incremental encoders.

5. **Experimental implementation**
   Implement the derived actuator driver software, sensor signal processing and control algorithms and validate the obtained performance improvement of the nano-motion system under study.

To show the applicability of the adopted procedure to improve the performance of nano-motion systems and meet the research objectives, three representative cases of nano-motion systems with piezo encoders and/or encoder sensors are selected, which will be described in the next section. So, instead of selecting an application to which a specific method can be applied, several applications representing a class of systems are selected as the starting point of this research.

1.4 Case descriptions

Three representative cases of nano-motion systems with piezo actuators and/or encoder sensors are selected, which include two piezo-driven nano-motion stages, one with a short stroke and one with a long stroke, and an encoder system. The long-stroke nano-motion system is a 1-DOF stage driven by an elliptical walking piezo motor employing four bimorph piezo legs together with an incremental encoder to measure the position. The short-stroke nano-motion system is a metrological atomic force microscope (AFM) with a 3-DOF stage driven by piezo stack actuators through a flexure mechanism. The AFM uses a laser interferometer to measure the position of the stage in all three DOFs. For the objective concerning the incremental encoders, the long-stroke piezo-driven stage is not used since the encoder signal also contains effects caused by system dynamics and/or the actuator driver. In order to isolate the encoder sensor, a third case is selected consisting of a rotating mass with encoders directly coupled to the motor and mass.

The three cases will be explained in more detail in the remainder of this section. For each case the encountered PLFs and the performance specifications are indicated.

1.4.1 Walking piezo actuator

The first case is a long-stroke nano-motion system consisting of 1-DOF stage driven by a walking piezo actuator. The walking piezo motor, shown in Fig. 1.2(a), contains four bimorph piezoelectric drive legs, which are driven by electric waveforms via the connector. Each leg is covered with an aluminum oxide drive pad. The walking piezo motor is fitted to the stage with a dedicated motor suspension. The drive pads are pressed against the drive surface of the stage using preload springs. The position of the stage is measured using an optical incremental encoder.

A schematic representation of the working principle of the piezo motor is shown in Fig. 1.2(b). Each bimorph piezo leg contains two electrically separated piezo stacks. The legs elongate if equal voltages are applied to the two stacks in a

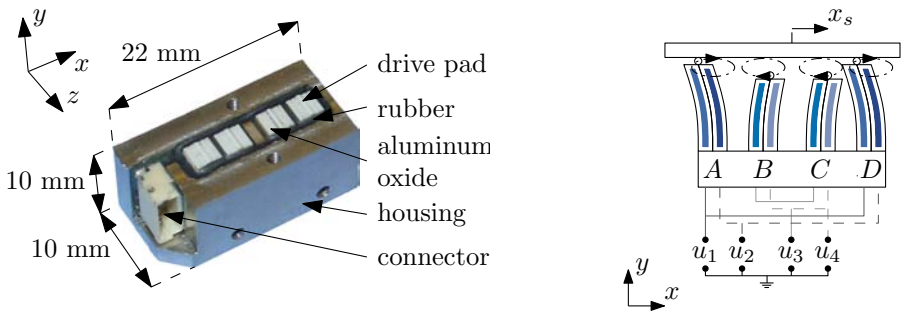

(a) The walking piezo motor [155].

(b) Working principle.

Figure 1.2: The walking piezo actuator and its working principle.

leg. Applying different voltages causes the legs to bend. By choice of the supply voltages u_i (V), $i \in \{1, 2, 3, 4\}$, the tips of the drive legs can be positioned in a working region in the (x, y)-plane. The four piezo legs drive the nano-motion stage in pairs of two by performing an alternating walking movement.

The linear drive nano-motion stage should be able to perform two types of setpoints. Firstly, the stage should be able to track constant velocity setpoints with velocities ranging from nanometers per second to millimeters per second. Secondly, point-to-point movements should be possible over a distance ranging from nanometers to the complete stroke of the stage. The desired accuracy of both types of movements is within nanometers up to micrometers for all setpoints.

The PLFs in the nano-motion stage driven by the walking piezo actuator are the non-optimal cooperation of the different legs in the actuator, the stick-slip effects between the drive legs and the stage, the repetitive disturbances introduced by the periodic walking movement and the changing system dynamics, which are dependent on the varying contribution of the legs in the drive direction over one drive cycle, prescribed by the electric drive waveforms to the piezo legs.

1.4.2 Atomic force microscope

The second case is a metrological atomic force microscope (AFM), which contains a 3-DOF stage driven by piezo stack actuators through a flexure mechanism. The metrological AFM, shown in Fig. 1.3(a), is used to calibrate transfer standards for commercial AFMs. The height of the samples is measured at (sub)nanometer resolution by scanning the surface of the sample using a cantilever with an atomically sharp tip. The metrological AFM consists of a Topometrix AFM head containing

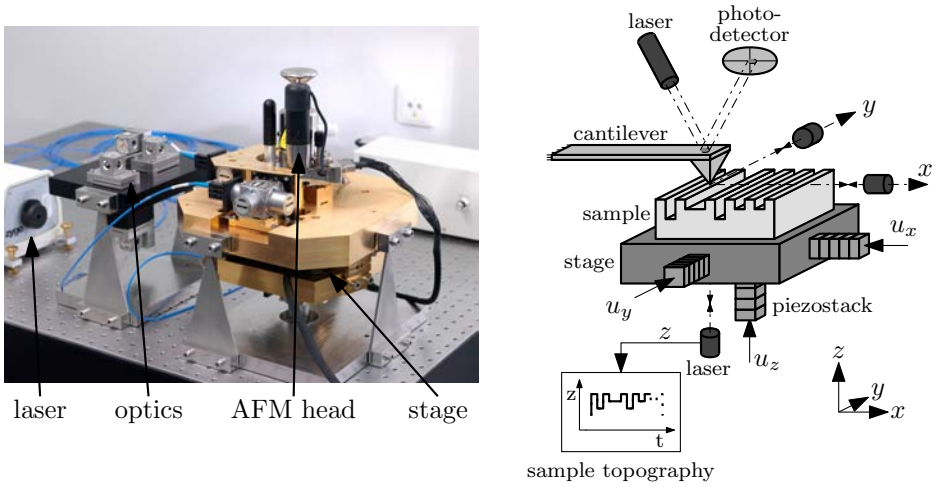

(a) The metrological AFM.

(b) Schematic representation.

Figure 1.3: The metrological AFM and a schematic representation of the working principle.

the cantilever, a 3-DOF piezo-driven stage and a laser interferometer to measure the stage position in all DOFs.

A schematic representation of the AFM is shown in Fig. 1.3(b). To position the sample, feedback control is applied using the inputs to all piezo stack actuators and the outputs of the laser measurements in the scanning x- and y-directions and of the photo-detector of the AFM head in z-direction.

For imaging purposes, the x- and y-directions perform a scanning movement over the sample where one axis is chosen to be the fast scanning axes, which tracks triangular setpoints, and the other axes moves the stage from line to line. The z-direction is controlled to a constant deflection of the cantilever, which reduces Abbe errors and makes it possible to measure the sample topography directly using the laser interferometer in z-direction. To obtain an accurate sample image and avoid postprocessing of the obtained image, a maximum tracking errors of one nanometer is desired for all axes.

The encountered PLFs in the metrological AFM with the short-stroke piezo-driven 3-DOF stage are the hysteresis in the piezo stack actuators, the dynamic coupling between the different axes of the stage and the repetitive disturbances introduced by the scanning movement of and the transfer samples under the AFM.

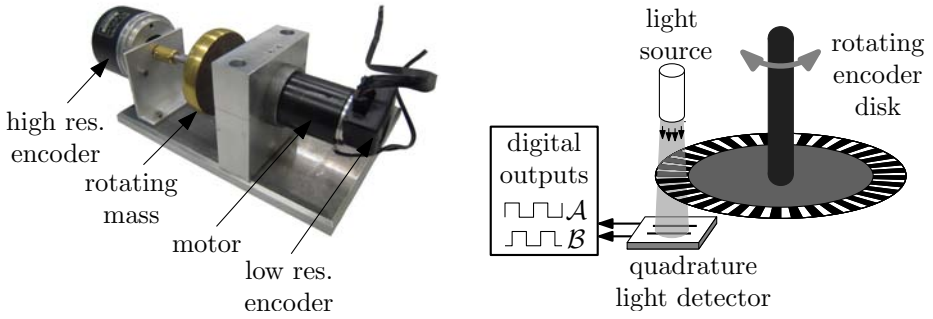

(a) The encoder system.

(b) Encoder working principle.

Figure 1.4: The encoder system and the working principle of an optical incremental encoder.

1.4.3 Encoder system

The third case is an encoder system, shown in Fig. 1.4(a). The encoder system consists of a rotating mass that is connected to a DC motor. On the motor an encoder is mounted with a resolution of 100 slits per revolution, to which the developed encoder signal processing algorithms are applied. The results are compared to a high-resolution encoder with 5000 slits per revolution as a reference, which is mounted onto the other side of the rotating mass.

A schematic representation of the working principle of an optical incremental encoder is shown in Fig. 1.4(b). The typical stair-cased position measurement of the encoder is obtained by counting the up and down changes of the pulse signals of the quadrature light detector, denoted by $\mathcal{A}$ and $\mathcal{B}$. The setup of Fig. 1.4(a) is combined with encoder time-stamping, which captures encoder events, consisting of the position transitions and their time instants, at a high-resolution clock and stores them in a hardware register in the data-acquisition device.

The typical setpoints for nano-motion systems are also applied to the encoder setup, i.e., constant velocity setpoints and point-to-point movements. Constant velocity setpoints are the most easy setpoint for signal processing algorithms due to the equidistant spacing of encoder events in both position and time. Therefore, also sinusoidal setpoints are used since they have a continuous variation in the velocity, thus also in the event rate of the encoder. The desired accuracy of the encoder signal processing algorithms is to make the output of the low resolution encoder as accurate as the measured position of the high-resolution reference encoder.

The PLFs in the encoder system are the quantization of the position measurement and the repetitive disturbances caused by the position dependent imperfections in the rotary encoder.

1.5 Outline

The main content of the thesis is split into three parts according to the three cases. The part is indicated by a small picture next to the page number, where indicates the long-stroke piezo-driven nano-motion stage, indicates the metrological AFM with the short-stroke 3-DOF piezo stage and indicates the encoder system.

The different encountered PLFs in nano-motion systems are addressed in different chapters for the various cases. The PLFs related to the actuator choice are the driver design and hysteresis effects. The system induced PLFs are stick-slip effects in the actuation, repetitive disturbances, coupling effects between axes and geometric nonlinearities. Finally, the quantization PLF is related to the encoder sensors.

In this thesis, we will propose new actuator driver software for the long-stroke nano-motion stage with the walking piezo actuator to compensate for the driver design and stick-slip PLFs. Feedback and feedforward control algorithms will be introduced to compensate for the geometric nonlinearities in the long-stroke nano-motion stage, for the repetitive disturbances in both the long-stroke nano-motion stage and the metrological AFM and for the hysteresis and coupling effects in the metrological AFM. Finally, the quantization effects and repetitive disturbances in the encoder setup will be compensated by introducing a new encoder signal processing method. Table 1.1 gives an overview of which PLFs will be addressed in the different chapters for the different cases. The outline of the different parts in this thesis is as follows.

In Chapter 2, the feedback control structure of the walking piezo actuator and the drive principle will be discussed. Also, a new drive principle with asymmetric waveforms will be proposed to improve the tracking performance of the nano-motion stage. A dynamic model of the walking piezo actuator will be presented in Chapter 3. The model can be used for design optimization of different motors with different properties and for a dynamic analysis to determine the maximum allowable walking frequency. A model of the stage and piezo motor containing the switching behavior between the drive legs, stick-slip effects and contact dynamics between the piezo legs and the stage will be derived in Chapter 4. With this model, new waveforms will be developed resulting in optimal drive properties at constant velocity of the stage. The repetitive disturbances introduced by the

Table 1.1: Overview of the selected performance limiting factors (PLFs) for the various experimental cases. Parts II and III consider piezo-driven nano-motion stages with a long and short stroke, respectively. Encoder sensors are contained in parts II and IV, but are studied in detail in part IV.

PLF	PART II: Piezo actuator (see Fig. 1.2)	PART III: AFM (see Fig. 1.3)	PART IV: Encoder (see Fig. 1.4)
Driver design	Chapters 2, 3, 4		
Hysteresis		Chapter 6	
Stick-slip	Chapter 4		
Repetitive	Chapter 5	Chapter 7	Chapter 9
Coupling		Chapters 6, 7	
Geometric nonlinearities	Chapters 2, 3		
Quantization			Chapters 8, 9

walking movement of the piezo motor will be compensated using a delay-varying repetitive control scheme in Chapter 5.

The coupling and hysteresis effects of the piezo stack actuators in the metrological AFM will be analyzed in Chapter 6. An adjusted Coleman-Hodgdon model will be developed to compensate for the asymmetric hysteresis in the metrological AFM. To reduce the coupling effects between the different axes and to compensate for the repetitive disturbances introduces by the scanning movement and the sample topography, MIMO and repetitive controllers will be developed and applied to the metrological AFM in Chapter 7.

To overcome the quantization errors in the encoder system, an online time-stamping based algorithm is developed to estimate the position, velocity and acceleration signals, which will be presented in Chapter 8. A method to determine the optimal settings for this algorithm and a compensation method for the repetitive disturbances introduced by the encoder imperfections will be described in Chapter 9.

Finally, in Chapter 10 the main conclusions of this research will be summarized and recommendations for future research will be given.

All chapters in this thesis are based on separately published papers, they can all be read independently. For the same reason, some sections of different chapters are overlapping.

Part II

The walking piezo actuator

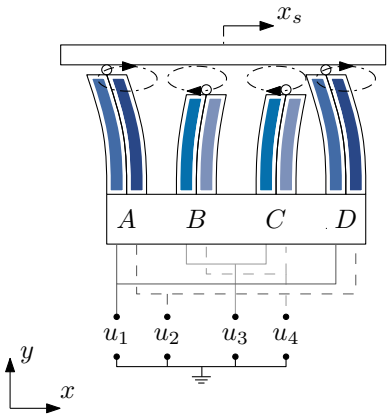

Chapter 2

Drive principle and feedback control

Abstract - Piezoelectric actuators are commonly used for micro-positioning systems at nanometer resolution. Increasing demands regarding the speed and accuracy are invoking the need for new actuators and new drive principles. A non-resonant walking piezoelectric actuator is used to drive a stage with one degree-of-freedom through four piezoelectric drive legs. In order to improve the positioning accuracy of the stage, a new drive principle and control strategy for the walking piezo motor are proposed in this chapter. The proposed drive principle results in overlapping tip trajectories of the drive legs, resulting in a continuous and smooth drive movement. Gain scheduling feedback in combination with feedforward control further improves the performance of the stage. With the developed drive principle and control strategy, the piezo motor is able to drive the stage at constant velocities between 100 nm/s and 1 μm/s with a tracking error below the encoder resolution of 5 nm. Constant velocities up to 2 mm/s are performed with tracking errors below 400 nm. Point-to-point movements between 5 nm and the complete stroke of the stage are performed with a final static error below the encoder resolution.

This chapter is based on: R. J. E. Merry, N. de Kleijn, M. J. G. van de Molengraft, and M. Steinbuch. Using a walking piezo actuator to drive and control a high precision stage. *IEEE/ASME Transactions on Mechatronics*, 14(1):21–31, February 2009.

2.1 Introduction

Piezoelectric elements are able to perform very small reproducible deformations. This makes them very attractive for use in micro positioning systems such as ultra-precision machine tools, miniature robots, microscopes, converters, and nano-motion stages. The ever increasing demands on micro positioning systems regarding speed and accuracy also invoke the need for faster and more accurate positioning systems.

Our interest in this chapter is to drive a nano-motion stage using a walking piezo actuator. The main challenge was to allow the stage to be driven in a wide range of velocities from mm/s to nm/s with an accuracy of sub-micrometer to nanometer, respectively. In addition, the velocity of the stage must be continuously adjustable.

In literature, piezo-driven nano-motion stages with large traveling lengths are actuated using piezo motors with two different working principles. The first type, the hybrid transducer motors or inchworm motors, use separate clamping and drive actuators to perform the motion [167, 178, 200, 222]. With this type of actuator, it is difficult to obtain a continuous and smooth motion due to the sequential alternation between three independent actuators. The second type, which we refer to as elliptical motors, excites the piezoelectric material such that the tip of the material performs an elliptical movement. Such actuators can be driven at frequencies above 20 kHz and are called ultrasonic motors [9, 55, 201]. The ultrasonic motors can reach velocities up to 100 mm/s. However, at low velocities stick-slip occurs. This makes the ultrasonic motors unsuitable for tracking low velocities. Alternatively, the elliptical motors can be driven at frequencies below the ultrasonic range (sub-ultrasonic frequencies). These motors exhibit significantly less stick-slip [209].

In order to avoid stick-slip, in this research we choose to use a special kind of elliptical motors, referred to as distributed micro-motion systems (DMMS) [12], in which multiple microactuators cooperate to perform a task. DMMS piezo systems can be used to construct actuators with multiple piezoelectric legs.

The DMMS actuator used in [209] employs multiple piezoelectric legs, driven at a fixed frequency of around 40 Hz: as a result of which it is very difficult to continuously adjust the drive velocity, which is desirable in nano-motion stages. A walking DMMS actuator with a few hundred legs is used in [161]. The elliptical motion of each rigid leg is obtained through phasing of three bimorph piezoelectric beams. The mechanical design results in a large spatial separation of the different legs, making the actuator unsuitable for use in nano-motion stages. A rotating DMMS robot with three piezoelectric elements, based on the inchworm principle, is

described in [65]. The three piezos are driven by rectangular waveforms and their sequence is determined by on/off-type control signals. Sawtooth driving pulses are used in [93] to obtain a movement of three piezo legs for micro-positioning purposes. Movement is obtained by slow bending and quick stretching of the piezo legs. The used drive principle is not useful for very low velocities (nm/s) and has an inherent slip between the legs and drive surface.

However, the above mentioned piezoelectric motors of both working principles are not capable of continuously adjusting the drive frequency and driving the stages at a wide range of velocities with the desired accuracy.

In order to improve the performance of high-precision nano-motion stages, we employ a piezo motor with a different working principle. The piezo motor will be used to drive a stage with two different movements; constant velocity profiles (also referred to as jogging mode) and point-to-point movements. These movements are common in many motion applications. To steer the four piezo legs and to enable the motor to be used in a feedback control configuration, an appropriate driver for the walking piezo motor is proposed. Furthermore, a control method is proposed to account for varying system dynamics that arise when altering the step size of the piezo motor during point-to-point movements. The performance limiting factors (PLFs) that are considered in this chapter are the non-smooth operation with the available actuator driver software and the varying system dynamics.

The employed piezo motor is a DMMS actuator driven at sub-ultrasonic frequencies. The piezo motor, called the Piezo LEGS motor, was developed by Piezomotor Uppsala AB [155]. The piezo motor uses four piezoelectric drive legs to perform a walking movement. The legs employ a bimorph working principle, i.e., they are composed of two electrically separated piezo stacks that are excited independently by different waveforms. The drive velocity of the piezo motor can be continuously adjusted.

Different waveforms and control methods are used to drive bimorph DMMS piezoelectric actuators. A comparison of triangular, rectangular and sinusoidal waveforms for an inchworm actuator is performed in [101], in which the sinusoidal and triangular waveforms perform best. Feedback control of piezo driven systems can be performed in different ways. In [66], an ultrasonic multilayered piezoelectric element is controlled using a measurement of the induced charge at the piezo. Since measurements of the electrodes at both ends of all piezo stacks are required, this method is not applicable to the walking piezo motor considered in this research. For non-walking actuators, the voltage to the piezo actuator can be controlled directly [40, 82]. However, to obtain the alternating walking movement of the different piezo legs, periodic waveforms must be used. In [42], the step frequency for a micro-robot containing bimorph legs is controlled using self-learning techniques.

A four legged multi-DOF piezoelectric resonant actuator is controlled in [59] using the amplitude of sinusoidal waveforms. The resonant working principle restricts the waveform design to sinusoidal shapes.

The movement of the piezo legs is by design restricted to a rhombic area. For smooth operation, electric driving waveforms should be selected such that the trajectory of the legs has a continuous derivative in the (x, y)-plane [92]. In this chapter, harmonic waveforms have been used to drive the four piezo legs with elliptical tip trajectories. The harmonic waveforms have a limited frequency content to avoid excitation of high frequent dynamics and to enable the motor to be used in a feedback control strategy by controlling the angular velocity of the legs through the frequency of the waveforms. Control of the amplitude and phase makes it possible to continuously adjust the step size of the piezo legs.

To improve the actuator driver software, we present alternative waveforms to drive the four legs of the piezo motor, resulting in overlapping tip trajectories and a reduced tracking error of the nano-motion stage. Furthermore, a control algorithm is described in which the frequency of the waveforms is controlled by position feedback. The control algorithm includes feedforward control and gain scheduling to adjust the step size through the amplitude and phase of the waveforms. The experimental results show the applicability of the proposed control algorithm and procedure for use in nano-motion applications.

This chapter is organized as follows. First, the working principle of the piezo motor will be explained in Section 2.2. In Section 2.3, the design of the motor suspension, the modeling, and the identification of the walking piezo motor will be discussed. The developed waveforms and control strategy will be described in Section 2.4. The results of the experiments will be presented in Section 2.5. Finally, conclusions will be drawn in Section 2.6.

2.2 The piezo motor

The piezo motor, shown in Fig. 2.1, has four piezoelectric drive legs. The drive legs are driven by electric waveforms via the connector. The top of each leg is covered with an aluminum oxide drive pad. The drive legs make contact with the drive surface through the drive pads. The legs are cast in rubber to add damping to the movement. The dimensions of the piezo motor of Fig. 2.1 are 22×10×10 mm. Its weight equals 15 g.

The piezoelectric legs consist of two electrically separated piezo stacks. The piezo stacks elongate when they are electrically charged. A schematic representation of

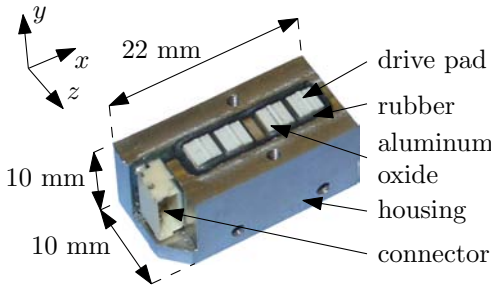

Figure 2.1: The used piezo motor [155].

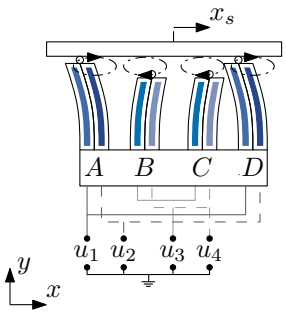

Figure 2.2: The working principle of the piezo motor.

the side view and the working principle of the piezo motor are shown in Fig. 2.2. The legs elongate in y-direction when an equal voltage is applied to the two stacks of one leg. Applying different voltages on the two stacks of one leg causes the leg to bend. By choice of the supply voltages, the tip of the drive leg can be put in a working region in the (x, y)-plane (see Fig. 2.2) spanned by the waveforms $u_i(t)$ (V), $i \in \{1, 2, 3, 4\}$ with $\min(u_i) = 0$ V and $\max(u_i) = 46$ V.

As can be seen in Fig. 2.2, the drive legs always work together in pairs. The first pair of legs p_1, consisting of legs A and D, is driven by the input waveforms $u_1(t)$ (V) and $u_2(t)$ (V). The second pair p_2, consisting of legs B and C, is driven by $u_3(t)$ (V) and $u_4(t)$ (V). The waveforms $u_i(t)$ (V), $i \in \{1, 2, 3, 4\}$ can be chosen such that the elongation of the pairs or legs in y-direction implies that at all times only one pair of legs is in contact with the drive surface and such that the pairs of legs perform a movement in x-direction to drive a stage. The position of the tip of the legs in x- (m) and y-direction (m) can be described as

$$\begin{aligned} x_{p_1}(t) &= c_x \left(u_1(t) - u_2(t)\right), \\ x_{p_2}(t) &= c_x \left(u_3(t) - u_4(t)\right), \\ y_{p_1}(t) &= c_y \left(u_1(t) + u_2(t)\right), \\ y_{p_2}(t) &= c_y \left(u_3(t) + u_4(t)\right), \end{aligned} \tag{2.1}$$

where c_x (m/V) and c_y (m/V) are the constant bending and extension coefficients, respectively [92]. The tip trajectories become elliptical when sinusoidal waveforms

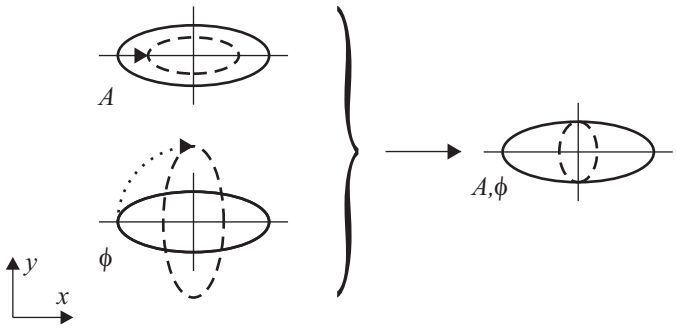

Figure 2.3: Influence of the amplitude A (V) and phase ϕ (rad) on the elliptical trajectory of the tip of the drive leg.

are used as

$$\begin{aligned} u_1(t) &= \frac{A}{2}\sin(\alpha(t)) + \frac{A}{2}, \\ u_2(t) &= \frac{A}{2}\sin(\alpha(t) + \pi/2 + \phi(t)) + \frac{A}{2}, \\ u_3(t) &= \frac{A}{2}\sin(\alpha(t) + \pi) + \frac{A}{2}, \\ u_4(t) &= \frac{A}{2}\sin(\alpha(t) + 3\pi/2 + \phi(t)) + \frac{A}{2}, \end{aligned} \tag{2.2}$$

where A (V) is the amplitude, α (rad) is the angle, and $\phi(t)$ (rad) is an additional phase shift. The phase difference of π rad between $u_1(t)$ and $u_3(t)$ and between $u_2(t)$ and $u_4(t)$, i.e., between the waveforms of the pair p_1 and the waveforms of the pair p_2, results in a phase shift of π rad between the movements of the two pairs of legs. The phase shift results in an alternation of the driving pair of legs such that only one pair is in contact with the drive surface at all times except for the transition point. To obtain an equal leg movement for both pairs, the additional phase shift $\phi(t)$ (rad) is chosen equal for both pairs of legs.

The angular velocity $\Omega(t) = d\alpha(t)/dt$ (rad/s) of (2.2) determines the number of elliptical trajectories per second. In addition, it only slightly influences the shape of the elliptical trajectory. The shape of the ellipsoid is determined mainly by the amplitude A and the phase ϕ. The amplitude A determines the size of the ellipse and the phase ϕ determines the orientation of the ellipse, as shown in Fig. 2.3.

The piezo motor used for the research of this chapter has a maximum input voltage of 46 V [92]. With an amplitude A of 46 V and phase difference of $\pi/2$ rad between the input waveforms of one pair, the maximum step size equals 4 μm. By adjusting A and ϕ, the step size can be varied between 100 nm and 4 μm.

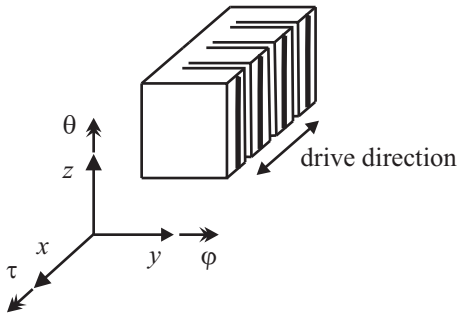

Figure 2.4: DOFs of the walking piezo motor.

2.3 System description and modeling

The piezo motor is used to drive a one degree-of-freedom (DOF) stage. The piezo motor is mounted onto the 1-DOF stage. Proper alignment between the motor and drive surface is necessary to obtain optimal efficiency of the motor, i.e., to minimize wear and slip of the drive legs. A motor suspension was designed that mounts the motor to the stage. The motor suspension prescribes all DOFs between the motor and the drive surface and allows for some degree of alignment. The suspension design will be discussed in Section 2.3.1.

In Section 2.3.2, a derived model of the system, consisting of the stage and the motor, will be presented. The model is based on first principles. The model parameters will be identified using experimental data.

2.3.1 Suspension design

The drive pads of the piezo motor should form proper line contacts with the drive surface of the stage. Therefore, the different DOFs as indicated in Fig. 2.4 should be prescribed by the suspension.

The motor suspension must prescribe the x- and z-DOFs to position the motor with respect to the drive surface of the stage. The translational DOF in y-direction and the rotational DOFs in τ- and θ-directions must be adjustable to create line contacts between the motor and the drive surface without introducing stress, which would cause deformation in the suspension or motor. Misalignment in τ-direction would cause wear of the drive pads. A deviation in θ-direction would induce some of the drive legs to lose contact with the drive surface. In y-direction a preload

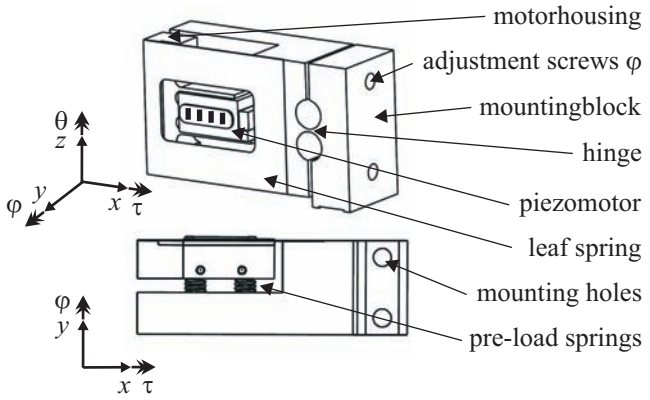

Figure 2.5: Design of the motor suspension.

is applied to create stiff line contacts. Finally the φ-direction must be adjustable to enable alignment between the motor and the drive surface. Misalignment in φ-direction would cause slip because the driving force in x-direction would also have a component in the z-direction.

The motor suspension design is shown in Fig. 2.5. The leaf spring constrains the x-, z- and φ-directions. Adjustment in φ-direction is made possible by an elastic hinge. Adjustment screws enable alignment of the motor by prescribing a rotation in φ-direction. Compression springs provide the preload in y-direction and press the legs against the drive surface of the stage, which prescribes the position in the y-, τ- and θ-directions. Alignment in τ-direction is obtained by the line contact of the legs through the preload springs and by the flexibility of the leaf spring in τ-direction. Table 2.1 gives an overview how the different DOFs are fixed or prescribed by the different parts in the motor suspension.

Table 2.1: Fixation and prescription of the different DOFs by the suspension for the walking piezo motor.

DOF	Fixed by	Prescribed through
x	leaf spring	-
y	-	line contacts between legs and stage
z	leaf spring	-
τ	-	line contacts between legs and stage
φ	leaf spring	adjustment screws φ
θ	-	line contacts between legs and stage

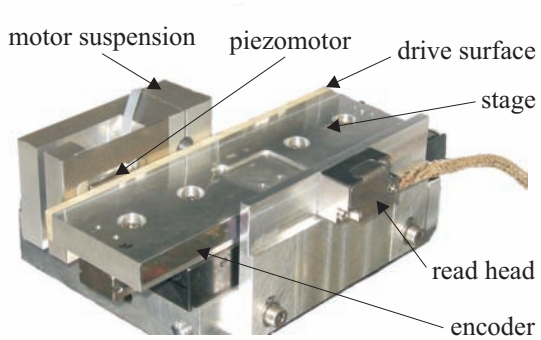

Figure 2.6: The experimental setup.

The motor suspension positions the drive legs of the walking piezo motor with respect to the drive surface of the 1-DOF stage. Since the drive legs of the piezo motor perform a walking movement, the motor suspension does not affect the stroke of the motor, which is unlimited by the working principle.

The preload in y-direction of the compression springs causes the drive legs of the piezo motor to be pressed against the drive surface. Therefore, at all times at least one pair of drive legs is in contact with the drive surface. The amount of preload determines the friction between the drive pads and the drive surface and thus the holding force F_h (N) of the motor as

$$F_h = \gamma F_p,$$

where F_p (N) is the preload force of the compression springs and γ (-) the friction coefficient. Since the friction force is independent on the contact area, the driving force is not determined by the number of legs that touch the drive surface.

2.3.2 System identification

The experimental setup of Fig. 2.6 consists of the motor suspension, the piezo motor, and a 1-DOF stage. The position of the stage is measured using a Heidenhain LIF 481 optical incremental linear encoder with a resolution of 5 nm [78]. The generation of the waveforms to the piezo motor and the position measurement of the encoder are performed using a TUeDACs AQI data-acquisition device [204], APEX PB51 amplifiers [10], and a computer. Environmental vibrations are isolated from the system by an air suspension.

A schematic model of the setup is shown in Fig. 2.7. The position of the pair of

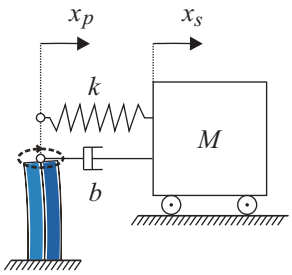

Figure 2.7: Schematic model of the setup of Fig. 2.6.

piezo legs, prescribed by (2.1) and (2.2), is denoted by x_p (m). When the legs are in the straight upright position, the position $x_p = 0$. The position of the stage is denoted by x_s (m). The spring incorporates the combined stiffness of the piezo legs and the motor suspension. The rubber casting, which surrounds the legs of the piezo motor (see Fig. 2.1), is modeled by a damper.

The equation of motion for the model of Fig. 2.7 is

$$M\ddot{x}_s(t) = k(x_p(t) - x_s(t)) + b(\dot{x}_p(t) - \dot{x}_s(t)). \tag{2.3}$$

Substitution of (2.1) in (2.3) gives

$$M\ddot{x}_s(t) = \begin{cases} k[c_x(u_1(t) - u_2(t)) - x_s(t)] + b[c_x(\dot{u}_1(t) - \dot{u}_2(t)) - \dot{x}_s(t)], \\ \qquad\qquad\qquad\qquad\qquad\qquad \text{if } y_{p_1}(t) \geq y_{p_2}(t), \\ k[c_x(u_3(t) - u_4(t)) - x_s(t)] + b[c_x(\dot{u}_3(t) - \dot{u}_4(t)) - \dot{x}_s(t)], \\ \qquad\qquad\qquad\qquad\qquad\qquad \text{if } y_{p_1}(t) < y_{p_2}(t). \end{cases}$$

The heights of the pair of drive legs (y_{p_1} and y_{p_2}) determine which pair of legs drives the stage.

The angular velocity $\Omega(t)$ of the sinusoidal waveforms $u_i(t),\ i \in \{1, 2, 3, 4\}$ (see (2.2)) determines the number of steps per second and is proportional to the speed of the stage. The velocity and thus the position of the stage are prescribed by controlling the angular velocity through the desired drive frequency $f_\alpha(t)$ (Hz) of the waveforms. The angle $\alpha(t)$ of the waveforms (2.2) is therefore chosen as

$$\alpha(t) = 2\pi \int_0^t f_\alpha(\tau) d\tau.$$

From (2.3) follows that the transfer function from the position of the legs x_p to the position of the stage x_s equals

$$\frac{X_s(s)}{X_p(s)} = \frac{bs + k}{Ms^2 + bs + k}. \tag{2.4}$$

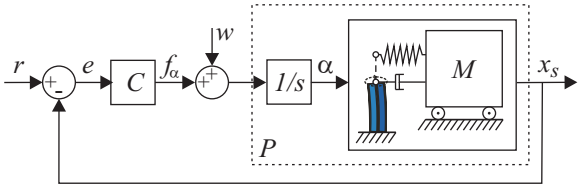

Figure 2.8: Control scheme for the FRF measurement.

Since the drive frequency of the waveforms is proportional to the velocity of the stage, the position of the drive legs is modeled as

$$x_p(t) = \frac{c}{2\pi}\alpha(t) = c\int_0^t f_\alpha(\tau)d\tau, \tag{2.5}$$

where c is the motor constant, representing the gain factor from the angle α to the position of the drive legs x_p. Using the Laplace transform, (2.5) becomes

$$X_p(s) = c\frac{1}{s}F_\alpha(s). \tag{2.6}$$

Combining (2.4) and (2.6) results in the model $\tilde{P}(s)$

$$\tilde{P}(s) = \frac{X_s(s)}{F_\alpha(s)} = \frac{bcs + kc}{Ms^3 + bs^2 + ks}. \tag{2.7}$$

It is assumed that the pairs of legs are identical and that at all times only one pair of legs is in contact with the stage. The nonlinearities introduced by the switch are assumed to be negligible.

The measured frequency response function (FRF) of the plant $P(j\omega)$ from the drive frequency $f_\alpha(t)$ to the position of the stage $x_s(t)$ is represented in Fig. 2.9 by the solid line. The FRF was measured while the stage tracked a constant velocity profile. The control scheme for the FRF measurement is shown in Fig. 2.8, where the reference signal $r(t)$ equals a constant velocity profile and $w(t)$ is a white noise signal. The controller $C(j\omega)$ is a stabilizing PI controller, tuned using time domain measurements of the output $x_s(t)$ and the error $e(t)$ [63]. From the time domain data of the noise w, control input $u = f_\alpha + w$, and the output x_s, the FRFs of the sensitivity function

$$S(j\omega) = \frac{1}{1 + P(j\omega)C(j\omega)}$$

and the process sensitivity function

$$S_P(j\omega) = \frac{P(j\omega)}{1 + P(j\omega)C(j\omega)} = P(j\omega)S(j\omega)$$

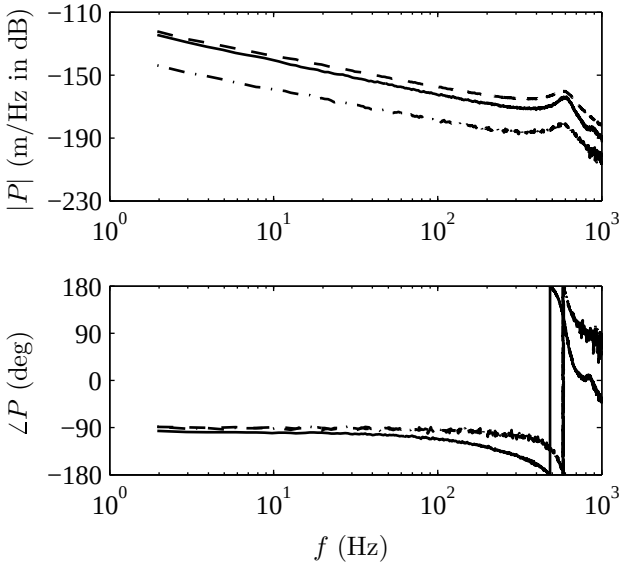

Figure 2.9: Measured FRF (solid), FRF of the model (dashed), and measured FRF with decreased amplitude A and phase ϕ (dash-dotted).

can be determined using the indirect closed-loop identification method and Welch's averaged periodogram method [116, 207]. The FRF of the system P can now be obtained by

$$P(j\omega) = \frac{S_P(j\omega)}{S(j\omega)}.$$

The measured FRF of Fig. 2.9 shows a decay of 20 dB/dec at frequencies below the resonance peak located at 575 Hz. The eigenfrequency leading to the resonance peak is caused by the combined stiffness k of the piezo legs and the motor suspension together with the mass M of the stage.

For the model, the mass of the system is measured as $M = 0.255$ kg. Using the resonance frequency of the measured FRF $f_{\text{res}} = 575$ Hz, the stiffness $k = 4\pi^2 M f_{\text{res}}^2 = 3.3 \cdot 10^6$ N/m. The damping b is determined by fitting an exponential envelope

$$g(t) = e^{-\frac{b}{2}t}$$

to the response of the system on a step-shaped input [63]. The identified damping of the model $b = 160$ Ns/m. Finally, the motor constant c is determined using

the amplitude of the measured FRF at low frequencies together with the transfer function of the model as

$$|P(j\omega)|_{f=10\text{ Hz}} = -138\text{ dB} = \frac{kc}{k2\pi f} \tag{2.8}$$

From (2.8) follows $c = 7.91 \cdot 10^{-6}$. The FRF of the model $P(j\omega)$ with the identified parameters is shown in Fig. 2.9 by the dashed line.

2.4 Control design

To obtain a smoother drive motion of the walking piezo actuator, new waveforms are designed, which will be presented in Section 2.4.1. The system of Fig. 2.6 is feedback controlled by prescribing the desired frequency $f_\alpha(t)$ of the waveforms and by measuring the position of the stage $x_s(t)$, which will be described in Section 2.4.2. Feedforward control of the amplitude A and phase ϕ of the waveforms $u_i(t)$, $i \in \{1, 2, 3, 4\}$ and gain scheduling were added, as will be explained in Section 2.4.3.

2.4.1 Waveforms

The resulting leg trajectories for the sinusoidal waveforms of (2.2) are shown in Fig. 2.10(a). The instant in time where the first pair of legs loses contact with the drive surface and the second pair takes over is called the transfer point. For the sinusoidal waveforms, the transfer point occurs when the legs have a zero velocity in the drive direction x. For constant velocity setpoints, i.e., in jogging mode, the take-over between the driving pair of legs occurs at zero velocity in the drive direction x, which leads to a large tracking error and thus to a high control effort.

In order to create a transfer point with a non-zero stage velocity in x-direction, the waveforms were altered such that the elliptical trajectories become overlapping, see Fig. 2.10(b). The elliptical trajectories were changed into overlapping trajectories by performing the non-contact part in a shorter time interval. This makes the waveforms asymmetric, as shown in the bottom axes of Fig. 2.10(b).

Let the period-time of the original sinusoidal waveforms be denoted by T_o (s). Define the amount of relative overlap between the trajectories of the drive legs as q, where $0 < q < 1$. The factor q determines the length of the contact part. The choice for the amount of overlap q is a compromise between the reduction

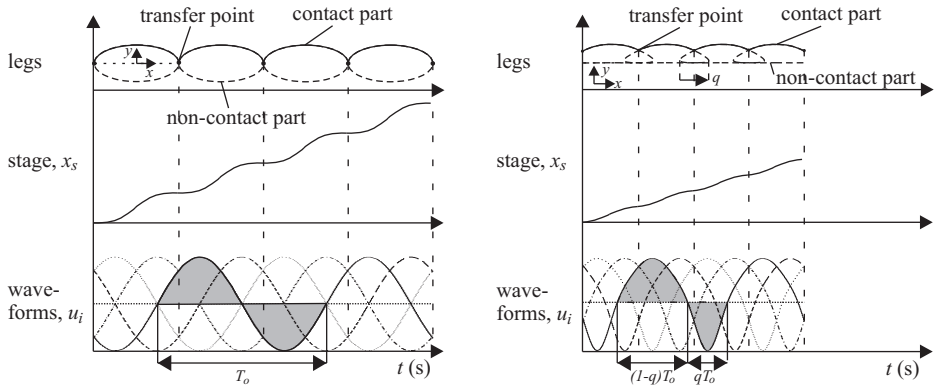

(a) Symmetric waveforms.

(b) Asymmetric waveforms.

Figure 2.10: Leg movement, stage motion and waveforms for the original sinusoidal waveforms and the new asymmetric waveforms.

of the tracking error and the reduction of the maximum motor velocity. For the trajectories to have an overlap q, the asymmetric waveforms are composed of a positive sinusoidal part with a time span equal to $(1-q)T_o$ (s) and a negative sinusoidal part with a time span of qT_o (s). The total period-time T_n (s) of the asymmetric waveforms becomes

$$T_n = (1-q)T_o + qT_o = T_o.$$

The period-time of the asymmetric waveforms is chosen equal to the period-time of the original symmetric waveforms. Due to the shift in the zero crossing of the waveforms in one period, the transfer point now occurs at a non-zero velocity in x-direction. However, the contact part is also shorter, as can be seen by the length of the solid line in the sequential leg trajectories in the top axes of Fig. 2.10. The shorter contact part results in a decrease of the stage velocity for the asymmetric waveforms, as can be seen in the second axes of Fig. 2.10. However, with the overlapping tip trajectories, the stage performs a smoother movement, thus reducing the tracking error and the control effort.

For the asymmetric waveforms used in the experiments of this chapter, the contact part was chosen to be 2/3 of the period, i.e., $q = 1/3$. The overlap resulted in a velocity reduction of approximately 15% compared to the original waveforms. The velocity reduction results in an increase in walking frequency in order to achieve an equal stage velocity as with the sinusoidal waveforms. For the velocity range of interest in this application the increase in walking frequency does not result in slip of the drive legs and therefore not in additional actuator wear. A further increase of the desired velocity could result in slip and actuator wear.

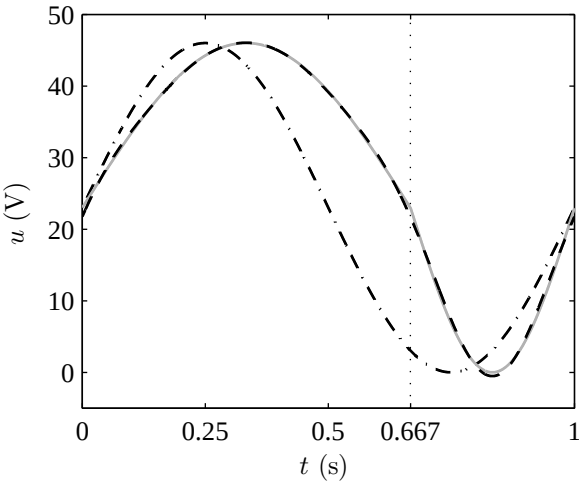

Figure 2.11: Normalized original sinusoidal waveform u (dash-dotted), asymmetric waveform u_{asym} (grey solid), and Fourier series fit $\tilde{u}_{asym}$ (2.9) (dashed) for $q = 1/3$.

To construct the asymmetric waveforms, first the original sinusoidal waveforms of (2.2) are normalized to frequency $\bar{f}_\alpha = 1$ Hz, with amplitude $\bar{A} = 46$ V and phase $\bar{\phi} = 0$ rad as shown in Fig. 2.11 by the dash-dotted line. The asymmetric waveforms can now be constructed with $q = 1/3$ as

$$u_{asym}(t) = \begin{cases} \dfrac{\bar{A}}{2}\sin\left(2\pi\dfrac{3}{4}t\right) + \dfrac{\bar{A}}{2}, & t \in [0, (1-q)], \\ \dfrac{\bar{A}}{2}\sin\left(2\pi\dfrac{3}{2}t + \pi\right) + \dfrac{\bar{A}}{2}, & t \in \langle (1-q), 1] \,. \end{cases}$$

The normalized asymmetric waveforms are shown in Fig. 2.11 by the grey solid line. For implementation issues, a fourth order Fourier series model [4] is fitted as

$$\tilde{u}_{asym}(t) = \frac{A}{\bar{A}}a_0 + \frac{A}{\bar{A}}\sum_{k=1}^{4}\left\{a_k\cos[k\alpha(t) + k\phi(t)] + b_k\sin[k\alpha(t) + k\phi(t)]\right\}, \quad (2.9)$$

where $a_0 = 28.80$, $a_1 = -10.78$, $b_1 = 18.73$, $a_2 = 2.387$, $b_2 = 4.097$, $a_3 = 1.985$, $b_3 = -0.007792$, $a_4 = 0.2298$ and $b_4 = -0.3901$. Note that the amplitude of the fitted waveforms is divided by $\bar{A}$, which scales the waveforms back and makes it possible to use and vary the original amplitude A again. The fitted asymmetric waveform is shown in Fig. 2.11 by the dashed line. The fitted fourth order Fourier series model $\tilde{u}_{asym}$ resembles the original asymmetric waveform u_{asym} very well.

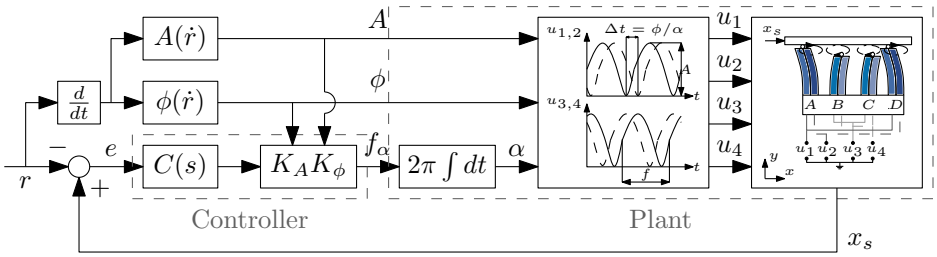

Figure 2.12: Control scheme with feedforward and gain scheduling.

2.4.2 Feedback control

On the basis of the FRF of the system (see Fig. 2.9), we designed a standard proportional and integral (PI) controller (2.10) employing loopshaping techniques [63]

$$C(s) = 1 \cdot 10^7 \frac{s + 2\pi}{s}. \tag{2.10}$$

Using the controller (2.10), the controlled system has a bandwidth f_{BW}, defined as $|P(f_{\mathrm{BW}})C(f_{\mathrm{BW}})| = 0$ dB, of approximately $f_{\mathrm{BW}} = 10$ Hz, a phase margin of 75° and a gain margin of 30 dB. A block diagram of the feedback controlled system is shown in Fig. 2.12. The asymmetric waveforms (2.9) of Section 2.4.1 are contained in the block with inputs α, ϕ and A. The outputs of the block with the asymmetric waveforms are $u_i(t)$ (V), $i \in \{1, 2, 3, 4\}$. The block diagram of Fig. 2.12 also contains the feedforward control and gain scheduling, which are the subject of the next section.

The purpose of the controller design is not to maximize the achievable cross-over frequency, although an increase would be possible based on the FRF of Fig. 2.9. To illustrate the performance improvement by the asymmetric waveforms and the feedforward control with gain scheduling of the next section combined with the limited measurement resolution of 5 nm, the bandwidth is limited to 10 Hz in this chapter.

2.4.3 Feedforward control with gain scheduling

For point-to-point movements, it is important that no static error remains and that the system is at a standstill at the end of the movement. Two specifications are important. Both the overshoot M_p and the settling time t_s have to be minimized. The overshoot M_p (nm) is defined as the amount by which the position exceeds

its steady-state output on its initial rise for a point-to-point movement. The settling time t_s (s) is defined as the time the stage takes to position within encoder resolution after the movement.

The stage position showed a large overshoot for point-to-point movements performed with the maximum step size of 4 μm, i.e., with $A = 46$ V and with a phase difference of $\pi/2$ rad between the waveforms of the layers of one pair of legs, i.e., $\phi(t) = 0$ rad in (2.2).

To reduce the overshoot, the step size of the piezo legs is altered based on the momentary setpoint velocity $\dot{r}(t)$ (m/s) of the stage during the point-to-point movement. The step size of the piezo motor can be adjusted by means of feedforward control by changing the amplitude $A(t)$ and phase $\phi(t)$ of the waveforms as described in Section 2.2 (see also Fig. 2.3). The feedforward adjustments of the amplitude $A(t)$ and phase difference $\Delta\phi(t)$ for the waveforms are chosen as

$$A(t) = \frac{A_{\max}}{v_{\max}}|\dot{r}(t)| + A_{\min}, \tag{2.11}$$

$$\Delta\phi(t) = \frac{\phi_{\max}}{v_{\max}}|\dot{r}(t)| + \phi_{\min}, \tag{2.12}$$

where $v_{\max} = \max_t(|\dot{r}(t)|)$ is the maximum reference velocity, $A_{\min} = 23$ V is the minimum amplitude and $A_{\max} = 46$ V is the maximum amplitude. The feedforward adjustment of the amplitude is bounded as $A \in [A_{\min}, A_{\max}]$. In (2.12), $\phi_{\min} = \pi/20$ rad denotes the minimum phase difference and $\phi_{\max} = \pi/2$ rad is the maximum phase difference to obtain the largest step size. The feedforward adjustment of the phase is bounded as $\Delta\phi \in [\phi_{\min}, \phi_{\max}]$. $\Delta\phi$ denotes the phase difference between the different input waveforms to each leg, i.e., the phase $\phi = \Delta\phi - \pi/2$ (rad) for the sinusoidal waveforms of (2.2).

Changes in A and ϕ affect the step size of the motor and with this the stage velocity. Both variables adjust the step size independently, i.e., a change in ϕ does not affect the amplitude A and vice versa (see also Fig. 2.3). Compared to the FRF measured with $A_{\max}$ and $\phi_{\max}$ (solid line in Fig. 2.9), a change in A and/or ϕ results in a decrease in magnitude in the FRF, as shown in Fig. 2.9 by the dotted line. The feedforward adjustments can only decrease the amplitude A and phase ϕ with respect to their nominal values $A_{\max}$ and $\phi_{\max}$. From (2.7), it follows that with a constant drive frequency f_α and a decreasing step size x_p, the FRF $P(j\omega)$ also decreases. To obtain an equal bandwidth, the gain change has to be compensated for. Therefore, the gain of the controller (2.10) is made dependent on the operating point. The feedback controller (2.10) is multiplied by a gain scheduling term $K(A, \Delta\phi)$, where

$$K(A, \Delta\phi) = K_A(A)K_\phi(\Delta\phi). \tag{2.13}$$

The functions $K_A(A)$ and $K_\phi(\Delta\phi)$ are obtained experimentally by determining the gain variation of the FRF in various operating conditions, i.e., for varying values of A and ϕ with respect to the FRF measured with $A_{\max}$ and $\phi_{\max}$ (solid line in Fig. 2.9). The values of A and ϕ are varied separately, while the other variable remains at the maximum value ($A_{\max}$ or $\phi_{\max}$). For the various operating points, the appropriate controller gains are determined, through which a fit is made in order to continuously adjust the controller gain dependent on the operating point [109, 162].

The introduction of the gain scheduling renders the controller time-varying. Notice that this time variation only occurs during the acceleration phase of the system since the gain scheduling parameter $K(A, \Delta\phi)$ is constant for constant velocity. The feedforward terms adjust the system gain through the sinusoidal waveforms, the gain scheduling term of the controller is in fact used to compensate for this.

2.5 Results

The designed asymmetric waveforms and the control strategy of Section 2.4 were tested by means of simulations and experiments. First, the gain scheduling terms K_A and K_ϕ were determined. Furthermore, tracking experiments were performed using both constant velocity reference signals and point-to-point movements.

The experimental configuration shown in Fig. 2.13 consists of the mechanical setup (Fig. 2.6), four amplifiers, a TUeDACs AQI data-acquisition device [204], and a computer. The AQI is used to measure the encoder output through a 32 bit quadrature counter. Furthermore, it is equipped with DAC outputs, which are used to generate the waveforms (2.2) to drive the setup via the amplifiers. The computer reads the encoder measurements of the AQI at a fixed sampling rate of 4 kHz. For this purpose, Xenomai Linux is used to communicate with the AQI in real-time. The computer is used to process the measured position and to calculate the required control signal to the system in order to track the reference signal.

2.5.1 Gain scheduling

The experimentally obtained gain differences of the FRFs for different values of A and ϕ with respect to the gain of the FRF with the nominal values $A_{\max}$ and $\phi_{\max}$ are shown in Fig. 2.14 together with the fitted functions for $K_A(A)$ and $K_\phi(\Delta\phi)$. The functions $K_A(A)$ and $K_\phi(\Delta\phi)$ are determined by fitting a first order power series [4] on a logarithmic scale by means of least squares fit through

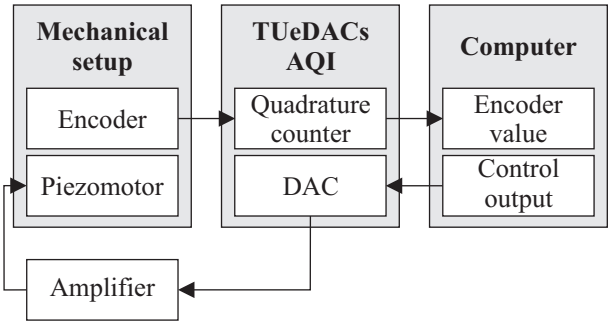

Figure 2.13: Overview of the experimental configuration.

the experimental results. The fitted functions equal

$$K_A(A) = 10^{\frac{\left|a_1 A^{b_1} - c_1\right|}{20}},$$
$$K_\phi(\Delta\phi) = 10^{\frac{\left|a_2 \phi^{b_2} - c_2\right|}{20}},$$

where $a_1 = -185.6$, $b_1 = -0.05866$, $c_1 = -184.9$, $a_2 = -152.0$, $b_2 = -0.05364$, and $c_2 = -148.7$. The step size of the piezo legs is independently changed by A and ϕ, therefore the complete gain scheduling term $K(A, \Delta\phi)$ can be constructed by multiplying K_A and K_ϕ (see (2.13)). The fitted function K_A increases slightly for $A > 43$ V. Since the gain scheduling is mainly required for low reference velocities, i.e., at the end of the point-to-point movement, which corresponds to small amplitudes A (see (2.11)), this mismatch for amplitudes $A > 43$ V does not lead to a performance degradation.

2.5.2 Tracking constant velocities

The constant velocity experiments are performed at the maximum step size ($A_{\max}$ and $\phi_{\max}$), i.e., without gain scheduling. In Fig. 2.15, the results for a tracking experiment with a constant velocity of 100 nm/s are shown. The tracking performance is the same both with the non-overlapping and the overlapping tip trajectories. The steps in the measured position are equal to the encoder resolution of 5 nm. The tracking error is maximally 3 nm, which is within the encoder resolution. At very low velocities, where the tracking error with the non-overlapping tip trajectories is already below encoder resolution, the overlapping tip trajectories

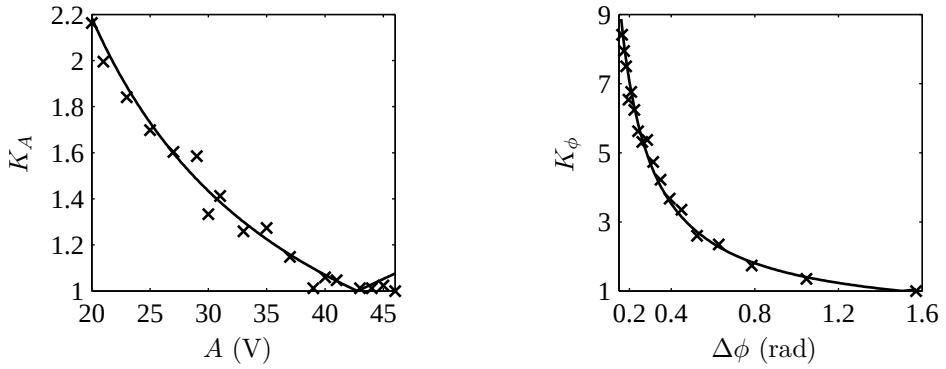

(a) $K_A(A)$. (b) $K_\phi(\Delta\phi)$.

Figure 2.14: Measured ($\times$) and fitted (solid) gain scheduling functions $K_A(A)$ and $K_\phi(\Delta\phi)$.

obviously do not improve the performance. The errors become larger than the encoder resolution for larger velocities. For a tracking experiment with a constant velocity of 1 mm/s, the tracking error with non-overlapping tip trajectories equals 0.85 μm and with overlapping tip trajectories 0.35 μm, as can be seen in Fig. 2.16. With the overlapping tip trajectories, the tracking error is approximately 2.4 times smaller than with the non-overlapping trajectories.

The maximum absolute tracking errors $e_{\max} = \max_t(|e(t)|)$, where $|\cdot|$ represents the absolute value operator, of the experiments with different reference velocities are shown in Table 2.2, both with non-overlapping and overlapping tip trajectories. For velocities < 100 nm/s, the errors are within encoder resolution regardless of the tip trajectories. For constant velocities up to 1 μm/s, the overlapping tip trajectories reduce the tracking error within the encoder resolution of 5 nm compared to the non-overlapping tip trajectories, resulting in an performance improvement of 92%. For larger reference velocities, the tracking errors obtained with the asymmetric waveforms exceed the encoder resolution. The overlapping tip trajectories reduce the tracking error between 50% and 68%, depending on the reference velocity.

2.5.3 Point-to-point movements

The results of a point-to-point movement over a distance of 0.1 mm with and without feedforward control and gain scheduling, as described in Section 2.4.3, are shown in Fig. 2.17. Both strategies result in a static error of ± 5 nm. The

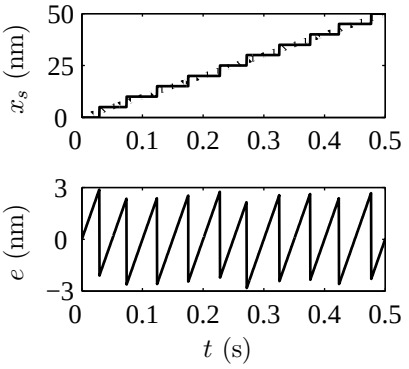

Figure 2.15: Reference (dotted) and measured (solid) positions and tracking error for a constant velocity of 100 nm/s.

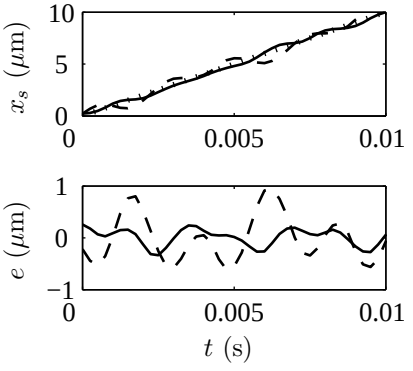

Figure 2.16: Reference (dotted) and measured positions and tracking errors with the non-overlapping (dashed) and overlapping (solid) tip trajectories for a constant velocity of 1 mm/s.

use of the maximum step size (original control strategy) yields a large overshoot $M_p = 4350$ nm and settling time $t_s = 0.9$ s, defined as the time needed to settle within encoder resolution (5 nm), as depicted in Fig. 2.17 by the dashed line. With feedforward control and gain scheduling, the elliptical trajectories and thus the step size of the legs were adjusted depending on the reference velocity according to Fig. 2.3. The overshoot M_p and settling time t_s reduced to $M_p = 190$ nm and $t_s = 0.6$ s with the feedforward control and gain scheduling, as can be seen in Fig. 2.17 by the solid line.

In Table 2.3, the overshoot and settling time for point-to-point movements of different sizes are shown. When no transitions of the legs occur, i.e., for point-to-point movements below the maximum step size of the motor (4 μm), the feedforward and the gain scheduling have no effect. This is because in these cases no steps are made by the motor and there is no difference between the two control strategies. For larger point-to-point movements, the overshoot M_p and settling time t_s are smaller with feedforward control and gain scheduling than without. The reduction in overshoot is approximately 96%. The settling times for point-to-point movements of 10 μm and 0.1 mm are reduced by 67% and 33%, respectively.

Table 2.2: Maximum absolute tracking errors of non-overlapping and overlapping tip trajectories for different constant velocities.

	$e_{\max}$ (nm)		
velocity (m/s)	non-overlapping	overlapping	reduction (%)
1e-7	< 5	< 5	
1e-6	$\pm$ 60	< 5	92%
1e-5	$\pm$ 150	$\pm$ 50	67%
1e-4	$\pm$ 400	$\pm$ 200	50%
1e-3	$\pm$ 850	$\pm$ 350	59%
2e-3	$\pm$ 1250	$\pm$ 400	68%

Table 2.3: Overshoot M_p and settling times t_s for point-to-point movements of different sizes with and without the use of feedforward and gain scheduling.

	No FF		With FF	
Step (m)	M_p (nm)	t_s (s)	M_p (nm)	t_s (s)
1e-7	<5	0.1	<5	0.1
1e-6	50	0.4	50	0.4
1e-5	405	0.6	13	0.2
1e-4	4350	0.9	190	0.6

2.6 Conclusions

The aim of this work was to improve the positioning accuracy of a 1-DOF nano-motion stage using a walking piezo motor. For this purpose, we proposed new waveforms to drive the legs of the piezo motor. Furthermore, a control strategy was developed employing feedback control, feedforward control, and gain scheduling. The experimental results show the improvement of the tracking behavior of the nano-motion stage.

The proposed waveforms for driving the piezoelectric legs of the walking piezo actuator result in overlapping tip trajectories, i.e., a transition point between the driving legs at non-zero velocity of the stage. A much smoother motion of the stage with a lower control effort and tracking error are obtained with the proposed overlapping tip trajectories. However, the overlapping tip trajectories reduce the attainable motor velocity. The optimal choice for the amount of overlap is a trade-

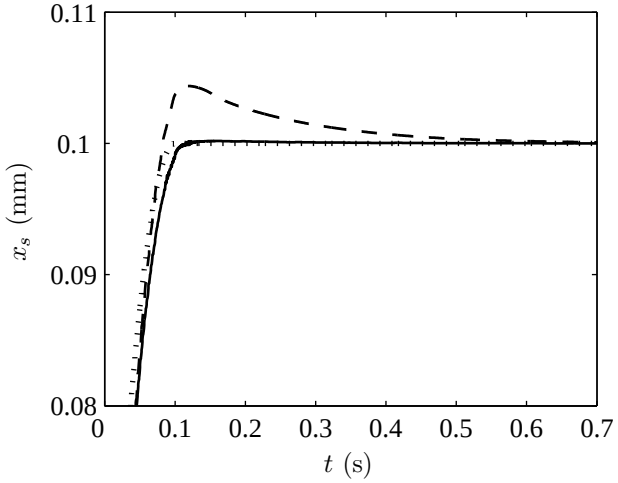

Figure 2.17: Reference (dotted), and measured positions with the original (dashed) and advanced (solid) control strategies for a point-to-point movement over 0.1 mm.

off between the velocity reduction and the reduction of the tracking error of the stage. The overlap in the tip trajectories reduces the tracking error between 50% and 92%, depending on the reference velocity.

For point-to-point movements, the overshoot and settling time can be reduced considerably when the end position is approached with smaller steps. The step size of the legs is adjusted depending on the momentary reference velocity by means of feedforward control of the amplitude and phase of the waveforms in combination with gain scheduling. With the feedforward control and gain scheduling, the overshoot is reduced by 96% and the settling time by up to 67%.

The stage with the walking piezo actuator and the proposed control strategy is capable of tracking velocities between 100 nm/s and 1 μm/s at the encoder resolution of 5 nm. Also, point-to-point movements between 5 nm and the complete stroke of the stage are possible with a static error below encoder resolution.

We expect the walking piezo motor to be able to track arbitrary trajectories and with velocities higher than 2 mm/s. However, for higher speeds the drive frequency will get close to the systems resonance frequency, which will be the subject of further study.

Future work will also include the extension of the model with the piezoelectric effects and the formal robust stability analysis of the system with gain scheduling.

Chapter 3

Modeling of a walking piezo actuator

Abstract - Piezoelectric actuators are often used in positioning devices that require (sub)nano-meter resolution. In this chapter, we develop an electro-mechanical dynamic model of a walking piezo actuator. The derived model structure can be used for the dynamic modeling of bimorph piezo motors in general. Furthermore, the physical nature enables the model to be used in design optimizations to derive new motors with different properties and for a dynamic analysis to investigate the maximum allowable driving frequency in relation to the dynamic effects of the motor. The walking piezo actuator contains four legs, each with two electrically separated piezo stacks. The legs are modeled as a connection of coupled mass-spring-damper systems. Using a Lagrange approach, the nonlinear system dynamics are derived. The variation in the system dynamics is assessed using linearization around different equilibrium positions. Also a static linearized approximation is derived, which describes the static relation between the supply voltages and the tip trajectories of the legs. The dynamic analysis shows that the motor can be modeled sufficiently accurate using a connection of six lumped mass-spring-damper systems. The variation in system dynamics appears to be most significant in the movement perpendicular to the leg orientation. Experiments show that the static linearized model accurately describes the tip trajectories of the legs for both sinusoidal and asymmetric waveforms.

This chapter is based on: R. J. E. Merry, M. J. G. van de Molengraft, and M. Steinbuch. Modeling of a walking piezo actuator. Submitted, 2009.

3.1 Introduction

Piezoelectric actuators are able to perform very small reproducible deformations and have attractive properties such as high stiffness, fast response, lack of backlash, extremely low speeds, high accuracy and inherent breaking when the power is removed [201]. This makes them very attractive for use in nano-positioning devices. A disadvantage of the piezoelectric actuators is their nonlinear behavior, including creep and hysteresis.

In this chapter, we consider the dynamic modeling of a linear walking piezoelectric actuator, shown in Fig. 3.1. The actuator has four piezoelectric legs, each of which uses a bimorph working principle through two electrically separated piezo stacks. For this motor, bimorph refers to the two separate stacks rather than to bimorph piezoelectric film actuators with two piezo elements. The dynamic model is used to analyze the geometric nonlinearities in the walking piezo actuator, which are the performance limiting factor (PLFs) in the obtained driving accuracy of the actuator.

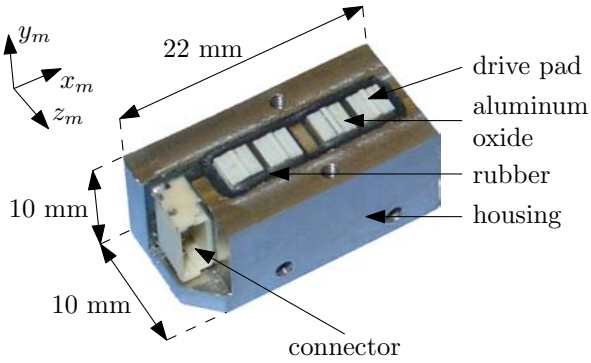

Figure 3.1: The walking piezo motor [155].

The presented model structure can be used to model piezo actuators that employ multiple piezo stacks, in particular bimorph piezo actuators. The physical nature of the model allows it to be used in design optimizations to derive new walking piezo actuators with different properties, e.g. with a different contact force, larger step sizes, etc. Due to the energy based modeling approach, the model can be easily extended with the dynamics of the system to be actuated and with nonlinear effects, such as hysteresis, stick-slip, etc. Furthermore, the model gives insight in the dynamics of the bimorph piezo motors and the maximum allowable drive frequency before which the dynamic effects become apparent.

The description of piezoelectric actuators involves combined mechanical and electrical effects. Although piezoelectric actuators exhibit an inherent hysteresis nonlinearity, often the operating conditions are chosen to achieve a nearly linear behavior [57]. In this chapter, we focus on modeling the structural dynamics of the bimorph walking piezo actuator.

Piezoelectric actuators are constructed using either piezo stacks or multimorph piezo elements, consisting of multiple films of piezo elements. The piezo stacks are capable of producing large forces, but generally have only a small displacement. The multimorph piezo elements on the other hand enable large displacements.

In literature, three different modeling approaches are used to describe the behavior of bimorph piezo actuators; bending beam analogies, thermal analogies and energy approaches.

A model incorporating hysteresis is derived using beam analogy in [119] for a three layer bimorph beam consisting of two piezo elements separated by a metal shim. Design equations for a multimorph piezo beam are derived in [212]. Beam analogies are generally used for piezo actuators that have wide thin piezo elements and that obtain the movement by bending the piezo elements, which is by design different from the working principle of the walking piezo actuator in this chapter.

Thermal analogy methods are based on the similarities between the piezoelectric strains and thermal strains [38, 48, 52]. Although software packages exist for dynamic analysis of thermal analogy models, the models are not easily extended with for example hysteresis or with the dynamics of the system surrounding the piezo actuator. Therefore, we have not adopted this modeling approach for the walking piezo actuator.

The electro-mechanical coupling of piezo actuators can be modeled using energy based methods [74]. The dynamics of single stacked piezo actuators are described using electro-mechanical models in [5, 35, 72]. The different layers of a piezo stack can be modeled as a chain of lumped mass-spring-damper systems [5]. Also, the nonlinear hysteresis effects are incorporated into the model. In [57], the electro-mechanical coupling in multilayered piezoelectric structures is modeled as an additional stiffness matrix to the constitutive equations. In [31], the single stack piezoelectric actuators of a x, y, θ_z micro-positioner are modeled as a single spring, damper and a displacement element. Although a Lagrangian energy approach is followed, the piezoelectric effects are only included in the finite element method (FEM) model.

In literature, several types of piezo motors have been modeled such as piezo tube actuators [69, 159], standing wave ultrasonic motors [156], inchworm actuators [194], L-shaped piezo actuators [219] and multimorphs [64]. To the authors

best knowledge, no model of a bimorph walking piezo actuator was published so far. In this chapter, we will model the walking piezo actuator using the Lagrange approach. The bimorph piezo stacks of the legs are modeled using lumped mass-spring-damper systems, incorporating the electro-mechanical coupling effects.

For the sake of completeness, the existing literature on modeling the nonlinear effects in piezoelectric actuators due to hysteresis is briefly mentioned. Hysteresis effects have been modeled using the generalized Maxwell slip model [72], the generalized Prandtl-Ishlinskii hysteresis model [6], the Preisach model [89, 181] and the Coleman-Hodgdon model [130]. In the model presented in this chapter, hysteresis is not included. However, the model structure is chosen such that it can easily be extended with a hysteresis model.

The contributions of this chapter are threefold. Firstly, an analytical model of the walking piezo legs actuator based on its physical properties is derived. Secondly, analytical expressions for the static approximation between the tip trajectories and the supplied voltages are derived. Finally, the results are experimentally validated.

This chapter is organized as follows. The walking piezo motor is described in more detail in Section 3.2. In Section 3.3, both the dynamic model of the walking piezo actuator and the static approximation are derived. Also, an analysis on the changing dynamics for different operating conditions is presented. The model identification is included in Section 3.4. Section 3.5 contains the static, dynamic and experimental results. Finally, conclusions are drawn in Section 3.6.

3.2 The piezo motor

The piezo motor, shown in Fig. 3.1, consists of four piezoelectric drive legs [155]. The drive legs are driven by electric waveforms via the connector. The top of each leg is covered with an aluminum oxide drive pad. The drive legs can be pressed onto a drive surface of a stage to transfer the movement to a translational movement with nanometer accuracy and with speeds in the range of nanometers per second to millimeters per second (see Chapter 2). The legs are cast in rubber to add damping to the movement. The dimensions of the piezo motor of Fig. 3.1 are $22\times10\times10$ mm. Its weight equals 15 g.

Each piezoelectric leg consists of two electrically separated piezo stacks and employs a bimorph working principle. The piezo stacks elongate when they are electrically charged. A schematic representation of the side view and the working principle of the piezo motor are shown in Fig. 3.2. The legs elongate in y-direction when an equal voltage is applied to the two piezo stacks of one leg. Applying

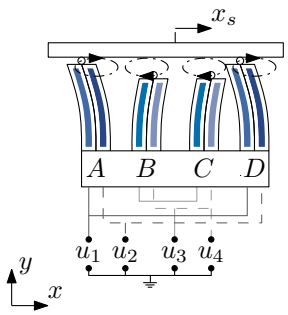

Figure 3.2: Working principle of the walking piezo motor.

different voltages on the two piezo stacks of one leg causes the leg to bend. By choice of the supply voltages, the tip of the drive leg can be placed in an arbitrary position within a working region in the (x, y)-plane (see Fig. 3.2) spanned by the waveforms $u_i(t)$ (V), $i \in \{1, 2, 3, 4\}$ with $\min(u_i) = 0$ V and $\max(u_i) = 46$ V.

As can be seen in Fig. 3.2, the drive legs always work together in pairs of two ($p_1 = \{A, D\}$ and $p_2 = \{B, C\}$). The first pair of legs p_1 is driven by the input waveforms $u_1(t)$ (V) and $u_2(t)$ (V), the second pair p_2 is driven by $u_3(t)$ (V) and $u_4(t)$ (V).

3.3 Modeling

The piezo legs work together in pairs. It is assumed that two legs of a single pair are identical. Therefore, each pair is modeled as a single leg. Since the model is based on physical properties, this only causes the dimensions in the model to be the combined dimensions of both legs in one pair. Because of similarity, in the remainder we will discuss only the modeling of one pair.

Each piezo stack in the bimorph piezo legs contains $n_t = 96$ piezoelectric elements. Since both stacks have an equal amount of elements, the leg can be considered to have n_t layers, each consisting of two piezoelectric elements, one in each stack. Each layer is modeled as two piezo elements, connected by a mass m, representing the total mass of that layer. A schematic overview of the model in the Cartesian (x, y)-plane for an example of $n = 3$ layers can be seen in Fig. 3.3(a). Each layer has a local coordinate frame, centered at the center of mass of the layer, as shown for the first layer in Fig. 3.3(b).

Due to the polarization of the piezo elements and the assumption of a uniform

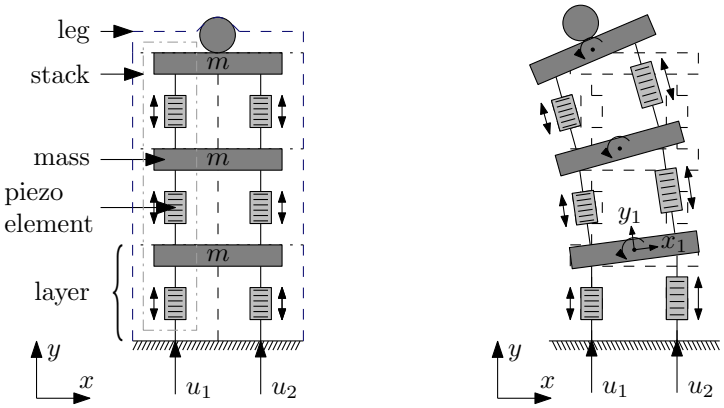

(a) Original state. (b) Bend.

Figure 3.3: Schematic representation of one pair of piezo legs for $n = 3$ layers.

electric field in the local y-direction, each piezo element is assumed to have only an extension in longitudinal direction, i.e., its local y_i-direction. The expansion of the individual piezoelectric elements in perpendicular direction, i.e., local x_i-direction, is assumed to be negligible small. If the input voltages $u_1(t)$ and $u_2(t)$ are equal, the piezo elements in each layer extend equally. This results in a translation of the mass' m in y-direction. Different input voltages $u_1(t)$ and $u_2(t)$ result in unequal extension of the piezo elements and with this in a rotation of the mass' m around each center of mass (see Fig. 3.3(b)).

Due to a different extension of the different piezo elements, the mass m of each layer rotates around its center of mass. Therefore, the mass of each layer has only a translation in the local y_i-direction (longitudinal) and a rotation around the center of mass due to the input voltages $u_1(t)$ and $u_2(t)$ on the different piezo stacks. The global x-translation of the leg is caused by stacking the model of one layer n times on top of each other, creating a lumped model structure (see Fig. 3.3).

3.3.1 Modeling the piezo elements

A single discrete piezoelectric element can be visualized as shown in the left of Fig. 3.4. If a voltage u (V) is provided to the electrodes of the piezo element, this will result in an electric charge Q (C) and with this in a force f_t (N) and a displacement Δ (m).

The constitutive equations of the piezo element, made of a one-dimensional piezo-

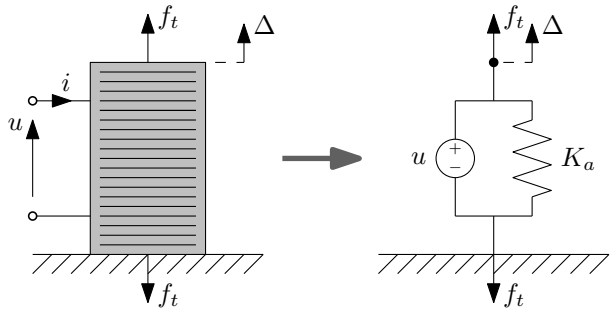

Figure 3.4: Model of a single piezoelectric element.

electric material, are [158]

$$D = \epsilon^T E + d_{33} T, \tag{3.1}$$

$$S = d_{33} E + s^E T, \tag{3.2}$$

where D (C/m^2) is the electric displacement, E (V/m) the electric field, T (N/m^2) the stress, S (-) the strain, ϵ^T (N/V^2) the dielectric constant under constant stress, s^E (m^2/V) the compliance when the electric field is constant and d_{33} (m/V) the piezoelectric constant.

If the electric field of the piezo element is assumed parallel to the poling direction and all the electrical and mechanical quantities are assumed uniformly distributed in a linear piezo element with n layers, integrating (3.1) over the volume of the piezo element gives [158]

$$\begin{bmatrix} Q \\ f_t \end{bmatrix} = \begin{bmatrix} C(1-k^2) & n d_{33} K_a \\ -n d_{33} K_a & K_a \end{bmatrix} \begin{bmatrix} u \\ \Delta \end{bmatrix}, \tag{3.3}$$

where Q (C) is the total electric charge on the electrodes of the piezo element, Δ (m) is the total extension, f_t (N) is the total force and u (V) the applied voltage between the electrodes of the piezo element. Furthermore, C (F) is the capacitance of the piezo element with no external force, k (-) the electro-mechanical coupling factor, n (-) the number of layers in the piezo stack and K_a (N/m) the stiffness with short-circuited electrodes.

When a voltage source is used, as done in this chapter, the effect of the piezoelectric element on a structure can be represented as a pair of self-equilibrating forces applied axially to the ends of the piezo element [158]. In that case, with (3.3) the total force in the piezoelectric element can be written as

$$f_t = - \underbrace{n d_{33} K_a u}_{\text{expansion under } u} + \underbrace{K_a \Delta}_{\text{spring}}. \tag{3.4}$$

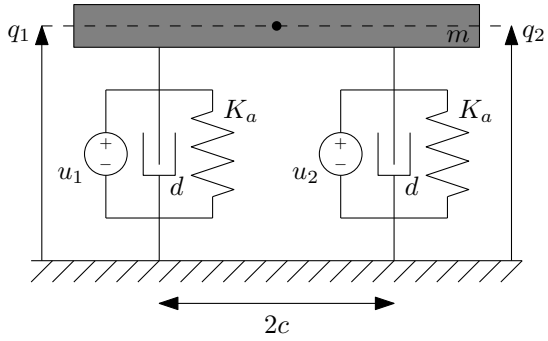

Figure 3.5: Model of a single layer.

So, each piezoelectric element can be represented as a parallel coupling of a force due to an applied voltage u and a spring with spring constant K_a. A schematic representation of the model of a single piezo element is shown in Fig. 3.4. When desired, (3.4) can be extended to incorporate hysteresis effects in the piezo element.

3.3.2 Complete model

Since the different legs of the walking piezo actuator are cast in rubber, also a damper is added to the model of the individual elements. This results in the model for a single layer of the piezo legs as shown in Fig. 3.5. Let the width of a single stack be denoted by b_s (m). Since the applied force of a single piezo stack is assumed to be located at the middle, i.e., through the center line of the stack (see also Fig. 3.4), the width $c = b_s/2$ (m). The width between the center lines of both stacks is denoted by $2c$ (m) in Fig. 3.5, i.e., the widths of both stacks are assumed to be equal and the separation layer is assumed to be negligible small.

The two piezoelectric elements apply different forces, resulting in a combined force F (N) and a moment M (Nm) on the mass m of each layer (see Fig. 3.6). Under the assumption that each piezo element only elongates longitudinally, the mass m rotates around the center of mass and translates only in the local y_i-direction. As stated before, the individual piezo elements are assumed to have no perpendicular displacement. The global x-translation results from stacking multiple layers, as shown in Fig. 3.3(b) and Fig. 3.6.

Let n_m be the number of layers in the model and n_t be the total number of layers in each stack of the bimorph piezo legs. As can be seen in Fig. 3.6, each layer can be described by two generalized coordinates q, representing the elongations of both piezoelectric elements in a layer. For n_m layers in the model, the vector of

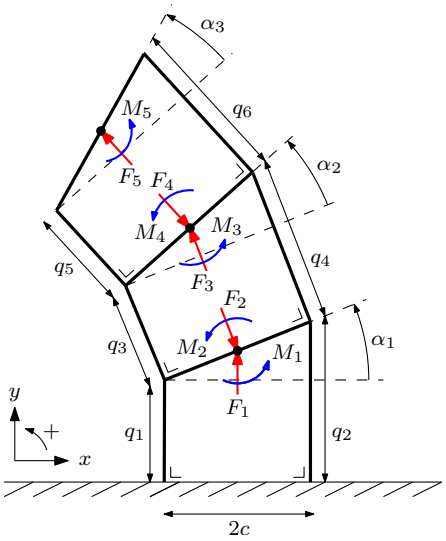

Figure 3.6: Stacked representation of multiple layers.

generalized coordinates becomes

$$\underline{q}(t) = \begin{bmatrix} q_1(t) & q_2(t) & \dots & q_{2n_m}(t) \end{bmatrix}^T, \quad \underline{q}(t) \in \mathbb{R}^{2n_m}.$$

The initial conditions are

$$\underline{q}_0 := \underline{q}(0) = \begin{bmatrix} L_0 & L_0 & \dots & L_0 \end{bmatrix}^T, \quad \underline{q}(0) \in \mathbb{R}^{2n_m},$$
$$\underline{\dot{q}}_0 := \underline{\dot{q}}(0) = \begin{bmatrix} 0 & 0 & \dots & 0 \end{bmatrix}^T, \quad \underline{\dot{q}}(0) \in \mathbb{R}^{2n_m},$$

where L_0 (m) denotes the initial length of the different layers. The inputs are the voltages $u_1(t)$ and $u_2(t)$. Since these are equal for each layer, the vector with inputs becomes

$$\underline{u}(t) = \begin{bmatrix} u_1(t) & u_2(t) \end{bmatrix}^T, \quad \underline{u}(t) \in \mathbb{R}^2.$$

The angles $\alpha_i(t)$, where $i \in \mathbb{Z}^{n_m}$ is the index number of the different layers, due to the elongations of the piezoelectric elements equal

$$\alpha_i(t) = \arcsin\left(\frac{q_{2i} - q_{2i-1}}{2c}\right), \tag{3.5}$$

where $\alpha_0 = 0$. The absolute angle of each center of mass (CM) is defined as

$$\beta_i(t) = \sum_{j=0}^{i} \alpha_j(t).$$

The absolute position of the CM of each layer $i \in \mathbb{Z}^{n_m}$ is

$$\underline{r}_{i,CM}(t) = \begin{bmatrix} -\sin(\beta_{i-1}(t)) \\ \cos(\beta_{i-1}(t)) \\ 0 \end{bmatrix} \frac{q_{2i-1}(t) + q_{2i}(t)}{2} + \underline{r}_{i-1}(t),$$

where $\underline{r}_{0,CM}(t) = \begin{bmatrix} 0 & 0 & 0 \end{bmatrix}^T$ and the absolute angle $\beta_i(t)$ is used.

Due to the angles α_i, $i \in \mathbb{Z}^{n_m}$, the base length increases slightly. This increase is considered to be negligible small, i.e., the extension of the base width due to the cosine term is linearized to be $2c$ (m).

The angular rotation vectors of the centers of mass for each layer are defined as

$$\underline{\phi}_{i,CM}(t) = \begin{bmatrix} 0 & 0 & \beta_i(t) \end{bmatrix}^T.$$

The force applied on the different masses due to the extension of each the piezoelectric elements can be combined into one force as

$$F(t) = f_1(t) + f_2(t),$$

where the exerted force by each piezo element due to an applied voltage follows from (3.4) as

$$f_i(t) = \frac{n_t}{n_m} d_{33} K_a u_i(t), \quad i \in \{1, 2\}. \tag{3.6}$$

The forces $\underline{F}_i \in \mathbb{R}^3$, $i \in \mathbb{Z}^{n_F}$, where $n_F = 2n_m - 1$ is the number of forces acting on all masses, equal

$$\underline{F}_i(t) = \begin{cases} \begin{bmatrix} -\sin(\beta_0(t)) \\ \cos(\beta_0(t)) \\ 0 \end{bmatrix} F(t), & \text{for } i = 1, \\ \begin{bmatrix} \sin(\beta_{i-1}(t)) \\ -\cos(\beta_{i-1}(t)) \\ 0 \end{bmatrix} F(t), & \text{for } i \in [2, 4, .., n_F - 1], \\ \begin{bmatrix} -\sin(\beta_{i-1}(t)) \\ \cos(\beta_{i-1}(t)) \\ 0 \end{bmatrix} F(t), & \text{for } i \in [3, 5, \ldots, n_F]. \end{cases}$$

The positions $\underline{r}_i(t)$, $i \in \mathbb{Z}^{n_F}$ where the forces act equal

$$\underline{r}(t) = [\, \underline{r}_{1,CM}(t) \quad \underline{r}_{1,CM}(t) \quad \cdots \quad \underline{r}_{n_F-1,CM}(t) \quad \underline{r}_{n_F-1,CM}(t) \quad \underline{r}_{n_F,CM}(t) \,].$$

The moment acting on each mass due to the extension of the piezo elements equals

$$M(t) = c(f_2(t) - f_1(t)).$$

The moments $\underline{M}_i(t) \in \mathbb{R}^3$, $i \in \mathbb{Z}^{n_M}$, where $n_M = 2n_m - 1$ is the number of moments, equals

$$\underline{M}_i(t) = \begin{cases} \begin{bmatrix} 0 \\ 0 \\ \cos(\alpha_i(t)) \end{bmatrix} M(t), & \text{for } i \in [1, 3, \ldots, n_M], \\ \begin{bmatrix} 0 \\ 0 \\ -1 \end{bmatrix} M(t), & \text{for } i \in [2, 4, \ldots, n_M - 1]. \end{cases}$$

The positions where the moments $\underline{\phi}_i(t)$, $i \in \mathbb{Z}^{n_M}$ act equal

$$\underline{\phi}(t) = [\ \underline{\phi}_{1,CM}(t) \quad \underline{\phi}_{1,CM}(t) \quad \cdots \quad \underline{\phi}_{n_M-1,CM}(t) \quad \underline{\phi}_{n_M-1,CM}(t) \quad \underline{\phi}_{n_M,CM}(t)\ ].$$

The damping forces $F_{d,i}(t)$, $i \in [1, \ldots, 2n_m]$ in the individual piezoelectric elements, acting on all individual generalized coordinates, equal

$$F_{d,i}(t) = d(\dot{q}_i(t) - \dot{q}_{0,i}).$$

The nonconservative generalized forces [43] can now be calculated as

$$Q^{nc} = \sum_{i=1}^{n_F} \left(\frac{\partial \underline{r}_i}{\partial \underline{q}} \right)^T \underline{F}_i + \sum_{j=1}^{n_M} \left(\frac{\partial \underline{\phi}_j}{\partial \underline{q}} \right)^T \underline{M}_i - \sum_{l=1}^{n_D} \left(\frac{\partial \dot{q}_l}{\partial \underline{\dot{q}}} \right) F_{d,l}. \tag{3.7}$$

The kinetic energy equals

$$T = \frac{1}{2} \sum_{i=1}^{n_m} m_i\ \underline{\dot{r}}_i^T\ \underline{\dot{r}}_i + \sum_{i=1}^{n_m} \frac{1}{2} J_i\ \underline{\dot{\phi}}_i^T\ \underline{\dot{\phi}}_i, \tag{3.8}$$

where $\underline{\dot{r}} = d/dt(\underline{r})$ and $\underline{\dot{\phi}} = d/dt(\underline{\phi})$ are the time derivatives of the position and rotation vectors, respectively. The potential energy equals

$$V = \frac{1}{2} \sum_{i=1}^{2n_m} k(q_i - q_{0,i})^2, \tag{3.9}$$

where $k = K_a$. For use in nano-motion stages, the piezo legs motor is rotated to have the legs horizontally pressed against a drive surface (see Chapter 2). Therefore, no gravity is added to the model. If desired, the gravity can be added easily by extending (3.9) with $V^{ex} = -mg \cdot \underline{r}_{CM}$, where g is the gravitational constant.

The Lagrange's equations of motion can now be calculated using [43]

$$\frac{d}{dt} \left(\frac{\partial T}{\partial \underline{\dot{q}}} \right) - \frac{\partial T}{\partial \underline{q}} + \frac{\partial V}{\partial \underline{q}} = \left(\underline{Q}^{nc} \right)^T. \tag{3.10}$$

3.3.3 Equilibrium dependent dynamics

The dynamic behavior of the walking piezo legs motor is dependent on the changing contribution of the piezo legs in the drive direction over one drive cycle as prescribed by the waveforms, i.e., on the momentary operating conditions. In order to evaluate this dependency, the Lagrangian equations of motion are linearized around different equilibrium positions $\underline{q}_e$.

The Lagrangian equations of motion of (3.10) can be rewritten as [43]

$$\underline{M}\left(\underline{q}\right)\ddot{\underline{q}} + \underline{H}\left(\underline{q},\dot{\underline{q}}\right) = \underline{S}\left(\underline{q}\right)\underline{\tau}, \tag{3.11}$$

where $\underline{M}\left(\underline{q}\right)$ is the mass matrix, $\underline{H}\left(\underline{q},\dot{\underline{q}}\right)$ contains the centripetal and Coriolis terms as well as the gravitational effects, $\underline{S}\left(\underline{q}\right)$ represents the generalized force directions and $\underline{\tau} = [f_1 \;\; f_2]^T$ contains the inputs.

The nonlinear dynamics of (3.11) can be linearized around an equilibrium position $\underline{q}_e$ by splitting the generalized coordinates as $\underline{q} = \underline{q}_e + \underline{q}_l$, where $\underline{q}_l$ are small perturbations around $\underline{q}_e$. Furthermore, define $\dot{\underline{q}}_e = \underline{0}$ and $\ddot{\underline{q}}_e = \underline{0}$. The external forces are split as $\underline{\tau} = \underline{\tau}_e + \underline{\tau}_l(t)$, where $\underline{\tau}_e$ is the equilibrium input corresponding to $\underline{q}_e$ and $\underline{\tau}_l(t)$ is the time-dependent part that causes the small perturbations $\underline{q}_l$, where in the equilibrium $\underline{\tau}_l(t) = 0$.

For the model of the walking piezo actuator, the global tip position of the top element in x- and y-direction is chosen as the output, which can be defined as

$$\underline{g}\left(\underline{q}\right) = \left[r_{n_m,x} \quad r_{n_m,y}\right]^T. \tag{3.12}$$

Now, rename the matrices using the following definitions

$$\underline{M} := \underline{M}(\underline{q}_e), \qquad \underline{D} := \left.\frac{\partial \underline{H}}{\partial \dot{\underline{q}}}\right|_{\substack{\underline{q}=\underline{q}_e \\ \dot{\underline{q}}=\underline{0}}},$$

$$\underline{S} := \underline{S}(\underline{q}_e), \qquad \underline{K} := \left.\frac{\partial \underline{H}}{\partial \underline{q}}\right|_{\substack{\underline{q}=\underline{q}_e \\ \dot{\underline{q}}=\underline{0}}} - \left.\frac{\partial \underline{S}\underline{\tau}_e}{\partial \underline{q}}\right|_{\underline{q}=\underline{q}_e},$$

to obtain the linearized system

$$\underline{M}\ddot{\underline{q}}_l + \underline{D}\dot{\underline{q}}_l + \underline{K}\underline{q}_l = \underline{S}\,\underline{\tau}_l(t). \tag{3.13}$$

Define the linearized output matrix $\underline{W}(\underline{q}) := \frac{\partial \underline{g}}{\partial \underline{q}}(\underline{q}_e)$. Let the state $\underline{x} = [\underline{q}^T \;\; \dot{\underline{q}}^T]^T := [\underline{x}_1^T \;\; \underline{x}_2^T]^T$ and the input array $\underline{u} := \underline{\tau}_l$. The linearized system in state space

description can now be written as

$$\begin{aligned} \underline{\dot{x}} &= \underline{A}\underline{x} + \underline{B}\underline{u}, \\ \underline{y} &= \underline{C}\underline{x}, \end{aligned} \tag{3.14}$$

where

$$\underline{A} = \begin{bmatrix} \underline{0} & \underline{I} \\ -\underline{M}^{-1}\underline{K} & -\underline{M}^{-1}\underline{D} \end{bmatrix},$$

$$\underline{B} = \begin{bmatrix} \underline{0} & \underline{M}^{-1}\underline{S} \end{bmatrix}^T,$$

$$\underline{C} = \begin{bmatrix} \underline{W} & \underline{0} \end{bmatrix}.$$

The transfer function can be calculated for every equilibrium position using the Laplace transform

$$\underline{X}(s) = \underline{C}\left(s\underline{I} - \underline{A}\right)^{-1}\underline{B}\underline{U}(s) = \underline{H}_{ru}(s)\underline{U}(s), \tag{3.15}$$

where

$$\underline{H}_{ru}(s) = \begin{bmatrix} H_{x,u_1}(s) & H_{x,u_2}(s) \\ H_{y,u_1}(s) & H_{y,u_2}(s) \end{bmatrix}.$$

3.3.4 Linear static relations

Since the mass of the different piezo elements is small and the stiffness high, the resonance frequencies are expected to be very high.

In [92, 155], the relation between the input voltages $u_{1,2}(t)$ and the tip positions in the Cartesian (x, y)-plane, denoted by x_t and y_t, is specified to be a linear static map as

$$x_t = c_x(u_1(t) - u_2(t)), \tag{3.16}$$

$$y_t = c_y(u_1(t) + u_2(t)), \tag{3.17}$$

where c_x (m/V) and c_y (m/V) are the constant bending and extension coefficients, respectively.

The relations (3.16) and (3.17) will be validated in two steps, 1) by deriving a static map of the model and 2) by linearizing the static map. The validity to use a static linear map to describe the true leg positions is not assessed at this point.

Another goal of the static linearization is to derive analytical expressions based on physical parameters for the bending and extension coefficients c_x and c_y in (3.16) and (3.17), respectively.

Analytical expressions for the bending and extension coefficients c_x and c_y as function of the physical parameters can be derived by linearizing the equations of motion for small movements $\underline{q}$.

For the static relation, first define $\ddot{\underline{q}} = 0$ and $\dot{\underline{q}} = 0$. Now we define

$$\underline{F}(\underline{q}, \underline{\tau}) := \underline{H}\left(\underline{q}, \underline{0}\right) - \underline{S}\left(\underline{q}\right)\underline{\tau} \tag{3.18}$$

and consequently (3.11) implies that the equilibrium equations are described by $F(\underline{q}_e, \underline{\tau}_e) = 0$.

Relation (3.18) is nonlinear in q_e and $\tau_e = [f_{1,e},\ f_{2,e}]^T$. For the validation of (3.16) and (3.17), a linear approximation is pursued. In (3.13) a linearization around an arbitrary equilibrium $\underline{q}_e$ is performed. For the static linearized model, a linearization around one specific equilibrium, i.e., with $\underline{\tau}_e = 0$ and $\underline{q}_e = \underline{q}_0$, is performed. If the linear perturbations around the equilibrium position and input are denoted by $\tilde{\underline{q}}$ and $\tilde{\underline{\tau}}$, the first order Taylor expansion of (3.18) can be written as

$$\underline{F}(\underline{q}_e, \underline{\tau}_e) \simeq \underline{F}(\underline{q}_0, \underline{0}) + \left.\frac{\partial \underline{F}}{\partial \underline{q}_e}\right|_{\substack{\underline{q}_e = \underline{q}_0 \\ \underline{\tau}_e = \underline{0}}} \tilde{\underline{q}} + \left.\frac{\partial \underline{F}}{\partial \underline{\tau}_e}\right|_{\substack{\underline{q}_e = \underline{q}_0 \\ \underline{\tau}_e = \underline{0}}} \tilde{\underline{\tau}}, \tag{3.19}$$

where $\tilde{\underline{\tau}} = [\tilde{f}_1,\ \tilde{f}_2]^T$ are the linearized inputs. Equating (3.19) to zero yields

$$\tilde{\underline{q}} \simeq \left(\frac{\partial \underline{F}}{\partial \underline{q}_e}\right)^{-1}\Bigg|_{\substack{\underline{q}_e = \underline{q}_0 \\ \underline{\tau}_e = \underline{0}}} \left[-\left.\frac{\partial \underline{F}}{\partial \underline{\tau}_e}\right|_{\substack{\underline{q}_e = \underline{q}_0 \\ \underline{\tau}_e = \underline{0}}} \tilde{\underline{\tau}} - \underline{F}(\underline{q}_0, \underline{0})\right]. \tag{3.20}$$

Note that the matrix $\partial \underline{F}/\partial \underline{q}_e$ must be invertible for the above expression to exist. For the static relation, also the nonlinear output equation (3.12) must be linearized as

$$\tilde{\underline{g}}(\tilde{\underline{q}}) \simeq g\left(\underline{q}_0\right) + \left.\frac{\partial \underline{g}}{\partial \underline{q}_e}\right|_{\underline{q}_e = \underline{q}_0} \tilde{q}. \tag{3.21}$$

Substitution of (3.20) in (3.21) gives the approximated static relation between the input $\tilde{\underline{\tau}} = [\tilde{f}_1,\ \tilde{f}_2]^T$ and the global position of the tip of the leg $\tilde{\underline{g}}$.

3.4 Model identification

Using an electron microscope, a detailed image of the piezo legs is made, from which construction details and physical properties are derived. The structure of

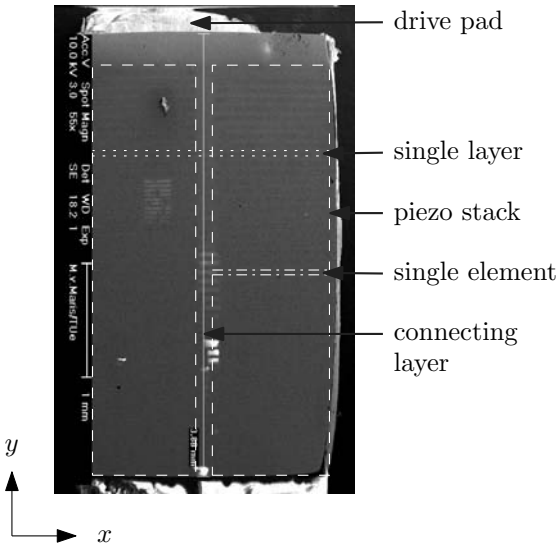

Figure 3.7: Picture of one piezo leg (side view).

one of the bimorph legs is shown in Fig. 3.7. Each leg contains two piezo stacks, indicated by the dashed boxes. Between the two stacks, there is a connecting layer. Each stack contains $n_t = 96$ piezo elements, one of which is indicated by the dash-dotted lines. Each layer in the model contains a piezo element from each stack and a part of the connecting layer, as indicated by the dotted lines.

Using the measurements of the legs obtained using the image from the electron microscope and the material properties for lead zirconate titanate (PZT) piezo material [121, 158, 200], the model parameters are identified as given in Table 3.1. Note that the mass m and the stiffness K_a are calculated using twice the area A since each pair of legs is modeled as a single leg.

In practice, the legs of the walking piezo motor are pressed against the drive surface of a stage using preload springs (see Chapter 2). If a preload force is applied, this can be represented by a linear spring with pre-tension stiffness K_p (N/m) in parallel with the separate piezo elements [158]. The equivalent properties of the prestressed piezo elements can be obtained using (3.3) by changing the short-circuited stiffness to $k = K_a + K_p$ [158].

The applied force of each piezoelectric element (3.4) now becomes [158]

$$f = -\frac{n_t}{n_m} d_{33} K_a u + (K_a + K_p)\Delta. \tag{3.22}$$

Table 3.1: The identified model parameters for the bimorph piezo leg.

Parameter	Unit	Value	Description
n_t	-	96	number of elements in stack
n_m	-	$[1, \ldots, n_t]$	number of layers in model
b_s	m	$1.5 \cdot 10^{-3}$	width single stack
c	m	$b_s/2$	half width neutral line
d_s	m	$3.0 \cdot 10^{-3}$	depth single stack
A	m^2	$b_s d_s$	area single stack
L_0	m	$3.9 \cdot 10^{-3}/n_m$	initial length of layer in model
e_{31}	N/(Vm)	-9.0	piezoelectric constant
d_{31}	m/V	$-310 \cdot 10^{-12}$	piezoelectric constant
s^E	m^2/N	d_{31}/e_{31}	tensor of compliance
d_{33}	m/V	$620 \cdot 10^{-12}$	piezoelectric constant
ρ	$\mathrm{kg/m}^3$	7600	density PZT
m	kg	$2\rho A L_0$	mass single layer in model
J	kgm^2	$\frac{1}{12} m(b_s^2 + L_0^2)$	inertia single layer in model
K_a	N/m	$2A/(s^E L_0)$	stiffness piezo element
K_p	N/m	$25.6 \cdot 10^3 n_m$	pre-tension piezo legs
k	N/m	$K_a + K_p$	total stiffness
d	Ns/m	$1 \cdot 10^{-3}$	damping

To press the piezo actuator against the drive surface of the stage, two springs with a stiffness of $12.8 \cdot 10^3$ N/m are applied. The equivalent spring stiffness for the two parallel preload springs equals $25.6 \cdot 10^3$ N/m. The preload springs are incorporated in the model of the individual layers. Due to the series connection of the different layers in the model the preload stiffness of the individual layers equals $K_p = 25.6 \cdot 10^3 n_m$ N/m, as specified in Table 3.1.

3.5 Results

In this section the results of the model derived in Section 3.3 with the model parameters of Table 3.1 will be presented. The dynamics of the piezo legs model will be presented in Section 3.5.1 for a varying number of layers n_m and different equilibrium positions $\underline{q}_e$. Furthermore, the derived static relation of Section 3.3.4 will be validated experimentally in Section 3.5.2.

3.5.1 Dynamic model

In this section, the dynamic properties of the model are assessed for both varying number of layers n_m and varying equilibrium positions $\underline{q}_e$.

Each pair of input forces of the piezo stacks $\underline{\tau}_e = [f_{1,e} \quad f_{2,e}]$ results in an equilibrium position $\underline{q}_e$. The elongations of the piezoelectric elements on the left side of the leg, i.e., the generalized coordinates with an uneven subscript, depend in steady-state only on the input voltage $u_{1,e}$. On the right side, i.e., with an even subscript, the equilibrium positions of the generalized coordinates depend on the input voltage $u_{2,e}$. The equilibrium vector can therefore be divided as

$$\underline{q}_e = \begin{cases} q_{1,e}, & \text{for } \underline{q} = \{q_1, q_3, \ldots, q_{2n_m-1}\}, \\ q_{2,e}, & \text{for } \underline{q} = \{q_2, q_4, \ldots, q_{2n_m}\}, \end{cases} \tag{3.23}$$

where the equilibrium positions $q_{i,e}$, $i \in \{1, 2\}$ are calculated using (3.20).

Varying number of layers n_m

The model order and thus the number of resonances is dependent on the number of layers n_m that are contained in the model. The frequency response function (FRF) of the system (3.15) is shown in Fig. 3.8 for $n_m \in [2, 4, 6, 8, 10]$ layers and an equilibrium input of $u_{1,e} = 20.2$ V, $u_{2,e} = 44.2$ V. The frequency of the first resonance and the static gain increase with increasing n_m.

When comparing the FRFs of the transfer functions from the input voltages $u_{1,2}$ to the tip positions in x- and y-direction, it can be seen that the variation in steady-state gain is only visible in the FRFs for the x-direction. A change in the number of layers n_m has more effect on the steady-state gain in x-direction than in y-direction. Furthermore, the steady-state gain in y-direction is larger than in x-direction due to the bimorph working principle, i.e., an x-displacement is caused by the difference of both the voltages u_1 and u_2 and since the x-displacement is obtained through stacking of multiple layers with a rotated mass m.

The FRFs of the voltage u_1 to the x-direction shows a difference from the FRF of u_2 to the x-direction. This difference is not visible in the FRFs of both voltages to the y-direction. The difference is caused by the orientation of the leg in which the FRFs are calculated, i.e., on the equilibrium position $\underline{q}_e$. For different equilibrium positions, a change in the voltages has a larger effect on the dynamics in x- as in y-direction and with this on the FRFs.

The high frequent resonance frequencies affect the steady-state gain. The steady-state gains and the first resonance frequency of $H_{x,u1}(s)$ are contained for $n_m \in$

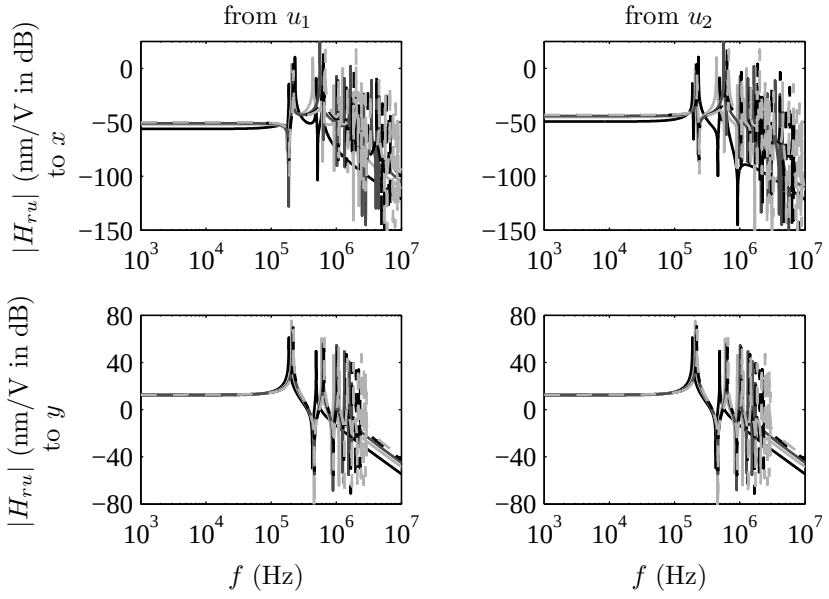

Figure 3.8: FRF of $\underline{H}_{ru}(s)$ (3.15) for $n_m \in [2, 4, 6, 8, 10]$.

Table 3.2: Steady-state gain and first resonance frequency of $H_{x,u1}$ for $n_m \in [2, 4, 6, 8, 10]$.

n_m	2	4	6	8	10
$\lvert H_{x,u1}(s \downarrow 0)\rvert$ in dB	-56.1	-51.9	-50.9	-50.4	-50.1
f_{res} (kHz)	187.7	207.0	215.0	219.0	221.7

$[2, 4, 6, 8, 10]$ layers in Table 3.2. The increase in the steady-state gain and of the first resonance frequency are considered negligible small for $n_m \geq 6$ layers. Therefore, the minimum number of layers in terms of the lowest model order with sufficient accuracy is $n_m = 6$. The steady-state gain of $\underline{H}_{ru}$ for $n_m = 6$ equals

$$\underline{H}_{ru}(s \downarrow 0) = \begin{bmatrix} -50.9 & -44.1 \\ 12.7 & 12.7 \end{bmatrix} \text{ dB},$$

the first resonance frequency is located at $f_{res} = 215.0$ kHz.

Varying equilibrium $\underline{q}_e$

In Chapter 2, sinusoidal input voltages and asymmetric input voltages, resulting in overlapping tip trajectories, are designed. The model is tested for both the sinusoidal voltages

$$\tilde{u}_{1,2}^{\sin}(t) = \frac{A}{2}\sin(\alpha(t) + \psi_{1,2}) + \frac{A}{2}, \tag{3.24}$$

and the asymmetric input voltages, which are described in Chapter 2 using a fourth order Fourier series as

$$\tilde{u}_{1,2}^{\text{over}}(t) = \frac{A}{\bar{A}}a_0 + \frac{A}{\bar{A}}\sum_{k=1}^{4}\left\{a_k\cos[k\alpha(t) + k\psi_{1,2}(t)] + b_k\sin[k\alpha(t) + k\psi_{1,2}(t)]\right\}, \tag{3.25}$$

with Fourier coefficients $a_0 = 28.80$, $a_1 = -10.78$, $b_1 = 18.73$, $a_2 = 2.387$, $b_2 = 4.097$, $a_3 = 1.985$, $b_3 = -0.007792$, $a_4 = 0.2298$, and $b_4 = -0.3901$. The amplitudes $\bar{A} = 46$ V and $A = 46$ V. The phases $\psi_1 = 0$ rad and $\psi_2 = \pi/2$ rad for the voltages u_1 and u_2, respectively.

In Fig. 3.9, the FRFs of the system (3.15) with $n_m = 6$ layers and varying angle $\alpha \in [0, \pi/36, \pi/18, \ldots, 2\pi]$ rad are shown. The width c is of order $\mathcal{O}(c) = 10^{-3}$ m and the elongations q_i are maximally of order $\mathcal{O}(q_i) = 10^{-6}$ m. To derive the linearized equations of motion (3.13) from (3.11), the angles $\alpha_i(t)$ are linearized as

$$\alpha_i(t) = \arcsin\left(\frac{q_{2i} - q_{2i-1}}{2c}\right) \approx \frac{q_{2i} - q_{2i-1}}{2c}.$$

For each value of α, the input voltages can be calculated using (3.24) or (3.25). The corresponding equilibrium positions $\underline{q}_e$ can be calculated using (3.23).

The steady-state gains of the transfer functions $H_{x,u_1}(s)$ and $H_{x,u_2}(s)$ vary for different equilibria, i.e., for different leg positions. The gain variations of $H_{x,u_1}(s)$ and $H_{x,u_2}(s)$ are equal for varying α over a complete cycle, i.e., $\alpha \in [0, 2\pi]$ rad. The variations of the steady-state gains $H_{y,u_1}(s) = Y(s)/U_1(s)$ and $H_{y,u_2}(s) = Y(s)/U_2(s)$ and the dynamics in y-direction for varying α are negligible small.

The results show that the model structure can be used to analyze the dynamic behavior of bimorph piezo actuators. However, the dynamics of the considered piezo actuator are located at frequencies $f > 215$ kHz and are therefore irrelevant for control design purposes, as addressed in this thesis. The static analysis is much more relevant in this respect. The static analysis allows analytical expressions based on physical properties to be derived for the static bending and extension coefficients of the bimorph piezo legs, which is the subject of the next section together with an experimental validation.

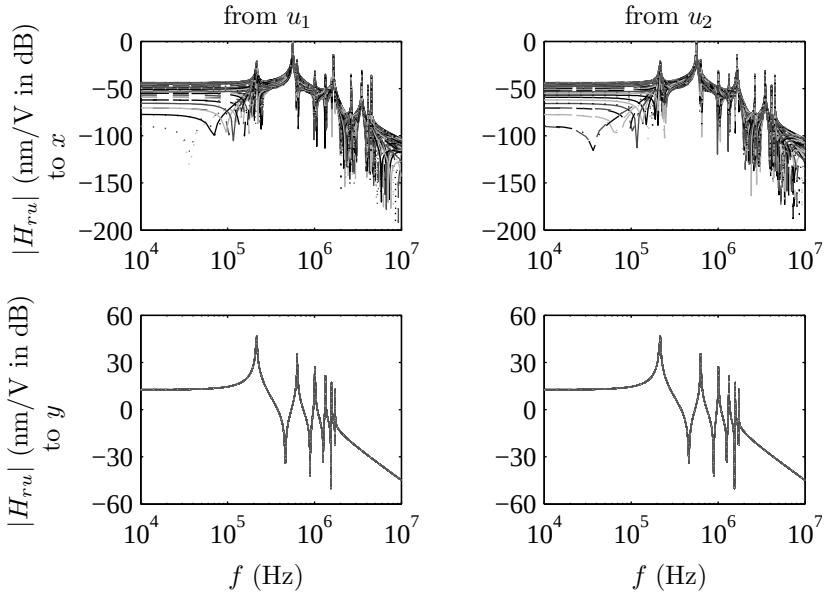

Figure 3.9: FRF of $\underline{H}_{ru}(s)$ (3.15) for different equilibria $\underline{q}_e$.

3.5.2 Static model

For the experimental validation of (3.20) and (3.21), the piezo legs motor is mounted to a one degree-of-freedom (DOF) stage as shown in Fig. 3.10. The drive pads of the legs are fitted to the drive strip of the 1-DOF stage using a motor suspension and preload springs such that the (x_m, y_m, z_m)-axes of the motor (see Fig. 3.1) coincide with the (x, y, z)-axes of the stage. The stage is equipped with a linear incremental encoder with a resolution of 0.64 nm. The movement of the back side of the motor is measured with a capacitive sensor with a resolution of 0.44 nm.

Experiments are performed using both the sinusoidal waveforms of (3.24) and the asymmetric waveforms of (3.25) for $\alpha(t) = 2\pi t$ rad. During the experiment, the second pair of legs is kept at its zero state, i.e., $u_3(t) = u_4(t) = 0$. Since the movement is performed at a low frequency, the stage and back of the motor are assumed to follow the tip movement of the leg directly.

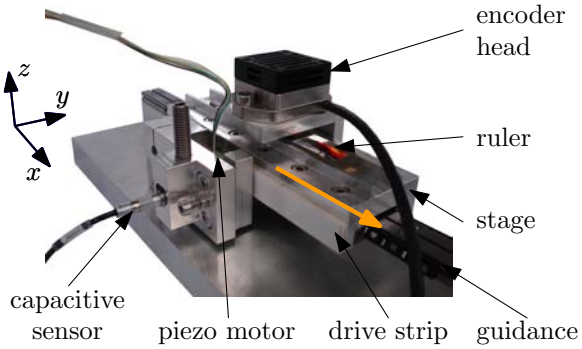

Figure 3.10: Experimental setup containing the walking piezo actuator fitted to a 1-DOF stage.

The static linearized output equations for $n_m = 6$ equal

$$\tilde{x} = \frac{15L_0}{2ck}\left(\tilde{f}_1(t) - \tilde{f}_2(t)\right), \tag{3.26}$$

$$\tilde{y} = \frac{3}{k}\left(\tilde{f}_1(t) + \tilde{f}_2(t)\right). \tag{3.27}$$

Combination of (3.26) and (3.27) with (3.6) results in

$$\tilde{x} = \frac{15L_0 n_t d_{33} K_a}{2cn_m k}\left(\tilde{u}_1(t) - \tilde{u}_2(t)\right), \tag{3.28}$$

$$\tilde{y} = \frac{3n_t d_{33} K_a}{n_m k}\left(\tilde{u}_1(t) + \tilde{u}_2(t)\right). \tag{3.29}$$

The constant bending and extension coefficients of [155] follow by comparison of (3.28) to (3.16) and (3.29) to (3.17) as

$$c_x = \frac{15L_0 n_t d_{33} K_a}{2cn_m k}, \quad c_y = \frac{3n_t d_{33} K_a}{n_m k}.$$

With the setup of Fig. 3.10, only relative measurements of the x- and y-positions are possible. Therefore, the contributions of x_0 and y_0 are not taken into account in (3.26) and (3.27). To compare the results of the static linearized model and the relative experimental data, the measurement results are shifted such the minimal values of the model and measurements data coincide.

The measured positions in x- and y-directions are shown in Fig. 3.11 for sinusoidal waveforms with the solid grey line. The tip trajectory according to (3.26) and (3.27) is shown by the dashed black line. It can be seen that the magnitude of the movement is approximately equal in both x- and y-direction.

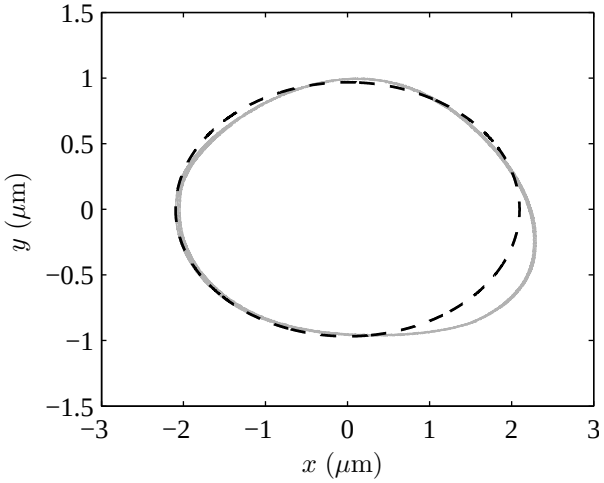

Figure 3.11: Measured (grey, solid) and calculated (black, dashed) tip trajectories for sinusoidal waveforms.

The measured and calculated time signals in x- and y-direction are shown in Fig. 3.12(a) and Fig. 3.12(b), respectively. The grey solid line represents the measured positions and the black dashed lines represents the modeled positions using (3.26) and (3.27). The errors between the calculated and measured positions, defined as $e_x = x - \tilde{x}$ and $e_y = y - \tilde{y}$ with x and y the measured positions in x- and y-direction, are also shown. The static relations describe the movement in x-direction with an accuracy of 77% and in y-direction with an accuracy of 90%. The cumulative power spectral densities of the errors, shown in Fig. 3.12(a), will converge for $f \to \infty$ to the squared rms values, which equal $\text{rms}(e_x) = 0.25$ μm and $\text{rms}(e_y) = 0.044$ μm.

Besides the good correspondence, there is also a remaining difference between the measured and modeled positions. The modeled tip position is symmetric around the origin in Fig. 3.11 whereas an asymmetry can be seen in the measured response. Also a small difference in amplitude in the x-direction is visible. These differences are probably caused by unmodeled phenomena, e.g., hysteresis, variation in lengths of the piezo stacks or different lengths of the legs in a single pair, or by measurement errors, e.g., sensor alignment.

The measured and modeled positions are shown for the asymmetric waveforms of (3.25) in Fig. 3.13. Also for these waveforms, the global shape of the trajectories shows a good resemblance. The deviations are thought to be caused by the same causes as for the sinusoidal waveforms.

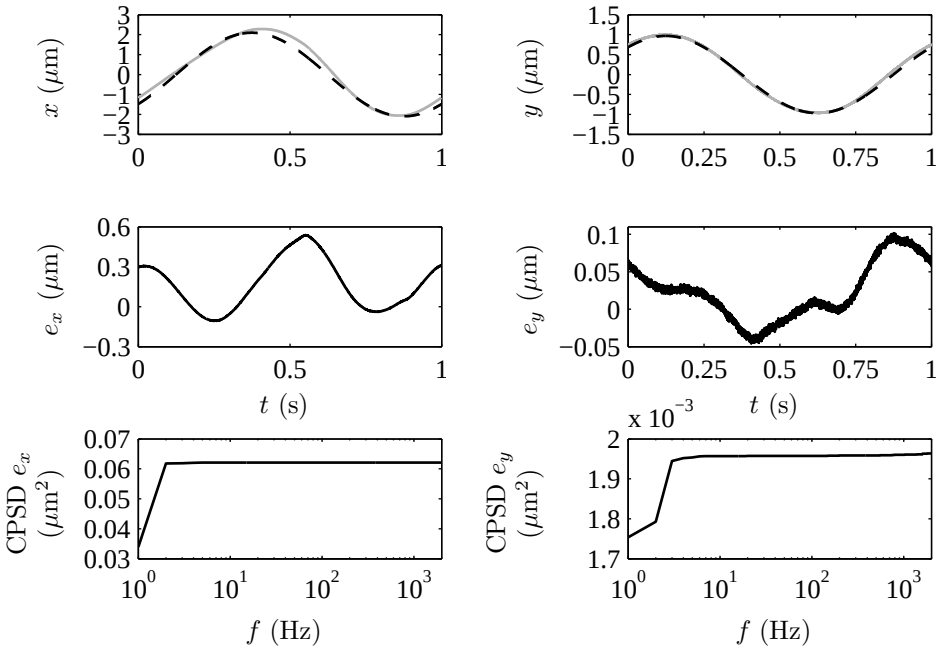

(a) x-direction. (b) y-direction.

Figure 3.12: Measured (grey, solid) and calculated (black, dashed) positions, errors and cumulative PSDs of the errors for sinusoidal waveforms.

The measured and modeled time signals are shown for the x- and y-direction in Fig. 3.14(a) and Fig. 3.14(b), respectively. Also in the time domain, the responses show a good resemblance. The root-mean-square (rms) values of the errors equal $\mathrm{rms}(e_x) = 0.15$ μm and $\mathrm{rms}(e_y) = 0.056$ μm, respectively. The errors show that for the asymmetric waveforms the x-direction is described with an accuracy of 87% and the y-direction with an accuracy of 85%. The cumulative power spectral densities of the errors are shown in the bottom axes of Fig. 3.14.

3.6 Conclusions

In this chapter, we have derived an electro-mechanical model of a bimorph walking piezo actuator. Each leg of the actuator consists of two electrically separated piezo stacks. The piezoelectric elements are modeled as a parallel coupling of an actuator force due to an applied voltage and a spring. The different layers in the bimorph

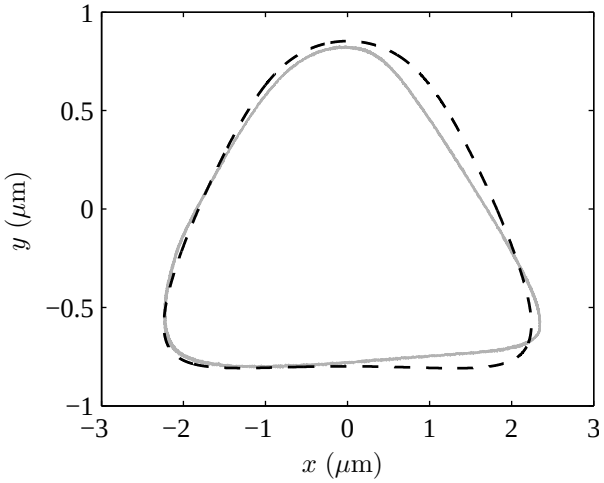

Figure 3.13: Measured (grey, solid) and calculated (black, dashed) tip trajectories for asymmetric waveforms.

piezo legs are modeled using a lumped structure of connected mass-spring-damper elements. The model is derived based on physical properties of the motor.

An energy based approach is used to derive the dynamic model of the walking piezo actuator through the Lagrange equations of motion. The varying system dynamics are assessed by linearization of the nonlinear dynamics around different equilibria. The resonance frequencies are located at frequencies $f \geq 215.0$ kHz. Therefore, the legs are considered static for control purposes. A linearization is performed to find a static relation between the input waveforms and the tip trajectories of the leg. The static linearization gives a physical interpretation of the constant bending and extension coefficients of the legs.

The modeled tip trajectories show a good correspondence to the experimentally obtained measurements for both sinusoidal and asymmetric waveforms. The model describes the tip trajectories with an accuracy between 77% and 90%.

Future work includes extending the model to better describe the experimental results by investigating the asymmetry in the measured results and by modeling the hysteresis in the piezo motor. Furthermore, the model will be used to obtain optimal input voltages to the legs using optimization techniques.

Since the analytical model is based on physical properties of the piezo actuator, new walking piezo actuators with different properties could be developed by using the model in a design optimization.

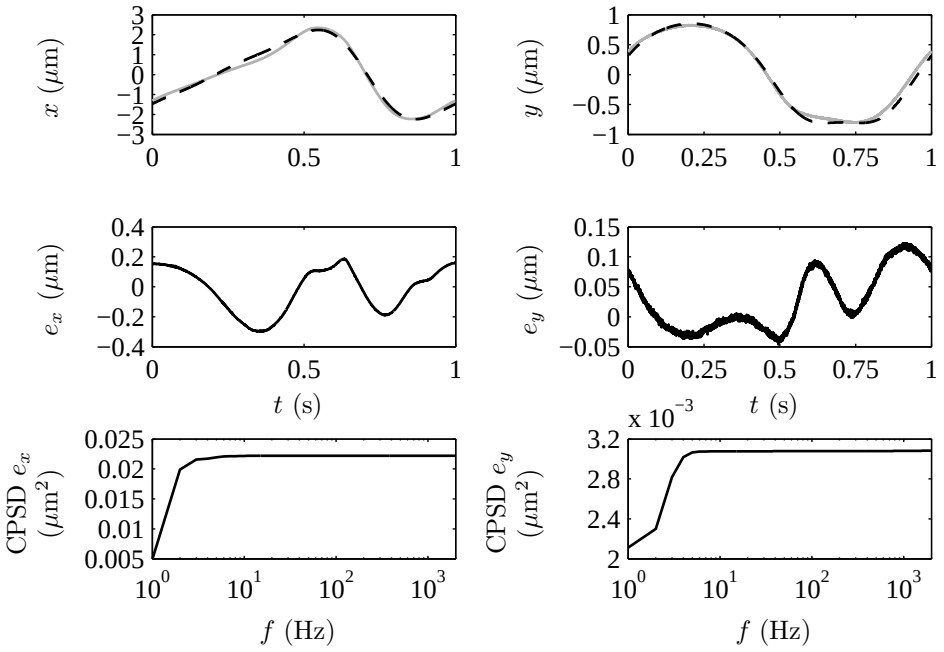

(a) x-direction. (b) y-direction.

Figure 3.14: Measured (grey, solid) and calculated (black, dashed) positions, errors and cumulative PSDs of the errors for asymmetric waveforms.

Chapter 4

Waveform optimization

Abstract - Piezo actuators are used in high-precision systems that require nanometer accuracy. In this chapter we consider a nano-motion stage driven by a walking piezo actuator, which contains four bimorph piezo legs. We propose a (model-based) optimization method to derive waveforms that result in optimal driving properties of the walking piezo motor. A model of the stage and motor is developed incorporating the switching behavior of the drive legs, the contact deformation and stick-slip effects between the legs and the stage. The friction-based driving principle of the motor is modeled using a set-valued friction model, resulting in a model in terms of differential-algebraic inclusions. For this model we developed a dedicated numerical time-stepping solver. Experiments show a good model accuracy in both the drive direction and the perpendicular direction. The validated model is used in an optimization, resulting in waveforms with optimal driving properties of the stage at constant velocity. Besides the model-based optimization, also a direct experimental data-based waveform optimization is performed. Experiments with the optimized waveforms show that compared to existing sinusoidal and asymmetric waveforms in literature the driving properties can be significantly improved by the model-based waveforms and even further by the data-based waveforms.

This chapter is based on: Roel Merry, Martijn Maassen, René van de Molengraft, Nathan van de Wouw and Maarten Steinbuch. Modeling and waveform optimization of a nano-motion piezo stage. Submitted, 2009.

4.1 Introduction

Piezo actuators are used in high-precision systems that require nanometer accuracy due to their attractive properties such as good reproducibility, high stiffness and fast response. Stepping piezo actuators are able to drive nano-motion stages at constant velocities in the order of nanometers per second to millimeters per second. To obtain good positioning and tracking performance of the stages, a driving principle of the stepping piezo actuators with a continuous actuation and smooth transitions between the driving piezo legs is desired.

In this chapter we consider a nano-motion stage driven by a walking piezo actuator. The walking piezo actuator employs four bimorph piezo legs to drive the stage in pairs of two. The orbits of the drive legs are defined by the electric drive waveforms to the motor. With the sinusoidal and asymmetric waveforms of Chapter 2 no satisfactory driving properties are obtained; stick-slip effects and different leg velocities at the transfer between the driving pairs of legs limit the actuation of the piezo legs at a constant velocity and result in a non-smooth stage behavior. To reduce the effect of these performance limiting factors (PLF), a model-based approach is followed to obtain new actuator driver software. In this chapter, we develop a model of the nano-motion stage and walking piezo actuator, which is experimentally validated and used to derive new waveforms by means of optimization techniques.

The model of the nano-motion stage with the piezo motor includes the alternating nature of the walking movement of the piezo legs, the contact dynamics and the stick-slip effects between the motor and the stage. Although the piezo legs contain some hysteresis, in most applications nearly linear operating conditions are selected [57]. Therefore, in this chapter hysteresis is not taken into account. An overview of models for contact dynamics for an ultrasonic piezo motor is given in [211]. The contact between the piezo legs and the drive strip of the nano-motion stage is modeled using a nonlinear contact stiffness. The driving principle of the walking piezo motor is based on friction. Therefore, accurate modeling of the friction between the stage and motor is important. In [98], three different friction models are compared for a friction drive piezo actuator. It is found that the variation of the friction force due to a variation in normal force should be taken into account. To model the friction force, which depends on the normal forces, and to properly model stiction, a set-valued friction model is used [71, 143].

Numerical simulation of the dynamic model including the set-valued friction model could be performed by smoothening of the set-valued nonlinearity, but this leads to (non-unique) approximations and stiff differential equations [3]. Event driven methods [153] are not favorable for our application since we split the model of

the piezo-driven nano-motion stage in a model in the drive direction and a model in the perpendicular direction, of which simulation results at each time-step have to be combined. Furthermore, the model results are compared to experimental data at an equidistant sampling grid. Since we are interested in the effect of friction on the global dynamics, but not in exact timing information of stick-slip transitions, we exploit time-stepping methods to perform numerical simulations with the dynamic model including the set-valued friction model [3, 108]. Here we formulate the model in terms of a differential-algebraic inclusion, for which we develop a dedicated time-stepping solver. The model and numerical solver can be used for the optimization of the waveforms to the piezo legs to optimize the legs orbit design.

In literature, several algorithms have been described for waveform optimization. In [152], a computationally efficient real-time trajectory optimization technique is proposed. Optimal input signals are derived in [61] for systems in which part of the trajectory is chosen fixed. Although interesting, these methods are not adopted in this chapter since, firstly, in our problem the optimization is performed off-line and as a consequence computational efficiency is not really an issue and, secondly, the input signals to be designed are completely free.

Waveforms for piezo devices have already been studied in literature. In [101], triangular, rectangular and sinusoidal waveforms for an inchworm actuator are compared. The sinusoidal and triangular waveforms perform best. The period time and slopes of triangular driving waveforms are optimized for maximum velocity in [90]. In [118], possible trajectories for a walking micro-robot employing six bimorph piezo legs are described. However, no trajectory optimization for a specific goal is performed. In [203], iterative learning control of two parameters is applied to obtain a smooth stepping function for a piezo stepper with six legs. To the authors best knowledge, no trajectory optimization for bimorph walking piezo motors has been described yet in literature. In Chapter 2, we proposed asymmetric waveforms, which improve the driving properties of the bimorph walking piezo motor. The optimized waveforms derived in this chapter will be compared to these asymmetric waveforms.

The cost functions for the optimizations in this chapter are typically nonlinear in the optimization parameters. Since we are interested in the global optimum, stochastic methods, such as simulated annealing or evolutionary algorithms, are preferred over nonlinear gradient-based methods [122,141]. The different results of comparative studies with genetic algorithms (GA) and simulated annealing (SA) as performed in [85, 177] indicate that the most suitable algorithm depends on the problem under study. Therefore, different methods have been tested, namely genetic algorithms (GA) [56, 80], simulated annealing (SA) [177] and the particle swarm optimization (PSO) [97] for the algorithms as proposed in [36] and [198].

For each method, also a two-phase approach is used, consisting of using the global optimization to approach the global minimum followed by a local gradient-based optimization [76, 151].

The contributions of this chapter are threefold. Firstly, a model of the nano-motion stage driven by the walking piezo actuator is presented. The model includes the switching behavior between the driving pair of piezo legs, the contact dynamics and the stick-slip behavior between the stage and the motor. Secondly, a dedicated time-stepping solver is developed for the derived model, which is described by a set of differential-algebraic inclusions. Finally, optimal waveforms are derived by means of a model-based optimization and a data-based optimization on the setup.

This chapter is organized as follows. In Section 4.2, the nano-motion stage and the walking piezo actuator will be discussed in more detail. The derivation of the model will be presented in Section 4.3, in which the dedicated time-stepping solver will also be introduced. The model identification and validation using experimental data will be shown in Section 4.4. Section 4.5 contains both the model-based and data-based waveform optimizations. Finally, conclusions will be drawn in Section 4.6.

4.2 The experimental setup

The one degree-of-freedom (DOF) nano-motion stage, shown in Fig. 4.1, is equipped with a roller cage bearing to minimize the amount of friction in the stage movement. The position of the stage in x-direction is measured using a linear incremental encoder with a resolution of 0.64 nm. The displacement of the back of the motor housing is measured using a capacitive sensor with a resolution of 0.44 nm and a root-mean-square (rms) value of the noise of 1.6 nm.

Using the dedicated motor suspension of Chapter 2, the drive pads of the walking piezo motor are pressed against the drive strip of the stage such that the (x_m, y_m, z_m)-axes of the motor coincide with the (x, y, z)-axes of the stage (see Fig. 4.1). The motor suspension is designed such that the motor is properly aligned with respect to the drive surface of the stage to minimize slip and wear of the drive legs, as described in Chapter 2. The drive pads of the piezo motor are pressed against the drive strip by two preload springs with a total preload force of 55 N.

The walking piezo motor contains four bimorph piezoelectric legs, which work together in pairs of two to drive the nano-motion stage. A schematic working principle of the walking piezo motor is shown Fig. 4.2. The first pair, denoted by p_1, consists of legs A and D, the second pair, p_2, consists of legs B and C. Each leg

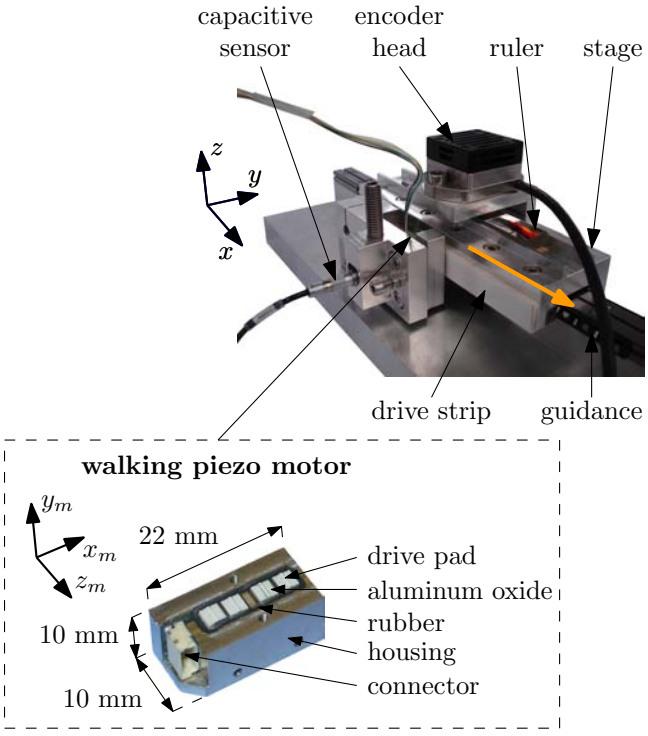

Figure 4.1: The nano-motion stage driven by the walking piezo actuator.

contains two electrically separated piezo stacks. Each stack is driven by an electric waveform $u_i(t)$ (V), $i \in \{1, 2, 3, 4\}$, which position the tips of the piezo legs in the (x_m, y_m)-plane (see Fig. 4.1). Applying equal voltages to the piezo stacks of one leg causes the leg to extend in y_m-direction. Different voltages introduce a bending of the leg in x_m-direction. The relative positions of the tips of the leg pairs p_1 and p_2 in x- and y-direction as function of the input waveforms can be written as [155]

$$\begin{aligned} x_{p_1} &= c_x(u_1(t) - u_2(t)), \\ y_{p_1} &= c_y(u_1(t) + u_2(t)), \\ x_{p_2} &= c_x(u_3(t) - u_4(t)), \\ y_{p_2} &= c_y(u_3(t) + u_4(t)), \end{aligned} \tag{4.1}$$

where c_x (m/V) and c_y (m/V) are the constant bending and extension coefficients, respectively.

By choosing the waveforms $u_i(t)$ (V), $i \in \{1, 2, 3, 4\}$ in (4.1), the tips of the piezo legs can perform a walking movement in the (x_m, y_m)-plane, which can be used

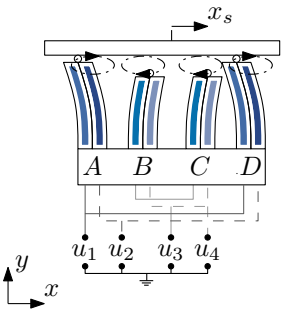

Figure 4.2: Schematic working principle of the walking piezo motor.

to drive the nano-motion stage. With sinusoidal waveforms or the asymmetric waveforms as proposed in Chapter 2, elliptical tip orbits and an alternating drive motion between the pair of legs are obtained. Due to the preload, at least one pair of legs is in contact with the drive strip of the stage at all times.

4.3 Modeling

This section contains the model of the walking piezo actuator and the nano-motion stage. First, the contact dynamics between the piezo legs and the stage are discussed, after which the models are presented. Since the model is described by a differential inclusion, we develop a dedicated time-stepping solver for the numerical simulations.

At low stage velocities the errors due to the shape of the input waveforms to the piezo motor are most apparent compared to other errors, e.g., due to measurement disturbances or system dynamics. Therefore, the model will be used for the waveform optimization at low stage velocities, corresponding to low drive frequencies of the piezo legs. The purpose of the model is to accurately describe the behavior of the system for frequencies $f < 50$ Hz, under the assumption that the stochastic disturbances and the high-frequent disturbances introduced by the hitting of the legs on the stage do not determine the performance.

Since the piezo legs are actuated in pairs by two input voltages as described in (4.1) and under the assumption that the legs in each pair are identical, each pair of legs can be lumped into as a single leg.

The leg positions are decomposed in an x- and y-displacement. Due to the decoupling of the x- and y-directions and the design of the motor suspension of

Chapter 2, the motor housing is assumed to move only in y-direction and the stage only in x-direction. Therefore, the model is split into two separate models for the x- and y-directions, respectively. This allows to compute the normal forces between the legs and the drive strip of the stage from the model in y-direction, which can then be used as an input for the model in x-direction to evaluate the friction forces between the legs and stage.

The voltage-actuated piezo legs are modeled as mass-spring-damper systems, analogous to existing piezo models [5, 31, 72, 158]. In Chapter 3, we showed that the dynamics of the piezo legs are located at frequencies $f > 215.0$ kHz, which is above the frequency range of interest for this model. The internal dynamics of the piezo legs can therefore be neglected. Also the contribution at lower frequencies of these high-frequent resonance modes of the piezo legs is assumed negligibly small. Since experiments show that the extensions of the different pairs of legs in (x, y)-direction are different and asymmetric, the static model of Chapter 3 and (4.1) is slightly extended by incorporating additional bending and extension coefficients as

$$\begin{aligned} x_{p_1}(t) &= c_{x_1} u_1(t) - c_{x_2} u_2(t), \\ y_{p_1}(t) &= c_{y_1} u_1(t) + c_{y_2} u_2(t), \\ x_{p_2}(t) &= c_{x_3} u_3(t) - c_{x_4} u_4(t), \\ y_{p_2}(t) &= c_{y_3} u_3(t) + c_{y_4} u_4(t), \end{aligned} \tag{4.2}$$

where x_{p_1} and x_{p_2} are respectively the x-positions of the first and second pair of legs and y_{p_1} and y_{p_2} are the corresponding positions of the leg models in y-direction.

4.3.1 Contact dynamics

Due to the preload springs at least one pair of legs is in contact with the stage at all times. However, this contact is not rigid. The contact deformation is assumed to exist in y-direction only and is modeled by a spring with stiffness $k_{c_{1,2}}$, which may nonlinearly depend on the contact deformation. The static contact deformation obtained by a FEM model of the aluminum oxide tip and drive strip with physical dimensions is shown in Fig. 4.3. A Hertzian contact model for a cilinder on a flat surface [16, 145] equals

$$y_c = \frac{2F_c\lambda}{L}\left(1 + \ln\left(\frac{L^3}{2\lambda F_c R}\right)\right), \tag{4.3}$$

where y_c (m) is the displacement, F_c (N) is the force, $L = 3$ mm is the contact length, $R = 0.2$ mm is the radius of the cylinder and $\lambda = \frac{1-\nu^2}{\pi E}$, with $\nu = 0.24$ the Poisson's ratio and $E = 377$ GPa the Young's modulus of the aluminum oxide

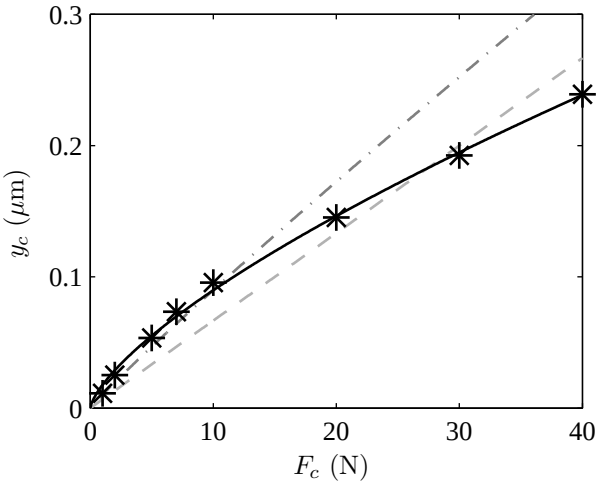

Figure 4.3: Contact deformation, FEM model ($*$), Hertz contact (dark grey, dash-dotted), linear fit (light grey, dashed) and nonlinear fit (black, solid).

material. The Hertzian contact model (4.3) resembles the contact deformation of the FEM model for contact forces $F_c < 10$ N, as shown in Fig. 4.3 by the dark grey dash-dotted line. Since the actual contact forces are larger, the Hertzian contact model is not applicable for this application. A fitted linear spring through the FEM data, shown by the light grey dashed line in Fig. 4.3, also does not give satisfactory model accuracy. Therefore, the following nonlinear restoring force model of the form

$$F_c = \left(\frac{y_c}{q_1}\right)^{1/q_2} \tag{4.4}$$

is fitted to the FEM data to obtain the parameter estimates $q_1 = 1.77 \cdot 10^{-8}$ and $q_2 = 0.705$. To gain insight in the force model (4.4), the equivalent nonlinear stiffness $k_c(y_c)$ for a contact force $F_c = k_c(y_c)y_c$ is calculated from (4.4) as

$$k_c(y_c) = \frac{1}{q_1}\left(\frac{y_c}{q_1}\right)^{\frac{1-q_2}{q_2}}.$$

The experimentally identified friction between the piezo legs and the stage in x-direction, obtained by measuring the angle at which the tilted stage with known mass starts sliding [16], showed a large variation, possibly due to the orientation of the contact surfaces between legs and motor at a microscopic level, environmental

conditions or contamination of the sliding surfaces [16,211]. Therefore, we confine ourselves to an elementary set-valued Coulomb friction model, which however does describe stick-slip phenomena:

$$\lambda \in \mu F_N \text{Sign}(v), \tag{4.5}$$

where μ is the friction coefficient, $F_{N_{1,2}}$ (N) the normal force in the two pairs of piezo legs, v (m/s) is the relative sliding velocity between the sliding surfaces and the set-valued Sign function is defined by

$$\text{Sign}(x) = \begin{cases} \{-1\}, & \text{for } x < 0, \\ [-1,1], & \text{for } x = 0, \\ \{1\}, & \text{for } x > 0. \end{cases} \tag{4.6}$$

Finally, experiments showed that the friction in the bearings is negligible.

4.3.2 Model x-direction

The model for the x-direction is shown in Fig. 4.4. Since the mass of the piezo legs is very small compared to the mass of the stage and since the dynamics of the piezo legs are located at frequencies $f > 215.0$ kHz, which is outside the frequency range of interest for the model, the legs are modeled as mass-less elements with stiffness $k_{x_{1,2}}$ (N/m) and damping $d_{x_{1,2}}$ (Ns/m). The subscripts $1,2$ denote the leg pair. The force exerted by the piezo legs in x-direction due to the applied voltages to the stacks of the legs equals

$$F_{x_1} = k_{x_1} x_{p_1} = k_{x_1}(c_{x_1} u_1(t) - c_{x_2} u_2(t)), \tag{4.7}$$
$$F_{x_2} = k_{x_2} x_{p_2} = k_{x_2}(c_{x_3} u_3(t) - c_{x_4} u_4(t)), \tag{4.8}$$

where we used (4.2). The position of the stage is denoted by x_s (m) and the positions of the legs by $x_{1,2}$ (m), i.e. for readability the subscript p has been omitted. The mass of the stage is represented by M_s (kg). The friction forces between the pairs and the stage are denoted by $\lambda_{1,2}$ (N). These friction forces depend on the normal forces of the leg pairs in y-direction and are described by a set-valued friction model, as described in (4.5).

The equations of motion for the model in x-direction are given by the following differential inclusions:

$$\begin{aligned} M_s \ddot{x}_s &= \lambda_1 + \lambda_2, \\ k_{x_1} x_1 + d_{x_1} \dot{x}_1 &= F_{x_1} - \lambda_1, \\ k_{x_2} x_2 + d_{x_2} \dot{x}_2 &= F_{x_2} - \lambda_2, \end{aligned} \tag{4.9}$$

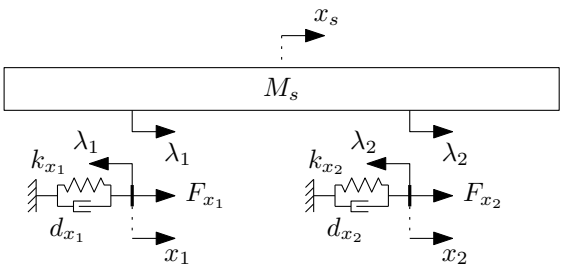

Figure 4.4: Model of the system in x-direction.

where the friction forces $\lambda_{1,2}$ in (4.9) satisfy the following set-valued force laws:

$$\begin{aligned} \lambda_1 &\in \mu F_{N_1} \text{Sign}(\dot{x}_1 - \dot{x}_s), \\ \lambda_2 &\in \mu F_{N_2} \text{Sign}(\dot{x}_2 - \dot{x}_s), \end{aligned} \tag{4.10}$$

in which the set-valued Sign function is defined by (4.6). The first equation of (4.9) describes the equation of motion for the stage and the latter two the equilibrium equations for the mass-less legs. The set-valued nature of the friction forces λ_1, λ_2 (4.10) between the leg and the stage allows for a non-zero friction force at zero relative velocity. The latter fact implies that real sticking (zero relative velocity) is modeled.

4.3.3 Model y-direction

A schematic representation of the system in y-direction is shown in Fig. 4.5(a). From top to bottom, the roller bearings are indicated by a spring with stiffness k_b (N/m) and damper with damping coefficient d_b (Ns/m). The mass of the stage is again denoted by M_s (kg). The contact dynamics are depicted as a nonlinear one-sided spring with stiffness $k_{c_{1,2}}$ (N/m). The piezo legs are shown as mass-spring-damper systems with mass M_l (kg), spring constants $k_{y_{1,2}}$ (N/m) and damping coefficients $d_{y_{1,2}}$ (Ns/m). The motor housing is represented by the mass M_h (kg) with position x_h (m). Finally, the stiffness of the preload springs is denoted by k_p (N/m).

For the model in y-direction the leg masses are again neglected. A frequency response function (FRF) measurement in y-direction from the input voltages to the piezo legs to the measured displacement of the housing shows a pure static gain for frequencies $f < 500$ Hz. Since we require the model to be accurate up to a frequency of 50 Hz, no masses are incorporated in the model. The compression of the preload springs due to the movement of the housing in y-direction is maximally

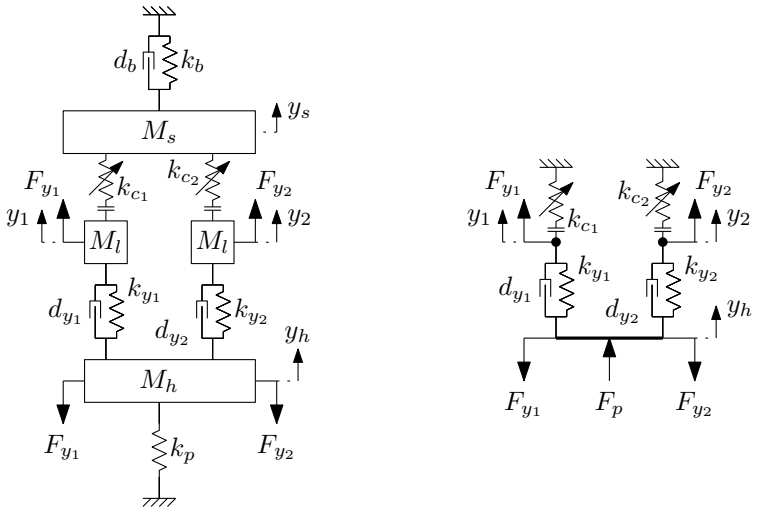

(a) Schematic representation. (b) Model y-direction.

Figure 4.5: Schematic representation and model of the system in y-direction.

0.03% for a maximal motor displacement of 1 μm and a compression of the preload springs of 3 mm. The resulting variation in preload force is assumed to be negligibly small. Therefore, the preload springs are modeled as a constant preload force F_p. This leads to the model in y-direction as shown in Fig. 4.5(b).

The exerted forces by the piezo legs in y-direction due to the applied voltages equal using (4.2)

$$F_{y_1} = k_{y_1} y_{p_1} = k_{y_1}(c_{y_1} u_1(t) + c_{y_2} u_2(t)), \tag{4.11}$$
$$F_{y_2} = k_{y_2} y_{p_2} = k_{y_2}(c_{y_3} u_3(t) + c_{y_4} u_4(t)). \tag{4.12}$$

The equations of motion of the model in y-direction are given by

$$\begin{aligned} k_{y_1}(y_h - y_1) + d_{y_1}(\dot{y}_h - \dot{y}_1) &= F_{c_1}(y_1) - F_{y_1}, \\ k_{y_2}(y_h - y_2) + d_{y_2}(\dot{y}_h - \dot{y}_2) &= F_{c_2}(y_2) - F_{y_2}, \end{aligned} \tag{4.13}$$

where the forces F_{y_1} and F_{y_2} exerted by the piezo legs due to the applied voltages follow from (4.11) and (4.12) and the subscript p in the leg positions has been omitted again to improve readability. The contact forces F_{c_1} and F_{c_2} are coupled through the motor housing and the constant given preload force F_p. Dependent on the contact properties between the leg pairs and the stage, the preload force is divided over the contact forces $F_{c_{1,2}}$ of one or two leg pairs dependent on their elongation.

The preload force F_p is equal to the sum of the two contact forces $F_{c_{1,2}}$

$$F_p = F_{c_1}(y_1) + F_{c_2}(y_2). \tag{4.14}$$

The forces in the one-sided contact springs as function of the elongation of both leg pairs $p_{1,2}$ in y-direction can be calculated using (4.4) as

$$F_{c_{1,2}}(y_{1,2}) = \begin{cases} 2\left(\dfrac{y_{1,2}}{q_1}\right)^{1/q_2}, & \text{if } y_{1,2} \geq 0, \\ 0, & \text{if } y_{1,2} < 0. \end{cases} \tag{4.15}$$

The factor two is added since one leg in the model represents a pair of legs, i.e., $F_{c_{1,2}} = 2F_c$. Since the damping in the piezo legs is very high, super- and subharmonic responses introduced by the one-sided contact [60] are not expected. The coupling between the models in x- and y-directions follow from the contact forces as $F_{N_{1,2}} = F_{c_{1,2}}$.

4.3.4 Numerical methods

In this section, the methods used for the numerical simulations of the models in x- and y-direction are described. To facilitate the coupling between the models in x- and y-direction, fixed time solvers with a time-step $\Delta t = 0.25$ ms are chosen for the simulations. Let the start of a time-step be denoted by t_A, then the end time equals $t_E = t_A + \Delta t$.

For the simulations in x-direction the normal forces $F_{N_{1,2}}$ are required. Solvers for differential-algebraic equations (DAEs) can be used to simulate the model in y-direction [75], of which we omit a description for the sake of brevity. The obtained normal forces $F_{N_{1,2}}$ from the simulation in y-direction are subsequently used in the simulation of the model in x-direction.

The model in x-direction as shown in Fig. 4.4 can be simulated using a time-stepping solver [108]. The model (4.9), (4.10) is in the form of a set of differential inclusions. A dedicated time-stepping algorithm is developed to simulate the specific problem of Fig. 4.4 including the mass-less elements. Using a backward Euler discretization scheme for the time derivatives $\dot{x}_s$ and $\dot{x}_{1,2}$, the equations of motion

(4.9) can be discretized as follows:

$$\begin{aligned}
\dot{x}_{s,E} &= \dot{x}_{s,A} + \frac{(\lambda_1 + \lambda_2)\Delta t}{M_s}, \\
x_{1,E} &= \frac{d_{x_1} x_{1,A} + (F_{x_1} - \lambda_1)\Delta t}{d_{x_1} + k_{x_1}\Delta t}, \\
x_{2,E} &= \frac{d_{x_2} x_{2,A} + (F_{x_2} - \lambda_2)\Delta t}{d_{x_2} + k_{x_2}\Delta t}, \\
x_{s,E} &= x_{s,A} + \dot{x}_{s,E}\Delta t,
\end{aligned} \tag{4.16}$$

where Δt is the fixed time-step and the subscripts $\cdot_A$ and $\cdot_E$ denote the values at the start and end times of the fixed step iteration, respectively. The discretized version of the friction law (4.10) is given by

$$\begin{aligned}
\lambda_1 &\in \mu F_{N_1} \mathrm{Sign}\left(\frac{x_{1,E} - x_{1,A}}{\Delta t} - \dot{x}_{s,E}\right), \\
\lambda_2 &\in \mu F_{N_2} \mathrm{Sign}\left(\frac{x_{2,E} - x_{2,A}}{\Delta t} - \dot{x}_{s,E}\right).
\end{aligned} \tag{4.17}$$

The iteration scheme for the dedicated time-stepping solver at each time-step is as follows:

1. Gather the known coordinates $x_{s,A}$, $\dot{x}_{s,A}$, $x_{1,A}$ and $x_{2,A}$, and actuator forces F_{x_1} and F_{x_2} at the beginning of each time instant, i.e., at time t_A.
2. Simulate the model in y-direction to retrieve the normal forces $F_{N_{1,2}}$ at the corresponding time instant.
3. Take the friction forces $\lambda_{1,2}$ from the previous time-step as an initial estimate for the current time-step.
4. Using a root finding algorithm, e.g., a fixed point iteration, compute the friction forces in the following iterative loop where the superscript L denotes the iteration number.
   (a) Evaluate $x_{1,E}$, $x_{2,E}$, $x_{s,E}$ and $\dot{x}_{s,E}$ from (4.16) for given $\lambda_{1,2}$.
   (b) Update the friction forces $\lambda_{1,2}^{L+1}$ as

$$\begin{aligned}
\lambda_1^{L+1} &= \mathrm{prox}_{C_1}\left(\lambda_1^L + r\left(\frac{x_{1,E} - x_{1,A}}{\Delta t} - \dot{x}_{s,E}\right)\right), \\
\lambda_2^{L+1} &= \mathrm{prox}_{C_2}\left(\lambda_2^L + r\left(\frac{x_{2,E} - x_{2,A}}{\Delta t} - \dot{x}_{s,E}\right)\right),
\end{aligned} \tag{4.18}$$

   where $r > 0$, $C_i = [-\mu F_{N_i},\ \mu F_{N_i}]$, $i \in \{1, 2\}$, is the set of admissible friction forces and

$$\mathrm{prox}_{C_i}(x) = \begin{cases} -\mu F_{N_i}, & \text{for } x \le -\mu F_{N_i}, \\ x, & \text{for } -\mu F_{N_i} < x < \mu F_{N_i}, \\ \mu F_{N_i}, & \text{for } x \ge \mu F_{N_i}, \end{cases} \tag{4.19}$$

in which $i \in \{1, 2\}$, is the proximal point to the convex set C_i. Note that the proximal point formulation of the set-valued friction law in (4.18) is equivalent to that in (4.17) and is introduced to be able to compute λ_1, λ_2 by solving (4.18) using a root-finding algorithm.

(c) If $\lambda_{1,2}^{L+1} - \lambda_{1,2}^{L} < \epsilon$ for a given desired accuracy ϵ, the simulation step is complete, otherwise continue to the next iteration at step 4a with the updated friction forces $\lambda_{1,2} = \lambda_{1,2}^{L+1}$.

In principle, the choice for $r > 0$ is free. The step size of the fixed point solver is determined by r. For small r the fixed point iteration is likely to converge but with low convergence speed, whereas higher r speeds up the convergence. If r is chosen too large, the scheme can become unstable (see also [3]). The choice for ϵ is a trade-off between convergence speed of the fixed point iteration and accuracy of the determined friction forces.

4.4 Experimental validation

This section deals with the identification of the model parameters and subsequent validation of the identified models using experimental data.

4.4.1 Parameter identification

For the parameter identification it is assumed that the material properties for both legs are identical. The constant parameters $P_f \in \{M_s, k_{x_{1,2}}, k_{y_{1,2}}, F_p, q_1, q_2\}$ are identified from separate experiments. Weighing the stage mass yields $M_s = 0.428$ kg. The parameters q_1 and q_2 are fitted to FEM data of the contact dynamics, as described in Section 4.3.1. The stiffness of the pairs of legs in y-direction is determined as $k_{y_{1,2}} = EA/L = 3.2 \cdot 10^8$ N/m, where the cross area $A = 9$ mm^2, the length $L = 4$ mm and the modulus of elasticity $E = 70$ GPa. The stiffness $k_{x_{1,2}}$ denotes a combined stiffness of the leg and motor suspension and is determined using the known mass M_s combined with the first resonance from the measured FRF in x-direction at 543 Hz (see Appendix A), which yields $k_{x_{1,2}} = 5.0 \cdot 10^6$ N/m. The preload force $F_p = 55$ N.

The remaining damping parameters, the bending and extension coefficients of the legs and the friction coefficient are determined using optimization techniques. For this purpose, experimental data obtained with the nano-motion stage at a fixed driving frequency of 10 Hz for differently shaped waveforms is used. The used waveforms are 1) sinusoidal, 2) asymmetric (see Chapter 2), 3) rhombic waveforms

(waveforms that lead to a tip trajectory with four linear sides of equal length) with 90 deg phase shift and 4,5) two manually obtained alternatives of the asymmetric waveforms. The parameters $P \in \{d_{x_{1,2}}, d_{y_{1,2}}, c_{x_1}, c_{x_2}, c_{x_3}, c_{x_4}, c_{y_1}, c_{y_2}, c_{y_3}, c_{y_4}, \mu\}$ are obtained by solving the following minimization problem

$$\min_P f(P) = \sum_{i=1}^{5} \left\{ \mathrm{rms}\left(\bar{r}_w - \hat{r}_w(P)\right) + \left|\left(\bar{r}_w(t_0) - \hat{r}_w(P, t_0)\right)\right| \right\}, \tag{4.20}$$

where $\mathrm{rms}(\cdot)$ denotes the root-mean-square value, $|\cdot|$ the absolute value operator and $w \in \{1, 2, 3, 4, 5\}$ the waveform number. Furthermore, $\bar{r}_w = \{\bar{x}_w, \bar{y}_w\}$ denotes the average experimental data over 10 periods for each individual waveform number w and $\hat{r}_w(P) = \{\hat{x}_w(P), \hat{y}_w(P)\}$ reflects the model output. The averaging is performed to minimize the effect of stochastic disturbances. The second term in the objective function weights the start points in order to obtain an equal starting point for the steps of the model compared to the experimental data. Since the average values of the model and the experimental data are removed in every iteration due to the relative measurements, the second term also weights the end point of each step due to the periodicity.

The minimization in (4.20) is performed using GA, SA and PSO algorithms. The PSO algorithm [36, 198] appears to be best suitable for the identification problem at hand, i.e., with the PSO algorithm results the lowest objective function value $f(P)$ is obtained the most times for 200 runs of the optimization problem.

Since the results of the model in y-direction are required for the model in x-direction, first the identification is performed in y-direction after which the x-direction is identified. The identified model parameter values are given in Table 4.1. When comparing the bending and extension coefficients of the different legs, it can be seen that the coefficients for the second pair are smaller than for the first pair, indicating that this pair makes smaller steps. Different values are also obtained for the coefficients within one pair, indicating an asymmetric step shape.

4.4.2 Model validation

The experimental results contain stochastic disturbances as well as disturbances caused by the roughness of the drive strip, contamination, etc. Therefore, the model response, obtained with the developed time-stepping solver of Section 4.3.4, is compared to the experimental data of 200 periods for each waveform. The model errors are defined as $e_x = \bar{x} - \hat{x}$ and $e_y = \bar{y} - \hat{y}$, where $\bar{\cdot}$ denotes the average measurement over the different periods and $\hat{\cdot}$ the simulated model output. The data is offset to an average value equal to zero since only relative measurements are performed.

Table 4.1: The obtained model parameters using PSO optimization of (4.20).

Parameter	Unit	Value
$b_{y_{1,2}}$	Ns/m	$1.86{\cdot}10^{6}$
c_{y_1}	m/V	$1.49{\cdot}10^{-8}$
c_{y_2}	m/V	$1.87{\cdot}10^{-8}$
c_{y_3}	m/V	$1.33{\cdot}10^{-8}$
c_{y_4}	m/V	$1.38{\cdot}10^{-8}$
$b_{x_{1,2}}$	Ns/m	$2.98{\cdot}10^{4}$
c_{x_1}	m/V	$5.29{\cdot}10^{-8}$
c_{x_2}	m/V	$7.02{\cdot}10^{-8}$
c_{x_3}	m/V	$2.63{\cdot}10^{-8}$
c_{x_4}	m/V	$3.33{\cdot}10^{-8}$
μ	-	0.587

For the validation of the model four additional waveforms, other than those used for the identification, are used. The waveforms numbered 6, 7 and 8 are different, manually obtained variations of the asymmetric waveforms of Chapter 2. Waveform 9 is a rhombic waveform with 45 deg phase shift. Furthermore, the performance of waveforms 6 and 8 is validated for different drive frequencies $f \in \{5, 10, 20\}$ Hz, whereas the identification is performed only with a drive frequency $f = 10$ Hz.

The time responses of the model and experiments are compared for the asymmetric waveform $w = 7$ and rhombic waveform $w = 9$, shown in Fig. 4.11. The model and experimental results for the manually obtained alternative asymmetric waveform $w = 7$ are contained in Fig. 4.7. It can be seen that the model response overlaps the experimental data of the 200 periods in both x- and y-directions. The mismatch between the measured position and the model position around $t = 0.09$ s is located at the take-over point, at which the model accuracy is somewhat limited due to the chosen friction and contact models. In y-direction a large deviation in measured position data is visible, which is caused by the limited accuracy of the measurements with the capacitive sensor, which is very sensitive to orientation errors and tilt of the motor housing. The cumulative power spectral densities (CPSDs) in the bottom figures show the accuracy of the model by the low CPSDs of the errors e_x and e_y. For frequencies $f \to \infty$, the CPSDs converge to the squared rms values of the signals.

The model also accurately describes the system response for non-harmonic waveforms such as rhombic waveforms ($w = 9$), as can be seen in Fig. 4.8. The CPSDs in the bottom figures of Fig. 4.8 show no increase in the errors at frequencies

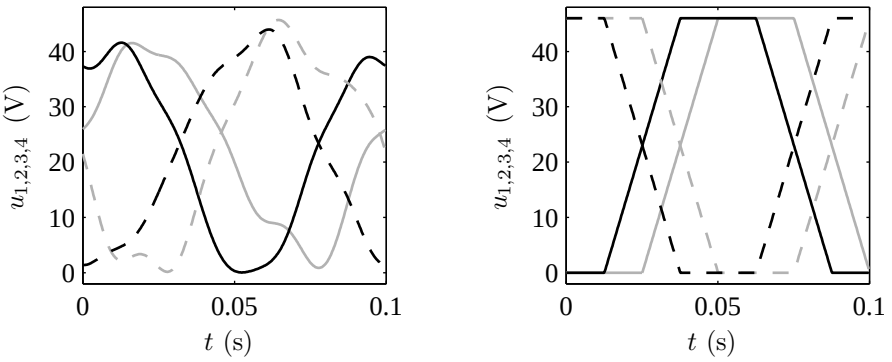

(a) Validation waveform $w = 7$. (b) Rhombic waveform $w = 9$.

Figure 4.6: Input voltages u_i, $i \in \{1, 2, 3, 4\}$ of the verification waveforms $w = 7$ and $w = 9$, u_1 (black, solid), u_2 (grey, solid), u_3 (black, dashed), u_4 (grey, dashed).

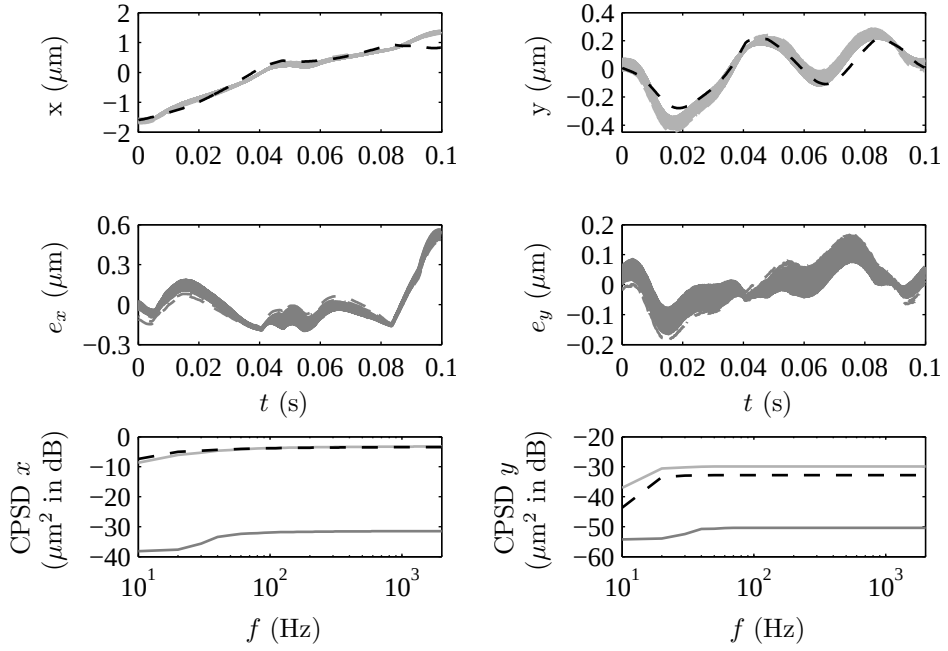

(a) x-direction (b) y-direction

Figure 4.7: Measured (solid, light-grey) and model (dashed, black) positions, errors (solid, dark-grey) and CPSDs of the position and error signals in x- and y-direction for validation waveform $w = 7$.

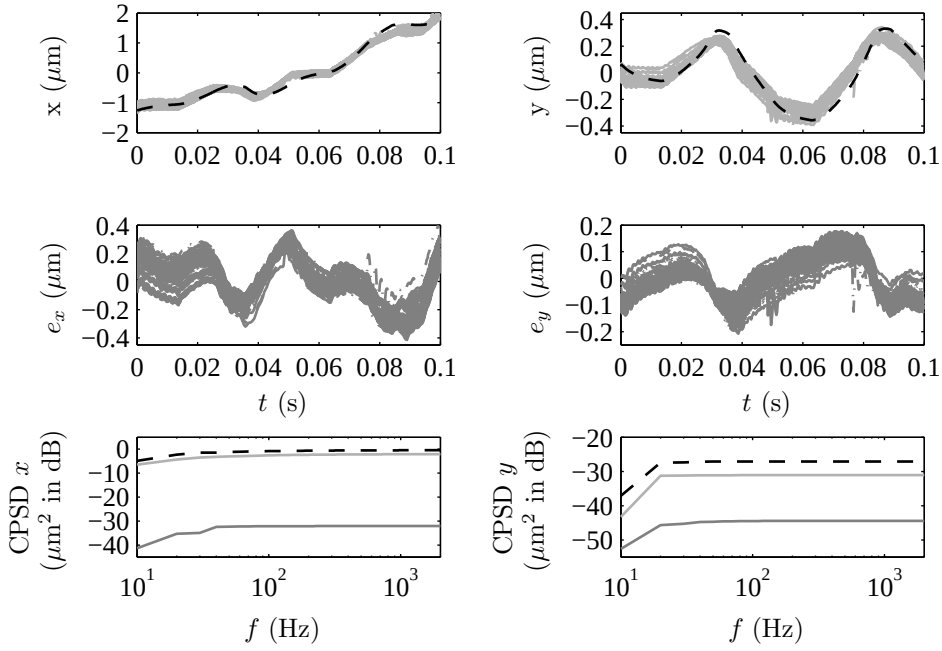

(a) x-direction (b) y-direction

Figure 4.8: Measured (solid, light-grey) and model (dashed, black) positions, errors (solid, dark-grey) and CPSDs of the position and error signals in x- and y-direction for validation waveform $w = 9$.

$f > 50$ Hz, so above the drive frequency of the experiments with which the model is identified. This confirms the assumption that the system performance is not determined by high-frequent disturbances.

The rms values of the errors in x- and y-direction for all identification and validation waveforms are shown in Fig. 4.9. The variation in the rms error over all 200 periods is also shown. In y-direction a larger variation in the model accuracy is present, which is caused by the larger noise bound of the capacitive sensor with an rms value of 1.6 nm. The average rms errors and sizes of the leg trajectories for the different waveforms are contained in Table 4.2 for a driving frequency of 10 Hz. The model describes the experimental data for all waveforms with an accuracy of 93% in x-direction and with an accuracy of 80% in y-direction. Note that the reduced model accuracy in y-direction is present for all identification and validation waveforms. Fig. 4.9 also shows that the model describes the experimental data obtained at drive frequencies $f \in \{5, 20\}$ Hz with the same accuracy. The model accuracy is approximately equal for the identification and validation waveforms.

Table 4.2: Sizes of the leg trajectories and model errors of the different waveforms at 10 Hz, waveforms 1-5 are used for the model identification and waveforms 6-9 for the model validation.

w	waveform type	stroke x (μm)	rms($\bar{e}_x$) (μm)	stroke y (μm)	rms($\bar{e}_y$) (μm)
1	sinusoidal	5.25	0.26	0.60	0.06
2	asymmetric	3.92	0.19	0.40	0.04
3	rhombic 90 deg.	5.23	0.30	0.56	0.11
4	identification	1.52	0.11	0.81	0.06
5	identification	3.29	0.22	0.58	0.04
6	verification	3.04	0.22	0.71	0.05
7	verification	2.95	0.16	0.61	0.05
8	verification	1.84	0.13	0.65	0.06
9	rhombic 45 deg.	3.05	0.16	0.56	0.08

This is because the used validation waveforms show a large correlation with some of the identification waveforms. The verification waveforms $w = \{6, 7, 8\}$ are similar to the identification waveforms $w = \{4, 5\}$ in the sense that all are described by fourth order Fourier series. Furthermore, the validation waveform $w = 9$ and the identification waveform $w = 3$ are both rhombic waveforms, but with a different phase.

With all waveforms (sinusoidal, asymmetric, rhombic and manual waveforms used for the model identification and validation) stick-slip effects between the piezo legs and the stage are observed in the simulation results. Since slip between the legs and the drive surface of the stage affects the stage velocity and determines the quality of the waveforms to achieve the desired performance, it is important to include stick-slip in the model used for the waveform optimization.

4.5 Waveform optimization

The model derived in Section 4.4 can be used to optimize the waveforms for driving the walking piezo motor with different objective functions such as minimal energy, minimal driving frequency, maximum step size, etc. In this research we focus on optimizing the shape of the tip trajectories through the input waveforms to obtain a constant stage velocity. First, a model-based waveform optimization will

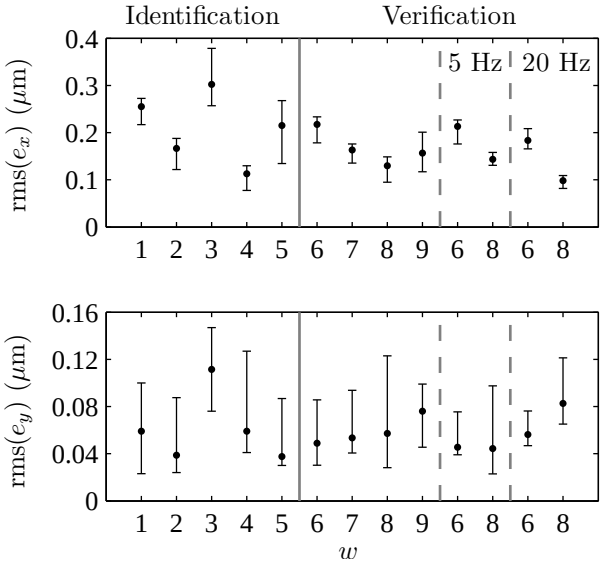

Figure 4.9: Model errors e_x (μm) and e_y (μm) for various identification and verification waveforms with waveform driving frequencies $f_\alpha \in \{5, 10, 20\}$ Hz.

be discussed, followed by a data-based experimental waveform optimization. The (dis)advantages of both methods are shown by means of experiments. The chosen reference velocity for the waveform optimization equals $\dot{x}_r = 50$ μm/s, which is chosen such that the required nominal drive frequency to achieve the reference velocity with asymmetric waveforms of Chapter 2 is in the frequency range where the model is accurate.

4.5.1 Model-based waveform optimization

The shape of the waveforms u_i (V), $i \in \{1, 2, 3, 4\}$ is chosen to be specified by eight equidistant points on one period $\alpha \in [0, 2\pi]$ rad. The optimization parameters ξ contain these eight points of each waveform that has to be optimized. For the optimization, different choices can be made for the specification of the four waveforms. If a single waveform shape is chosen for all waveforms u_i, $i \in \{1, 2, 3, 4\}$, this requires only eight $\xi = 8$ parameters. This is the case with the sinusoidal and asymmetric waveforms of Chapter 2, where the different waveforms have a phase difference of $\Delta\phi = 90$ deg. Specifying each individual waveform u_i, $i \in \{1, 2, 3, 4\}$ by eight separate points would require $\xi = 32$ waveform parameters to be optimized. However, this also adds a lot of freedom to the optimization to improve the

drive velocity while incorporating the specific leg characteristics such as different lengths of the stacks, asymmetry, etc. Also intermediate optimizations are possible, e.g., allowing different waveform shapes for different leg pairs, for the different stacks in one pair, or by allowing a variable phase between different waveforms. In general, the more freedom is allowed, the better the results can become, but at the cost of additional parameters and probably CPU effort in the optimization.

From the optimization parameters ξ_i, $i \in \{1, 2, 3, 4\}$, of each waveform, the input voltages to the stacks are obtained by fitting a Fourier series model of order $n = 4$ in a least-squares sense through the optimized points on one period described by ξ_i as

$$\{a_{k,i}^*, b_{k,i}^*\} = \arg \min_{a_{k,i}, b_{k,i}} (\xi_i - \hat{u}(\alpha, a_{k,i}, b_{k,i})), \tag{4.21}$$

where $a_{k,i}$ and $b_{k,i}$ are the Fourier coefficients and the Fourier series model

$$\hat{u}(\alpha, a_{k,i}, b_{k,i}) = \sum_{k=0}^{n} a_{k,i} \cos(k\alpha) + b_{k,i} \sin(k\alpha). \tag{4.22}$$

The waveforms u_i, $i \in \{1, 2, 3, 4\}$ for each iteration of the optimization now follow from (4.22) with the fitted Fourier coefficients $a_{k,i}^*$ and $b_{k,i}^*$, i.e., $u_i(\alpha) = \hat{u}(\alpha, a_{k,i}^*, b_{k,i}^*)$. The Fourier series model is chosen because the waveforms should describe period signals. The input signals $u_{1,2}$ determine the trajectory of the tips for the first pair of legs p_1 in the (x, y)-plane and analogously $u_{3,4}$ for the second pair of legs p_2. By changing the shapes of the waveforms, the leg orbits change and thus the drive properties of the motor.

One might argue that direct optimization of the Fourier coefficients, i.e., $\xi_i = \{a_{k,i}, b_{k,i}\}$ would give the same results. Although direct optimization of the Fourier coefficients is possible and both sets of optimization parameters ξ_i could describe the same waveforms, different optimization problems are solved. The two sets of optimization points ξ_1 and ξ_2 of waveforms u_1 and u_2 directly describe eight points on the leg orbits of pair p_1 as described by (4.1). A change of one of the eight points on the waveforms directly influences the optimized leg orbit. This direct relation of the optimization parameters to the leg orbits is not present when optimizing the Fourier coefficients $a_{k,i}, b_{k,i}$ since a change of one of these parameters changes a harmonic component in the waveform throughout the complete period of the waveform and thus on the complete leg orbit.

The goal of the optimization is twofold, namely to design waveforms that, firstly, are able to accurately drive the stage at a given reference velocity and, secondly, minimize slip between the legs and stage to prevent wear of the drive surfaces and to optimize the efficiency of the actuator. Intuitively one would choose the velocity

error between the reference velocity and the obtained stage velocity of the model, i.e., $e_v = \dot{x}_r - \dot{x}_s$, to be minimized in the waveform optimization. This would however only address the first criterion and may lead to waveforms introducing extensive amounts of slip. Therefore, we opt for an objective function incorporating the leg velocities. The difference between the velocity of the legs and the reference velocity is minimized when the legs are in proximity of the stage. By doing so, slip is less likely to occur since the leg velocity already matches the desired velocity (of the stage) when the leg approaches the stage, thereby avoiding large velocity differences between the leg and stage upon contact. The desired clearance between the legs and the drive strip at which the relative velocity between legs and stage should be zero is denoted by δy, where $\delta y = 0$ denotes the model-based contact point and $\delta y < 0$ denotes an open distance between the legs and the drive strip. Note that by minimizing the occurrence of slip by optimizing the legs velocities when they are close to or in contact with the stage, we are effectively optimizing for the stage velocity as well.

Let the amplitudes of the points on the waveforms be contained in ξ. The optimization problem can now be formulated as

$$\min_{\xi} g(\xi) = \text{rms}(\dot{x}_r - \dot{x}_1^*(\xi)) + \text{rms}(\dot{x}_r - \dot{x}_2^*(\xi)), \tag{4.23}$$

where the weighted leg velocities based on the desired clearance δy equal

$$\dot{x}_{1,2}^*(\xi) = \begin{cases} \dot{x}_{1,2}(\xi), & \text{if } y_{1,2} \geq \delta y, \\ 0, & \text{if } y_{1,2} < \delta y. \end{cases} \tag{4.24}$$

If the leg positions $y_{1,2} < 0$, the specific legs are not in contact with the stage. Also, if $y_{1,2} < \delta_y$, the legs are outside the region in which the leg velocity is taken into account in the optimization. Note that slip is only implicitly minimized by (4.23). The main objective is to obtain a smooth reference velocity and no explicit slip minimization is taken into account. Slip could be minimized by extending the objective function (4.23), e.g., by the error between the individual leg velocities in the proximity of the stage. This is a subject of future research.

The objective function is calculated at each optimization step in the following steps:

1. Generate the waveforms to the piezo legs by fitting an nth order Fourier series through the optimization points ξ on the waveform period according to (4.21) and (4.22).
2. Perform a simulation with the new waveforms and the models in x- and y-direction as derived in Section 4.3.
3. Derive the objective function value using (4.23).

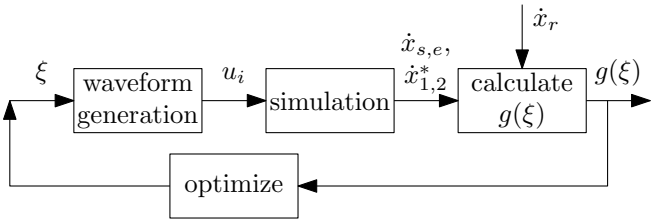

Figure 4.10: Calculation objective function.

This procedure is schematically shown in Fig. 4.10. For the waveform optimization of (4.23) also GA, SA and PSO algorithms are tested. For this problem, the lowest objective function value $g(\xi)$ is obtained the most times for 200 optimization runs using simulated annealing (SA) [177].

In the next section, the results for a model-based optimization with 8 individual parameters per waveform, i.e., ξ contains 32 parameters, and a clearance of $\delta y = 0.05$ μm are shown. For this optimization, the driving frequency is chosen as $f_\alpha = 14$ Hz. The driving frequency f_α (Hz) is chosen based on the required driving frequency to achieve a velocity of 50 μm/s with the asymmetric waveforms of Chapter 2.

4.5.2 Validation of new waveforms

In this section the results of the experiments with the waveforms obtained from the model-based optimization are presented. The optimal waveforms are shown in Fig. 4.11(a). It can be seen that the shapes of all waveforms are different. This indicates that the waveform optimization accounts for the differences in the piezo legs (see also Table 4.1).

Since the objective of the waveform optimization is to obtain a constant stage velocity of 50 μm/s, the performance will be evaluated using the resulting stage velocity. The velocity errors of the simulations and experiments, defined as $e_{v,s} = \dot{x}_r - \dot{x}_s$ and $e_{v,e} = \dot{x}_r - \dot{x}_{s,e}$, respectively, are shown for the model-based optimal waveforms in Fig. 4.12. The velocity $\dot{x}_{s,e}$ is obtained from the experiment by numerical differentiation of the encoder output and a subsequent anti-causal filtering of the differentiated signal by a fifth order low-pass filter with a cut-off frequency $f_c = 500$ Hz.

Fig. 4.12 shows that the velocity error of the stage obtained with the model-based waveforms is much smaller in simulation than during the experiment. The

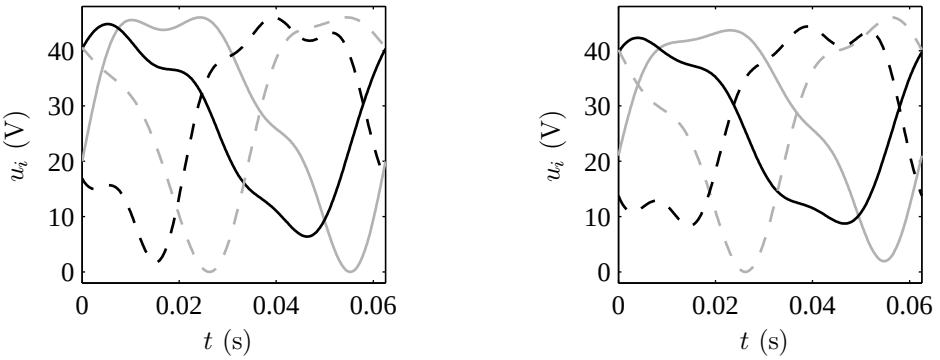

(a) Model-based waveforms.

(b) Data-based waveforms.

Figure 4.11: Resulting waveforms of the model-based and data-based optimizations, u_1 (black, solid), u_2 (grey, solid), u_3 (black, dashed), u_4 (grey, dashed).

rms values of the velocity errors equal $\text{rms}(e_{v,s}) = 10.24$ μm/s and $\text{rms}(e_{v,e}) = 25.14$ μm/s (note that the reference velocity is 50 μm/s). The cumulative PSDs of the velocity errors show the difference between simulation and experiment, which is caused by the model error. The model mismatch is influenced by the contact dynamics and friction model, both of which could only be identified with limited accuracy due to the sensitivity of the capacitive sensor in the setup. The influences of even small model errors become more apparent in the velocity signals.

4.5.3 Data-based waveform optimization

To eliminate the influence of the model mismatch, also a data-based experimental waveform optimization is performed. For this purpose, the simulation in the calculation of the objective function (see also Fig. 4.10) is replaced by an experiment with the nano-motion stage and walking piezo leg actuator. For the data-based waveform optimization the leg velocities cannot be measured. Therefore, the error between the reference velocity $\dot{x}_r$ and the measured stage velocity $\dot{x}_{s,e}$ is minimized, resulting in the following objective function:

$$\min_{\xi} g(\xi) = \text{rms}(\dot{x}_r - \dot{x}_{s,e}(\xi)). \tag{4.25}$$

The sampling frequency for the experiments equals 4 kHz.

The obtained waveforms of the data-based optimization are shown in Fig. 4.11(b). Comparison of the waveforms of Fig. 4.11(a) and Fig. 4.11(b) shows that globally

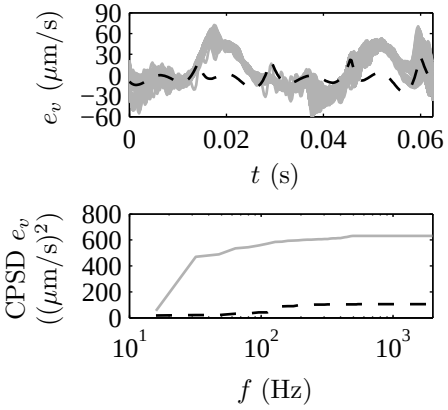

Figure 4.12: Velocity errors obtained with the model (black, dashed) and experiments (solid, grey) and cumulative PSDs of the errors for the model-based optimization.

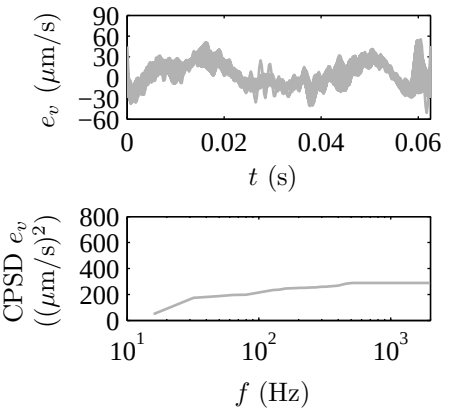

Figure 4.13: Velocity errors and cumulative PSD of the error for the data-based optimized waveforms.

the shapes look similar. However, on a more detailed level there are some differences. The velocity errors of 200 periods, shown in Fig. 4.13, are smaller than the velocity errors of the model-based waveforms. The rms value of the velocity error equals $\mathrm{rms}(e_{v,e}) = 17.01$ μm/s.

4.5.4 Discussion

Since the experiments show that the error of the model-based optimization is larger than the data-based optimization, the latter is recommended. Alternatively, the derivation of a model that even more accurately describes the velocity of the stage and piezo legs could further improve the model-based waveform optimization results. This is a subject for future research.

In Fig. 4.14 the velocity errors of experiments at different driving frequencies $f_\alpha \in \{10, 12, 14, 16, 18, 20\}$ Hz are shown for the asymmetric waveforms of Chapter 2, the model-based optimized waveforms and the data-based waveforms. It can be seen that both optimized waveforms outperform the asymmetric waveforms for all driving frequencies, i.e., at all velocities. The best performance is obtained with the data-based optimized waveforms. A least squares fit through the experimental data is shown in Fig. 4.14 by the solid lines. For a velocity of 50 μm/s, the model-based waveforms outperform the asymmetric waveforms by 24%. The data-based

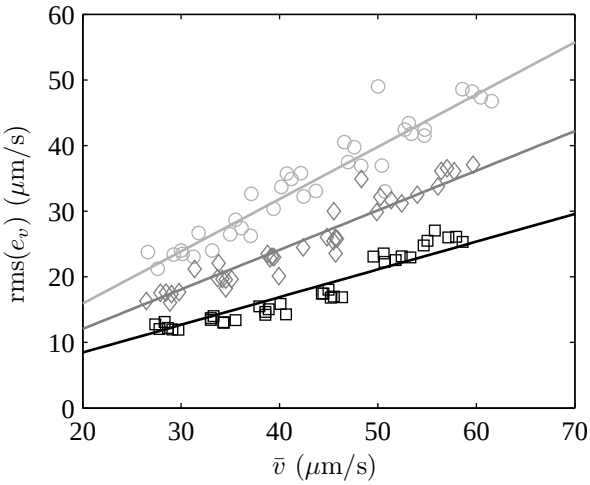

Figure 4.14: Velocity errors for experiments with asymmetric waveforms (light grey), model-based optimized waveforms (dark grey) and data-based optimized waveforms (black) for driving frequencies $f_\alpha \in \{10, 12, 14, 16, 18, 20\}$ Hz.

optimized waveforms reduce the velocity error by 47% compared to the asymmetric waveforms and by 30% compared to the model-based waveforms.

The results shown in this chapter are all obtained in open-loop experiments. Using the walking piezo motor with the optimal waveforms in a closed-loop setting, as described in Chapter 2, is expected to further improve the performance of the nano-motion stage.

By describing each waveform by independent parameters, more freedom is obtained in the optimization to better account for the characteristics of the specific motor, thus improving the results. However, these characteristics might change between motors. So, the optimal waveforms obtained with more independent optimization parameters, might not be optimal for a batch of motors.

The optimized waveforms are described by eight parameters, representing points on one period of the waveforms. The Fourier series model (4.21) fitted through the eight points can exceed the allowable voltage range. If the range is exceeded, linear scaling is applied such that the fitted waveforms do not exceed the allowable range of $u_i \in [0, 46]$ V, $i \in \{1, 2, 3, 4\}$.

4.6 Conclusions

In this chapter, a model of a nano-motion stage driven by a walking piezo actuator is presented. The model includes the alternating drive principle of the drive legs of the piezo motor, the contact dynamics and the stick-slip behavior between the legs and the stage. Since the driving principle of the motor depends on friction, it is important that the exact friction force is known at each time instant. Therefore, the friction is modeled using a set-valued force law to accommodate for non-zero friction forces at zero relative velocity. For the resulting model, formulated in terms of a differential inclusion, we developed a dedicated time-stepping solver. Furthermore, the model is used in a waveform optimization, which derives optimal leg orbits to improve the driving properties of the motor. Finally, a data-based waveform optimization was applied to further improve the driving properties of the motor.

The dedicated time-stepping solver is able to simulate the model in terms of a set of differential inclusions. The model is identified using experimental data for different waveforms. The identification and validation experiments show that the model describes the experimental data in the driving x-direction with an accuracy of 93% and in the perpendicular y-direction with an accuracy of 80% for all tested waveforms.

Waveforms are optimized for a constant stage velocity using a model-based optimization. The limited accuracy of the obtained velocity by the model limits the results of the experiments with the model-based waveforms. Therefore, a data-based optimization is performed to further improve the waveforms and obtain a better performance of the nano-motion stage. Compared to the asymmetric waveforms of Chapter 2, the model-based waveforms result in a reduction of the velocity error of 24%. The data-based optimized waveforms reduce the velocity error by 47% compared to the asymmetric waveforms and by 30% compared to the model-based waveforms.

Future work will include the derivation of a model that more accurately predicts the leg and stage velocities, which could further improve the results of the model-based waveform optimization.

Chapter 5

Delay-varying repetitive control

Abstract - The performance of systems that exhibit repetitive disturbances can be significantly improved using repetitive control. If the repetitive disturbance is periodic with respect to time, perfect asymptotic disturbance rejection can be achieved by well known methods. However, many systems have a repetitive nature with respect to a variable other than time. For this type of systems, we propose a delay-varying repetitive control (DVRC) method, which employs a time-varying delay in the repetitive controller that is continuously adjusted based on the repetitive variable. An $\mathcal{H}_\infty$ norm based criterion is derived that guarantees stability of the time-varying delay system for a given range of variations of the repetitive delay. To show the strengths of this new repetitive control scheme it is applied to a nano-motion stage driven by a walking piezo actuator. The repetitive nature of the walking movement introduces repetitive disturbances in the system, which are periodic with respect to the angular orientation of the legs, but not with respect to time. Experiments show that DVRC can successfully suppress these repetitive disturbances. The performance of the nano-motion system is improved significantly by DVRC compared to standard repetitive control.

This chapter is based on: R.J.E. Merry, D.J. Kessels, M.J.G. van de Molengraft, W.P.M.H. Heemels and M. Steinbuch. Delay-varying repetitive control applied to a walking piezo actuator. Submitted, 2009.

5.1 Introduction

The performance of systems that perform repetitive tasks or that are subject to repetitive disturbances can be improved significantly using repetitive control (RC). In most available RC methods it is assumed that the repetitive variable is time, meaning that the disturbances are periodic with respect to time. This leads to a fixed value for the repetitive delay in the memory loop of RC, for which many RC schemes with guaranteed properties and asymptotic disturbance rejection are available in the literature [34, 77, 81].

However, many systems have a repetitive nature with respect to another variable than time. One such example, which is studied in detail in this chapter, is a nano-motion stage driven by a walking piezo actuator. The walking piezo actuator employs four bimorph piezo legs to obtain a periodic walking movement. This introduces repetitive disturbances in the system, which become the performance limiting factor (PLF). These disturbances are fully repetitive with respect to the angular orientation of the piezo legs, but are not periodic in time. Existing RC schemes for disturbances periodic in time, i.e., with a constant repetitive delay, are not applicable in these circumstances in a straightforward manner.

Several solutions for the application of RC to systems that are subject to repetitive disturbances with a (slowly) varying period with respect to time have already been proposed in literature. Adaptive RC methods continuously estimate the time-varying period of the repetitive disturbance and adjust the sampling frequency accordingly [30] or use a multi-rate implementation [27]. Adaptive RC suffers from the drawback that it is implemented at a variable sampling rate, which complicates the use in real-time in combination with a feedback controller at a fixed sampling frequency. In contrast with [27, 30], the adaptive RC scheme proposed in [53] does not change the sampling frequency, but adapts the delay in the memory loop based on a physical model of the time-varying character of the repetitive delay. Since the variation is assumed to be slowly in time, the delay is adjusted at a fixed rate that is much less than the controller sampling rate. Furthermore, no stability guarantees of the feedback system including the switching repetitive controller are given. The assumption on the slow variation of the period-time is not valid in various applications, including the walking piezo actuator considered in this chapter.

High-order RC uses multiple memory loops to provide robustness against small variations in the period-time of repetitive disturbances [32, 185]. High-order RC makes a trade-off between robustness for changes in the period-time and the reduction of the error spectrum in-between the harmonic frequencies of the repetitive disturbances [187]. A systematic design approach for high-order RC yielding op-

timal performance trade-offs is developed in [157]. The performance indications are incorporated in the repetitive controller design using linear matrix inequalities (LMIs). Although this approach is very interesting, it is not considered in this chapter due to the resulting large size of the LMIs with matrices in the order of 250×250.

Another line of research considers systems that exhibit spatially repetitive disturbances, e.g., disturbances that are periodic with respect to a rotation angle in motor/gear transmission systems [33] and internal combustion engines [191]. Transformation of these systems to the rotational-angle domain renders the delay constant in the new independent variable being the rotation angle. However, the design of the stabilizing feedback controller becomes very complicated since the transformed system becomes nonlinear.

In this chapter, we propose a delay-varying repetitive control (DVRC) scheme for systems that have a repetitive variable other than time. DVRC makes use of a measured or observed repetitive variable, e.g., the angular orientation of the legs in the walking piezo actuator, to adjust the repetitive delay in the RC scheme. The proposed method overcomes many of the mentioned drawbacks of existing schemes, e.g., it is applicable in real-time at a fixed sampling-time and it can cope with fast and large variations in the repetitive delay. As the resulting closed-loop system is time-varying in nature, a stability analysis is required. A small tutorial on discrete-time delay-systems is given, followed by a formal stability proof of DVRC incorporating time-varying delays, leading to frequency domain design criteria for the learning filters. Note that design methods for robust RC are available [111, 213, 216]. However, these RC schemes are made robust to system variations, while robustness to varying delays has not been considered. Finally, the proposed DVRC method is applied to a walking piezo actuator, used to drive a nano-motion stage. Experimental results show the significant improvement of DVRC compared to standard RC. The results are compared to high-order RC as presented in [185]. The applicability of DVRC for setpoints with varying velocity, i.e., with an inherent variation in the repetitive delay, shows the strength of the proposed DVRC method.

This chapter is organized as follows. Standard RC is briefly addressed in Section 5.2. The DVRC method is introduced in Section 5.3. The stability of DVRC incorporating the time-varying delay is assessed in Section 5.4. The experimental setup and the learning control design for standard RC, DVRC and high-order RC are presented in Section 5.5. The experimental results on the nano-motion stage are given in Section 5.6. Finally, conclusions are drawn in Section 5.7.

5.2 Repetitive control

RC is applied to control loops (as in Fig. 5.1 without the $M(z, \alpha)$ block) in which repetitive disturbances and/or references are present for which further performance enhancement is required. The repetitive nature of the disturbances (similar for references) means that these disturbances are periodic with respect to some variable α in the system. In standard RC schemes [34, 77, 81] this repetitive variable α is the (continuous) time t, in which case the repetitive disturbances d_r are periodic with respect to time, i.e., $d_r(t + P_\alpha) = d_r(t)$ for all $t \in \mathbb{R}_+$ and some $P_\alpha \in \mathbb{R}_+$, called the repetitive period. In a discrete-time implementation one normally chooses the sampling time T_s of the controller such that $P_\alpha = T_s N$, with $N \in \mathbb{N}$ the number of samples corresponding to the repetitive period. Basically, RC employs the internal model principle [62] to enable asymptotic rejection of the periodic disturbances. To suppress the periodic disturbances in time, a memory loop is included in the discrete-time repetitive controller using a constant delay of N samples. There might also be non-repetitive disturbances d_{nr} that are not compensated for by RC. However, they also enter the memory loop and affect the achievable performance of RC [133].

To explain standard RC, in which the repetitive variable α is equal to time, the single-input-single-output (SISO) case is briefly addressed. For the application of RC to multiple-input-multiple-output (MIMO) systems, the reader is referred to [44]. However, the derived stability criterion in Section 5.4 is also applicable in a MIMO setting. A schematic representation of a feedback controlled system with RC is shown in Fig. 5.1, where $G(z)$ denotes the transfer function of a linear time-invariant discrete-time system with input u and output y. The feedback controller is denoted by $K(z)$ with sampling time T_s (s). The tracking error is given by $e = r - y$, where r is the reference. The repetitive controller $M(z, \alpha)$ is depicted within the dashed block, in which $L(z)$ is the learning filter with a delay of l samples and $Q(z)$ the linear-phase robustness filter with a phase delay of q samples. Since in standard RC the repetitive variable α is time, the repetitive delay, denoted in Fig. 5.1 by $z^{-N(\alpha)}$, is constant, i.e., $N(\alpha) = N = P_\alpha/T_s$ (samples).

For standard RC with a constant repetitive delay N, the transfer function of the repetitive controller $M(z, \alpha) = M(z)$, i.e., the transfer function between the tracking error e and the output w, equals

$$M(z) = \frac{W(z)}{E(z)} = \frac{L(z)Q(z)z^{-(N-l-q)}}{1 - Q(z)z^{-(N-q)}}, \tag{5.1}$$

where $W(z)$ and $E(z)$ are the discrete Laplace transforms of the time signals

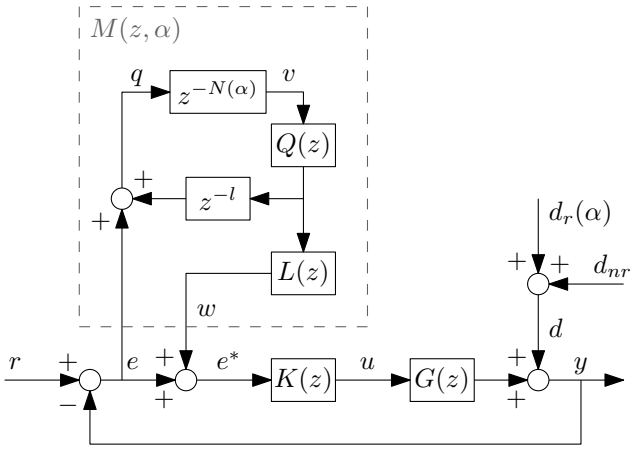

Figure 5.1: Block diagram of a feedback controlled system with DVRC.

w and e, respectively. The sensitivity function $S(z)$, relating the independent disturbances d to the tracking error e is given by

$$S(z) = \frac{E(z)}{D(z)} = \frac{1}{1 + G(z)K(z)(1 + M(z))}. \tag{5.2}$$

Substitution of (5.1) in (5.2) gives

$$S(z) = (1 + G(z)K(z))^{-1} M_s(z), \tag{5.3}$$

where $\bar{S}(z) = (1 + G(z)K(z))^{-1}$ is the sensitivity function of the system without RC. The modifying sensitivity function $M_s(z)$ [32] is given by

$$M_s(z) = \frac{1 - Q(z)z^{-(N-q)}}{1 - Q(z)z^{-(N-q)}\left(1 - \bar{T}(z)L(z)z^{+l}\right)}, \tag{5.4}$$

where $\bar{T}(z) = G(z)K(z)/(1+G(z)K(z))$ is the complementary sensitivity function.

5.2.1 Stability when the repetitive variable is time

For a constant delay of N samples, the stability of the system of Fig. 5.1 can be evaluated using the equivalent error system of (5.3) and (5.4) [188]. Stability of the closed-loop system with RC is achieved if the following two conditions are fulfilled:

1. the sensitivity $\bar{S}(z)$ has all poles in the open unit circle of the complex plane,
2. the following criterion is fulfilled

$$|Q(z)\left(1-\bar{T}(z)L(z)z^{+l}\right)|<1, \tag{5.5}$$

for all $z \in \mathbb{C}$ with $|z| = 1$.

Above conditions give a sufficient criterion for stability [187], where (5.5) is based on the small gain theorem [179]. Indeed, considering Fig. 5.1 as the feedback interconnection of $H(z) = Q(z)z^{-l}(1-\bar{T}(z)L(z)z^{+l})$, being the transfer function from input v to output q, and a contant delay block z^{-N}, for which $|z^{-N}| = 1$ (see also Fig. 5.2 below), the result follows from small gain arguments.

5.2.2 Filter design when the repetitive variable is time

From the criterion (5.5) it follows that a straightforward choice for the learning filter is the inverse of the complementary sensitivity function, i.e., $L(z) = \bar{T}^{-1}(z)$. In case an exact inverse cannot be obtained, e.g., when $\bar{T}(z)$ is non-minimum phase and/or non-proper, an approximation of the inverse is made. One generally used method to obtain a proper and stable inverse is using the zero-phase-error-tracking-control (ZPETC) method [197].

For the determination of the fixed delay value N, the tracking error e containing the repetitive disturbances d_r is measured without RC. From the spectrum of e, the repetitive period P_α can be determined as the lowest harmonic in the signal. The fixed delay value then follows as $N = P_\alpha/T_s$, as discussed before.

The filter $Q(z)$ is designed to account for mismatches between $L(z)$ and $\bar{T}^{-1}(z)$. For standard RC with a fixed delay, the filter $Q(z)$ is designed such that the criterion (5.5) is fulfilled. The use of the $Q(z)$ filter restricts the learning performance of RC in certain frequency bands since part of the frequency content in the tracking error is reduced [185]. The filter $Q(z)$ is constructed to have a linear phase of q samples. The introduced phase delay of the L and Q filters can be compensated for in the memory loop of N samples (see Fig. 5.1) by redefining $N := N - q - l$.

5.3 Delay-varying repetitive control

In this section, the problem formulation leading to the development of DVRC is described. Furthermore, a design procedure for the learning filters and the delay-variation of DVRC is provided.

5.3.1 Problem formulation

In many practical situations disturbances are periodic with respect to other variables α than time, e.g., angles in rotating systems or the angular orientation of the piezo legs in the walking piezo actuator of Section 5.5. Essentially, any variable can be a repetitive variable. The only properties that we impose on the repetitive variable α is that it is monotonically increasing in time[1] and that the relevant disturbances $d_r(\alpha)$ are periodic in α: there is a $P_\alpha \in \mathbb{R}_+$ called the repetitive period such that $d_r(\alpha + P_\alpha) = d_r(\alpha)$ for all $\alpha \in \mathbb{R}_+$.

Clearly, variations in the rate $\dot{\alpha}$ result in disturbances that are not fully repetitive in time. To suppress these types of disturbances, we develop an alternative RC scheme, referred to as delay-varying repetitive control (DVRC). The rate-variation of the repetitive variable α is incorporated in the scheme by making the repetitive delay time-varying as $N(\alpha(t))$. The dependency of the delay $z^{-N(\alpha)}$ on the repetitive variable α results in an α-dependency of the repetitive controller $M(z,\alpha)$ (5.1), of the modified sensitivity function $S(z,\alpha)$ (5.3) and of the modifying sensitivity function $M_x(z,\alpha)$ (5.4).

The assumption that the repetitive variable α is monotonically increasing in time and $\alpha(0) = 0$[2] guarantees that there is a one-to-one correspondence between the repetitive variable $\alpha \in \mathbb{R}_+$ and the (continuous) time $t \in \mathbb{R}_+$. Hence, for each value of $\alpha(t)$ there is a unique corresponding time $t = \alpha^{-1}(\alpha(t))$, where $\alpha^{-1} : \mathbb{R}_+ \to \mathbb{R}_+$ denotes the inverse function of α. Clearly, $t = \alpha^{-1}(\theta) \in \mathbb{R}_+$ is the time at which the repetitive variable α takes the value $\theta \in \mathbb{R}_+$. The time-varying delay $N(\alpha(t))$ in $z^{-N(\alpha(t))}$ at time $t \in \mathbb{R}_+$ is equal to

$$N(\alpha(t)) = t - \alpha^{-1}(\alpha(t) - P_\alpha) \text{ for } \alpha(t) \geq P_\alpha \tag{5.6}$$

in continuous time. The calculated delay $N(\alpha(t))$ is the elapsed time between the current time t (at which the repetitive variable is equal to $\alpha(t)$) and the time at which the repetitive variable α was exactly one repetitive period P_α less than $\alpha(t)$.

In a discrete-time implementation with sampling time $T_s > 0$ as used here, all signals including the repetitive variable α are considered at discrete times kT_s, $k \in \mathbb{N}$. To accommodate for this discrete nature in (5.6), we determine at each sample k the sample index k^* at which α is closest to $\alpha(kT_s) - P_\alpha$, which is given by

$$k^*(\alpha(kT_s)) = \arg\min_{l \in \mathbb{N}} \left(\alpha(lT_s) - \alpha(kT_s) + P_\alpha\right)^2. \tag{5.7}$$

[1] In case α is monotonically decreasing one can take $-\alpha$ as the repetitive variable.

[2] In case $\alpha(0) = a \neq 0$ the same reasoning applies for $\alpha : \mathbb{R}_+ \to [a, \infty)$ and $\alpha^{-1} : [a, \infty) \to \mathbb{R}_+$.

The time-varying delay as in (5.6) can now be approximated as

$$N(\alpha_k) = k - k^*(\alpha_k) \text{ for } \alpha_k \geq P_\alpha, \tag{5.8}$$

where $\alpha_k = \alpha(kT_s)$. Interestingly, standard RC with $\alpha(t) = t$ is recovered as a special case of the DVRC scheme as in (5.8) $N(\alpha_k) = N(kT_s) = N$ and in (5.7) $k^*(\alpha_k) = k^*(kT_s) = k - N$. Also the design conditions will reduce to the ones described above (including the stability condition (5.5), cf. (5.9) below).

5.3.2 Design procedure for DVRC

The design of standard RC involves determining the constant repetitive delay N, the learning filter L and the robustness filter Q. For DVRC, the repetitive delay is continuously adjusted using (5.8) once α and P_α are chosen. For the design of the learning filters and the stability guarantee of DVRC the following design procedure can be used.

1. Choose the repetitive variable α, determine the repetitive delay $N(\alpha_k)$ as in (5.8) and implement the time-varying delay $z^{-N(\alpha_k)}$ at $k \in \mathbb{N}$.
2. The complementary sensitivity $\bar{T}(z)$ is not affected by the time-varying delay $z^{-N(\alpha)}$. The learning filter $L(z)$ for DVRC can therefore be designed analogous to standard RC as $L(z) = \bar{T}^{-1}(z)$.
3. Criterion (5.5) is not valid anymore for DVRC due to the time-varying delay. Let the time-varying delay $N(\alpha)$ satisfy $N(\alpha_k) \in [m, M]$, for $k \in \mathbb{N}$, where m and M denote the minimum and maximum repetitive delay, respectively. Using a robust approach (as proven in Section 5.4), the following generalized criterion of (5.5) for stability of the DVRC scheme with time-varying delay $N(\alpha)$ can be derived:
   (a) $\bar{S}(z)$ has all poles in the open unit circle of the complex plane,
   (b) the following criterion is fulfilled

$$|Q(z)\left(1 - \bar{T}(z)L(z)z^{+l}\right)| < \frac{1}{\sqrt{M - m + 1}}, \tag{5.9}$$

   for all z with $|z| = 1$.

   The linear-phase Q filter is designed to fulfill (5.9).

The sufficiency of (5.9) for stability is proven next.

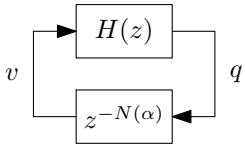

Figure 5.2: Feedback interconnection of a system $H(z)$ with a time-varying delay $z^{-N(\alpha)}$.

5.4 Stability analysis

The stability criterion (5.5) holds for fixed values of the delay, i.e., $N(\alpha_k) = N$ for all $k \in \mathbb{N}$. However, when the delay $z^{-N(\alpha_k)}$ becomes time-varying, the criterion (5.5) is no longer applicable. In this section, it is proven that (5.9) guarantees stability of the RC scheme when the repetitive delay lies in a given range, i.e., $N_k := N(\alpha_k) \in [m, M]$, where $m, M \in \mathbb{N}$ with $0 \leq m \leq M$.

If we ignore the external signals d and r for the moment, the system in Fig. 5.1 can be represented as the feedback interconnection of the discrete-time system

$$x_{k+1} = Ax_k + Bv_k;\ q_k = Cx_k \tag{5.10a}$$

and the varying delay block

$$v_k = q_{k-N_k}, \tag{5.10b}$$

where $x_k \in \mathbb{R}^{n_x}$ is the state and $v_k \in \mathbb{R}^{n_v}$ and $q_k \in \mathbb{R}^{n_q}$ are the interconnection variables at discrete time $k \in \mathbb{N}$. System (5.10a) is a state space representation of the transfer function $H(z) = Q(z)z^{-l}\left(1 - \bar{T}(z)L(z)z^{+l}\right)$ between v and q in Fig. 5.1. Hence, Fig. 5.1 reduces to Fig. 5.2 using this perspective. The delay N_k is time-varying, but assumed to lie in the interval $[m, M] \cap \mathbb{N}$ with bounds $0 \leq m \leq M$, i.e., $m \leq N_k \leq M$ for all $k \in \mathbb{N}$. The varying delay block (5.10b) can also be written in state space notation as

$$\zeta_{k+1} = \begin{bmatrix} 0 & 0 & 0 & \dots & 0 & 0 \\ I_{n_q} & 0 & 0 & \dots & 0 & 0 \\ 0 & I_{n_q} & 0 & \dots & 0 & 0 \\ \vdots & & & & \vdots & \vdots \\ 0 & 0 & \dots & 0 & I_{n_q} & 0 \end{bmatrix} \zeta_k + \begin{bmatrix} I_{n_q} \\ 0 \\ 0 \\ \vdots \\ 0 \end{bmatrix} q_k, \tag{5.11a}$$

$$v_k = \begin{bmatrix} \Gamma_1(N_k) & \dots & \Gamma_M(N_k) \end{bmatrix} \zeta_k + \Gamma_0(N_k) q_k \tag{5.11b}$$

with $\zeta_k = (q_{k-1}^T, \dots, q_{k-M}^T)^T$ and for $i = 0, 1, \dots, M$

$$\Gamma_i(N) = \begin{cases} I_{n_q}, & \text{when } N = i, \\ 0, & \text{when } N \neq i. \end{cases} \tag{5.12}$$

Here, I_m denotes the identity matrix of dimension $m \times m$. Although in the setup in Fig. 5.1 all signals are scalar valued (i.e., $n_q = n_v = 1$), we present the stability for MIMO plants for reasons of generality.

5.4.1 A short tutorial on stability of discrete-time delay systems

We quickly review some of the methods to analyse discrete-time delay systems. A recently proposed method [79] is lifting the model (5.10) by using the augmented state vector $\xi_k = (x_k^T, \zeta_k^T)^T = (x_k^T, q_{k-1}^T, \ldots, q_{k-M}^T)^T$, which results in the system

$$\xi_{k+1} = \Lambda(N_k)\xi_k \tag{5.13}$$

with

$$\Lambda(N) = \begin{bmatrix} A + \Theta_0(N)C & \Theta_1(N) & \ldots & \Theta_{M-1}(N) & \Theta_M(N) \\ C & 0 & \cdots & 0 & 0 \\ 0 & I_{n_q} & \cdots & 0 & 0 \\ \vdots & & \ddots & & \vdots \\ 0 & 0 & \cdots & I_{n_q} & 0 \end{bmatrix} \tag{5.14}$$

and

$$\Theta_i(N) = \begin{cases} B, & \text{when } i = N, \\ 0, & \text{when } i \neq N, \end{cases} \tag{5.15}$$

for $i = 0, 1, \ldots, M$. Since $N_k \in [m, M] \cap \mathbb{N}$ one can now search for a parameter-dependent Lyapunov function $V(N_k, \xi_k) = \xi_k^T P_{N_k} \xi_k$ (see e.g. [39]) for the switched linear system (5.13), which amounts to checking feasibility of the linear matrix inequalities (LMIs)

$$\begin{bmatrix} P_i & \Lambda(i)^T P_j \\ P_j \Lambda(i) & P_j \end{bmatrix} \succ 0 \text{ for } i, j = m, \ldots, M, \tag{5.16}$$

where the inequality indicates positive definiteness of the matrix. In case that $C = I_{n_x}$ it was observed in [79] that the Lyapunov function $V(N_k, \xi_k) = \xi_k^T P_{N_k} \xi_k$ is equivalent to a so-called Lyapunov-Krasovskii functional (LKF) for the system (5.10) given by

$$V(N_k, x_k, x_{k-1}, \ldots, x_{k-M}) = \sum_{i=0}^{M} \sum_{j=0}^{M} x_{k-i}^T P_{N_k}^{(i,j)} x_{k-j}, \tag{5.17}$$

where $P_{N_k}^{(i,j)}$ denotes the (i, j) block element of P_{N_k}. LKFs are typically chosen as quadratic forms that depend on the current and delayed states. Classically the

LKF approach was the common method to assess stability of time delay systems as in (5.10) (both in continuous and discrete time). The general delay-dependent LKF in (5.17) encompasses all of the earlier forms of quadratic LKFs used in the literature as proven in [79]. For instance, the discrete-time LKFs given in [183] for $m = 1$ are of the form

$$x_k^T P x_k + \sum_{i=1}^{M} \sum_{j=k-i}^{k-1} x_j^T Q x_j \tag{5.18}$$

with P and Q positive definite matrices, which are obviously a special case of (5.17). Also extended variants of the LKFs in (5.18) as in e.g. [68] are still a particular case of (5.17). Based on the LKFs as in (5.18) the following sufficient conditions for stability of (5.10) with $m = 1$ are provided in [183].

Lemma 1 *[183] Suppose there exist positive definite matrices P and Q such that the following LMI is satisfied:*

$$\begin{bmatrix} P - A^T P A - MQ & A^T P B C \\ C^T B^T P A & Q - C^T B^T P B C \end{bmatrix} \succ 0. \tag{5.19}$$

Then the system (5.10) *with $N_k \in [1, M] \cap \mathbb{N}$ is asymptotically stable.*

Due to the results in [79] feasibility of the conditions in Lemma 1 implies feasibility of the LMIs in (5.16). Hence, from a conservatism point of view, the lifted model approach using the condition (5.16) is preferred. However, given the large size of the maximal delay M (in the order of 5500 for the working range of the experimental system considered in Section 5.5) the state dimension of the lifted model (5.13) becomes prohibitively large for the available LMI solvers to solve (5.16). Even the LMI in (5.19) is of a reasonably large size due to the orders of $C(z)$, $G(z)$, $Q(z)$ and $L(z)$ (e.g., the dimension of A in (5.10a) is in the order of 118 for the experimental system), which causes numerical and memory problems as well.

Due to the fact that today's LMI solvers cannot handle (yet) such large size LMI problems, it is more convenient to obtain $\mathcal{H}_\infty$ characterizations for stability such as in (5.5). This has the additional advantage that such a frequency domain characterization would be more in line with the frequency domain based tuning of ILC and RC in the literature.

5.4.2 Frequency domain characterizations of stability

The condition (5.5) is based on small gain arguments by observing that (5.10) is the feedback interconnection of a linear system (5.10a) and the delay block (5.10b)

(see Fig. 5.2). Indeed, as a constant delay block has $\mathcal{H}_\infty$ norm equal to 1 (see also Theorem 8 below), the small gain theorem would prove that (5.5) guarantees stability. The condition (5.5) only applies when $m = M$, but not for a varying delay $N_k \in [m, M] \cap \mathbb{N}$ with $m \neq M$. To provide frequency domain characterizations of stability in the latter case as well, we introduce some terminology.

Definition 2 [ℓ_2 **gain**] *A general discrete-time system*

$$x_{k+1} = f(x_k, N_k, v_k);\ q_k = g(x_k, N_k, v_k) \tag{5.20}$$

with state x_k, (disturbance) input v_k, uncertainty N_k and output q_k at discrete time $k \in \mathbb{N}$ is said to have ℓ_2 gain equal to γ^* for disturbances in the set Υ, if γ^* is the smallest $\gamma \geq 0$ such that for initial condition $x_0 = 0$ and any input sequence $\{v_k\}_{k\in\mathbb{N}}$ with $\sum_{k=0}^{\infty} \|v_k\|^2 < \infty$ and any disturbances sequence $\{N_k\}_{k\in\mathbb{N}}$ of uncertainties with $N_k \in \Upsilon$ for all $k \in \mathbb{N}$, it holds that the corresponding output sequence $\{q_k\}_{k\in\mathbb{N}}$ satisfies $\sum_{k=0}^{\infty} \|q_k\|^2 \leq \gamma^2 \sum_{k=0}^{\infty} \|v_k\|^2$.

For linear systems the following result on ℓ_2 gains is well known. See [54,67] for a proof.

Theorem 3 *The following statements are equivalent:*

1. *system* (5.10a) *has ℓ_2 gain smaller than γ,*
2. *the $\mathcal{H}_\infty$ norm $\sup_{z\in\mathbb{C},|z|=1} \bar{\sigma}(H(z))$ with $H(z) = C(zI - A)^{-1}B$ is smaller than γ, where $\bar{\sigma}$ denotes the maximum singular value,*
3. *there exist a matrix P and a $\beta > \frac{1}{\gamma}$ satisfying*

$$\begin{bmatrix} P - A^T P A - \beta^2 C^T C & -A^T P B \\ -B^T P A & I - B^T P B \end{bmatrix} \succeq 0 \text{ and } P \succ 0. \tag{5.21}$$

Now we state a stability result of (5.10) for time-varying delays when $m = 0$.

Theorem 4 *Consider system* (5.10a) *with A Schur and ℓ_2 gain smaller than $\frac{1}{\sqrt{M+1}}$ for $M \in \mathbb{N}$. Then system* (5.13) *with time-varying $N_k \in [0, M] \cap \mathbb{N}$, $k \in \mathbb{N}$ is asymptotically stable.*

Proof: Eq. (5.13) is just the closed-loop form of (5.10a) and (5.11). Take the Lyapunov function $V(\xi_k) = \bar{V}(x_k) + \sum_{i=1}^{M} (M-i+1) q_{k-i}^T q_{k-i}$ with $\bar{V}(x_k) = x_k^T P x_k$ and P satisfying (5.21) for some $\beta^2 > M + 1$. This Lyapunov function is a special case of the one used in [183].

Then

$$\begin{aligned} V(\xi_{k+1}) - V(\xi_k) = \bar{V}(x_{k+1}) - \bar{V}(x_k) + \\ \sum_{i=1}^{M} (M-i+1) q_{k+1-i}^T q_{k+1-i} - \\ \sum_{j=2}^{M+1} (M-j+2) q_{k+1-j}^T q_{k+1-j} \\ \leq v_k^T v_k - \beta^2 q_k^T q_k + (M+1) q_k^T q_k - \sum_{l=0}^{M} q_{k-l}^T q_{k-l}, \end{aligned}$$

where we used that (5.21) implies that $\bar{V}(x_{k+1}) - \bar{V}(x_k) \leq v_k^T v_k - \beta^2 q_k^T q_k$. Since $v_k = q_{k-N_k}$ for some $N_k = 0, 1, \ldots, M$ (see (5.10b)), the term $v_k^T v_k$ is canceled by one of the terms in $\sum_{l=0}^{M} q_{k-l}^T q_{k-l}$ and thus

$$V(\xi_{k+1}) - V(\xi_k) \leq -(\beta^2 - M - 1) q_k^T q_k. \tag{5.22}$$

Clearly, (5.22) proves Lyapunov stability as $V(\xi_{k+1}) \leq V(\xi_k)$ for all $k \in \mathbb{N}$ and $c_1 \|\xi\|^2 \leq V(\xi) \leq c_2 \|\xi\|^2$ for all ξ for some $0 < c_1 \leq c_2$. To show that $\lim_{k\to\infty} \xi_k = 0$, note that by summing (5.22) for $k = 0, 1, \ldots, \ell$ we obtain that

$$V(\xi_{\ell+1}) - V(\xi_0) \leq -\alpha \sum_{k=0}^{\ell} \|q_k\|^2 \tag{5.23}$$

with $\alpha := \beta^2 - M - 1 > 0$ and thus $\sum_{k=0}^{\infty} \|q_k\|^2 \leq \frac{1}{\alpha} V(\xi_0)$. This implies that $q_k \to 0$ $(k \to \infty)$ and due to (5.10b) also that $v_k \to 0$ $(k \to \infty)$. Since A is Schur, this yields that $\lim_{k\to\infty} x_k = 0$ and thus $\lim_{k\to\infty} \xi_k = 0$. ■

The following result is a simple corollary of Theorem 4, which shows so-called input-to-state stability (ISS) [91, 184] (and thus also bounded-input bounded output (BIBO) stability) of the system (5.13) when external inputs are present (e.g., the references r and d as in Fig. 5.1). Including the external signals changes the system description (5.10a) into

$$x_{k+1} = Ax_k + Bv_k + Ed_k;\ q_k = Cx_k, \tag{5.24}$$

where, for shortness, we included all external disturbances (including the reference r) into the signal d by a suitable choice of E. In the lifted model notation as in (5.13) we obtain

$$\xi_{k+1} = \Lambda(N_k)\xi_k + \begin{bmatrix} E^T & 0 & 0 \end{bmatrix}^T d_k. \tag{5.25}$$

For self-containedness we recall the definition of input-to-state stability for the system (5.25). A function $\varphi : \mathbb{R}_+ \to \mathbb{R}_+$ belongs to class $\mathcal{K}$ if it is continuous,

strictly increasing and $\varphi(0) = 0$ and to class $\mathcal{K}_\infty$ if, additionally, $\varphi(s) \to \infty$ as $s \to \infty$. A function $\beta : \mathbb{R}_+ \times \mathbb{R}_+ \to \mathbb{R}_+$ belongs to class $\mathcal{KL}$ if for each fixed $k \in \mathbb{R}_+$, $\beta(\cdot, k) \in \mathcal{K}$ and for each fixed $s \in \mathbb{R}_+$, $\beta(s, \cdot)$ is decreasing and $\lim_{k\to\infty} \beta(s, k) = 0$.

Definition 5 *The system given by* (5.13) *with uncertainty set* $\Upsilon \subseteq \mathbb{N}$ *is called* input-to-state stable *(ISS) with respect to d, if there exist a* $\mathcal{KL}$*-function* β *and a* $\mathcal{K}$*-function* γ *such that, for each* $\xi_0 \in \mathbb{R}^n$*, all* $\{d_k\}_{k\in\mathbb{N}}$ *and all* $\{N_k\}_{k\in\mathbb{N}}$ *with* $N_k \in \Upsilon$*,* $k \in \mathbb{N}$*, it holds that* $\|\xi_k\| \leq \beta(\|\xi_0\|, k) + \gamma(\sup_{k\in\mathbb{N}} \|d_k\|)$ *for all* $k \in \mathbb{N}$*.*

Corollary 6 *Consider system* (5.25) *with A Schur and* ℓ_2 *gain of* (5.10a) *smaller than* $\frac{1}{\sqrt{M+1}}$ *for* $M \in \mathbb{N}$ *with* $M \geq 0$*. Then system* (5.25) *with uncertainty set* $[0, M] \cap \mathbb{N}$ *is ISS with respect to d.*

Proof: The proof is based on observing that since A is Schur the system (5.10a) has a finite ℓ_2 gain from v to x. Since the $\mathcal{H}_\infty$ norm from v to q is (strictly) smaller than $\frac{1}{\sqrt{M+1}}$, this implies that there is an $\varepsilon > 0$ (small enough) such that the system (5.10a) has a $\mathcal{H}_\infty$ norm smaller than $\frac{1}{\sqrt{M+1}}$ from v to a new output $[q^T \; x^T]^T = [C^T \; I]^T x$. Applying Theorem 3 yields that there exist a $P > 0$ and a $\beta > M + 1$ satisfying the LMIs

$$\begin{bmatrix} P - A^T P A - \beta^2 C^T C - \varepsilon I & -A^T P B \\ -B^T P A & I - B^T P B \end{bmatrix} \succeq 0. \tag{5.26}$$

Applying now the reasoning as in the proof of Theorem 4 gives after some straightforward manipulations that

$$V(\xi_{k+1}) - V(\xi_k) \leq -\mu_1 \|\xi_k\|^2 + \mu_2 \|d_k\|^2 \tag{5.27}$$

for the system (5.25), where μ_1 and μ_2 are positive constants. As (5.27) is a Lyapunov characterization for ISS [91, 104] this proves ISS. ■

The case $m \neq 0$ is covered in the next corollary.

Corollary 7 *Consider system* (5.10a) *with A Schur and* ℓ_2 *gain smaller than* $\frac{1}{\sqrt{M-m+1}}$*, where* $M \geq m \geq 0$*. Then system* (5.13) *with time-varying* $N_k \in [m, M] \cap \mathbb{N}$*,* $k \in \mathbb{N}$ *is asymptotically stable. In addition, system* (5.25) *with uncertainty set* $[m, M] \cap \mathbb{N}$ *is ISS with respect to d.*

Proof: The system (5.10) is equivalent to the feedback connection of a varying delay block z^{-p_k} with $p_k \in [0, M-m] \cap \mathbb{N}$ on the one hand and the series connection

of (5.10a) with the constant delay block ($z^{-m}I_{n_y}$) on the other. The latter series connection can be represented in a state space realization by

$$\xi_{k+1}=\begin{bmatrix}A & 0\\ C & 0\\ 0 & I_{(m-1)n_y}\end{bmatrix}\xi_k+\begin{bmatrix}B\\ 0\\ 0\end{bmatrix}v_k;\ \bar{q}_k=(0\ \ldots\ 0\ I_p)\xi_k. \tag{5.28}$$

The transfer matrix of (5.28) is $H(z)z^{-m}$ with $H(z)$ the transfer matrix of (5.10a), which implies that the $\mathcal{H}_\infty$ norm (and thus the ℓ_2 gain according to Theorem 3) of (5.28) is smaller than $\frac{1}{\sqrt{M-m+1}}$. Applying now Theorem 4 to (5.28) yields that its feedback interconnection with z^{-p_k} with $p_k \in [0, M-m]\cap\mathbb{N}$ is asymptotically stable and thus that (5.13) with time-varying $N_k \in [m, M]$ is asymptotically stable. The ISS result follows similarly. ■

Interestingly, this corollary shows that the size of the variation in the delay determines the requirement on the $\mathcal{H}_\infty$ norm of the linear system, not the (absolute) size of the delay itself. Actually in case there is no variation in the delay a condition of the form (5.5) suffices for closed-loop stability, but the $\mathcal{H}_\infty$ conditions become more stringent if the delay is time-varying. The following result sheds some light why this is the case.

Theorem 8 *Consider the system $v_k = q_{k-N_k}$ that can be represented in state space realization as in* (5.11)*. Let the varying N_k, $k \in \mathbb{N}$ be contained in $[m, M]\cap\mathbb{N}$ with $m, M \in \mathbb{N}$ and $0 \le m \le M$. The ℓ_2 gain of the delay system* (5.11) *with disturbance set $[m, M]\cap\mathbb{N}$ is equal to $\sqrt{M-m+1}$.*

Proof: First of all we show that the ℓ_2 gain is larger than or equal to $\sqrt{M-m+1}$ by taking the input signal

$$q_k=\begin{cases}q, & \text{when } k=0,\\ 0, & \text{otherwise.}\end{cases}$$

Note that the input energy is given by $\sum_{k=0}^{\infty}\|q_k\|^2=\|q\|^2$. If the varying delay acts as

$$N_k=\begin{cases}k, & \text{when } k\in[m,M],\\ \text{arbitrary}, & \text{otherwise,}\end{cases}$$

then the corresponding output v_k satisfies for $k \in [m, M]$ that $v_k = q$ and for $k \notin [m, M]$ that $v_k = 0$. Hence, $\sum_{k=0}^{\infty}\|v_k\|^2=(M-m+1)\|q\|^2$ thereby showing that the ℓ_2 gain is larger than or equal to $\sqrt{M-m+1}$. To prove that the ℓ_2 gain is smaller than or equal to $\sqrt{M-m+1}$, observe that due to $v_k = q_{k-N_k}$ with

$N_k \in [m, M] \cap \mathbb{N}$ we have that

$$\sum_{k=0}^{\infty} \|v_k\|^2 \leq \sum_{k=0}^{\infty} \max_{l \in [k-M, k-m]} \|q_l\|^2 \leq \sum_{k=0}^{\infty} \sum_{l=k-M}^{k-m} \|q_l\|^2 = \sum_{k=0}^{\infty} (M-m+1)\|q_k\|^2,$$

where we used that due to initial state 0, $q_{-M} = q_{-M+1} = \ldots = q_{-1} = 0$. This completes the proof. ■

Theorem 8 explains why the ℓ_2 gain or equivalently the $\mathcal{H}_\infty$ norm of (5.10a) should be smaller than $\frac{1}{\sqrt{M-m+1}}$. Indeed, as the ℓ_2 gain of a varying delay block z^{-N_k} with $N_k \in [m, M]$ is equal to $\sqrt{M-m+1}$, small gain arguments would require that the $\mathcal{H}_\infty$ norm of (5.10a) is smaller than $\frac{1}{\sqrt{M-m+1}}$ to guarantee closed-loop stability of (5.10).

Remark 9 *Alternative frequency domain characterizations for discrete-time delay systems as in* (5.10) *are given in [95]. In particular, if for all* $z \in \mathbb{C}$ *with* $|z| = 1$ $\left|\frac{H(z)}{1-H(z)}\right| < \frac{1}{M|z-1|}$, *[95] implies that the system as in Fig. 5.2 is stable for* $N_k \in [0, M] \cap \mathbb{N}$. *These conditions are in various situations more conservative than our* $\mathcal{H}_\infty$ *based conditions. For instance, for* $H(z) = \frac{0.1}{z}$ *stability is guaranteed by our condition for* $N_k \in [0, 98] \cap \mathbb{N}$ *as the* $\mathcal{H}_\infty$ *norm of* $H(z)$ *is equal to* 0.1, *while the condition in [95] only guarantees stability for* $N_k \in \{0, 1, 2, 3, 4\}$. *For this reason and the fact that in our setup* $H(z)$ *always represents an asymptotically stable system by design, we use the novel conditions derived here. Note that the conditions in [95] have the advantage that they also apply when* $H(z)$ *does not represent a stable system with a finite* $\mathcal{H}_\infty$ *norm.*

Remark 10 *Since we consider arbitrary variations of* $N(\alpha)$ *and do not use possible smoothness or structure in the variation, conservatism is introduced in the criterion* (5.9) *besides the usual conservatism present in the small gain criterion as is also present in* (5.5).

5.5 Application and controller design

In this section, first the experimental setup and the control configuration are discussed. Afterwards, the designed learning filters for DVRC and for high-order control are presented.

5.5.1 Nano-motion stage

The nano-motion stage, depicted in Fig. 5.3, is driven by a walking piezo motor. The piezo motor consists of four bimorph piezoelectric drive legs, each of which consist of two electrically separated piezo stacks that can be driven by electric waveforms through the connector [155]. The drive pads of the legs are pressed against the drive strip of a one degree-of-freedom (DOF) stage using a motor suspension and preload springs such that the (x_m, y_m, z_m)-axes of the motor coincide with the (x, y, z)-axes of the stage. The position of the stage is measured using an optical incremental encoder with a resolution of 0.64 nm. The movement of the back of the motor housing in y_m-direction is measured using a capacitive sensor with a resolution of 0.44 nm.

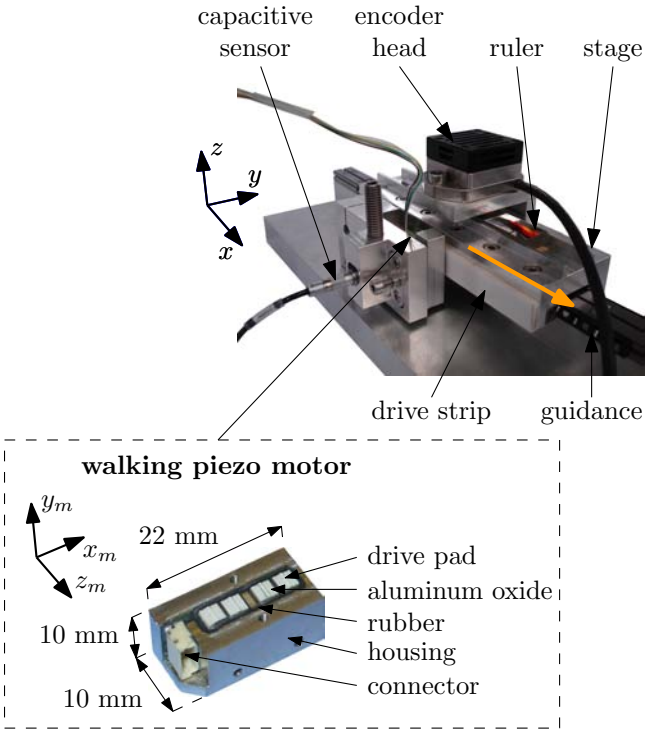

Figure 5.3: The 1-DOF nano-motion stage with the walking piezo actuator.

The drive legs of the walking piezo motor employ a bimorph working principle through two electrically separated piezo stacks. A schematic working principle of the walking piezo motor is shown in Fig. 5.4. It can be seen that the piezo legs

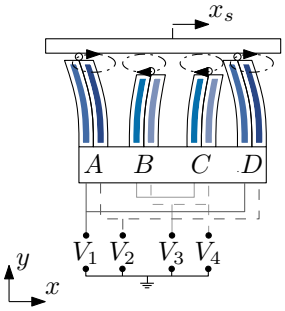

Figure 5.4: Working principle of the walking piezo motor with leg trajectories for sinusoidal waveforms $V_i(t),\ i \in \{1,2,3,4\}$.

are driven by four independent waveforms $V_i(t)$ (V), $i \in \{1,2,3,4\}$. Each pair of piezo legs, $p_1 = \{A, D\}$ and $p_2 = \{B, C\}$, is driven by two waveforms. When the waveforms of one pair of legs are equal, the legs elongate in y_m-direction, different waveforms result in a bending of the leg in x_m-direction. This can be described as [155]

$$\begin{aligned} x_{m,p_1}(t) &= c_x(V_1(t) - V_2(t)), \\ y_{m,p_1}(t) &= c_y(V_1(t) + V_2(t)), \\ x_{m,p_2}(t) &= c_x(V_3(t) - V_4(t)), \\ y_{m,p_2}(t) &= c_y(V_3(t) + V_4(t)), \end{aligned} \tag{5.29}$$

where the bending and extending coefficients equal $c_x = 64.5$ nm/V and $c_y = 29.8$ nm/V, respectively. In Chapter 2, asymmetric waveforms have been developed, which result in periodic tip trajectories with a take-over between the driving pair of legs at a non-zero velocity of the legs in x-direction. The asymmetric waveforms enable the stage to be driven continuously at velocities in the range of nanometers per second to millimeters per second. The asymmetric waveforms are defined as

$$V_i(t) = \frac{A}{\bar{A}} a_0 + \frac{A}{\bar{A}} \sum_{k=1}^{4} \left\{ a_k \cos[k\alpha(t) + k\psi_i(t)] + b_k \sin[k\alpha(t) + k\psi_i(t)] \right\}, \tag{5.30}$$

where $i \in \{1,2,3,4\}$ and the Fourier coefficients $a_0 = 28.80$, $a_1 = -10.78$, $b_1 = 18.73$, $a_2 = 2.387$, $b_2 = 4.097$, $a_3 = 1.985$, $b_3 = -0.007792$, $a_4 = 0.2298$, and $b_4 = -0.3901$. The maximum amplitude $\bar{A} = 46$ V. For the experiments of this chapter, the maximum step size is used, i.e., $A = 46$ V. The phases equal $[\psi_1, \psi_2, \psi_3, \psi_4] = [0, \pi/2, \pi, 3\pi/2]$ rad. In (5.30), $\alpha(t)$ denotes a nominal angle of the legs on the tip trajectory. The angle $\alpha(t)$ follows from the drive frequency $f_\alpha(t)$ as $\alpha(t) = 2\pi \int_0^t f_\alpha(\tau) d\tau$.

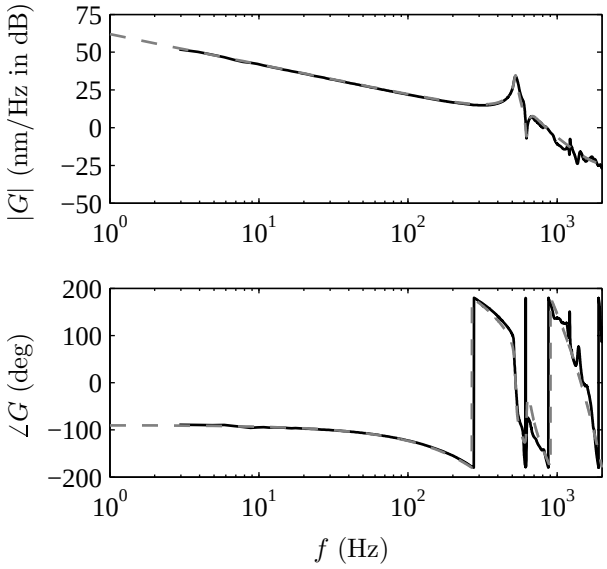

Figure 5.5: Measured FRF (solid, black) and model (dashed, grey).

5.5.2 Control configuration

The shape of the tip trajectories of the legs is fixed and described by (5.29) and (5.30). For feedback control, the angular frequency of the legs f_α (Hz) is chosen as the control input to the system, i.e., $u(t) = f_\alpha(t)$ in Fig. 5.1. The output of the system is the stage position $x_s(t)$. The measured frequency response function (FRF) from the angular frequency $f_\alpha(t)$ (Hz) to the stage position $x_s(t)$ (nm), shown in Fig. 5.5 with the solid black line, shows a decay of 20 dB/decade at low frequencies. At a frequency of 527 Hz the first resonance can be seen, directly followed by an anti-resonance and resonance at 624 Hz and 650 Hz, respectively. At higher frequencies, more (anti-)resonances are present. Furthermore, the FRF shows a phase delay of three samples at a sampling frequency of $f_s = 4$ kHz.

To design the feedback controller and the learning filters, a parametric model containing a pure integrator, two resonances and one anti-resonance is fitted to the measured FRF as

$$\hat{G}(s) = \frac{2\pi}{s} \; \frac{c}{s^2 + 2\pi f_{p1} b_{p1} s + (2\pi f_{p1})^2} \frac{s^2 + 2\pi f_{z1} b_{z1} s + (2\pi f_{z1})^2}{s^2 + 2\pi f_{p2} b_{p2} s + (2\pi f_{p2})^2}, \tag{5.31}$$

where $c = 14.9 \cdot 10^9$, $f_{p1} = 527$ Hz, $b_{p1} = 0.033$, $f_{z1} = 624$ Hz, $b_{z1} = 0.02$, $f_{p2} = 650$ Hz and $b_{p2} = 0.175$. The phase delay of three samples is added to the

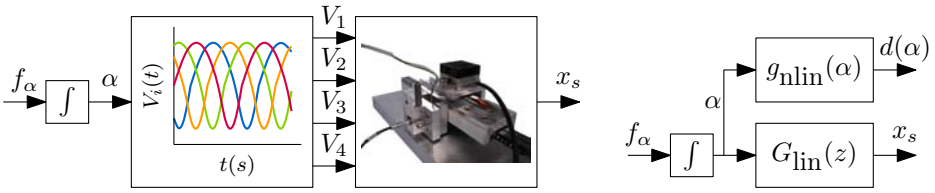

(a) Original nonlinear system. (b) Equivalent system.

Figure 5.6: System representation, original and equivalent system containing a linear part $G_{\text{lin}}(z)$ and an additive nonlinearity $G_{\text{nlin}}(z)$.

model by multiplying it after discretization with a discrete-time delay z^{-3}. The model $\hat{G}(s)$ approximates the measured FRF well, as shown by the dashed line in Fig. 5.5.

The system of Fig. 5.3 has an inherent nonlinearity since the output $x_s(t)$ contains for a constant input drive frequency $f_\alpha(t)$ repetitive components with other period-times than $1/f_\alpha$ (s). This nonlinearity is caused by the harmonic components in the waveform generation (5.30), resulting in a repetitive movement of the drive legs (see also Chapter 2). The disturbances introduced by the walking movement are fully repetitive with respect to the angular orientation α, which is chosen to be the repetitive variable. The system is considered to be composed of a linearized system model $G(z) = X_s(z)/F_\alpha(z)$ (see Fig. 5.5), which is used for the feedback control, and a nonlinear disturbance generating model, which generates the repetitive disturbance $d_r(\alpha) = g_{\text{nlin}}(\alpha)$ (see also Fig. 5.6(b)).

For the stability analysis of the DVRC scheme with the system of Fig. 5.6, the nonlinear part $g_{\text{nlin}}(\alpha)$ is not explicitly modeled. However, based on the physical nature of the repetitive nonlinear part, being the periodic leg movement, the repetitive disturbances $d_r(\alpha)$ are bounded in amplitude. The (bounded-input bounded-output) stability of the DVRC scheme with the bounded repetitive disturbances $d(\alpha)$ follows then from the input-to-state stability (ISS) property (Def. 5) as will be proven based on Corollary 6, i.e., the learning filters will be designed such that the condition (5.9) will be satisfied (see Section 5.5.3 below).

A continuous-time controller $K(s)$ is designed using loopshaping techniques [63] as $K(s) = k\frac{s+2\pi f_{zc}}{s}$, where the gain $k = 2.8 \cdot 10^{-3}$ and the $f_{zc} = 5$ Hz, resulting in a closed-loop bandwidth $f_{BW} = 5$ Hz. The controller is then discretized using a Tustin discretization at a sampling frequency of $f_s = 4$ kHz.

5.5.3 Learning filters DVRC

The tracking error for an experiment with a reference velocity $\dot{r} = 10$ μm/s, depicted in Fig. 5.7, shows on the first sight a repetitive structure. The power spectral density (PSD) of a part of the repetitive error shows that on average over a larger time span a base repetitive frequency of 1.98 Hz is present, which corresponds to $N = 2020$ samples for a sampling frequency of $f_s = 4$ kHz. However, a closer look shows that the period-time of the repetitive disturbances is not constant over time as can be seen in the bottom figure of Fig. 5.7. The repetitive delay $N(\alpha)$ shows for $t > 40$ s, i.e., after the transient response, a fast variation in the range $N(\alpha) \in [2006, 2029]$ samples. The amount of variation, i.e., $M - m$ in Section 5.4, is a function of the reference velocity. Therefore, the Q filter should be designed for the worst-case range of variation in $N(\alpha)$ over all relevant references. For the working range of the nano-motion stage of Fig. 5.3 with velocities ranging from nanometers per second to millimeters per second the worst case variation in repetitive delay equals $M - m = 180$ samples. The absolute number of samples delay $N(\alpha)$ can reach up to 5500 for a sampling frequency $f_s = 4$ kHz.

The learning filter $L(z)$ is derived as a proper stable approximation of a discrete-time model of the complementary sensitivity function $\hat{T}(z) = \hat{H}(z)C(z)/(1 + \hat{H}(z)C(z))$ using the ZPETC method [197], i.e., $L(z)\hat{T}(z) \approx 1$. The FRFs of $\hat{T}$ and L have an exact inverse phase, as shown in Fig. 5.8 by the solid black and grey dashed line, respectively. The magnitude of L deviates mainly at high frequencies from $\hat{T}^{-1}$ to obtain a proper and stable learning filter.

For a variation in the repetitive delay of $M - m = 180$ samples, the $\mathcal{H}_\infty$ norm bound in the stability criterion (5.9) equals $\frac{1}{\sqrt{M-m+1}} = 1/\sqrt{181} = -22.6$ dB (black, dashed line in Fig. 5.9). The criterion (5.9) without Q filter, shown in Fig. 5.9 by the black solid line, exceeds the allowed $\mathcal{H}_\infty$ norm of -22.6 dB for frequencies $f > 228$ Hz. To guarantee stability of DVRC, a low-pass $Q(z)$ FIR filter with 100 taps and a cut-off frequency of 220 Hz is used. With the robustness filter $Q(z)$ stability is guaranteed, as shown in Fig. 5.9 with the grey dashed line.

The change in the cut-off frequency of the Q filter due to the variation of the repetitive delay can be seen in Fig. 5.9 by the dashed and dotted vertical lines. The frequency up to which learning can be applied is reduced from 590 Hz to 228 Hz due to the variation in the repetitive delay. At low frequencies the level of the convergence criterion is mainly determined by the quality of the model used to determine the learning filter. With the current model a maximum deviation of -25 dB, i.e., 6%, is achieved. This level can be further reduced using a more accurate model.

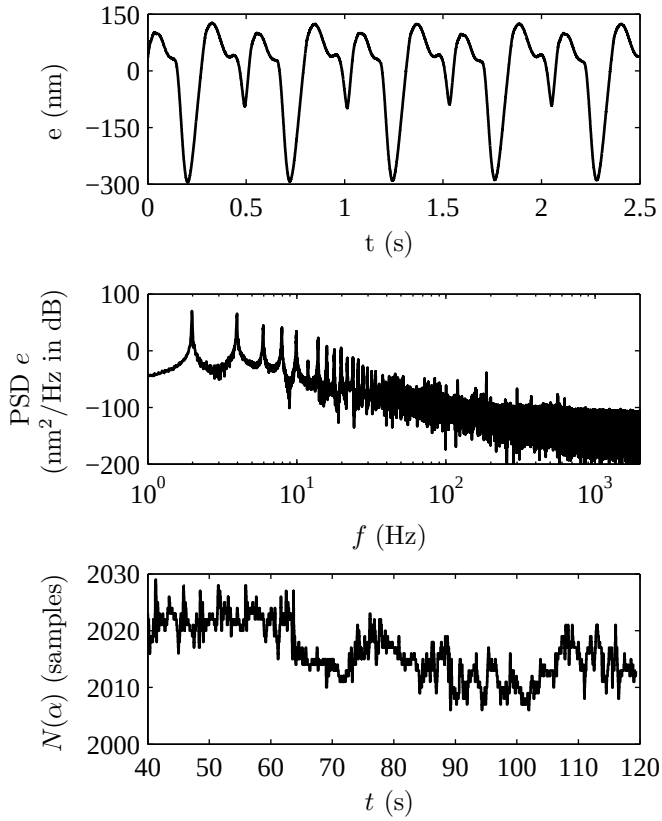

Figure 5.7: Tracking error, PSD of the tracking error and variation in $N(\alpha)$ for an experiment without RC and $\dot{r} = 10$ μm/s.

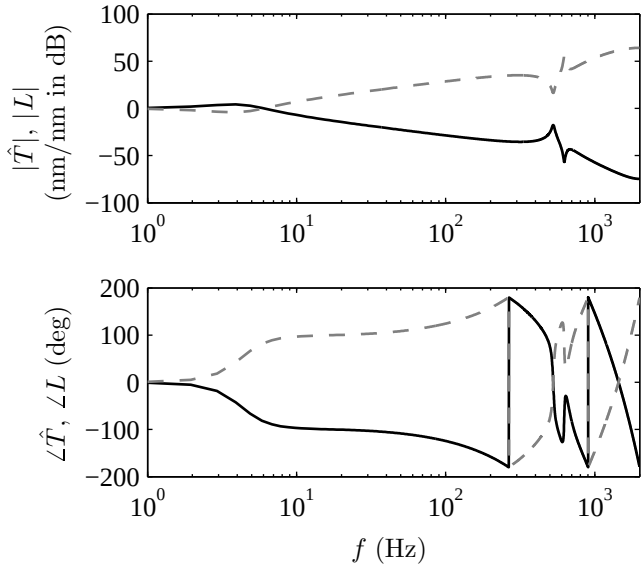

Figure 5.8: Bode diagrams of the complementary sensitivity $\hat{T}(z)$ (black, solid) and the learning filter $L(z)$ (grey, dashed).

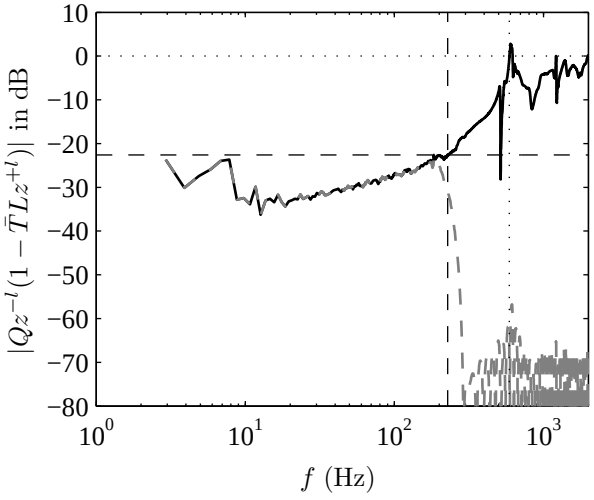

Figure 5.9: Convergence criterion (5.5) without (black, solid) and with (grey, dashed) Q filter.

5.5.4 High-order repetitive controller

For comparison, a high-order repetitive controller that incorporates two periods, i.e., with two memory loops [185], is designed. The high-order repetitive controller equals

$$M_{HO}(z) = \frac{L(z)W(z)Q(z)z^{-(N-q-l)}}{1 - Q(z)W(z)z^{-(N-q)}},$$

where $W(z)$ is the high-order repetitive function

$$W(z) = \sum_{i=1}^{n_{HO}} w_i z^{-(i-1)N}$$

and $n_{HO} = 2$ is the order. The optimal weighting filter for a second order repetitive controller is determined in [185] as $W_{opt} = (w_{opt,1}, w_{opt,2}) = (2, -1)$.

5.6 Results

In this section, the results of standard RC and DVRC are discussed for both constant velocity setpoints and a setpoint with a sinusoidal velocity profile. For comparison, the constant velocity experiments are also performed using a high-order RC [185].

For the nano-motion stage driven by the walking piezo actuator, the repetitive variable α is a rotational angle. The repetitive period equals $P_\alpha = 2\pi$ rad, i.e., one complete cycle of the piezo legs. The delay $z^{-N(\alpha)}$ varies with changing leg velocity, i.e., with varying angular frequency $\dot{\alpha}(t) = 2\pi f_\alpha(t)$.

5.6.1 Constant velocity

The tracking errors of the experiments with standard RC, DVRC and the high-order RC for $\dot{r} = 10$ μm/s are shown in Fig. 5.10. The rms value of the tracking error without RC (top left figure) equals $\text{rms}(e(t)) = 109$ nm. A clear repetitive structure is present in the error, as shown in the zoom plot of Fig. 5.11 by the light grey line.

Standard RC reduces the tracking error to $\text{rms}(e_{RC}) = 18.3$ nm (top right figure in Fig. 5.10). Although the error is reduced significantly, a clear fluctuation in the

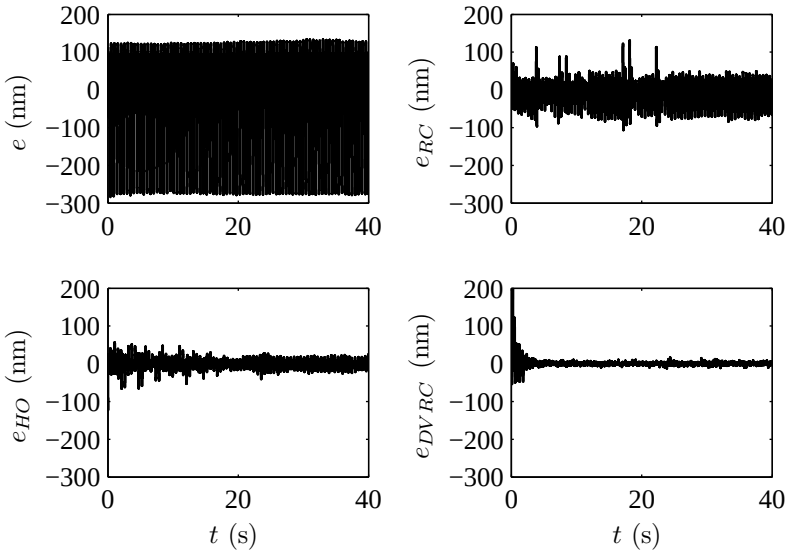

Figure 5.10: Tracking errors of the experiments with $\dot{r} = 10$ μm/s without RC, with RC, with high-order RC and with DVRC.

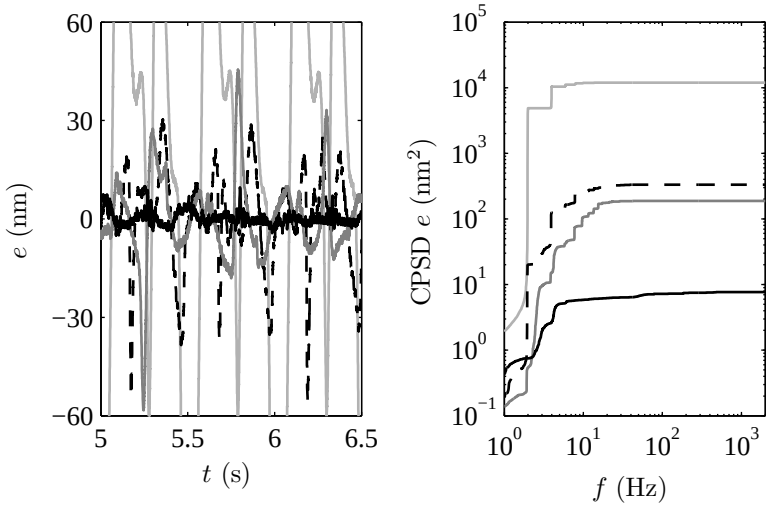

Figure 5.11: Zoom plot and CPSDs of the errors of the experiments of Fig. 5.10 without RC (light grey), with RC (black dashed), with high-order RC (dark grey) and with DVRC (black).

magnitude of the error is visible, which is caused by the fact that the repetitive variable is not time. The zoom plot of Fig. 5.11 shows that the remaining error with RC (black dashed line) still contains a significant repetitive part.

The high-order repetitive controller, shown in the bottom left figure of Fig. 5.10, reduces the tracking error further to $\text{rms}(e_{HO}) = 13.7$ nm. The convergence of the error is clearly visible. However, the second order repetitive controller is not able to completely remove the fluctuation in the error, indicating that it is not able to cope with the amount of variation in the repetitive delay. Increasing the order of the repetitive controller would slightly increase the robustness to the variation, but requires a larger memory buffer to incorporate an additional period.

The tracking error with DVRC, shown in the bottom right figure of Fig. 5.10, significantly reduces the tracking error to $\text{rms}(e_{DVRC}) = 2.77$ nm and has a faster convergence rate. DVRC reduces the tracking error by 97% compared to the tracking error without RC, by 85% compared to standard RC and by 80% compared to the high-order repetitive controller. After convergence no deterministic part is visible anymore in the tracking error as can be seen from the solid black line in Fig. 5.11. Also, the cumulative power spectral densities (CPSDs) of the tracking errors in Fig. 5.11 clearly show the reduction of the tracking error by DVRC with respect to the other RC experiments. For frequencies $f \to \infty$, the CPSDs converge to the squared rms values of the tracking errors.

The rms values of the errors with the different repetitive controllers for constant velocity setpoints $\dot{r} \in [1, 10, 100, 1000]$ μm/s are given in Table 5.1. The range of $N(\alpha_k)$ varies with varying setpoint, i.e., m and M are dependent on the specific setpoint r. However, the robustness filter Q is designed using the worst-case variation for all relevant setpoints to guarantee stability. It can be seen that the errors are significantly reduced by DVRC except for the lowest velocity, for which a deteriorated performance is obtained. At this velocity the repetitive errors are very small and large non-repetitive errors exist. The time-varying delay $N(\alpha(t))$ is more sensitive to the influences of the non-repetitive disturbances, e.g., measurement noise, than the fixed delay of standard RC. At large reference velocities DVRC outperforms high-order RC, but not standard RC. This is caused by the reduction in the cut-off frequency of the Q filter needed to account for the delay variations in DVRC. For large velocities, the repetitive disturbances have a frequency content that is located above the cut-off frequency of the Q filter used for DVRC, resulting in a degraded performance with respect to standard RC. Besides these observations, for velocities in the range of 10 μm/s to 0.1 mm/s the DVRC scheme results in a significant error reduction compared to the experiments without RC, with standard RC and with high-order RC.

Table 5.1: Tracking errors for different constant reference velocities $\dot{r} \in [1, 10, 100, 1000]$ μm/s without RC, with RC, with high-order RC and with DVRC.

velocity	1 μm/s	10 μm/s	0.1 mm/s	1 mm/s
rms(e)	5.1 nm	109.4 nm	192.5 nm	274.8 nm
rms(e_{RC})	5.1 nm	18.3 nm	29.0 nm	54.2 nm
rms(e_{HO})	∞ nm	13.7 nm	20.6 nm	123.4 nm
rms(e_{DVRC})	21.0 nm	2.8 nm	5.3 nm	99.3 nm

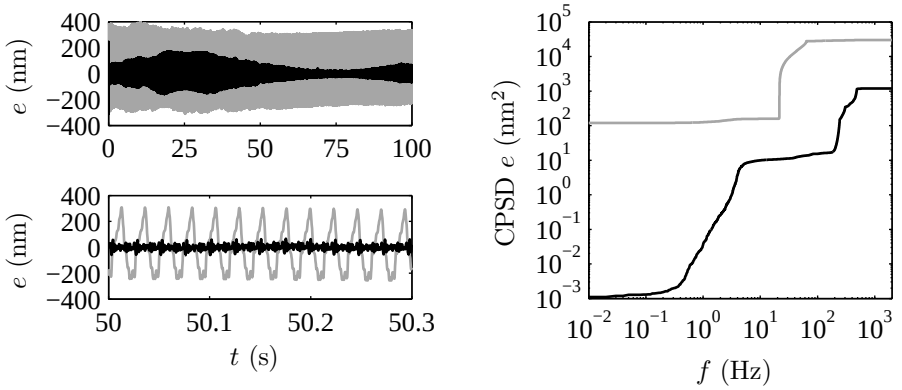

Figure 5.12: Tracking errors and CPSDs of the experiments without (grey) and with DVRC (black) for a varying reference velocity.

5.6.2 Varying velocity

Since the repetitive delay is continuously adjusted in DVRC, it can be used for setpoints that have a varying velocity, i.e., which have an inherent variation in repetitive delay for the walking piezo actuator. For an experiment with a time-varying reference velocity $\dot{r}(t) = 2 \cdot 10^{-4} + 10^{-4} \sin\left(\frac{2\pi}{100} t\right)$ the variation in the repetitive delay equals 124 samples. For this experiment the same Q filter as for the experiments with a constant reference velocity is used. The results of the experiment with the time-varying reference velocity are shown in Fig. 5.12. DVRC clearly reduces the tracking error compared to the experiment with only feedback control. The zoom plot in the bottom axis of Fig. 5.12 shows that with DVRC hardly any repetitive structure is present anymore in the tracking error. Standard RC and high-order RC are not applied since they cannot cope with such fast and large changes in the repetitive delay.

The sinusoidal shape of the tracking error with DVRC in Fig. 5.12 corresponds to the variation in velocity and is larger for higher reference velocities (larger drive frequency f_α) and smaller for low velocities (small f_α). This corresponds to the magnitude of the sensitivity $\bar{S}$ on which the repetitive 'notches' are placed, which has a smaller magnitude for low frequencies (low velocities) and vice versa. The rms values of the errors over the complete experiment equal $\text{rms}(e) = 173.3$ nm and $\text{rms}(e_{DVRC}) = 34.3$ nm, which is a reduction of 80%.

The CPSDs of the error signals without and with DVRC clearly show applicability of DVRC for reference signals with a varying velocity. The variation in the velocity directly results in a variation of the repetitive delay. The CPSDs show that the largest error reduction is obtained by DVRC at low frequencies $f < 5$ Hz, i.e., in the frequency range where the base repetitive frequencies are contained. Furthermore, it can be seen that DVRC reduces the tracking error for all frequencies up to the cut-off frequency of the Q filter, i.e., for $f < 200$ Hz.

5.7 Conclusions

In this chapter, we presented a delay-varying repetitive control (DVRC) method, which is applicable for systems that have a repetitive nature with respect to a repetitive variable other than time. Interestingly, DVRC has the standard repetitive control (RC) scheme as a special case when the repetitive variable is time. DVRC uses knowledge of the repetitive variable of the system to determine and adjust the time-varying repetitive delay accordingly.

Due to the time-varying delay in the RC memory loop, the conventional stability criteria for standard RC are not applicable anymore. After giving a short tutorial on existing stability analysis methods for discrete-time delay systems, we derived a new $\mathcal{H}_\infty$ norm based stability criterion for the proposed DVRC method. This novel stability criterion gives a sufficient condition for stability using the variation in the repetitive delay, while still allowing the design of the learning filters using frequency domain techniques as is common in RC.

The performance of DVRC is compared experimentally to standard RC and high-order RC using a nano-motion stage driven by a walking piezo actuator. The walking movement of the piezo motor has as a repetitive variable the angular orientation of the piezo legs and hence even for constant velocity references a time-varying delay is needed. We showed that the developed DVRC method is able to significantly suppress the periodic disturbances induced by the walking movement of the piezo motor, while we can formally guarantee the stability of the scheme. In addition DVRC reduces the tracking error by 85% compared to

standard RC and by 80% compared to high-order RC.

Since the repetitive delay can be continuously adapted by DVRC, it is also able to cope with references that have a varying velocity, i.e., which have an inherent time-varying repetitive delay. Experimental results show that for these setpoints DVRC also significantly improves the tracking performance.

DVRC can be applied for any repetitive variable as long as it is monotonically increasing (or monotonically decreasing) with respect to time. This condition corresponds in the walking piezo actuator to a continuously increasing (or decreasing) angle of the legs and thus a velocity of the nano-motion system that does not change sign. Future work involves extending the DVRC scheme to allow also non-monotonically increasing repetitive variables, i.e., references with a changing sign of the velocity. However, the derived stability criterion is already applicable in these circumstances.

Part III

The metrological AFM

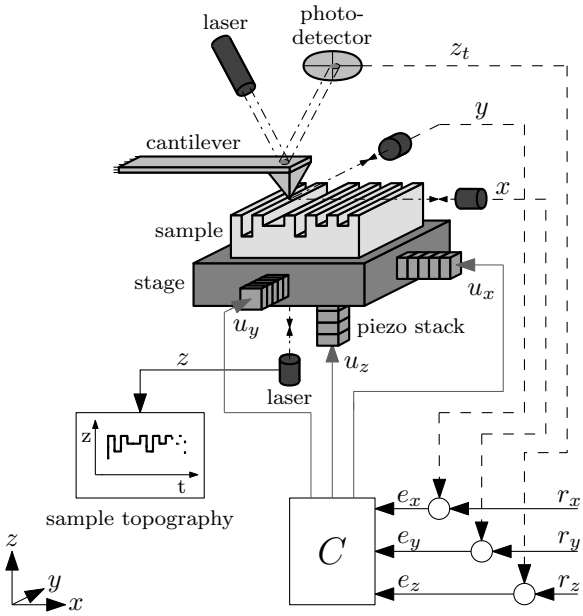

Chapter 6

Identification, control and hysteresis compensation

Abstract - Atomic Force Microscopes (AFMs) are widely used for the investigation of samples at the nanometer scale. The metrological AFM used in this work uses a three degree-of-freedom (DOF) stage driven by piezo stack actuators for sample manipulation in combination with a fixed cantilever. The piezo stack actuators suffer from hysteresis, which acts as a nonlinear disturbance on the system and/or can change the system dynamics. The contributions of this chapter are the application of feedback control to all three DOFs of the metrological AFM and the design and application of a hysteresis feedforward for the asymmetric hysteresis present in the system. The amount of coupling between the DOFs is assessed by a non-parametric MIMO identification. Since the dynamics appear to be decoupled in the frequency range of interest, feedback controllers are designed for each DOF separately. For the modeling of the asymmetric hysteresis an extended Coleman-Hodgdon model is proposed. This model is used for feedforward compensation of the hysteresis. The combination of feedback control for all DOFs and the asymmetric hysteresis feedforward enables the AFM to track scanning profiles within the sensor bound of 5 nm. Real-time imaging of the sample is possible with an accuracy of 2 nm.

This chapter is based on: R.J.E. Merry, M. Uyanik, M.J.G. van de Molengraft, K. R. Koops, M.G.A. van Veghel and M. Steinbuch. Identification, control and hysteresis compensation of a 3 DOF metrological AFM, *Asian Journal of Control*, 11(2):130–143, 2009.

6.1 Introduction

Atomic force microscopes (AFMs) are a specific type of scanning probe microscopes (SPMs) in which the surface of a sample is scanned by an atomically sharp probe. The sample to be investigated can either be moved under the probe (scanning sample mode) or the probe can be moved over the sample (scanning tip mode). The sample causes the cantilever, to which the tip is attached, to deflect. The deflection can be used to obtain the height information of the sample. The atomic force microscope was invented in 1986 by Binning, Quate and Gerber [17] and is widely used for sample imaging, the characterization of materials and the manipulation of particles at nanometer scale [171].

In this chapter, a metrological AFM is considered. The metrological AFM is used to calibrate transfer standards for commercial AFMs. In contrast to commercial AFMs, the accuracy of the measurements is much more important than the scanning speed. Furthermore, the measurements have to be traceable to the standard of length. This imposes different constraints on both the mechanical and control design of the AFM.

In current AFMs, the positioning of the sample under the probe, i.e., the scanning motion in x- and y-direction, is often done using piezoelectric actuators in an open-loop manner [149,176]. Examples of these techniques are $\mathcal{H}_\infty$ based [165,176,189] and model-inverse based [226] feedforward control. However, due to the presence of disturbances in AFMs the performance can benefit from applying feedback control in the scanning directions [171]. Another issue is that the piezoelectric actuators exhibit nonlinear behavior such as hysteresis and creep, which limit the positioning accuracy of the sample. Furthermore, the manipulation of samples in multiple degrees of freedom inherently makes the AFM a multiple-input-multiple-output (MIMO) control system. The increasing interest in AFMs for nano-applications requires a higher precision and therefore an increasing closed-loop bandwidth for disturbance attenuation.

During the last decades a lot of research on the design, operating mode and control of AFMs has been done. The sample manipulation is often performed using tube piezo actuators [40], which can move the sample in three directions using one actuator. The lateral bending of the piezo-tubes results in a large cross coupling to the vertical direction, which distorts the image of the AFM. Tripod scanners employ three piezoelectric stack actuators, one for each translational axis [17]. The path lengths are determined by the length of the stack piezos, resulting in either a small range or in low-frequency mechanical resonances and thus low speeds [171]. Resonant scanners use an oscillating tuning fork as actuator to obtain fast scanning [84]. However, the scan rate is dependent on the resonance frequency of the

tuning fork and cannot be chosen independently. Stages where the piezo-actuators for the various degrees-of-freedom (DOFs) are stacked on top of each other typically have a large moving mass, which results in a low-frequency first resonance and low scanning speed [8]. Rigid scanners combine piezoelectric stack actuators with a flexure mechanism [99,172], which decouples the different axes of motion to a large extent in combination with a high performance. In this chapter, a 3-DOF rigid scanner driven by three piezoelectric stack actuators is used [154].

Probing of the sample surface can be performed in contact or tapping mode. In this chapter we will only consider contact scanning, in which the tip and sample are in contact at all times. The image of the sample is commonly retrieved based on the control effort of the actuator in the imaging z-direction. The deflection of the tip can be controlled either in constant force mode, where the force between the sample and the tip is held constant, or in constant height mode, where the feedback is disabled completely [173]. The constant height mode allows for faster imaging, but the varying force can damage the sample and/or tip. The constant force mode gives a high-resolution, but only at low speed. In this chapter, we use constant force scanning in combination with a scanning sample mode to obtain a fully traceable image of the sample.

SPM stages are mostly designed to minimize coupling between the different DOFs, especially with respect to the imaging z-axis. However, practically always an amount of coupling is present, e.g., due to alignment errors or manufacturing tolerances. In literature, the AFMs are mainly identified and modeled as three separate SISO systems in x-, y- (scanning motion) and z-directions (imaging). For control design purposes the MIMO aspects often assumed to be negligible small [149]. MIMO identification of the scanning motion only is performed for a tube piezoelectric actuator in [40] and for a 2-DOF nano-positioner driven by piezo stack actuators in [176]. The coupling to the imaging z-axis is not taken into account. To assess the coupling, which appears as a performance limiting factor (PLF) in the AFM, a MIMO identification in all three directions is performed and the coupling effects between the various axes are assessed.

The asymmetry in the used 3-DOF rigid scanner results in an asymmetric hysteresis in the system [182]. The hysteresis in the metrological AFM shows an asymmetry between increasing and decreasing voltage paths and different offsets for various voltage ranges. In literature, several models and methods are proposed for asymmetric hysteresis. An extended Preisach model for asymmetric hysteresis requires 80 parameters to be identified [180], which makes it difficult and time consuming to find a general model for the complete operating range. Separate Preisach models for each voltage range are identified in [89]. For the compensation, switches between a large number of models have to be made based on the different parts in the reference trajectory. A Bouc-Wen model, using only 9 parameters, is

identified in [102] using genetic algorithms. However, the model only incorporates asymmetry near zero velocity of the stage. A Bouc-Wen model for symmetric hysteresis is combined to a PI feedback compensation for the asymmetric part in [113], which does not utilize the a-priori knowledge about the asymmetry. A generalized Bouc-Wen model that splits the hysteresis in 6 different parts [182] requires a lot of parameters for the identification and a lot of switches between different models during the compensation. In [50], a Coleman-Hodgdon model is proposed for the modeling and compensation of symmetric hysteresis in a scanning microscope. The model only requires five parameters to be identified. The variations in the offset for various voltage ranges are included in an enhanced Coleman-Hodgdon model in [217]. However, for each voltage range a new model has to be identified. To compensate for the hysteresis PLF, an extended Coleman-Hodgdon model is proposed to incorporate the variations in the offset. Furthermore, different models are identified for increasing and decreasing voltages. For the feedforward compensation, this requires only a switch between two models at standstill of the stage.

The contributions of this chapter are threefold. Firstly, we justify SISO-based controller design for the MIMO AFM system by assessing the amount of coupling between the three axes. Secondly, feedback control is applied to all three DOFs, so also to the scanning motion. Loopshaping techniques have been employed to tune three feedback controllers at bandwidths below which the coupling effects can be neglected. Finally, an extended Coleman-Hodgdon model is proposed to model the asymmetric hysteresis in the system. Using the proposed model, a hysteresis feedforward is designed, which efficiently compensates hysteretic disturbances in the system. The combination of feedback control and hysteresis feedforward control allows the sample to be positioned with a tracking error within the sensor bound of 5 nm.

This chapter is organized as follows. In Section 6.2, the metrological AFM is discussed in more detail. In Section 6.3, MIMO identification is used to assess the amount of coupling between the various axes of the AFM. The extended Coleman-Hodgdon model to describe the asymmetric hysteresis is also discussed in Section 6.3. The design of the feedback and hysteresis feedforward controllers is presented in Section 6.4. The results of the experiments with the metrological AFM are shown in Section 6.5. Finally, conclusions are drawn in Section 6.6.

6.2 The metrological AFM

The metrological AFM, shown in Fig. 6.1, consists of a Topometrix AFM head, a piezo stack driven 3-DOF stage and a ZYGO laser interferometer to measure the stage position in all DOFs. The PI P517.3CL 3-DOF stage [154] is a rigid stage

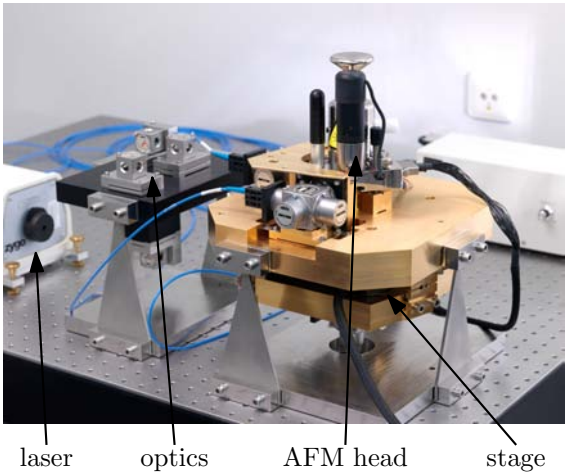

Figure 6.1: Picture of the metrological AFM containing a Topometrix AFM head, a piezo stack driven 3-DOF PI P517.3CL stage and a ZYGO laser interferometer.

containing three piezo stack actuators, which can move the stage through a flexure mechanism in a range of 100 μm in x- and y-directions and in a range of 20 μm in z-direction. The PI 3-DOF stage is designed to minimize the amount of coupling between the different DOFs, especially to the imaging z-axis. Furthermore, in each direction it has an angular deviation of maximum 2 arcsec over the entire range. A mapping as function of the position can be made to correct for this small deviation, thus eliminating the need for a full 6 DOF stage. The mirrors and lasers of the interferometer are aligned such that the laser spots in all DOFs are exactly aligned with the tip of the cantilever. This eliminates Abbe errors, i.e., a change in orientation between the sample and tip of the cantilever does not affect the measurements of the ZYGO laser interferometers. The deflection of the cantilever in the AFM head is measured by an optical sensor consisting of a laser and a photo-detector. The measurement resolution of the ZYGO laser interferometer equals 0.15 nm in all directions. The cantilever deflection can be measured with a resolution of 0.05 nm. The resolution and noise bounds of the different sensors are given in Table 6.1. The noise bound is defined as the measured output range of the sensors when the stage is at standstill and the input to the piezo actuators is decoupled.

A schematic representation of the AFM and the feedback control loop is shown in Fig. 6.2. For clarity the flexure mechanisms between the piezo stack actuators and the stage are not shown. Feedback control is applied in x- and y-directions by steering the piezo stack actuators using the ZYGO position measurements. In

Table 6.1: Resolution and noise bound of the different sensors.

Sensor	Resolution	Noise bound
ZYGO x	0.15 nm	$\pm$5 nm
ZYGO y	0.15 nm	$\pm$4 nm
ZYGO z	0.15 nm	$\pm$2 nm
Head z_t	0.05 nm	$\pm$0.15 nm

z-direction, the tip is controlled in constant force mode while the stage with the sample is moved in 3 DOFs under the cantilever. The setpoint to the cantilever is a constant deflection, which is realized by moving the stage in z-direction. Keeping the deflection of the cantilever constant has the advantage that the orientation of the tip compared to the sample topography remains constant, thus minimizing Abbe errors. Since the tip is controlled to a constant deflection, the laser of the head cannot be used to obtain the sample topography. Instead of using the control effort in z-direction, the height of the sample is measured directly using the ZYGO laser interferometer in z-direction. Since the stage position in x- and y-directions is directly traceable to the standard of length, the image of the sample topography can be constructed using all three ZYGO laser interferometer measurements.

The piezoelectric actuators in the 3-DOF stage suffer from hysteresis, which act as nonlinear disturbances on the system and/or change the system dynamics. Hysteresis can contribute to loss of robustness, performance degradation or instabilities in feedback controlled piezoelectric devices [140]. The measured hysteresis in the system is shown in Fig. 6.3 for separate symmetric scans in x-direction and voltage ranges $V_R \in \{2, 10, 20, 40, 60, 80, 100\}$ V while controlling the stage in y- and z-direction to a constant value.

In Fig. 6.3 can be seen that the level of hysteretic distortion varies depending on the maximum value of the input voltage. Let for each voltage range V_R, the offset ϵ be defined as

$$\epsilon(V_R) = \frac{1}{2}\left(x_M(V_R) - x_m(V_R)\right),$$

where x_M is the maximum position and x_m is the minimum position of the measured response for a given voltage range V_R. For the hysteresis curves of various voltage ranges V_R (Fig. 6.3), the offsets $\epsilon(V_R)$ are not equal. Furthermore, the trace (increasing voltage) and retrace (decreasing voltage) directions of each hysteresis curve are different in shape. For the feedforward compensation of the hysteresis a model that incorporates the voltage range dependent offset $\epsilon(V_R)$ and the non-symmetry between the trace and retrace directions will be derived in Section 6.3.2.

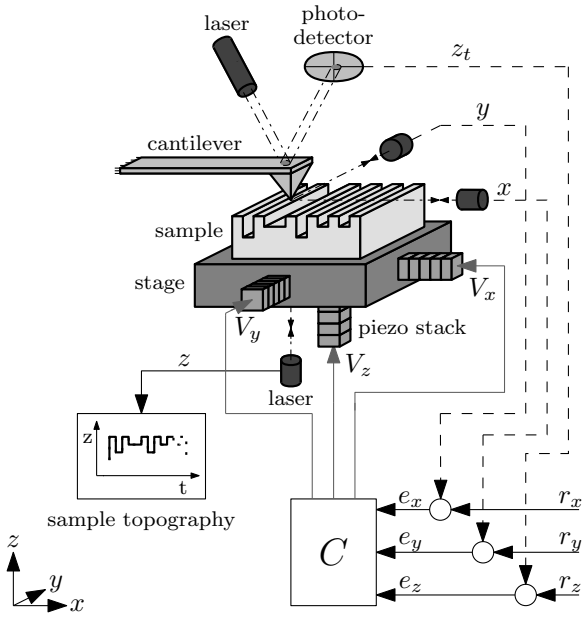

Figure 6.2: Schematic representation of the AFM and the feedback control. Each DOF is driven by a piezo stack actuator, thus minimizing the amount of coupling. The ZYGO laser interferometers are aligned on the cantilever tip to eliminate Abbe errors. The sample topography is measured directly by the interferometer in z-direction.

6.3 Identification

Although ideally the different axes of the 3-DOF stage are decoupled, practically a certain amount of cross coupling will still be present due to alignment errors or parasitic dynamics. In this section, non-parametric MIMO identification of the metrological AFM is performed to assess the amount of coupling between the various DOFs. Furthermore, an extended Coleman-Hodgdon model is proposed to model the asymmetric hysteresis.

6.3.1 MIMO identification

In order to investigate the amount of coupling between the different axes, full non-parametric MIMO identification of the system is performed. The system inputs are the voltages V_i, $i \in \{x, y, z\}$ to the piezo stack actuators and the outputs are the

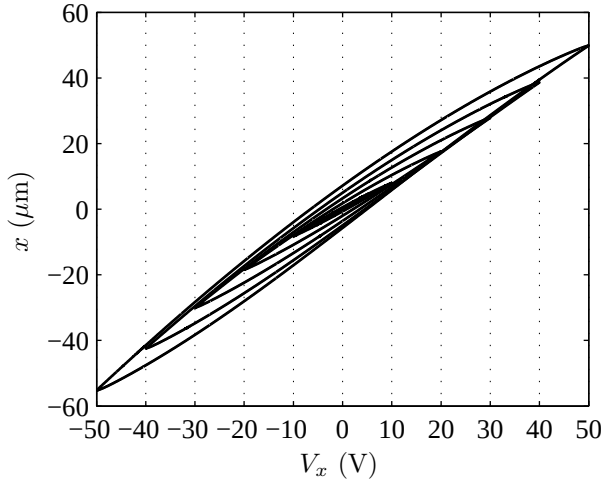

Figure 6.3: Measured hysteresis for various voltage ranges. The hysteresis curves are asymmetric with respect to the trace and retrace direction. The offset of the hysteresis curves is dependent on the voltage range.

position measurements of the ZYGO laser interferometer in x- and y-directions and of the optical sensor in the AFM head in z-direction. The system can be written as

$$P(f) = \begin{bmatrix} P_{xx}(f) & P_{xy}(f) & P_{xz}(f) \\ P_{yx}(f) & P_{yy}(f) & P_{yz}(f) \\ P_{zx}(f) & P_{zy}(f) & P_{zz}(f) \end{bmatrix}, \tag{6.1}$$

where $P_{ji}(f)$ denotes the frequency response function (FRF) from the input V_i in direction i to the output in direction j as a function of the frequency f (Hz) and $i, j \in \{x, y, z\}$.

The different FRFs $P_{ji}(f)$ of (6.1) are determined using the non-parametric open-loop identification method and Welch's averaged periodogram method [116]. On each input independently a zero-mean white noise signal with a variance of $\sigma^2 = 0.05\ \mathrm{V}^2$ is applied while all outputs are measured. The Bode magnitude plots of the different FRFs are shown in Fig. 6.4. The FRFs show a zero slope at low frequencies. At frequencies $f \geq 40$ Hz several resonances can be seen. It can be seen that for frequencies $f < 100$ Hz the magnitude of the off-diagonal FRFs is approximately 40 dB lower than the diagonal FRFs. For frequencies $f \geq 100$ Hz the amplitudes of all FRFs are in the same order of magnitude.

To investigate the amount of coupling between the different axes, the frequency-dependent relative gain array (RGA) [22, 179] of the non-singular square complex

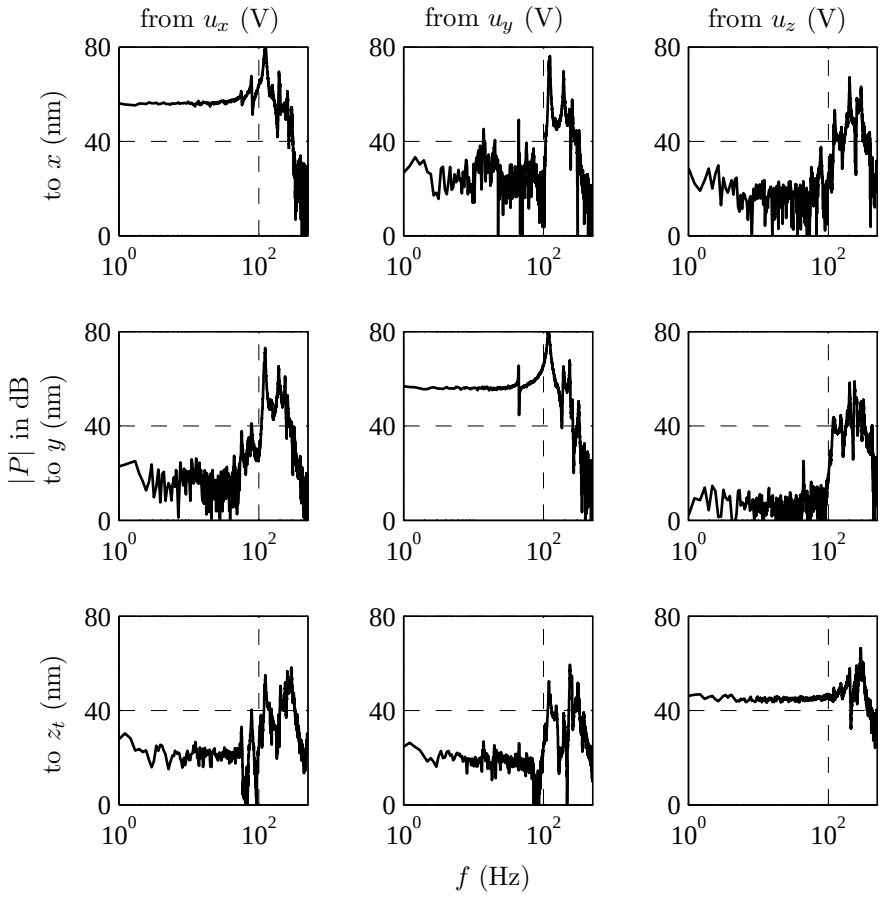

Figure 6.4: Bode magnitude plots of the MIMO system (6.1). Up to the first resonance at ±40 Hz, the FRFs show a zero slope. For frequencies $f < 100$ Hz the magnitude of the off-diagonal terms is ±40 dB lower than the magnitude of the diagonal terms.

matrix $P(f)$ is calculated

$$\mathrm{RGA}(P(f)) = P(f) \times (P(f)^{-1})^T, \tag{6.2}$$

where $\times$ denotes element-wise multiplication. The rows and columns of the RGA sum to one for all frequencies f (Hz). The RGA provides a measure for the amount of interaction between the different axes. If the $\mathrm{RGA}(f) = I$, $\forall f$, perfect decoupling is achieved. The RGA for the FRFs of Fig. 6.4 is shown in Fig. 6.5. It can be seen that for frequencies $f < 100$ Hz, the RGA is almost equal to the identity matrix. Therefore, for the purpose of feedback controller design the axes are assumed to be decoupled for frequencies up to 100 Hz. However, the small amount of coupling for $f < 100$ Hz will still affect the performance of the stage by approximately 1% (40 dB) in an open-loop manner. Possibly, this can even be lower by the virtue of feedback. For frequencies $f \geq 100$ Hz, $\mathrm{RGA}(f) \neq I$ as the axes are clearly coupled in this frequency range. Note that the coupling to the imaging z-axis is still smaller than the coupling between the scanning x- and y-axes.

6.3.2 Hysteresis model

The Coleman-Hodgdon model was formulated in 1986 to describe rate-independent hysteresis in ferromagnetically soft materials [37]. In [50], the Coleman-Hodgdon model is applied successfully to describe the hysteresis in a scanning probe microscope driven by piezo actuators, i.e., the hysteresis between the applied voltage V and the resulting position x. For closed hysteresis loops, the position $x(V)$ can be described as

$$x(V) = \begin{cases} bV - \frac{b-u}{\alpha}\left(1 - \frac{2}{e^{-\alpha V_m} + e^{-\alpha V_M}} e^{-\alpha V}\right), & \text{if } \dot{V} \geq 0, \\ bV + \frac{b-u}{\alpha}\left(1 - \frac{2}{e^{\alpha V_m} + e^{\alpha V_M}} e^{\alpha V}\right), & \text{if } \dot{V} < 0, \end{cases} \tag{6.3}$$

where $\dot{V} = \frac{dV}{dt}$. The parameters b, $\alpha > 0$ and u are the constant parameters to be identified. The linear asymptote of the hysteresis curve has a slope determined by b and a position at 0 V of $\pm\frac{b-u}{\alpha}$ dependent on the scan direction.

The sensitivity of the hysteresis curve, bV in (6.3), is for the metrological AFM of Fig. 6.1 not linear as function of V_R [49]. Expansion of (6.3) with an exponential asymptotic sensitivity gives

$$x(V) = \begin{cases} \left(b - ae^{-cV_R}\right) V - \frac{b-u}{\alpha}\left(1 - \frac{2}{e^{-\alpha V_m} + e^{-\alpha V_M}} e^{-\alpha V}\right), & \text{if } \dot{V} \geq 0, \\ \left(b - ae^{-cV_R}\right) V + \frac{b-u}{\alpha}\left(1 - \frac{2}{e^{\alpha V_m} + e^{\alpha V_M}} e^{\alpha V}\right), & \text{if } \dot{V} < 0, \end{cases}$$

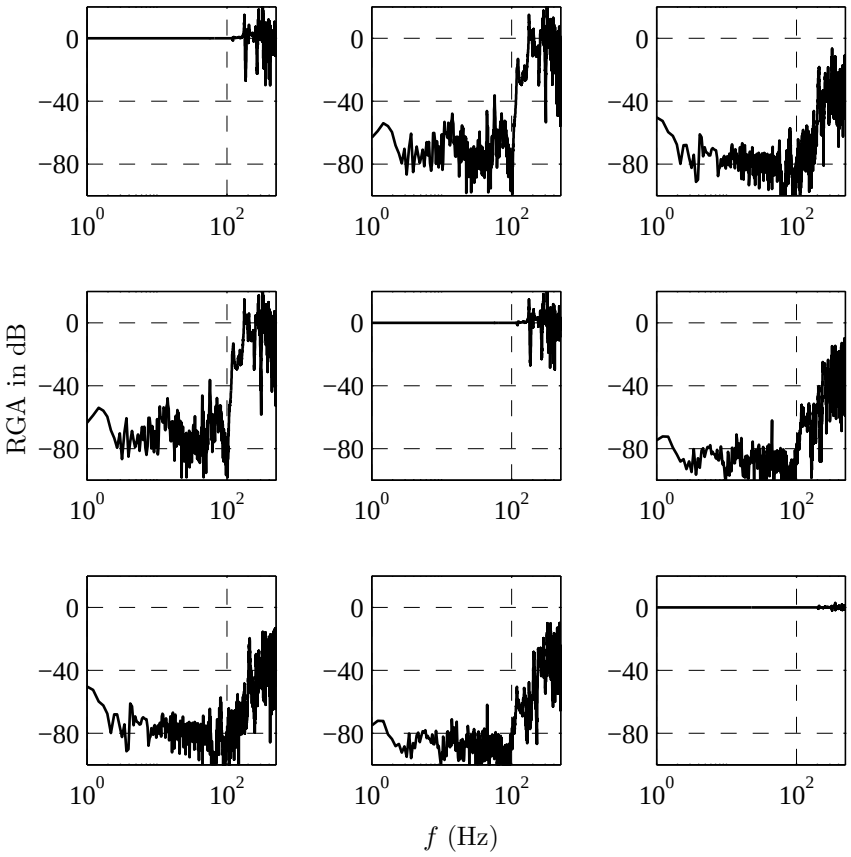

Figure 6.5: RGA (6.2) of the MIMO system (6.1). For frequencies $f < 100$ Hz, the RGA resembles an identity matrix and can be assumed decoupled. For frequencies $f \geq 100$ Hz the axes show a significant amount of coupling.

where the voltage range $V_R = V_M - V_m$ with V_m and V_M the minimum and maximum voltage, respectively. The above model does not incorporate any voltage range dependent offset $\epsilon(V_R)$. Since the hysteresis in the metrological AFM shows an offset that is dependent on the voltage range V_R (see also Fig. 6.3) and because the trace and retrace directions are not symmetrical, we propose an extended Coleman-Hodgdon model as

$$x(V) = \begin{cases} \epsilon_t(V_R) + \left(b_t - a_t e^{-c_t V_R}\right) V - \frac{b_t - u_t}{\alpha_t} \left(1 - \frac{2}{e^{-\alpha_t V_m} + e^{-\alpha_t V_M}} e^{-\alpha_t V}\right), \\ \qquad\qquad\qquad\qquad\qquad\qquad\qquad\qquad \text{if } \dot{V} \geq 0, \\ \epsilon_r(V_R) + \left(b_r - a_r e^{-c_r V_R}\right) V + \frac{b_r - u_r}{\alpha_r} \left(1 - \frac{2}{e^{\alpha_r V_m} + e^{\alpha_r V_M}} e^{\alpha_r V}\right), \\ \qquad\qquad\qquad\qquad\qquad\qquad\qquad\qquad \text{if } \dot{V} < 0, \end{cases} \tag{6.4}$$

where $\epsilon_{t,r}(V_R)$ describes the voltage range dependent offset. The offset as a function of V_R is shown in Fig. 6.6. It can be seen that the offset changes quadratically with the voltage range. Therefore, the functions $\epsilon_{t,r}(V_R)$ are chosen as

$$\epsilon_t(V_R) = d_t V_R^2 + e_t V_R + f_t,$$
$$\epsilon_r(V_R) = d_r V_R^2 + e_r V_R + f_r.$$

The identification of the model parameters $\{a, b, c, u, \alpha, d, e, f\}_{t,r}$ is done by means of an optimization over the measured first-order reversal hysteresis curves for various voltage ranges $V_R \in \{2, 10, 30, 40, 60, 80, 100\}$ V. The optimization is performed using a nonlinear least-squares data-fitting method, because the model described by (6.4) is highly nonlinear. The initial parameters are chosen based on an explorative measurement in combination with the findings from [49]. For the trace direction x_t ($\dot{V} \geq 0$) and the retrace direction x_r ($\dot{V} < 0$), different models are identified of which the parameters are given in Table 6.2.

In Fig. 6.7 the errors between the measured and modeled hysteresis are shown for various voltage ranges V_R. By comparing the hysteresis curves of Fig. 6.3 to the errors of Fig. 6.7, it can be seen that the model accurately describes the asymmetric hysteresis of the system. The model described by (6.4) with the trace/retrace parameters of Table 6.2 describes the hysteresis in the metrological AFM of all voltage ranges with an accuracy of 97%. This model will be used for the feedforward compensation, discussed in the next section.

6.4 Controller design

Based on the RGA of Fig. 6.5, for controller design purposes the axes of the metrological AFM are assumed decoupled for frequencies $f < 100$ Hz. Using the

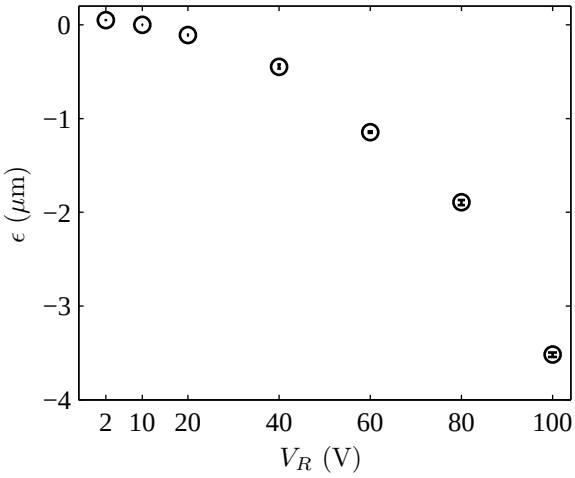

Figure 6.6: Offset hysteresis curves versus voltage range. The offset changes quadratically with the voltage range.

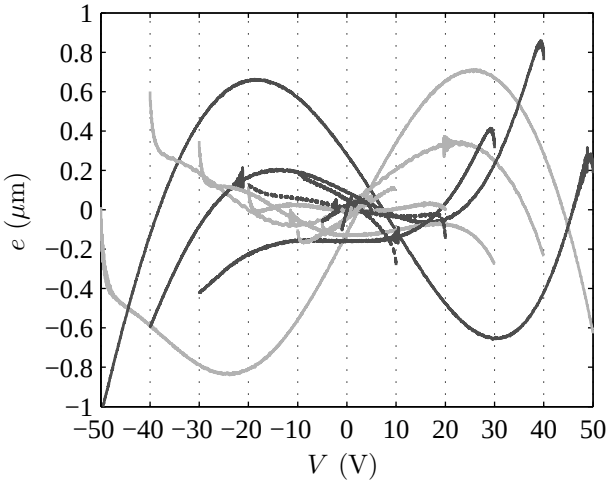

Figure 6.7: Errors between the modeled and measured hysteresis of the trace (light grey) and retrace (dark grey) directions for various voltage ranges. Comparing the errors to the hysteresis curves of Fig. 6.3, it can be concluded that the model accurately describes the hysteresis of all voltage ranges.

Table 6.2: The identified parameters of the extended Coleman-Hodgdon model for both the trace and retrace directions.

Parameter	Value trace x_t	Value retrace x_r
a (μm/V)	$2.6570{\cdot}10^{-1}$	$3.0892{\cdot}10^{-1}$
c (V^{-1})	$2.3318{\cdot}10^{-2}$	$9.2649{\cdot}10^{-2}$
b (μm/V)	1.1530	1.3555
u (μm/V)	$9.4970{\cdot}10^{-1}$	$8.7338{\cdot}10^{-1}$
α (V^{-1})	$5.5306{\cdot}10^{-2}$	$2.5985{\cdot}10^{-2}$
d (μm/V)	$-2.9444{\cdot}10^{-4}$	$-3.0051{\cdot}10^{-4}$
e (μm/V)	$-2.8998{\cdot}10^{-3}$	$-1.4058{\cdot}10^{-3}$
f (μm)	$6.2200{\cdot}10^{-2}$	$8.4353{\cdot}10^{-2}$

measured FRFs of Fig. 6.4, three SISO controllers are designed using loopshaping techniques, all resulting in bandwidth frequencies $f_{BW} < 100$ Hz, i.e., where no coupling is present. Here, we use the definition bandwidth f_{BW} as the cross-over frequency of each diagonal loop gain $L_{ji}(f) = P_{ji}(f)C_{ji}(f),\ i = j,\ i,j \in \{x,y,z\}$.

Moreover, for the x- and y-axes, position and hysteresis feedforward controllers are designed and applied separately. The performance of the hysteresis feedforward will be compared to the position feedforward in Section 6.5.2.

6.4.1 Feedback

Using the FRFs of the diagonal elements of (6.1), stabilizing feedback controllers $C_{ji},\ i = j,\ i,j \in \{x,y,z\}$ are designed such that the modulus margin $\|S_{ji}(f)\|_\infty = \max_f |S_{ji}(f)| < 6$ dB, or

$$|S_{ji}(f)| = \left| \frac{1}{1 + P_{ji}(f)C_{ji}(f)} \right| \leq 6 \text{ dB}, \quad \forall f.$$

This corresponds to a phase margin $\phi \geq 30$ deg and an amplitude margin $A \geq 6$ dB. The controllers consist of an integrating action and a low-pass filter as

$$C_{ji}(s) = k \underbrace{\frac{1}{s}}_{\text{integrator}} \underbrace{\frac{2\pi f_{LP}}{s + 2\pi f_{LP}}}_{\text{low-pass}}, \tag{6.5}$$

where k denotes the controller gain and f_{LP} (Hz) the cut-off frequency of the low-pass filter. In Table 6.3, the controller parameters, the resulting bandwidths f_{BW}

Table 6.3: The controller parameters and the resulting bandwidth, phase margin and amplitude margin for the different axes.

Axis	k	f_{LP} (Hz)	f_{BW} (Hz)	$\|S\|_\infty$ in dB
x	0.07790	50	7.87	3.635
y	0.07790	50	8.03	4.052
z	0.1198	100	45.6	4.939

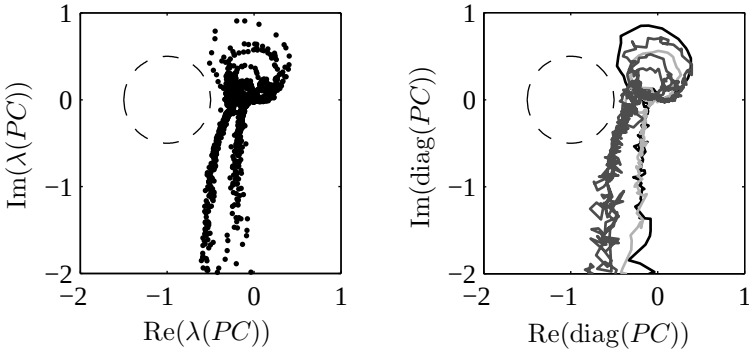

Figure 6.8: Characteristic loci $\lambda(P(f)C(f))$ (left part) and Nyquist plots of the separate diagonal loop gains (right part) in x-direction (black), y-direction (dark grey) and z-direction (light grey). The characteristic loci show that the SISO controlled MIMO system has a good phase margin and is stable. The resemblance between the two figures indicates that the axes are almost decoupled.

and the modulus margin $\|S\|_\infty$ for the different axes are shown. The margins are chosen somewhat higher to be robust against shifts in the resonance frequencies due to the nonlinearities in the piezo stack actuators [176].

The characteristic loci $\lambda(PC)$ [179] of the SISO controlled MIMO system are shown in the left part of Fig. 6.8. The characteristic loci show that the controlled MIMO system has a good MIMO phase margin. The Nyquist plots of the separate diagonal loop gains, depicted in the right part of Fig. 6.8, almost coincide with the characteristic loci, i.e., $\lambda(PC) \approx \lambda(\text{diag}(PC))$. This again indicates that the different axes are almost decoupled. Furthermore, Fig. 6.8 shows that the diagonal loop gains are stable and do not enter the circle with radius 0.5 centered at (Re,Im)=(-1,0), indicating that $\|S(f)\|_\infty < 6$ dB.

6.4.2 Hysteresis feedforward

The extended Coleman-Hodgdon model of (6.4) describes the position x as function of the applied voltage V. In order to use the model for a feedforward hysteresis compensation, expressions of the voltage as function of the position are required. These expressions equal

$$V(x) = \begin{cases} \frac{x-p_{4,t}}{p_{1,t}} - \frac{1}{p_{3,t}} \mathrm{L_W}\left(\frac{p_{2,t}p_{3,t}}{p_{1,t}}\, e^{\frac{p_{3,t}(x-p_{4,t})}{p_{1,t}}} \right), & \text{if } \dot{x} \geq 0 \\ \frac{x-p_{4,r}}{p_{1,r}} - \frac{1}{p_{3,r}} \mathrm{L_W}\left(\frac{p_{2,r}p_{3,r}}{p_{1,r}}\, e^{\frac{p_{3,r}(x-p_{4,r})}{p_{1,r}}} \right), & \text{if } \dot{x} < 0, \end{cases} \tag{6.6}$$

where $\mathrm{L_W}$ denotes the LambertW function, which is the inverse of the function of $z(W) = We^W$, and

$$\begin{aligned} p_{1,t} &= b_t - a_t e^{-c_t V_R}, & p_{1,r} &= b_r - a_r e^{-c_r V_R}, \\ p_{2,t} &= \tfrac{2(b_t-u_t)}{\alpha_t(e^{-\alpha_t V_m}+e^{-\alpha_t V_M})}, & p_{2,r} &= \tfrac{2(b_r-u_r)}{\alpha_r(e^{\alpha_r V_m}+e^{\alpha_r V_M})}, \\ p_{3,t} &= -\alpha_t, & p_{3,r} &= \alpha_r, \\ p_{4,t} &= -\tfrac{b_t-u_t}{\alpha_t} + d_t V_R^2 + e_t V_R + f_t, & p_{4,r} &= \tfrac{b_r-u_r}{\alpha_r} + d_r V_R^2 + e_r V_R + f_r. \end{aligned}$$

Eq. (6.6) describes the required voltage as a function of the position x. If the input of (6.6) is chosen to be the reference position of the control loop r_x, the model can be used for feedforward control purposes. The model parameters of Table 6.2 are identified for the x-direction of the metrological AFM. For the other axes, model parameters can be obtained in an analogous manner.

Since the hysteresis is asymmetric with respect to the trace and retrace direction, the hysteresis feedforward consists of two parts, one for each direction. The switch between the two parts $V_t(r_x)$ and $V_t(r_x)$ depends on the direction of the reference position, i.e., on the sign of the reference velocity. For increasing reference position r_x ($\dot{r}_x \geq 0$) the feedforward of the trace part $V_t(r_x)$ is used and for decreasing reference position r_x ($\dot{r}_x < 0$) the retrace hysteresis feedforward part $V_r(r_x)$ is used. The switch between the two hysteresis feedforward models is performed at standstill of the stage, i.e., outside the imaging region. A schematic overview of the implementation of the hysteresis feedforward for the x-axis is shown in Fig. 6.9.

6.5 Results

In this section, the results of the experiments on the metrological AFM are discussed. Scanning experiments are performed in x-direction. The y-direction is controlled to a constant position.

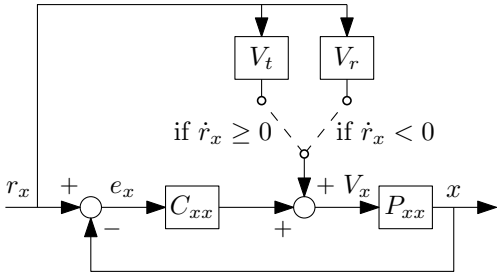

Figure 6.9: Schematic representation of the hysteresis feedforward implementation. At the turnaround points where $\dot{r}_x = 0$, the hysteresis feedforward switches between the trace (V_t) and retrace (V_r) hysteresis feedforward or vice versa.

6.5.1 Hysteresis

The hysteresis feedforward of Section 6.4.2 is first tested in an open-loop experiment. The reference trajectory is a forward and backward scan in x-direction over a range of ± 18 μm. The resulting voltage of the hysteresis feedforward, described by (6.6), is applied to the piezo stack actuator in x-direction. The reference position r_x, the stage position in x-direction and the input voltage V are shown in Fig. 6.10. The resulting voltage of the feedforward (6.6) also has an offset and asymmetry in order to obtain the desired symmetric stage movement. The discontinuity at the turnaround point in the reference also results in a discontinuity in the hysteresis compensation due to the switching between the two models. This results in ringing of the positioning error. However, the ringing only occurs in a short time-span after the turn-around point, i.e., outside the imaging region. The stage position x closely matches the reference position r_x, with a maximum absolute error $\max(|e_x|) = \max(|r_x - x|) = 0.2941$ μm.

6.5.2 Scanning motion

In Fig. 6.11, the results of a closed-loop experiment for a scan in x-direction over ± 18 μm with a speed of 7.2 μm/s are shown. The use of only feedback control results in a tracking error of $\max(|e_x|) = 160.9$ nm, as can be seen with the light-grey line in Fig. 6.11.

Since the piezo stack actuators act as position actuators, a position feedforward can be used to improve the performance of the stage [129]. The control input of the position feedforward can be added to the output of the feedback controllers

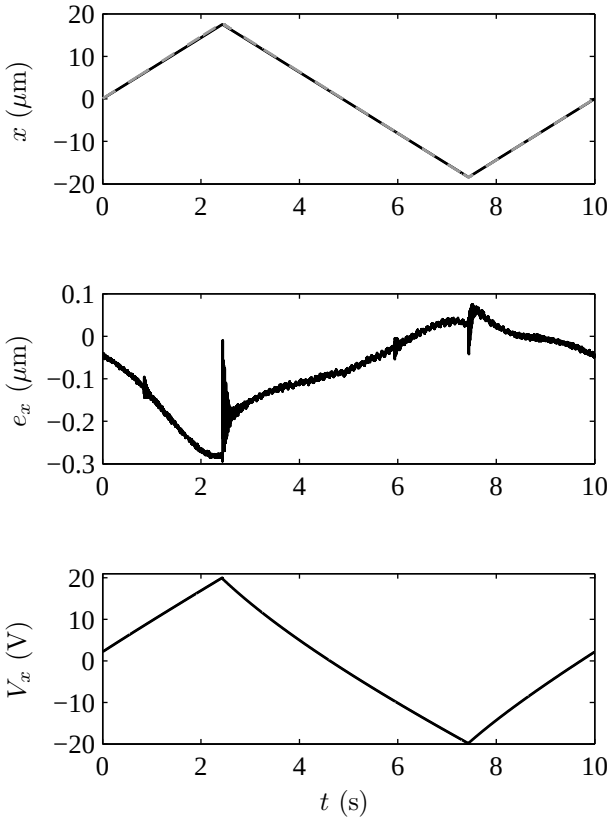

Figure 6.10: Results of the open-loop hysteresis experiment, reference (black) and measured position (grey, dashed), error and voltage resulting from the model. The stage position in x-direction resembles the reference position r_x closely. The ringing of the error at the turnaround points is caused by the discontinuity of the hysteresis feedforward due to the switch between models.

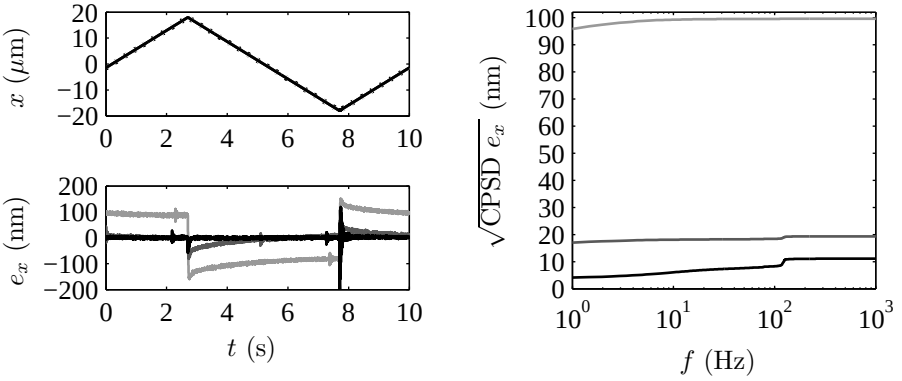

Figure 6.11: Measured positions, tracking errors and square root of the cumulative PSDs of the tracking errors in x-direction for the closed-loop experiments, reference (dotted), without feedforward (light-grey), with position feedforward (dark-grey) and with the hysteresis feedforward (black). The hysteresis feedforward improves the tracking performance with 89% compared to the feedback only case and with 43% compared to the feedback with position feedforward case.

$V_i,\ i \in \{x, y\}$, resulting in a new input to the system V_i^* as

$$V_i^*(t) = V_i(t) + K_i r_i(T),\ i \in \{x, y\}, \tag{6.7}$$

where r is the reference signal and K the feedforward gain. The results for a closed-loop experiment with a position feedforward $K_x = K_y = 11$ V/μm are shown in Fig. 6.11 with the dark grey line. The position feedforward largely reduces the tracking error to $\max(|e_x|) = 86.11$ nm.

The results of the experiment with feedback control and the hysteresis feedforward of Section 6.4.2 are shown in Fig. 6.11 by the black line. Compared to the position feedforward the hysteresis feedforward reduces the tracking error even further. The ringing of the input voltage due to the discontinuity by the switching of the hysteresis feedforward at the turnaround point results in a ringing of the tracking error. At these points, the feedback controller reduces the tracking error very quickly to the noise bound of ±5 nm.

The right part of Fig. 6.11 shows the square root of the cumulative power spectral densities (CPSDs) of the tracking errors for the various experiments. For frequencies $f \to \infty$, the cumulatieve PSDs converge to the squared root-mean-square (rms) value of the respective errors. The rms values of the errors are for the experiment without feedforward $\text{rms}(e_{\text{no FF}}) = 99.57$ nm, with the position feedforward $\text{rms}(e_{\text{pos FF}}) = 19.34$ nm and with the hysteresis feedforward $\text{rms}(e_{\text{hyst FF}}) = 11.08$ nm. The hysteresis feedforward added to the feedback

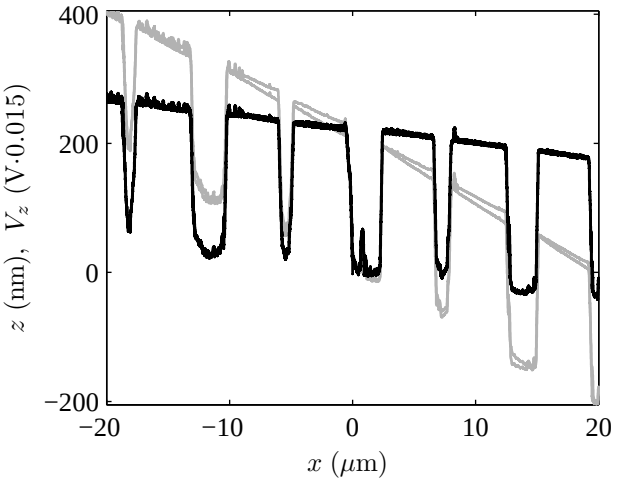

Figure 6.12: Measured topography of the sample with the ZYGO laser interferometer (black) and constructed topography using the control effort in z-direction (grey). Misalignment and calibration issues cause the reconstructed topography to show an additional global slope. Also, the reconstructed topography shows a difference between the trace and retrace direction, which is not present in the direct topography measurement.

controller improves the tracking performance compared to using only the feedback control case with 89% and compared to the case with feedback control and position feedforward with 43%.

The sample topography, measured by the ZYGO laser interferometer in z-direction, is shown as a function of the x-position in Fig. 6.12. Since a triangular shaped reference in x-direction is used, the topography of Fig. 6.12 contains the measured height of the sample for the scan in both positive and negative x-direction. No large deviations in the measured height between the two directions can be seen. The measured topography shows a decaying height in x-direction, indicating that the sample is tilted under the AFM. Since the output of the ZYGO laser interferometer is used instead of the control effort in z-direction as is done in most literature, the height of the sample is directly measurable and traceable to the standard of length.

The reconstructed topography using the control effort in z-direction, shown in Fig. 6.12 by the grey line, clearly shows a global slope difference between the measured height by the ZYGO laser and the constructed height. This difference is likely to be caused by misalignments between the piezo stack actuator and the

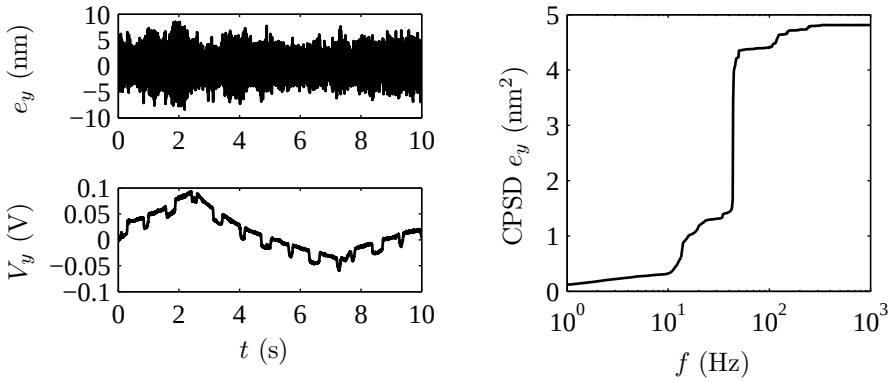

Figure 6.13: Tracking error (top left), control effort (bottom left) and CPSD (right) in y-direction. A clear correlation between the control effort in y-direction and the sample topography of Fig. 6.12 can be seen, indicating a coupling between the axes.

ZYGO laser interferometer in z-direction and by the fact that the piezo stack actuator is not calibrated. Furthermore, a clear distinction can be made between the reconstructed height in positive and negative x-direction as two lines are visible. The control effort in z-direction also contains influences of the hysteresis and creep of the piezo stack actuators and the small amount of coupling between the different DOFs. This causes the errors in the constructed topography image. Further postprocessing of the data in combination with an accurate system model is required to better reconstruct the sample topography from the control effort in z-direction.

During the experiment, the y-axis is controlled to a fixed position. The tracking error in y-direction is shown in Fig. 6.13 together with the control effort. The shape of the control effort of Fig. 6.13 clearly shows a correlation with the sample topography of Fig. 6.12 and the triangular scanning movement in x-direction. Based on the FRF of the system (see Fig. 6.4) a coupling of 1% between the axes was expected for frequencies $f < 100$ Hz. The CPSD of e_y (right figure in Fig. 6.13) converges for $f \to \infty$ to 4.83 nm, so $\text{rms}(e_y) = 2.20$ nm.

6.5.3 Scanning speed

The tracking errors are dependent on the scanning speed. Real-time imaging of the sample is only possible if the scanning movement is controlled within the sensor noise bound during the imaging periods, except for the turning points where no

Table 6.4: Root-mean-square (rms) values of the tracking errors over the complete scanning movement for varying reference speeds.

Speed (μm/s)	3.6	7.2	14.4	28.8
rms($\lvert e_x(t)\rvert$) (nm)	7.317	11.08	14.38	23.28

image is made. The rms values of the tracking errors for experiments with feedback and hysteresis feedforward control are shown in Table 6.4 for various scans speeds. The error increases with increasing scanning speed.

In order to increase the scanning speed, the tracking errors have to be reduced. One possible solution is the increase of the bandwidth of the system. However, this would require MIMO control since decoupling of the axes is no longer guaranteed when increasing the bandwidth f_{BW} much further (Fig. 6.5).

6.6 Conclusions

Using a full non-parametric MIMO model of the system, the coupling between the different axes has been investigated using the frequency dependent relative gain array (RGA). The RGA shows that for feedback controller design the axes can be considered to be decoupled up to a frequency of 100 Hz.

For all DOFs separately, feedback controllers are designed using loopshaping techniques, resulting in bandwidth frequencies below which the coupling effects may be disregarded for the feedback control design. The characteristic loci show that the SISO controlled MIMO system has a good MIMO phase margin.

An extended Coleman-Hodgdon model containing a scan range dependent offset has been identified in x-direction for the trace and retrace directions separately to account for the asymmetry in the hysteresis. The generic extended model describes the hysteresis with an accuracy of 97%. Similar models can be identified for the other axes.

A hysteresis feedforward has been made using two different extended Coleman-Hodgdon models, one for the trace and one for the retrace direction. The switch between the models is done at standstill of the stage. The application of the hysteresis feedforward improves the tracking performance by 89% compared to using only feedback control and by 43% compared to using feedback control and a position feedforward.

With the presented control method, the AFM can perform scanning movements with a velocity up to 3.6 μm/s and a tracking error within the sensor bound of ± 5 nm. A separate laser is used to measure the sample topography directly through the stage movement in vertical direction. Sample images are obtained with a sensor bound of 2 nm.

Although for controller design purposes the system is assumed decoupled for frequencies $f < 100$ Hz, still 1% coupling is present in the performance. Furthermore, the position measurements of the stage in all DOFs suffer from disturbances, which deteriorate the achievable performance of the AFM. In future research, MIMO control methods will be employed to further increase the bandwidth and with this the achievable scanning speed and to account for the disturbances acting on the MIMO system.

Reduction of the discontinuity of the hysteresis feedforward at the switching instances is also subject of further research. Reduction of the discontinuity is expected to result in a reduction of the ringing in the input voltage and an improved positioning accuracy.

Chapter 7

MIMO and repetitive control

Abstract - Atomic force microscopes (AFMs) are used for sample imaging and characterization at nanometer scale. In this work, we consider a metrological AFM, which is used for the calibration of transfer standards for commercial AFMs. The metrological AFM uses a three degree-of-freedom (DOF) stage to move the sample with respect to the probe of the AFM. In this chapter, a MIMO controller is designed for the three DOFs simultaneously, i.e., for the scanning and imaging axes. Despite the small amount of coupling, it is shown that a better disturbance suppression and decoupling can be obtained with the MIMO controller in comparison with a high-gain decentralized controller. The triangular scanning movement and the repetitive sample topography introduce repetitive disturbances in the system. To suppress these disturbances, repetitive control (RC) is applied to the imaging axis. A rotated sample orientation with respect to the actuation axes introduces a non-repetitiveness in the originally fully repetitive errors and yields a deteriorated performance of RC. Directional repetitive control is introduced to align the axes of the scanning movement with the sample orientation under the microscope. Experiments show that the proposed directional repetitive controller significantly reduces the tracking error as compared to standard repetitive control.

This chapter is based on: R.J.E. Merry, M.J.C. Ronde, M.J.G. van de Molengraft, K. R. Koops and M. Steinbuch. MIMO $\mathcal{H}_\infty$ and directional repetitive control of a metrological AFM. Submitted, 2009.

7.1 Introduction

Atomic force microscopes (AFMs) are widely used for the investigation of samples at sub-nanometer resolution. The AFM, invented in 1986 by Binning, Quate and Gerber [17], uses an atomically sharp probe to scan the surface of a sample under the microscope. Applications include the imaging of (biological) samples [166,173, 174], characterization of materials [2] and nano fabrication [47].

In this chapter, we consider a metrological AFM (see Fig. 7.1), which employs a piezo stack driven three degree-of-freedom (DOF) stage. The metrological AFM is used for the calibration of transfer samples for commercial AFMs. For calibration purposes, accuracy of the measurements is more important than the scanning speed. However, to limit the influence of changing operating conditions (e.g., temperature, humidity, drift) to the measurement uncertainty, the scan time should be limited, i.e., a higher scan speed is required.

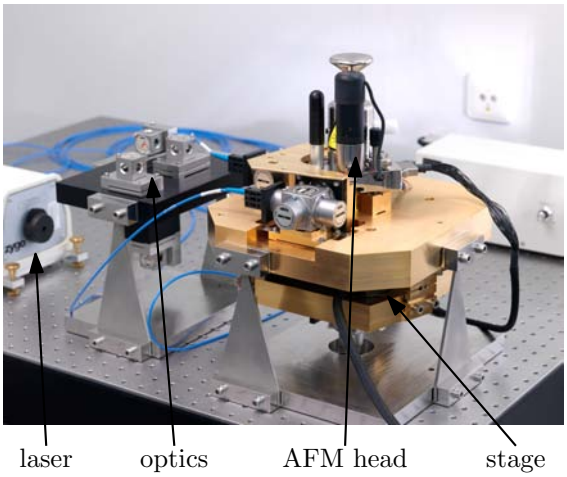

Figure 7.1: The metrological AFM.

In Chapter 6, we applied decentralized control on all three DOFs of the metrological AFM combined with a hysteresis feedforward. The experimental results clearly illustrated the coupling effects between the different axes and the repetitive nature of the disturbances introduced by the repetitive sample topography of the transfer standards and the scanning movement. Both the coupling and the repetitive disturbances appear as the next performance limiting factors (PLFs) in this application. Hence, to further increase the performance of the metrological AFM, we focus in this chapter on (1) the application of a MIMO controller to

account for the coupling effects that are present in the stage and (2) on the application of repetitive control to suppress the repetitive disturbances introduced by the repeating scanning movement and the repetitive structure of the sample.

In many AFMs the sample positioning is currently done in an open-loop manner, whereas some AFMs use sensors for the sample positioning in feedback [149, 176]. Operation of AFMs in constant height mode requires no feedback control. Feedback control can be applied to the imaging direction when the AFM is operated in constant force mode or dynamical tapping mode, which can improve the imaging results [173].

In literature, MIMO controllers are not commonly used for AFMs [26]. MIMO identification of a piezo stack driven 2-DOF nano-positioner is combined with SISO control in [176]. A 3-DOF parallel kinematics nano-positioner with three actuators oriented at a 120 deg angle is controlled in [51] using MIMO techniques without considering the possibility of geometric decoupling. AFMs that use piezo tube scanners inherently have a coupling between the different axes [171]. Although, MIMO identification of these scanners has been performed in [40], the coupling terms are not incorporated in the control design, resulting in separate SISO control loops. In this chapter, we perform a MIMO identification and controller synthesis for a metrological AFM driven by a 3-DOF piezo stack driven stage. The control design includes the scanning x- and y-directions as well as the imaging z-direction.

For the second PLF, being the repetitive disturbances, data-based learning control techniques have been applied in literature to AFMs and piezo scanners. In [195], inversion based iterative learning control (ILC) is applied to compensate for the dynamic coupling from the scanning x-, y-axes to the imaging z-axis in a piezo tube scanner. The hysteresis effects in the piezo scanners of AFMs are compensated using ILC in [11, 105, 214]. In the imaging z-direction, a 1-scan delay feedforward controller can be used to improve the performance under the assumption that two adjacent scan lines are quire similar [26, 174, 175]. The same assumption is made for the application of ILC to the imaging z-direction in [215]. Although the performance is improved by ILC, still a repetitive component is clearly visible in the remaining tracking error. Furthermore, ILC assumes identical initial conditions at the beginning of each iteration, which is not the case for continuous scanning movements. For this purpose, we use repetitive control (RC) in this chapter to suppress the repetitive disturbances of the scanning movement and the sample topography of the transfer standards.

To the authors best knowledge, RC has not yet been applied to the scanning and/or imaging directions in an AFM. Although both ILC and RC are based on similar ideas, the design and application are clearly different. ILC requires identical initial conditions every iteration and is an inherent feedforward technique, whereas the

equal initial conditions are not required for RC, which acts in feedback and can thus affect the time domain stability. Sometimes it is wrongfully posed that RC is not implementable in real-time [51]. In this chapter, we show the real-time applicability of RC to the imaging axis of the metrological AFM. An extension of the general RC method is proposed, in which the reference and controller axes are aligned with the orientation of the sample topography under the AFM.

In this chapter, we design a MIMO controller for all three DOFs of the metrological AFM. The performance of the MIMO controller is experimentally compared to a high-gain decentralized controller with an equal cross-over frequency of the diagonal loop gains. Although the amount of coupling between the axes is small, the MIMO controller can reduce the amount of coupling even further, thus improving the accuracy of the AFM. Furthermore, we a apply RC to the imaging axis of the AFM. Since the sample orientation is generally not perfectly aligned with the scanning axes, we propose an adjusted RC scheme, called directional repetitive control (DRC). In DRC, the scanning axes are rotated to correspond with the orientation of the sample under the metrological AFM. Experiments show the performance improvement of DRC in comparison with standard RC for the imaging z-axis.

This chapter is organized as follows. The metrological AFM and its control architecture will be discussed in Section 7.2 together with the model identification. In Section 7.3, the decentralized and MIMO control designs and the corresponding stability assessments will be treated, as well as the comparison of the two controllers. DRC will be presented in Section 7.4. The results of the experiments with the decentralized and MIMO controllers and of the experiments with DRC are contained in Section 7.5. Finally, conclusions are drawn in Section 7.6.

7.2 The metrological AFM

The metrological AFM, shown in Fig. 7.1, consists of a Topometrix AFM head, a 3-DOF stage and a ZYGO laser interferometer to measure the stage position in all DOFs. The 3-DOF stage is driven by piezo stack actuators through a flexure mechanism in a range of 100 μm in the scanning x, y-directions and in a range of 20 μm in the imaging z-direction. The mirrors on the AFM, the optics and the laser of the interferometer are aligned such that the laser spots in all DOFs intersect at the tip of the cantilever, thus minimizing Abbe errors [170]. The deflection of the cantilever in the AFM head is measured by an optical sensor, consisting of a laser and photo-detector. The measurements of the ZYGO laser interferometer in all DOFs are traceable to the standard of length. The resolution and root-mean-square (rms) values of the standstill noise with decoupled piezo actuators are given for all sensors in Table 7.1.

Table 7.1: Resolution and rms values of the noise for the different sensors.

Sensor	Resolution	Noise rms value
ZYGO x	0.15 nm	3.56 nm
ZYGO y	0.15 nm	3.06 nm
ZYGO z	0.15 nm	1.25 nm
Head z_t	0.05 nm	0.14 nm

7.2.1 Control architecture

A schematic representation of the metrological AFM and the feedback control architecture is shown in Fig. 7.2. For clarity, the flexure mechanism is omitted. For the application of feedback control, the inputs of the system are the voltages $u_i,\ i \in \{x, y, z\}$ to the piezo stack actuators in all DOFs. The outputs of the system are the measurements of the ZYGO laser interferometers in the scanning x, y-directions in nanometers and the output of the optical sensor z_t of the AFM head in the imaging z-direction in Volts. The output z_t can be translated to nanometers using the sensitivity of the cantilever and the optical sensor as $1\ V \equiv 20.83$ nm. For the application of feedback control to the imaging z-axis, the output does not have to be converted to nm, but can be directly used.

The tip of the cantilever is controlled in constant force mode while the stages moves the sample with respect to the cantilever in all three DOFs. The setpoint of the cantilever is a constant deflection, which is realized by moving the stage in z-direction while moving the sample with respect to the cantilever. In this way the orientation of the tip compared to the sample topography remains constant, thus minimizing Abbe errors.

The output of the ZYGO laser interferometer in z-direction is not used for feedback control, but to measure the height of the sample directly. Using the measurements of the ZYGO laser interferometer in all three DOFs, a fully traceable image of the sample topography can be constructed.

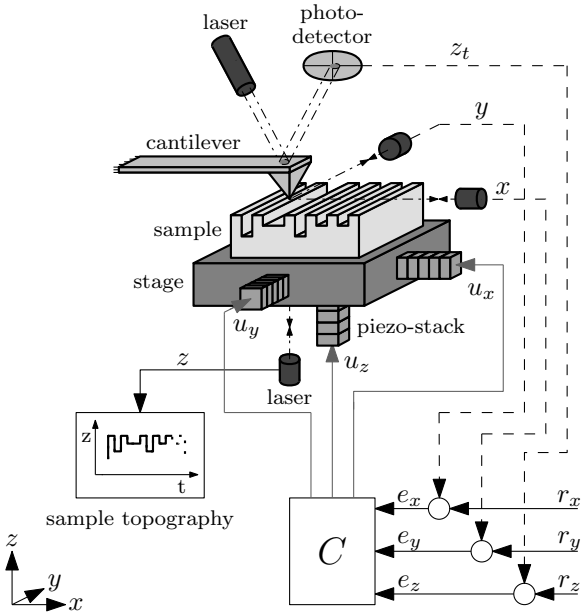

Figure 7.2: Schematic representation of the metrological AFM and the feedback control.

7.2.2 Identification

The system G with input $u = \begin{bmatrix} u_x & u_y & u_z \end{bmatrix}^T$ and output $y = \begin{bmatrix} x & y & z_t \end{bmatrix}^T$ is defined as

$$G(f) = \begin{bmatrix} G_{xx} & G_{xy} & G_{xz} \\ G_{yx} & G_{yy} & G_{yz} \\ G_{zx} & G_{zy} & G_{zz} \end{bmatrix}. \tag{7.1}$$

In Chapter 6, a full nonparametric MIMO identification of the system together with an analysis of the amount of coupling between the different axes is performed. The magnitudes of the measured non-parametric frequency response functions (FRFs) of (7.1) are shown in Fig. 7.3 by the grey line. This FRF is measured under closed-loop conditions, by measuring the closed-loop sensitivity $S = (I + GK)^{-1}$ and the process sensitivity GS while sequentially exciting one of the axes by a zero mean white noise signal [207]. Then, G follows from $G = GS \cdot S^{-1}$.

For the MIMO $\mathcal{H}_\infty$ control synthesis a linear plant model is required. Modeling the system G with subspace techniques [208,210] requires very high order models to fit the diagonal terms sufficiently accurate. Even then, the model does not describe

the low frequent off-diagonal terms with sufficient accuracy [160]. Furthermore, a high order model leads to high order controllers, which is generally not favorable. The model order can be reduced using model reduction techniques, but always at the cost of a reduced model accuracy. Recently emerging robust-control-relevant modeling techniques [147,148] show a very promising approach to the identification step, but are at this stage not applied to the problem of interest in this chapter. Since the order of the $\mathcal{H}_\infty$ controller is equal to the model order plus the order of the weighting filters, a low order model is desired. Therefore, a model was made by fitting the various elements of G. The diagonal terms are approximated by a second order model, representing the mass of the stage, which is connected to the fixed world through the combined stiffness of the piezo stack actuators and the flexure mechanism. The off-diagonal terms are modeled by constants, representing a static coupling between the axes, e.g., as introduced by alignment errors. The fitted model $\tilde{G}$ equals

$$\tilde{G}(s) = \begin{bmatrix} \tilde{G}_{xx} & -80 & 300 \\ -150 & \tilde{G}_{yy} & 230 \\ -4.5 & -3.5 & \tilde{G}_{zz} \end{bmatrix},$$

where

$$\tilde{G}_{xx}(s) = \frac{6000}{1.65 \cdot 10^{-6} s^2 + 7.70 \cdot 10^{-5} s + 1},$$
$$\tilde{G}_{yy}(s) = \frac{5100}{1.58 \cdot 10^{-6} s^2 + 5.03 \cdot 10^{-5} s + 1},$$
$$\tilde{G}_{zz}(s) = \frac{72.4}{2.72 \cdot 10^{-7} s^2 + 1.41 \cdot 10^{-5} s + 1}.$$

The resonance peaks at 124 Hz and 126 Hz in G_{xx} and G_{yy}, respectively, represent two different modes [18] despite their close frequency location. The gains of the off-diagonal terms are chosen to match the magnitude of the measured FRF in the frequency range of the desired bandwidth of 10 Hz. Some off-diagonal terms have a minus sign in order to let the phase correspond to the phase at low frequencies in the measured FRF (grey line in Fig. 7.3).

The Bode magnitude plot of $\tilde{G}$ is shown in Fig. 7.3 by the black line. It can be seen that the model accurately describes the DC gains and first main resonance peak of the diagonal terms. The small resonances and resonances at higher frequencies are not taken into account in the model in order to keep the model order as low as possible. Furthermore, since a high-frequent roll-off will be enforced, these resonances are not considered to be relevant for the controller synthesis. The off-diagonal terms show a good correspondence with the measured FRF around the desired control bandwidth of 10 Hz. Note that a model of equal order identified using subspace techniques turned out to be less accurate, as it does not accurately describe the static gain and first resonance of the diagonal terms.

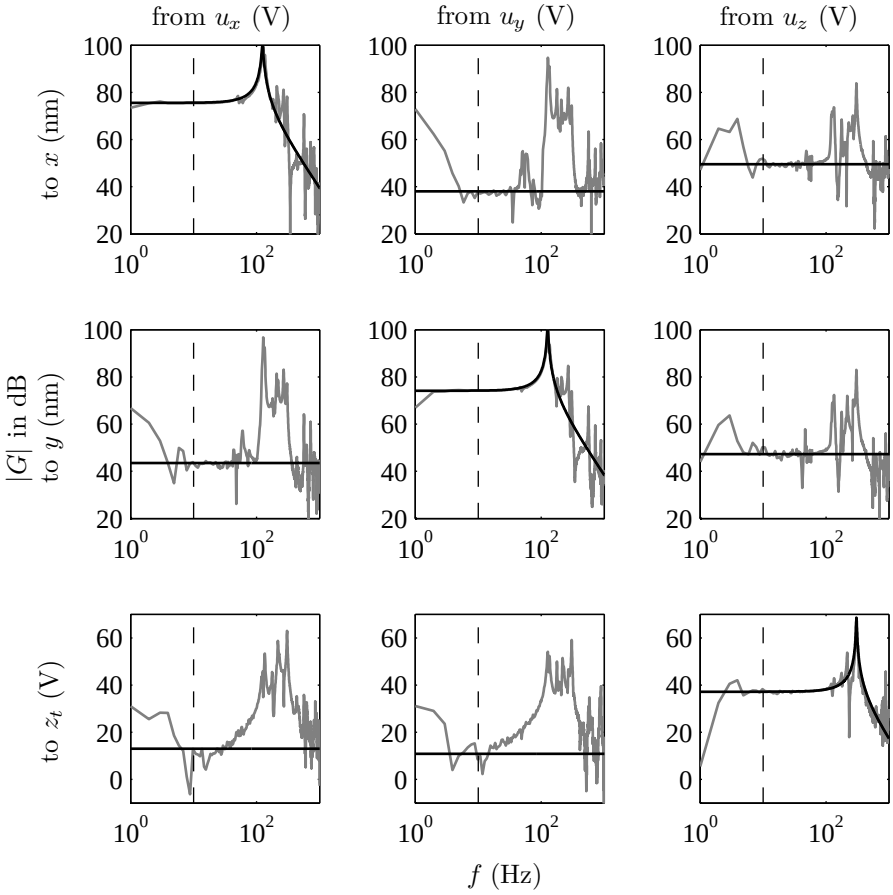

Figure 7.3: Bode magnitude plots of the measured FRF (grey) and the parametric model (black).

7.3 Control design

In this section, the control design for the metrological AFM is discussed. First, the design and stability analysis for a decentralized controller are discussed. Afterwards, the MIMO $\mathcal{H}_\infty$ control design is presented.

The purpose of the controller design is not to maximize achievable cross-over frequencies. Since the amount of coupling for frequencies $f < 100$ Hz is very small (see Chapter 6), equal cross-over frequencies should be achievable with a proper synthesis in both methods. The purpose is to compare the differences of the decentralized and MIMO controller, which have an equal amount of integrators and equal cross-over frequencies of the loop gains on the diagonal terms.

7.3.1 Decentralized control

Using the non-parametric FRF of Fig. 7.3 a decentralized controller is designed employing loopshaping techniques [63] as

$$K_d = \begin{bmatrix} K_{xx} & 0 & 0 \\ 0 & K_{yy} & 0 \\ 0 & 0 & K_{zz} \end{bmatrix}, \tag{7.2}$$

where

$$\begin{aligned} K_{xx} &= \frac{0.56}{s^2}\,\frac{s/(10\pi)+1}{s/(90\pi)+1}\,\frac{1}{s^2/(240\pi)^2 + s/(240\pi)+1}, \\ K_{yy} &= K_{xx}, \\ K_{zz} &= \frac{2.2}{s}\,\frac{1}{s^2/(200\pi)^2 + 1.4s/(200\pi)+1}. \end{aligned}$$

In x- and y-direction equal controllers are used, containing a double integrator to track constant velocity setpoints without steady-state error, a lead filter to create a phase gain around the bandwidth frequency and a second order low-pass filter to obtain high-frequent roll-off. In z-direction, a single integrator is used since step shaped disturbances caused by the sample structure of the transfer standards are expected and to limit the amplification of disturbances at high frequencies due to the Bode sensitivity integral. The Bode magnitude plot of the decentralized controller K_d is shown in Fig. 7.4 by the black lines.

The cross-over frequencies of each diagonal loop gain $L_{ji}(f) = G_{ji}(f)K_{ji}(f)$, $i = j,\ i,j \in \{x,y,z\}$ equal $\{16.7, 14.7, 25.4\}$ Hz. The loop gains can be further increased by including a notch filter in the controllers of especially the x- and y-directions. However, since the resonance frequencies may shift due to position

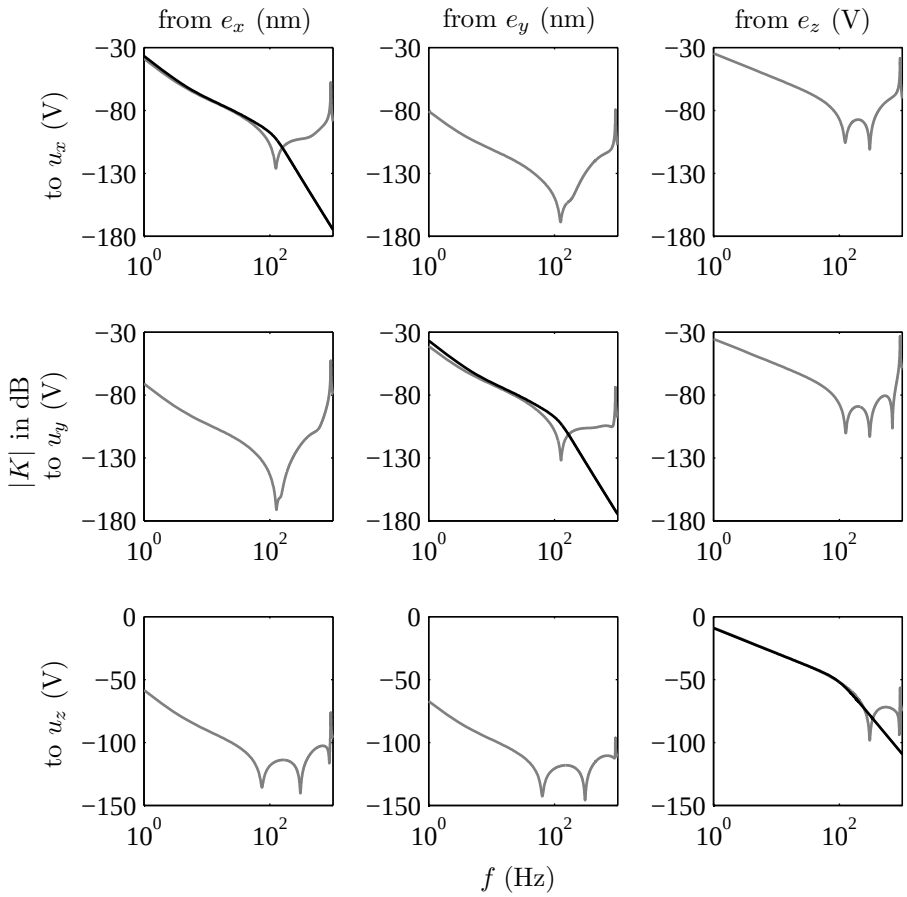

Figure 7.4: Bode magnitude plots of the decentralized (black) and MIMO (grey) controllers.

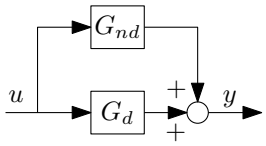

(a) Additive perturbation.

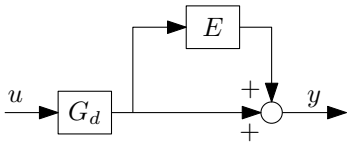

(b) Output multiplicative perturbation.

Figure 7.5: Plant representation with an additive perturbation and multiplicative output perturbation.

dependency of the 3-DOF stage, this has not been done at this point. For the comparison intended in this chapter, it is also not necessary.

The stability of a MIMO controlled system can be evaluated using the characteristic loci $\lambda(GK(f))$, defined as the eigenvalues of the open-loop frequency response. The system is closed-loop stable when the characteristic loci do not encircle the point (-1,0). Notice however that the margins only indicate stability with respect to a simultaneous parameter change in all of the loops [179].

The non-diagonal parts G_{nd} of the plant can be considered as an additive perturbation of the diagonal terms $G_d = \text{diag}(G)$ as $G = G_d + G_{nd}$ (see also Fig. 7.5(a)). The stability of the system with a decentralized controller K_d can be evaluated using the structured singular value [18, 73]. The diagonal closed-loop transfer functions equal

$$S_d = (I + G_d K_d)^{-1},$$
$$T_d = I - S_d.$$

The interaction due to the non-diagonal terms of the plant can be described as an output multiplicative perturbation E as shown in Fig. 7.5(b) such that

$$E = (G - G_d)G_d^{-1}. \tag{7.3}$$

If $G(s)$ is stable and $(I + G_d(s)K_d(s))^{-1}$ is stable, a sufficient condition for the stability of the MIMO system $(1 + G(s)K_d(s))^{-1}$ equals for $s = j\omega$ [18, 73]:

$$\bar{\sigma}(T_d(j\omega)) < \mu_{T_d}^{-1}(E(j\omega)),\ \forall\omega, \tag{7.4}$$

where $\bar{\sigma}(\cdot)$ are the maximum singular values and $\mu_{T_d}(\cdot)$ is the structured singular value with respect to the block diagonal structure of T_d.

Condition (7.4) is shown in Fig. 7.6 for the decentralized controller of (7.2), where the grey line represents the inverse of the structured singular value $\mu_{T_d}^{-1}$ and the

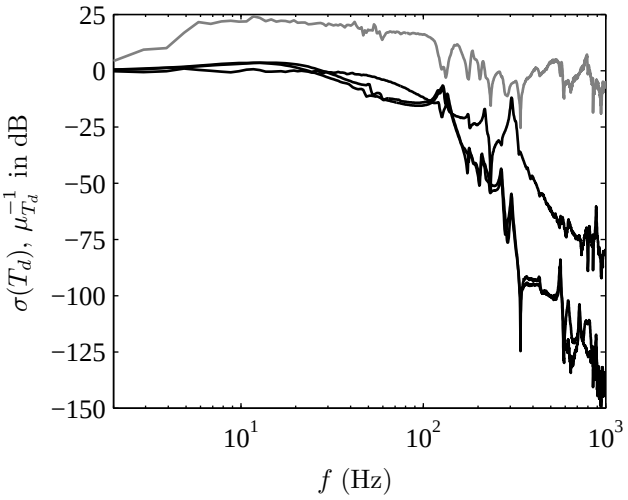

Figure 7.6: Sufficient condition (7.4) for the decentralized control loop with K_d from (7.2), $\sigma(T_d)$ (black) and $\mu_{T_d}^{-1}$ (grey).

three black lines the singular values σ of T_d. It can be seen that condition (7.4) is satisfied for all frequencies, i.e., the decentralized controller stabilizes the MIMO system.

7.3.2 MIMO control

For the norm based $\mathcal{H}_\infty$ control synthesis, the system is transformed into a standard plant configuration as shown in Fig. 7.7(a). The generalized plant is denoted by P and the MIMO controller by K. The external inputs (disturbances, sensor noise and reference trajectories) are contained in the vector w. The control variables are contained in z, which are typically the servo errors and control actions. The vector v contains the measured variables and u the input variables. The generalized plant P contains the modeled system dynamics $\tilde{G}$ and the weighting filters used for the controller synthesis. The generalized plant can be written as

$$\begin{bmatrix} z \\ v \end{bmatrix} = \underbrace{\begin{bmatrix} P_{11} & P_{12} \\ P_{21} & P_{22} \end{bmatrix}}_{P} \begin{bmatrix} w \\ u \end{bmatrix}. \tag{7.5}$$

For a given controller K, the closed-loop performance is analyzed using the system N, which is an interconnection of the controller K and standard plant P [179].

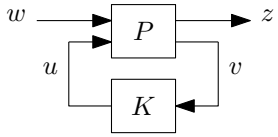

(a) Standard plant for controller synthesis.

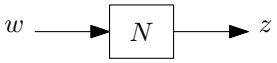

(b) N structure for performance evaluation.

Figure 7.7: Standard plant configuration for controller synthesis and N structure for performance analysis.

The closed-loop transfer function N from w to z is given by the lower fractional transformation (LFT) [224], denoted by $\mathcal{F}_l$, as

$$N = \mathcal{F}_l(P, K) = P_{11} + P_{12}K(I - P_{22}K)^{-1}P_{21}, \tag{7.6}$$

The MIMO controller K is designed such that the closed-loop system is internally stable and that the influence of the exogenous variables on the regulated variables is minimized with respect to the $\mathcal{H}_\infty$ norm. The controller K is optimized among all stabilizing controllers as [179]

$$\gamma_{\text{opt}} := \min_K \|N(P, K)\|_\infty = \min_K \sup_\omega \bar{\sigma}(N(j\omega)). \tag{7.7}$$

For the controller synthesis, weighting filters W_S, W_{KS} and W_T are added to the sensitivity (for performance), the control sensitivity (to penalize the control effort) and the complementary sensitivity (for robustness and to avoid sensitivity to noise), respectively. The feedback loop with the weighting filters is schematically shown in Fig. 7.8, where the reference is contained in $w = -r$ and the tracking error $v := e = r - y$. This results in a generalized plant P [179] as

$$\begin{bmatrix} z_1 \\ z_2 \\ z_3 \\ v \end{bmatrix} = \underbrace{\begin{bmatrix} 0 & W_{KS}I \\ 0 & W_TG \\ W_SI & W_SG \\ -I & -G \end{bmatrix}}_{P} \begin{bmatrix} w \\ u \end{bmatrix}, \tag{7.8}$$

where the output sensitivity $S_o = (I + GK)^{-1}$ and the complementary output sensitivity $T_o = GK(I + GK)^{-1}$. The controller K is optimized by minimizing $\|N(K)\|_\infty$ with respect to K, where

$$N = \begin{bmatrix} W_{KS}KS_o \\ W_TT_o \\ W_SS_o \end{bmatrix}. \tag{7.9}$$

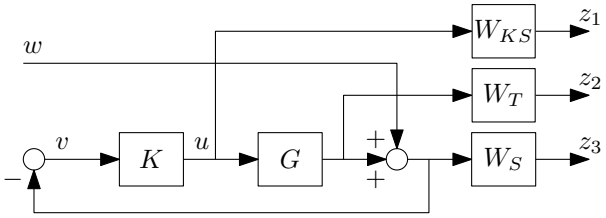

Figure 7.8: Schematic representation of the feedback loop with the weighting filters.

The weighting filters W_S, W_T and W_{KS} are designed employing classical loop-shaping knowledge. The weight on the sensitivity W_S is designed to enforce low frequent disturbance suppression, an integrating action at low frequencies and such that the peak value is below 6 dB for all frequencies. The weight on the control sensitivity W_{KS} is chosen constant to limit the maximum input. To prevent amplification of sensor noise, the weight on the complementary sensitivity W_T can be used to enforce high-frequent roll-off. To compare the MIMO controller to the decentralized controller of Section 7.3.1, the filters are chosen such that the number of integrators in the controller and the cross-over frequencies of the diagonal loop gains are approximately equal. The diagonal filters W_S, W_T and W_{KS} equal

$$W_S(i,j) = \begin{cases} k_S \frac{(s+2\pi f_{S1}(i))(s+2\pi f_{S2}(i))}{(s+2\pi f_{S3}(i))(s+2\pi 10^{-6})}, & \text{if } i=j, \\ 0, & \text{if } i \neq j, \end{cases} \tag{7.10}$$

$$W_{KS}(i,j) = \begin{cases} c, & \text{if } i=j, \\ 0, & \text{if } i \neq j, \end{cases} \tag{7.11}$$

$$W_T(i,j) = \begin{cases} k_T \alpha_T^2 \frac{s^2+4\pi\beta_T f_T(i) s+(2\pi f_T(i))^2}{s^2+4\pi\beta_T\alpha_T f_T(i) s+(2\pi\alpha_T f_T(i))^2}, & \text{if } i=j, \\ 0, & \text{if } i \neq j, \end{cases} \tag{7.12}$$

where $i,j \in \{x,y,z\}$. Furthermore, $k_S = 0.5$, $c = 0.5$, $k_T = 0.5$, $\alpha_T = 100$ and $\beta_T = 0.7$. The axis dependent parameters f_{S1}, f_{S2}, f_{S3} and f_T are contained in Table 7.2. For the z-axis the parameters $f_{S2} = 0$ Hz and $f_{S3} = 0$ Hz and thus only a single integrator is enforced in the controller in z-direction (see also (7.10)), instead of a double integrator as in the controllers in x- and y-directions.

With the generalized plant (7.8) and the weighting filters (7.10), (7.11) and (7.12), a controller K is obtained with $\gamma_{\text{opt}} = \|N\|_\infty = 0.91$. This implies that all the objectives specified by the weighting filters are satisfied in the obtained closed-loop system. Furthermore, the individual transfer functions in N and the controller K are all stable.

Table 7.2: Parameters of the weighting filters W_S, W_{KS} and W_T.

axis	f_{S1} (Hz)	f_{S2} (Hz)	f_{S3} (Hz)	f_T (Hz)
x	10	10	10^{-6}	23
y	8	8	10^{-6}	19
z	40	0	0	45

The Bode magnitude plot of the derived MIMO controller K is shown in Fig. 7.4 by the grey lines. The MIMO controller is of order 17, which is equal to the order of the plant model $\tilde{G}$ plus the order of the weighting filters. The cross-over frequencies of each loop gain (diagonal elements of the open-loop transfer function matrix $L = GK$) equal $\{15.9, 13.4, 22.9\}$ Hz, which are comparable to the cross-over frequencies for the decentralized controller. The decentralized and MIMO controllers show a large similarity on the diagonal terms. Besides the obvious difference that the MIMO controller is a full 3×3 matrix, the MIMO controller contains several notches in all elements. Since the $\mathcal{H}_\infty$ controller synthesis results in a proper controller, additional zeros are located in the controller around the Nyquist frequency, resulting in the increased controller gain above these frequencies as can be seen in Fig. 7.4. Due to the roll-off present in the system (see Fig. 7.3), the increased controller gain does not affect the stability. This effect could be reduced by enforcing additional roll-off in the weighting filter W_T for the complementary sensitivity.

The stability of the MIMO controller is assessed by evaluating the characteristic loci $\lambda(GK)$ calculated with the measured FRF of Fig. 7.3. The characteristic loci, shown in Fig. 7.9, show that the MIMO controller K stabilizes the system.

7.3.3 Controller comparison

The output sensitivities calculated with the measured FRF and, respectively, the decentralized and MIMO controllers are shown in Fig. 7.10. The output sensitivity S_o obtained with the MIMO controller K is smaller than S_o obtained with the decentralized controller K_d in the off-diagonal terms at the frequencies where the MIMO model is accurate, i.e., around 10 Hz. This indicates that the coupling effects of the disturbances to the errors in the different DOFs are reduced by the MIMO controller in this frequency range. However, at high frequencies the coupling effects of the disturbances are amplified by the MIMO controller.

The obtained reduction in the off-diagonal terms of the output sensitivity by the MIMO controller is not enforced in the controller synthesis since only diagonal

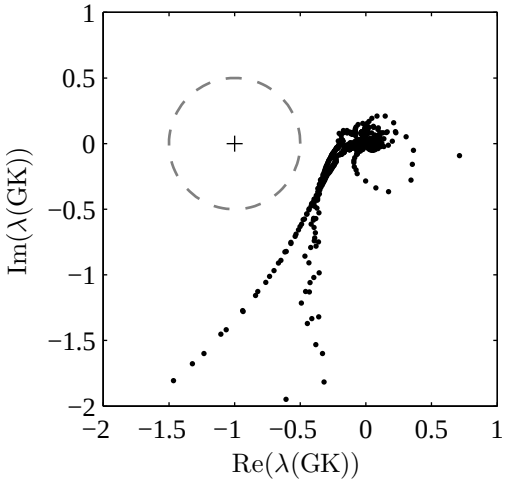

Figure 7.9: Characteristic loci $\lambda(GK)$ of the MIMO controller K evaluated with the measured FRF of Fig. 7.3.

weighting filters are used. The design of non-diagonal weighting filters to enforce certain desired properties is non-trivial since the non-diagonal filters are hard to interpret as relevant closed-loop bounds in the frequency domain and are therefore hard to tune [206]. In the control synthesis the directional information of the disturbances acting on the AFM system is not taken into account. Incorporating the directional information of the disturbances in the control synthesis can further improve the results [19], which is subject of future research.

The amount of reduction by the MIMO controller could be possibly increased further, especially at higher frequencies, by decreasing the model mismatch. Since the reduction in the off-diagonal terms of the output sensitivity S_o is influenced by a combination of several terms of the system G and the controller K, the model mismatch should be reduced in all terms simultaneously.

7.4 Directional repetitive control

The triangular scanning movement of the AFM and the repetitive sample topography, which is typical for transfer standards for the metrological AFM, introduce repetitive disturbances in the system. These disturbances can be asymptotically suppressed using repetitive control (RC) [34, 77, 81].

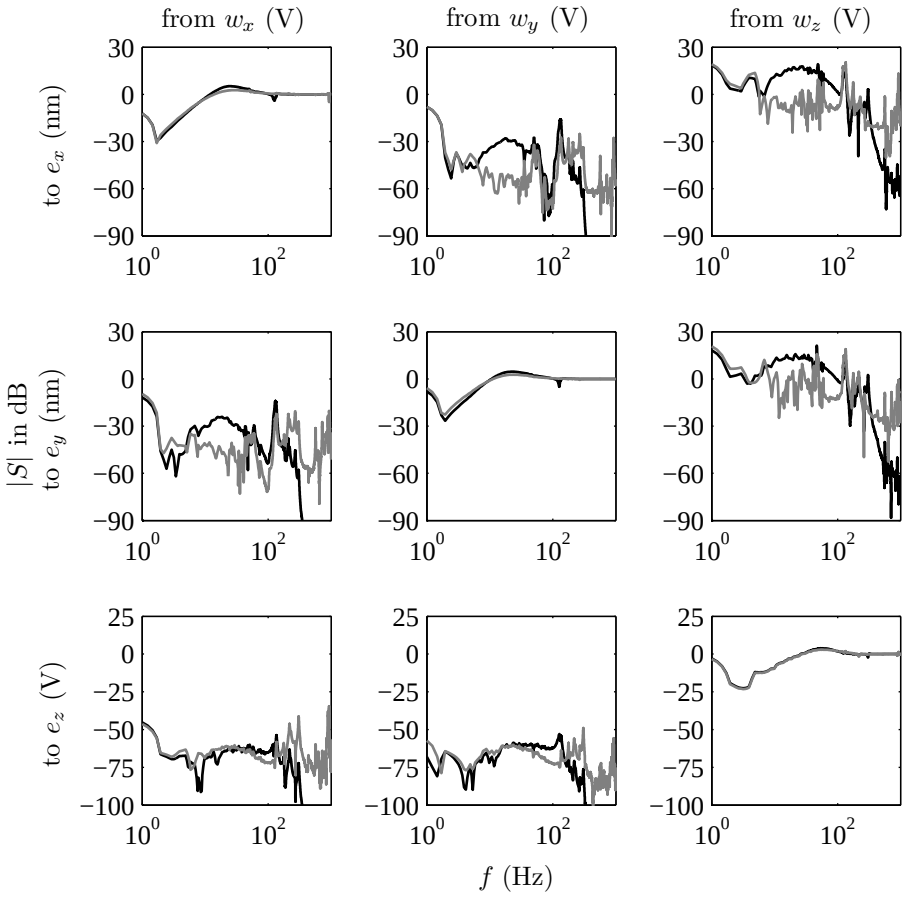

Figure 7.10: Output sensitivities $S_o = (I+GK)^{-1}$ obtained with the decentralized controller K_d (black) and the MIMO controller K (grey).

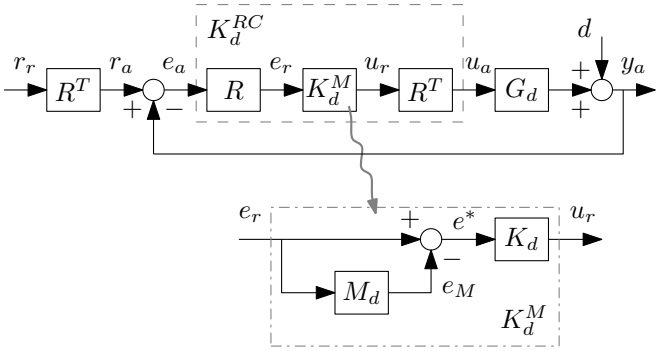

Figure 7.11: Block diagram of a 1-DOF feedback controlled system with RC added.

In this section, first standard RC will be addressed briefly. Next, directional repetitive control (DRC) is introduced, in which the scanning directions of the repetitive controller are adjusted based on the orientation of the sample under the AFM. For an in-depth treatment of RC, see [185, 187].

7.4.1 Repetitive control

For the metrological AFM, RC can be applied to the fast scanning and the imaging axes since these have a repetitive reference trajectory (triangular) and a repetitive external disturbance (transfer sample), respectively. The repetitive controllers are combined with the decentralized controllers K_d of the corresponding axes, as described in Section 7.3.1. The decentralized controllers are used since this allows RC to be added directly to the control loop, whereas the combination of RC with a MIMO controller would require a redesign of the MIMO controller K [44].

Fig. 7.11 shows a block diagram of the feedback controlled system for one DOF with RC added. For the moment, consider the matrix $R = I$, i.e., $r_a = r_r$, $e_r = e_a$ and $u_a = u_r$. In Fig. 7.11, G_d represents the diagonal system dynamics of one DOF, K_d the decentralized controller and M_d the repetitive controller of that specific DOF, respectively. The signal d contains the repetitive disturbances acting on the system.

From the transfer function from the error e_r to the output e_M follows for the repetitive controller $M_d(z)$

$$M_d(z) = \frac{L(z)Q(z)z^{-(N-q-l)}}{1 - Qz^{-(N-q)}}, \tag{7.13}$$

where $L(z)$ is the learning filter with a phase delay of l samples, $Q(z)$ is the robustness filter with a phase delay of q samples and N is the number of samples that determines the length of the repetitive period. With the repetitive controller M_d, the modified sensitivity, describing the effect of the repetitive disturbances d on the tracking error e_a, equals

$$S = \frac{1}{1 + G_d K_d (1 + M_d)} = \frac{1}{1 + G_d K_d} M_S, \tag{7.14}$$

where the modifying sensitivity function [32]

$$M_S = \frac{1 - Q z^{-(N-q)}}{1 - Q z^{-(N-q)}(1 - T L z^{+l})}. \tag{7.15}$$

For SISO systems, the closed-loop system with RC is stable if the original diagonal sensitivity $S_d = (1 + G_d K_d)^{-1}$ is asymptotically stable and if for all frequencies

$$|Q(1 - T L z^{+l})| < 1. \tag{7.16}$$

The criterion (7.16) is a sufficient condition for stability of SISO systems with RC and is derived using the small gain theorem [179].

For MIMO systems, a framework for the synthesis of MIMO repetitive controllers is presented in [44], which is based on the internal-model-principle. In a MIMO framework, the stability can be evaluated using (7.16) with the complementary sensitivity $T = RGR^T K (I + RGR^T K)^{-1}$ and full transfer matrices for the robustness filter Q, learning filter L and delays. An independent design of the learning filter L and feedback controller K is not recommended in a MIMO setting [44]. Since the addition of RC to a MIMO controller requires a redesign, direct comparison is not possible. To show the applicability of DRC, we will restrict ourselves in this chapter to the SISO case. DRC will be applied to the z-axis only since a sample rotation is most likely to occur around this axis due to the positioning of the sample on the stage.

The learning filter $L(z)$ compensates for the dynamics between the input and output of the repetitive controller, namely the complementary sensitivity T_d. Therefore, ideally the learning filter equals $L(z) = T_d^{-1}(z)$. In case T_d is non-proper or has non-minimum phase zeros, an approximation $L(z) \approx T_d^{-1}(z)$ is made to obtain a stable, proper learning filter. The approximated learning filter can be obtained using the zero-phase-error-tracking-control (ZPETC) method [197].

The Q filter provides robustness against modeling errors and is designed such that the convergence criterion (7.16) holds. The use of the Q(z) filter also restricts the working principle of the repetitive controllers in certain frequency bands [185]. If the filter Q(z) is constructed to have a linear phase of q samples, the introduced phase delay of the filter can easily be compensated for in the memory loop of N samples, provided that $N > q$ [111].

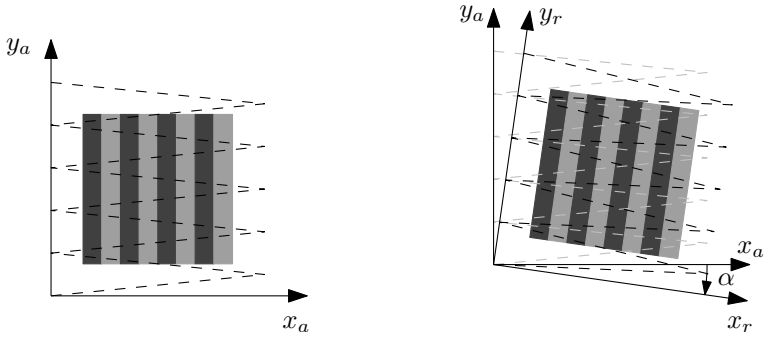

(a) Perfectly aligned. (b) Rotated.

Figure 7.12: Sample orientation with respect to the scanning axes x_a and y_a.

7.4.2 Sample dependent scan directions

For RC, the disturbances need to be fully repetitive. The sample topography introduces a perfectly repetitive disturbance over the different scan lines if the sample orientation is perfectly aligned with the actuation directions, as shown in Fig. 7.12(a). However, in general, especially on a nanometer scale, the sample under the metrological AFM is not perfectly aligned with the actuation directions. The largest rotation is expected in the positioning of the sample on the sample holder, i.e., a rotation around the z-axis. The misalignment of the sample causes the disturbances introduced by the sample topography to be non-repetitive in time while scanning the sample in x- and y-direction, as indicated in Fig. 7.12, where the actuation directions are indicated by the subscript a and the rotated sample axes by the subscript r. The sample is rotated around the z-axis over an angle of α (rad) with respect to the actuation directions.

By rotating the scan trajectory over the angle α such that the scan lines are aligned with the rotated axes x_r, y_r, the sample disturbance becomes fully repetitive again over the subsequent scan lines. The rotation of the coordinate system (x_a, y_a) to (x_r, y_r) as shown in Fig. 7.12(b) can be described by the rotation matrix $R(\alpha)$ as

$$\begin{bmatrix} x_r \\ y_r \\ z_r \end{bmatrix} = \underbrace{\begin{bmatrix} \cos(\alpha) & -\sin(\alpha) & 0 \\ \sin(\alpha) & \cos(\alpha) & 0 \\ 0 & 0 & 1 \end{bmatrix}}_{R(\alpha)} \begin{bmatrix} x_a \\ y_a \\ z_a \end{bmatrix}. \tag{7.17}$$

For the rotation matrix holds that $R^T R = I$. The rotation only involves a rotation in the plane of the sample, i.e., in the scanning direction. Possible tilt of the sample

caused by a rotation around the axes x_a and/or y_a is not taken into account in this analysis, but could be incorporated in a similar manner with an additional rotation matrix.

The rotation is incorporated in the reference trajectories to the different axes and in the decentralized feedback controllers with RC K_d^{RC} as shown in Fig. 7.11. The RC scheme with the rotated axes is referred to as DRC.

7.4.3 Rotation estimation

For the application of DRC, the sample orientation, i.e., the angle α, should be known. To determine the orientation, two line scans are performed in the fast scanning y-direction at different constant positions $x_{1,2}$. Under the assumption that the sample structure is identical for the two scan lines, the orientation and thus α can be determined from the recorded sample heights $z_{1,2}$ of the laser interferometer in z-direction. The number of samples phase shift between the sample features of the two recorded sample heights $z_1(t)$ and $z_2(t)$ is determined by calculating the correlation $\mathcal{R}$ as

$$\mathcal{R}_{z_1,z_2}(\tau) = \mathbb{E}\{(z_1(t) - \mu_1)(z_2(t-\tau) - \mu_2)\}, \tag{7.18}$$

where τ is the number of samples phase shift, μ_1 and μ_2 are the mean values of the sample heights of the two line scans respectively and $\mathbb{E}\{\cdot\}$ denotes the expected value operator. The correlation is maximal when the phase shifted sample heights are similar. The number of samples phase shift δ_s can be determined as

$$\delta_s = \arg\left(\max_{\tau}(\mathcal{R}_{z_1,z_2}(\tau))\right). \tag{7.19}$$

Using the scanning velocity v_y (nm/s) and the sampling time t_s (s), the difference in distance between the sample features over the scanning lines δ_y (nm) can be calculated as

$$\delta_y = \delta_s t_s v_y. \tag{7.20}$$

The accuracy of δ_y is dependent on the scanning velocity and sampling frequency. To determine the orientation α accurately, the scanning speed should be chosen low and a high sampling frequency is preferred. The sample rotation angle α can finally be calculated as

$$\alpha = \arctan\left(\left|\frac{\delta_y}{x_2 - x_1}\right|\right). \tag{7.21}$$

Summarizing, the orientation of the sample can thus be obtained in a five step procedure as:

1. perform a line scan in the fast scanning y-direction at constant x_1-position and record the sample height z_1,
2. perform a second line scan at a different constant x_2-position and record the sample height z_2,
3. determine the phase shift between the sample heights $z_{1,2}$ using (7.19),
4. determine the shift in position between the sample features using (7.20),
5. calculate the sample rotation angle α from (7.21).

The non-repetitive disturbances present in the measured sample heights $z_{1,2}$ of the two scan lines affect the calculated sample rotation α. To reduce the influence of the disturbances on α, more line scans can be performed. Averaging of the different obtained angles α of two subsequent line scans reduces the influence of the non-repetitive disturbances.

7.5 Experimental results

This section contains the results of the experiments with the decentralized controller K_d, the MIMO controller K and DRC applied to the metrological AFM. The proposed DRC method has the largest influence in z-direction, i.e., where the sample topography acts as a repetitive disturbance. Therefore, the experimental results of RC and DRC in z-direction are shown.

For the experiments, a constant velocity setpoint of 125 nm/s is used for the slow scanning x-direction. In the fast scanning y-direction a triangular shaped setpoint profile over a range of ± 25 μm with a velocity of 25 μm/s is used, i.e., with a period-time of 4 s. The z-direction is controlled to a constant tip deflection. The controller sampling frequency for the experiments equals $f_s = 2$ kHz. The repetitive period for the RC experiments is determined by the setpoint in y-direction and equals $N = 8000$ samples.

7.5.1 Decentralized versus MIMO control

The largest output disturbance is introduced by the unknown sample topography in z-direction. The largest reduction in coupling by the MIMO controller K is obtained from the disturbance in z-direction to the x-direction, as shown in Fig. 7.10. Therefore, the time response of the x-direction is presented.

The tracking errors $e_x = r_x - x$ of the experiments with the decentralized controller K_d and the MIMO controller K are shown in Fig. 7.13. The tracking error

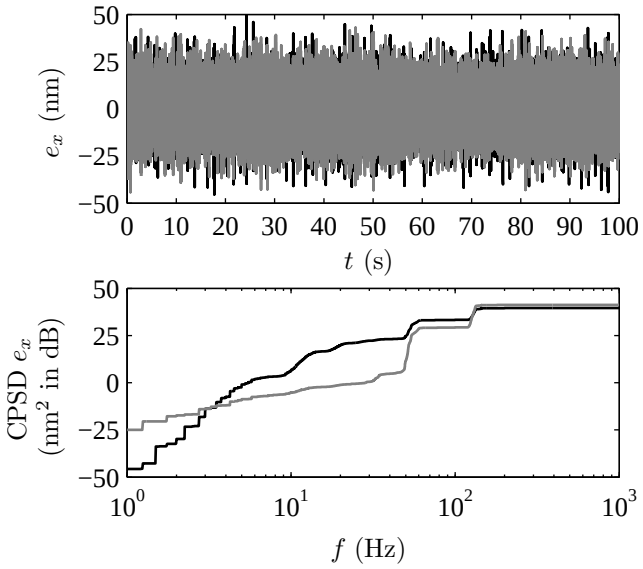

Figure 7.13: Tracking errors e_x and cumulative PSDs of the errors obtained with the decentralized (black) and MIMO controllers (grey).

looks similar in time with both controllers. The rms values of the errors equal $\text{rms}(e_{x,K_d}) = 44.3$ nm and $\text{rms}(e_{x,K}) = 51.3$ nm, respectively. The slight increase in error obtained with the MIMO controller is caused by the high-frequent external disturbances acting on the system in combination with the larger magnitudes of the off-diagonal output sensitivities at high frequencies (see Fig. 7.10).

The cumulative power spectral densities (CPSDs) of the errors, shown in Fig. 7.13, show the reduction of the error in x-direction in the frequency region where the model terms $\tilde{G}_{xy}$ and $\tilde{G}_{xz}$ are accurate, i.e., around the desired bandwidth of 10 Hz. The frequencies at which the error is reduced correspond to the frequencies where the coupling from the disturbances in y and z are reduced to the error in x-direction, as shown in Fig. 7.10.

Although the rms value of the error is slightly increased by the application of the MIMO controller, the error is reduced in the frequency range where a reduction was expected by the controller design. With a better MIMO model, possibly an overall performance improvement by application of MIMO control can be obtained. The derivation of a more accurate MIMO model in the high frequency region will be part of future research.

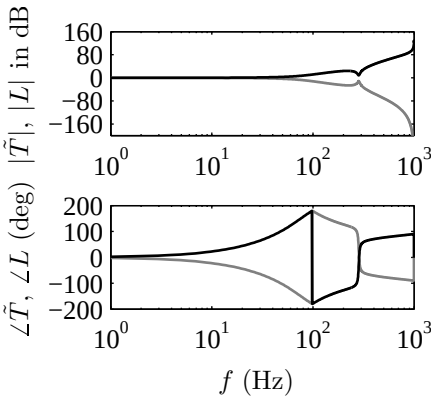

Figure 7.14: Bode diagram of the complementary sensitivity $\tilde{T}$ (grey) and learning filter L (black) in z-direction.

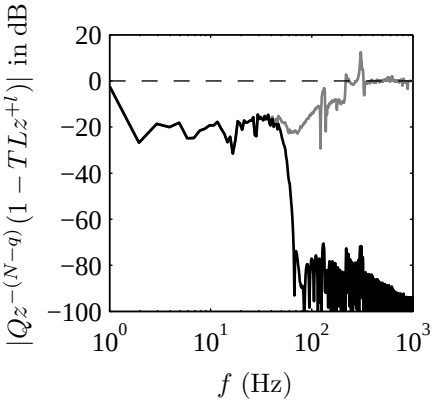

Figure 7.15: Convergence criterion in z-direction evaluated with the measured FRF, without Q filter (grey) and with Q filter (black).

7.5.2 Results DRC

Since timing is crucial for the success of the repetitive controller, a zero-phase error is required. Using a discrete model of the complementary sensitivity $\tilde{T}_d$ in z-direction and the ZPETC method [197], the learning filter $L_z(z)$ is derived as a proper, stable approximation of the inverse complementary sensitivity, i.e., $L_z(z) \approx \tilde{T}_{d,z}^{-1}(z)$. The Bode diagrams of the complementary sensitivity function $\tilde{T}_d(z)$ and learning filter $L(z)$ in z-direction are shown in Fig. 7.14. It can be seen that the phase of the learning filter is an exact inverse of the complementary sensitivity function. The magnitude of the learning filter approximates the inverse complementary sensitivity very well, but has a slight deviation in amplitude at high frequencies in order to obtain a stable and proper filter $L(z)$.

The convergence criterion (7.16) is plotted in Fig. 7.15 using the measured FRF data with and without the $Q(z)$ filter. The convergence criterion evaluated without Q filter (grey line in Fig. 7.15) exceeds 0 dB for frequencies $f > 215$ Hz. To guarantee stability of the RC scheme and to restrict the modified sensitivity (7.14) to $S < 10$ dB, a low-pass $Q(z)$ FIR filter with 200 taps and a cut-off frequency of 50 Hz is used. With the low-pass robustness filter $Q(z)$ the convergence criterion (7.16) is fulfilled as shown in Fig. 7.15 by the black solid line.

In order to show the applicability of the proposed DRC method, the sample is intentionally rotated under the metrological AFM at two different angles α (rad).

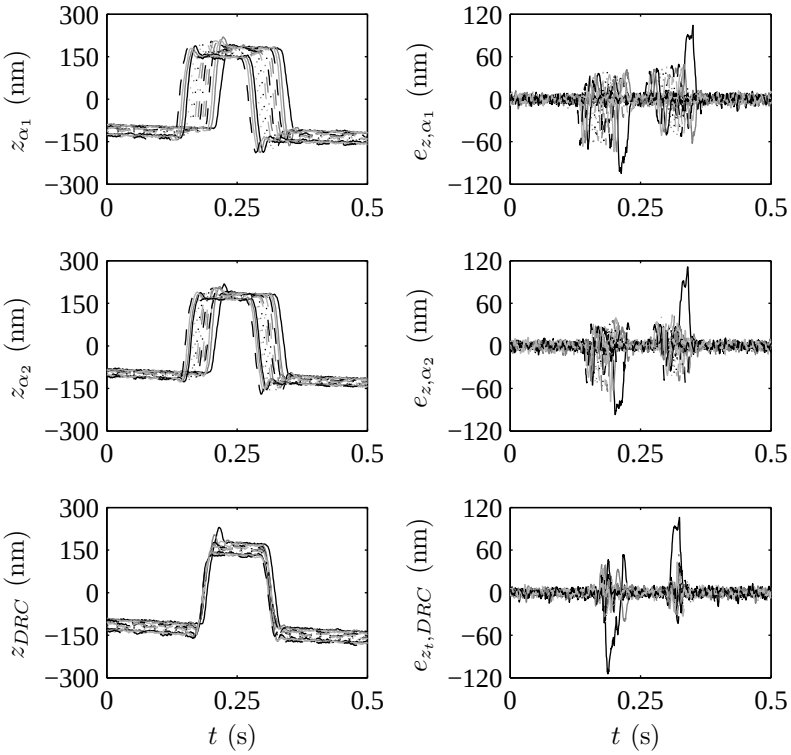

Figure 7.16: Measured sample topographies z (left column) and tracking errors e_z (right column) for various scan lines with RC for rotations $\alpha_1 = 0.22$ rad (top) and $\alpha_2 = 0.15$ rad (middle) and with DRC (bottom).

The measured sample topographies of different scan lines for the two experiments with a rotated sample are shown in Fig. 7.16 in the top left two figures. The shift in the sample topography in between the subsequent scan lines is clearly visible. The rotation in the second experiment is smaller since the phase shift between the different lines is smaller. Using the procedure described in Section 7.4.3, the sample orientations are determined as $\alpha_1 = 0.22$ rad and $\alpha_2 = 0.15$ rad, respectively.

The tracking errors of the RC experiments with the rotated sample over $\alpha_{1,2}$ rad contain a phase shift and large oscillations for the various scan lines, as shown in the top right figures in Fig. 7.16. The root-mean-square (rms) values of the errors of the different iterations are shown in Fig. 7.17(a) as function of the iteration number. It can be seen that despite of the phase shifts RC is still able to reduce the tracking error. Furthermore, the rms value of the tracking error for $\alpha_1 = 0.22$ rad is larger than for $\alpha_2 = 0.15$ rad. After convergence, the rms values of the errors of

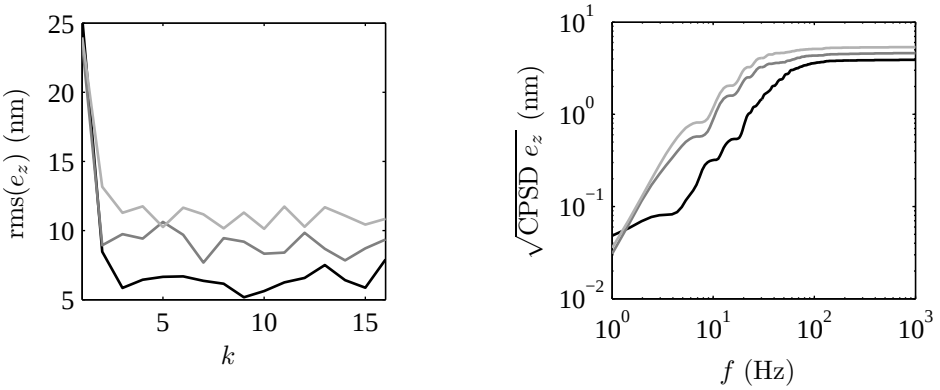

(a) Error convergence.

(b) Cumulative PSD of e_z at $k = 15$.

Figure 7.17: Convergence plot and cumulative PSD of the errors at iteration $k = 15$ for the experiments with RC and $\alpha_1 = 0.22$ rad (light grey) and $\alpha_2 = 0.15$ rad (dark grey) and with DRC (black).

the various iterations fluctuate due to the presence of non-repetitive disturbances.

If DRC is applied, the measured sample topography over the different scan lines does not show a phase shift, as shown in the bottom left axis of Fig. 7.16. The measured tracking errors of the different iterations, shown in the bottom right axis of Fig. 7.16, are only present at the time instants where a transition in the measured sample topography is detected. With DRC, no phase shift or large oscillations at other time instants are present in the tracking errors. The rms values of the errors of the different iterations are shown in Fig. 7.17(a) by the black line. DRC reduces the tracking error e_z for a rotated sample over $\alpha_1 = 0.22$ rad by 44% from $\text{rms}(e_{z,\alpha_1}) = 10.42$ nm to $\text{rms}(e_{z,DRC}) = 5.86$ nm. For a rotated sample over $\alpha_2 = 0.15$ rad, the error is reduced by 33%. Furthermore, the rms values of the errors are for all iterations smaller for DRC than for RC with a rotated sample. The rms values of the errors at the iterations $k = 1$ and $k = 15$ of the experiments of RC applied with $\alpha_1 = 0.22$ rad and $\alpha_2 = 0.15$ rad and DRC are given in Table 7.3. Note that the errors at iteration $k = 1$ are only influenced by the feedback controller K_d, i.e., the repetitive controllers are not active during the first iteration since no repetitive error is available yet. In Fig. 7.17(b) the square root of the CPSDs of the tracking errors of RC with the rotated sample and of DRC are shown for iteration $k = 15$. The reduction in tracking error by DRC can clearly be seen. For frequency $f \to \infty$, the square root of the CPSDs converge to the rms values of the tracking errors.

Table 7.3: rms values of the errors at iterations $k = 1$ and $k = 15$ for the RC experiments in z-direction with $\alpha_1 = 0.22$ rad and $\alpha_2 = 0.15$ rad and for the DRC experiment in z-direction.

Iteration	rms(e_{z,α_1})	rms(e_{z,α_2})	rms($e_{z,DRC}$)
$k = 1$	23.96 nm	23.54 nm	25.39 nm
$k = 15$	10.42 nm	8.71 nm	5.86 nm

7.6 Conclusions

In this chapter, a MIMO $\mathcal{H}_\infty$ controller design for a metrological AFM has been presented together with a novel directional repetitive control (DRC) scheme, which aligns the scanning axes with the sample orientation.

Using a low order system model, a MIMO $\mathcal{H}_\infty$ controller is derived. The MIMO controller is compared to a high-gain decentralized controller that has comparable cross-over frequencies of the diagonal loop gains. Despite the small amount of coupling present in the system, the output sensitivity is shown to have a better disturbance suppression using the MIMO controller compared to the decentralized controller.

The orientation of the sample under the AFM is not necessary aligned with the direction of actuation. This causes the topography of the transfer samples to result in non-repetitive disturbances, thus limiting the performance of repetitive learning controllers. The DRC scheme aligns the actuation axes with the sample orientation. The required coordinate transformation is obtained from a scan over a couple of lines.

The experimental results of the imaging z-axis of the metrological AFM show the applicability of the proposed directional repetitive controller. Even for a small sample rotation of 0.22 rad, DRC is shown to reduce the tracking error by 44% compared to a standard repetitive controller.

The improved disturbance suppression and decoupling properties of the MIMO controller are not explicitly enforced in the controller synthesis step since only diagonal weighting filters are used. The MIMO $\mathcal{H}_\infty$ controller design with non-diagonal weighting filters is subject of future research.

The combination of MIMO and RC could improve the results even further. This requires a simultaneous redesign of both the MIMO feedback controller and the learning controller, which will be subject of future research.

Part IV

Optical incremental encoders

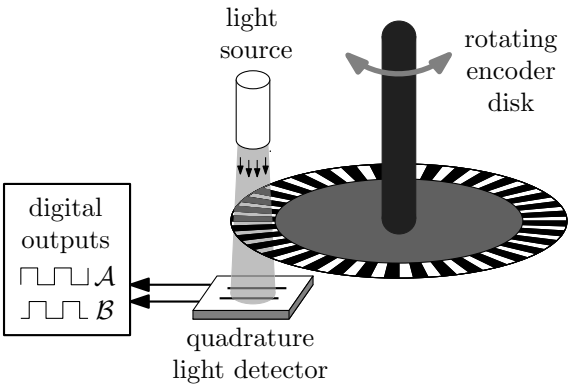

Chapter 8

Time-stamping with velocity and acceleration estimates

Abstract - Optical incremental encoders are extensively used for position measurements in motion systems. The position measurements suffer from quantization errors. Velocity and acceleration estimations obtained by numerical differentiation largely amplify the quantization errors. In this chapter, the time-stamping concept is used to obtain more accurate position, velocity and acceleration estimations. Time-stamping makes use of stored events, consisting of the encoder counts and their time instants, captured at a high-resolution clock. Encoder imperfections and the limited resolution of the capturing rate of the encoder events result in errors in the estimations. In this chapter, we propose a method to extend the observation interval of the stored encoder events using a skip operation. Experiments on a motion system show that the velocity estimation is improved by 54% and the acceleration estimation by 92%.

This chapter is based on: R.J.E. Merry, M.J.G. van de Molengraft and M. Steinbuch. Velocity and acceleration estimation for optical incremental encoders. *Mechatronics*, accepted, 2009.

8.1 Introduction

Optical incremental encoders are widely used to apply feedback control on motion systems where the position is measured at a fixed sampling frequency. They are available in both rotational and linear form. The position accuracy is limited by the quantized position measurement of the encoder, i.e., it is limited by the number of slits on the encoder disk.

The quantization errors can be reduced using more expensive encoders with more increments at the expense of increased cost price. Velocity and acceleration information is often obtained by numerical differentiation of the quantized position signal. Direct differentiation mostly leads to signals that are not useful [94]. The quantization errors limit the performance in high-accuracy control applications.

Smart signal processing techniques can be used in combination with cheap low-resolution encoders to obtain position estimations with the same accuracy as expensive high-resolution encoders. In literature, several methods have been proposed to improve the accuracy of velocity and acceleration estimations for optical incremental encoders. The methods can be divided into two kinds; fixed-time (clock-driven) methods and fixed-position (encoder-driven) methods.

For real-time control purposes, a fixed-time method is desired since the controller is generally evaluated at fixed-time intervals. Fixed-time velocity and acceleration estimations can be obtained using three different approaches; predictive postfiltering techniques, linear state observers and indirect measurement techniques.

Predictive postfiltering techniques perform a filtering on differentiated position signals. Euler based methods [115] and polynomial delayless predictive differentiators [202] both disregard the variable rate of occurrence of the encoder events to estimate the velocity or acceleration. The transition based logic algorithm of [110] estimates only the velocity under the assumption that the sampling frequency is much larger than the rate of the encoder events.

Linear state observer techniques use the encoder position measurements, without the need for differentiation. Dual-sampling rate observers [100] and Kalman filters [13] require accurate system models to be available. The non-model based observer of [196] switches between two estimation filters based on an estimation error, which is generally not available. Data-based observers using neural networks [29] or fuzzy logic [221] estimate the velocity using only the position information, thus disregarding the non-constant time occurrence of the encoder events.

Indirect measurement techniques are based on analog or digital postprocessing of available position and/or velocity signals. In [164], the velocity is estimated by a

polynomial fit through a number of encoder counts. No time information of the encoder events is taken into account and no acceleration information is obtained. In [23], both encoder counts and their time instants are used to estimate the velocity. This is called the time-stamping concept. However, only simulations are performed at a practically unrealistic sampling frequency of 1 MHz and all encoder events are taken into account, which is not practically applicable.

Since for control purposes fixed-time methods are desired and since the encoder events have a fixed-position nature, occurring at a varying rate in time, a combination of the two approaches would be favorable. To reduce the effect of quantization, which is the performance limiting factor (PLF) in optical incremental encoders, we propose a method to accurately estimate the position, the velocity as well as the acceleration using the time-stamping method of [23]. The time-stamping concept was used for position estimation in combination with the calibration and compensation of encoder errors in [132]. The time-stamping concept involves the capturing of encoder events, i.e., the encoder transitions and their time instants, at a high-resolution clock added to the encoder in the data-acquisition hardware. The encoder events are stored in a register and transferred to the controller at a lower fixed sampling rate. Polynomial interpolation through the encoder events and extrapolation of the obtained polynomial make it possible to estimate position, velocity and acceleration at the time of interest.

In this chapter, we propose a skip option for the event selection as an extension of the time-stamping concept of [132]. The need for the skip option is originated by two factors. Firstly, the storage register for encoder events is of finite length. The skip option is a selection method for the storage of the encoder events captured at the high-resolution clock in the data-acquisition hardware and enables a more flexible use of the available register space. Secondly, the velocity and acceleration estimation using time-stamping are distorted by the presence of encoder imperfections. For this use, the skip option can perform a spatial low-pass filter on the encoder events to reduce the effect of the encoder imperfections. Since the most recent event is always included in the register, the skip option effectively does not influence the resolution or the quadrature of the encoder. It only influences the spatial data history in the register used for the polynomial interpolation.

The proposed method is an indirect measurement approach which is fully data-based, so no model of the system is required. Note that the required model for estimation of the position, velocity and acceleration is different from the model required for feedback controller design, e.g., the model required for estimation purposes should include friction, which is difficult to model accurately.

Experiments on a motion system show the applicability of the proposed method to obtain more accurate velocity and acceleration signals. Since the skip option and

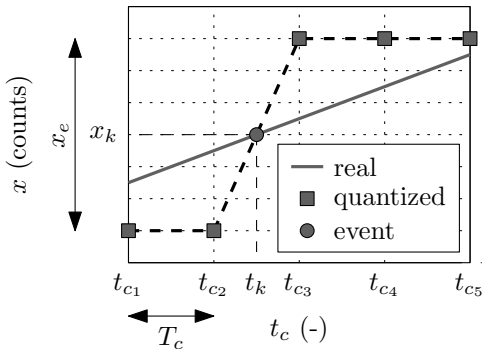

Figure 8.1: Time-stamping concept; the encoder transition x_k and time t_k are captured and stored as an event.

the capturing of the encoder events are implemented in hardware, the estimation of the signals is of the fixed-time kind. Therefore, the proposed method is applicable in real-time closed-loop experiments.

This chapter is organized as follows. The time-stamping concept will be explained in more detail in Section 8.2. The position reconstruction method will be briefly addressed in Section 8.3. In Section 8.4, the principle of skip in time-stamping will be introduced and its effects on the position reconstruction will be described. The influence of skip will be shown in Section 8.5 by means of experiments on a motion system. Finally, conclusions will be drawn in Section 8.6.

8.2 Time-stamping concept

In most motion control applications the position is measured by reading out the quadrature encoder counter value at the fixed controller sampling rate T_c. This introduces even for ideal encoders a quantization error in the position measurement of maximally half the encoder resolution x_e. The quantized signal contains the encoder counter value at the controller sampling times t_c, as can be seen in Fig. 8.1.

A possibility for increasing the accuracy of the position information with the same resolution encoders is using the concept of time-stamping [23]. The time-stamping concept stores the time instants t_k of a number of encoder transitions together with their position x_k. The pair (t_k, x_k) is called an encoder event. The encoder events are captured by a high-resolution clock with a sampling-period $T_e << T_c$.

8.3 Position reconstruction

The use of encoder events for feedback control is not trivial since the encoder events are obtained at a variable rate proportional to the instantaneous velocity of the system during the measurement. To obtain a position estimation at the equidistant sampling times of the controller, a polynomial is fitted through a number of past encoder events. This polynomial is extrapolated to the desired time instant of the controller. Velocity and acceleration estimations are obtained by differentiation of the fitted polynomial with respect to time and extrapolation to the fixed sampling times of the controller.

For the position, velocity and acceleration estimations, a low order polynomial is fitted through a number of encoder events by the least squares method. Let n be the number of encoder events used in the fit, m the order of the fit, and k the index number of the events. Furthermore, let $p_{0,\ldots,m}$ be the polynomial coefficients to be estimated, $t_{1,\ldots,n}$ the time information of the encoder events, and $x_{1,\ldots,n}$ the position information of the encoder events. Now define the matrices $A \in \mathbb{R}^{n\times m+1}$, $P \in \mathbb{R}^{m+1}$, and $B \in \mathbb{R}^{n}$ as follows

$$A = \begin{bmatrix} t_{k-n+1}^{m} & t_{k-n+1}^{m-1} & \cdots & 1 \\ \vdots & \vdots & & \vdots \\ t_{k-1}^{m} & t_{k-1}^{m-1} & \cdots & 1 \\ t_{k}^{m} & t_{k}^{m-1} & \cdots & 1 \end{bmatrix}, \tag{8.1}$$

$$P = \begin{bmatrix} p_m & p_{m-1} & \cdots & p_0 \end{bmatrix}^T, \tag{8.2}$$

$$B = \begin{bmatrix} x_{k-n+1} & \cdots & x_{k-1} & x_k \end{bmatrix}^T. \tag{8.3}$$

To prevent numerical problems with the higher-order terms in (8.1), the time variable t can be redefined to be zero every controller sampling time t_c, i.e., $t := t - t_c$.

If $n = m$, an exact fit is made through the events. For the least squares method $n > m$. The over-determined system of linear equations to be solved for the polynomial fit equals

$$AP = B.$$

The polynomial coefficients can be calculated using the least squares method as

$$P = (A^T A)^{-1} A^T B. \tag{8.4}$$

The polynomial coefficients P of (8.4) have to be calculated in real-time. For this purpose, LU-factorization without pivoting is used [103]. The inverse matrix will

not be calculated in a recursive manner since the events contained in the register are likely to vary every sampling time of the controller and thus the information contained in the A matrix is different every time. Instead, (8.4) will be solved at each controller sample.

If the time instants between the events in the register are very small, the A matrix can become ill-conditioned. To avoid numerical problems, the time span Δt_K in-between the time instants of the first and last event is scaled to 1 for the polynomial fit. In this way, the time instants of the events are of order 1 and the A matrix is well conditioned.

As an example of the time scaling, let the true time instants of the last five encoder events equal $t_K = \begin{bmatrix}1 & 2 & 3 & 4 & 5\end{bmatrix} \cdot 10^{-5}$ s. The time range of the events equals $\Delta t_K = 4 \cdot 10^{-5}$ s. The time instants are scaled as $t_K^* = \frac{t_K}{\Delta t_K} = \begin{bmatrix}0.25 & 0.5 & 0.75 & 1 & 1.25\end{bmatrix}$ s. The scaled time instants are of order 1 and the scaled time range equals exactly 1. For a second order fit with five events, i.e., $m = 2$ and $n = 5$, the condition number of the A matrix (8.1) with the scaled time instants equals $\text{cond}(A(t_K^*)) = 26.96$ whereas the condition number of the A matrix with the original time instants equals $\text{cond}(A(t_K)) = 5.976 \cdot 10^9$. The time scaling improves the conditioning properties of the A matrix for the estimation of the polynomial coefficients.

Since the position, the velocity and the acceleration estimations are required at the sampling times of the controller, the polynomial with the fitted coefficients P is extrapolated to the desired time instant t_c. The extrapolation of the polynomial to the time instant t_c results in an estimated position $\hat{x}$, estimated velocity $\dot{\hat{x}}$, and estimated acceleration $\ddot{\hat{x}}$ as

$$\begin{aligned}\hat{x}(t)|_{t=t_c} &= p_m(t_c\Delta t_K)^m + p_{m-1}(t_c\Delta t_K)^{m-1} + \ldots + p_0,\\ \dot{\hat{x}}(t) &= \dot{\hat{x}}(t),\\ \ddot{\hat{x}}(t) &= \ddot{\hat{x}}(t).\end{aligned}$$

The time scaling factor used for the estimation of the polynomial coefficients is accounted for in the extrapolation to obtain the correct position, velocity and acceleration estimations.

If the estimation exceeds the quantized position measurement by more than one count, the estimation is replaced by the quantized measurement. This results in an used estimation signal $\hat{x}^*(t)$ as

$$\hat{x}^*(t) = \begin{cases} \hat{x}(t), & \text{if } |\hat{x}(t) - \bar{x}(t)| \leq 1\\ \bar{x}(t), & \text{else,}\end{cases}$$

where $\bar{x}(t)$ (counts) denotes the quantized position measurement. This can for example occur when no new events are detected over a longer time interval.

The easiest motion profile for the time-stamping concept would be a constant velocity reference since this would result in an equally distributed series of events in time. Oscillating signals that change sign in the velocity are more difficult to be handled since these signals have a lower event rate at the turnaround points. In this chapter we consider sinusoidal setpoint profiles since these have a constant changing event rate in time and also contain the turnaround points.

8.4 Skip option

The encoder events (t_k, x_k) suffer from errors due to encoder imperfections, such as a non-uniform slit distribution, misplacement of the sensor photodiodes, eccentricity of the encoder disc, etc. The encoder imperfections introduce an error between the real and observed encoder event. The time instant t_k of the encoder event can have an error of maximum T_e due to the limited resolution T_e of the high-resolution clock.

For real-time experiments, n events are used in the polynomial fit. The errors in the encoder events act as disturbances on the position information. These disturbances are amplified in the velocity estimation and even more in the acceleration estimation. A possible solution would be to increase the number of events. However, in most hardware, the number of available events is limited. In this section, a skip option is proposed to extend the time span covered by the n events in the fit without the need for more events.

8.4.1 Skip

The skip option makes it possible to skip a fixed number of events in between two stored events. In Fig. 8.2, the skip option is shown graphically for a skip of $\sigma = 2$ counts. The real signal and the quantized signal are shown by the solid and dashed line, respectively. The arrows show the events to be discarded since the last stored event. The stored events are shown by the dark grey circles. The light grey circles are the discarded events. In between two dark circles always $\sigma = 2$ events are skipped.

The skip option performs a low-pass filtering on the encoder events with a spatial cut-off frequency that is dependent on the momentary event rate.

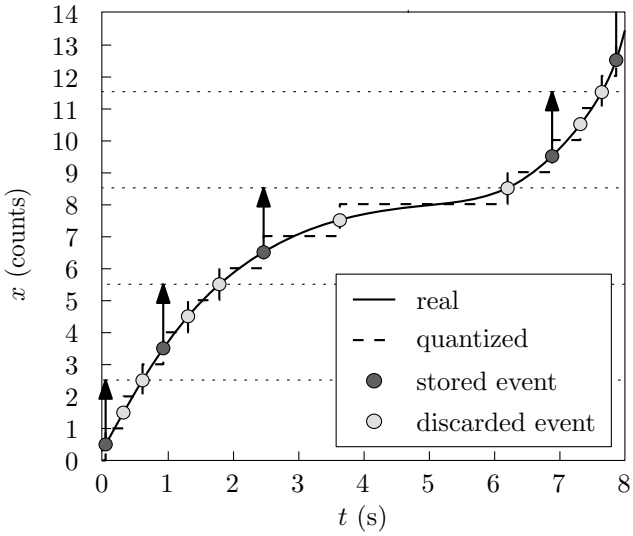

Figure 8.2: Visualization of the skip option in time-stamping for $\sigma = 2$ counts.

For a skip factor of σ (counts), the index numbers of the events to be stored and used for the polynomial fit can be calculated using

$$k_\sigma(k, i) = k - \mathrm{mod}(k - 1, \sigma + 1) - (i - 1)(\sigma + 1), \tag{8.5}$$

where $i \in [1, \ldots, n]$ and the modulus after division is defined as

$$\mathrm{mod}(x, y) = x - y\lfloor x/y \rfloor, \tag{8.6}$$

in which $\lfloor q \rfloor = \max\{p \in \mathbb{Z} \mid p \leq q\}$ denotes the floor function.

8.4.2 Position reconstruction

The events to be used for the position reconstruction with skip are determined by (8.5). In most control applications, the controller is sampled at a fixed sample interval. With skip it can occur that the last event before a controller interrupt is discarded. However, the last encoder event before a controller interrupt is the most recent measurement. Despite the skip option, we choose to always store the most recent encoder even k. This results in the set $K \in \mathbb{R}^n$ with the index number of the events to be stored in the register for a skip option of σ (counts) as

$$K(k) = \begin{cases} [k \quad k_\sigma(k,1) \quad k_\sigma(k,2) \quad \ldots \quad k_\sigma(k,n-1)], & \text{if } k \neq k_\sigma(k,1), \\ [k_\sigma(k,1) \quad k_\sigma(k,2) \quad \ldots \quad k_\sigma(k,n)], & \text{if } k = k_\sigma(k,1). \end{cases} \tag{8.7}$$

When using skip, the matrices A and B for the polynomial fit of (8.4) equal

$$A_\sigma = \begin{bmatrix} t_K^m & t_K^{m-1} & \cdots & 1 \end{bmatrix}, \quad B_\sigma = [x_K].$$

8.4.3 Discussion

One might think that the obtained position information when using the skip option is equal to using a lower resolution encoder or to cancelation of the quadrature signal in the case that $\sigma = 3$ counts. However, the skip option only affects the information that is stored in the register and which occurred in history. Since the most recent event, i.e., the encoder event just before a controller interrupt, is always included in the register (see Section 8.4.2) the resolution or quadrature of the encoder is not affected by the skip option.

As an illustrative example, the position information for a signal when using the skip option and with a lower resolution encoder are compared in Fig. 8.3. To illustrate both the effects of a lower resolution encoder and cancelation of the quadrature, a skip option of $\sigma = 3$ counts is chosen. The true signal is shown in Fig. 8.3 with the solid black line. The encoder events captured at a high-resolution clock are shown by the dots. The light grey circles are skipped events and the dark grey circles denote events that are stored in the register to be used for the polynomial fit. Note that for the fit at $t = 20$ s, the last event before this time is also stored. The position information used for the polynomial fit with $\sigma = 3$ counts is clearly different from the information of an encoder with a four times lower resolution as indicated by the black dashed line in Fig. 8.3. A fit through the stored events in Fig. 8.3 can yield a more accurate position estimation than the low-resolution quantized position.

8.5 Experimental results

In this section, the results of the application of the time-stamping concept to a motion system are discussed. Experiments are performed for different skip values σ and for sinusoidal reference profiles.

The experimental setup consists of the mechanical setup, an amplifier, a TUeDACs Microgiant data-acquisition device [205] and a computer, as shown in the block diagram of Fig. 8.4.

The mechanical setup, shown in Fig. 8.5, consists of a DC motor, which is connected to a rotating mass. On the DC motor, a HEDS-5540 encoder [1] with a re-

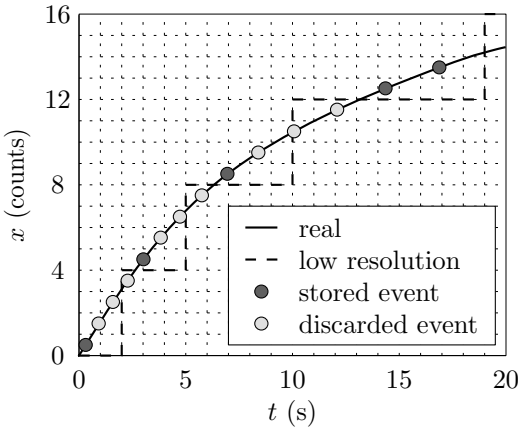

Figure 8.3: Position information for using the skip option with $\sigma = 3$ counts and a 4 times lower resolution encoder.

solution of 100 slits/revolution ($1.5707 \cdot 10^{-2}$ rad/slit) is mounted. On the opposite site, a Heidenhain ROD-426 encoder with 5000 slits/revolution ($3.1416 \cdot 10^{-4}$ rad/slit) is connected to the rotating mass. The output of the Heidenhain encoder will be used as a reference to determine the improvement of the time-stamping concept.

The data-acquisition device, shown in Fig. 8.6, is equipped with 32 bit quadrature counter inputs with a clock frequency of 20 MHz and can thus capture encoder events with a time resolution of 50 ns [205]. Up to five encoder events can be stored in a register. The data of the register is transferred to the controller through USB at a fixed sampling rate of 1 kHz. Furthermore, the Microgiant is equipped with a DAC output, which is used to drive the mechanical setup. The selection and storage of the encoder events when using skip is also performed in the Microgiant.

The real-time application is hosted by a fully preemptive Linux kernel. The computer reads the time-stamping registers of the Microgiant for the polynomial fitting and generates the control signal to the system in order to track a reference profile.

To compare the results for different skip values σ, the system must follow a known reference profile. Therefore, the system is feedback controlled using the high-resolution reference encoder at a bandwidth of $f_{BW} = 10$ Hz. The time-stamping concept is applied with a second order polynomial fit ($m = 2$) though five encoder events ($n = 5$). Experiments are performed without skip and with skip values $\sigma \in \{1,\ 2,\ 3,\ 4,\ 5,\ 10,\ 20\}$. The calculation time of the polynomial fit and the extrapolation is in the order of microseconds, which is much smaller than the controller sampling time $t_c = 1$ ms and can thus be performed in real-time.

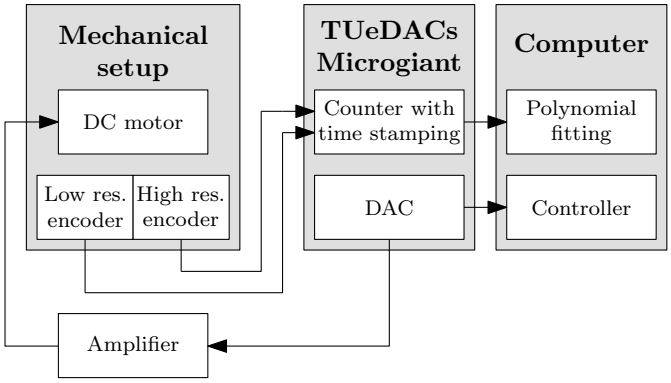

Figure 8.4: Block diagram of the experimental setup.

In order to evaluate the estimation accuracy, reference signals are made by off-line anti-causal filtering of the high-resolution position measurement by a fifth order low-pass filter $L(s)$ with cut-off frequency at 50 Hz. The bandwidth of the low-pass filter $L(s)$ is chosen sufficiently above the frequency of the reference profile and with a sufficiently high order to suppresses the quantization effects present in the high-resolution reference encoder. The reference position, velocity and acceleration are denoted by x_r, $\dot{x}_r$ and $\ddot{x}_r$, respectively. The estimation errors are defined as $e_x = x_r - \hat{x}$, $e_v = \dot{x}_r - \hat{\dot{x}}$ and $e_a = \ddot{x}_r - \hat{\ddot{x}}$.

The skip option performs a time-independent spatial filtering on the encoder events. For constant velocity setpoints, the smallest errors are obtained for maximum skip values. This results in an observation window with the largest position history and thus maximally reduces the effect of the generally high frequent event errors. In this chapter, sinusoidal setpoint profiles are used since these contain varying event rates in time and turnaround points.

Experiments are performed with sinusoidal reference signals $r(t) = A\sin(2\pi f t)$. The influence of varying amplitudes on the estimations is investigated. A changing frequency does not affect the optimal skip option since a changing frequency only affects the time properties of the signal and not the amplitude. The position estimations of time-stamping with $\sigma = 0$ and $\sigma = 3$ are shown in Fig. 8.7 for $f = 1$ Hz and $A = \pi/2$ rad. For the sake of clarity, the position curves are offset from each other by 0.2 rad. The largest errors occur at the maxima of the reference signal, where the velocity equals zero and the time in between events is large.

The measured and the estimated velocities without skip and with $\sigma = 3$ are depicted in Fig. 8.8. For clarity, the overlapping curves are offset from each other by 2 rad/s. The velocity obtained by differentiation of the quantized position (grey

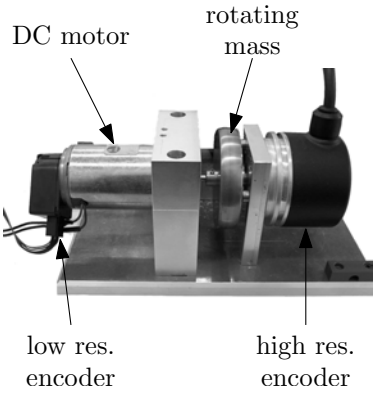

Figure 8.5: The mechanical setup.

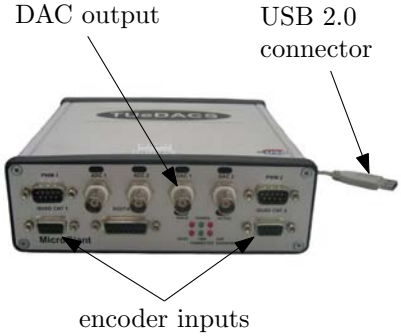

Figure 8.6: The TUeDACs Microgiant data-acquisition device.

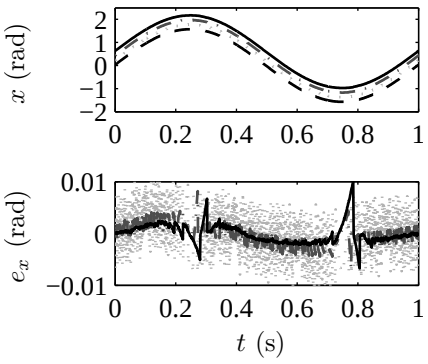

Figure 8.7: Position signals, reference (dashed, black), measurement (dotted, light grey, added offset = 0.2 rad), estimated with $\sigma = 0$ (dash-dotted, dark grey, added offset = 0.4 rad) and with $\sigma = 3$ (solid, black, added offset = 0.6 rad).

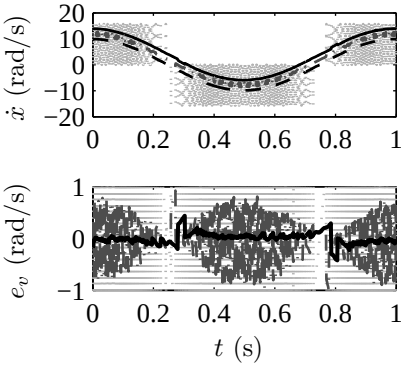

Figure 8.8: Velocity signals, reference (dashed, black), measurement (dotted, light grey), estimated with $\sigma = 0$ (dash-dotted, dark grey, added offset = 2 rad/s) and with $\sigma = 3$ (solid, black, added offset = 4 rad/s).

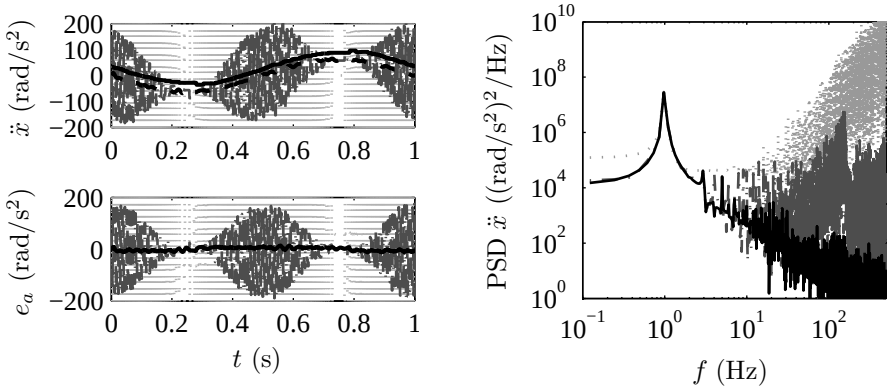

Figure 8.9: Acceleration signals and PSDs, reference (dashed, black), measurement (dotted, light grey), estimated with $\sigma = 0$ (dash-dotted, dark grey) and with $\sigma = 3$ (solid, black, added offset = 30 rad/s^2).

dotted) is clearly not useful for control purposes. With $\sigma = 3$ counts, the estimated velocity (black) results in a lower error than with $\sigma = 0$ counts (dark grey). The momentary oscillations caused by the event errors are filtered out by the skip option. The estimation with $\sigma = 3$ is 54% more accurate than without skip ($\sigma = 0$).

The measured and estimated acceleration signals are shown in Fig. 8.9, for clarity, the overlapping curves are offset from each other by 30 rad/s^2. The quantized acceleration obtained by two times differentiation of the quantized position is completely useless. The acceleration obtained with time-stamping and $\sigma = 0$ counts shows large bursts and is not useful for control purposes. With a skip of $\sigma = 3$ counts, an acceleration signal that is useful for control purposes is estimated. The acceleration estimation with $\sigma = 3$ is 92% more accurate than with $\sigma = 0$ counts.

The power spectral densities (PSDs) of the measured and estimated acceleration signals, depicted in Fig. 8.9, show the influence of time-stamping and the skip option. The PSD of the quantized acceleration is for all frequencies located above the PSDs of the estimated accelerations. The PSD of the estimation with $\sigma = 3$ counts clearly shows the reduction of the high frequencies in the estimation.

The estimation errors for a frequency $f = 1$ Hz and a varying amplitude $A \in \{\pi/16,\ \pi/4,\ \pi/2,\ \pi\}$ are shown in Fig. 8.10. For varying amplitude, the optimal skip value varies. A change in the amplitude changes the amount of encoder counts over one period. Since the skip values perform a spatial low-pass filtering based on the encoder counts, a change in the amplitude changes the cut-off frequency for

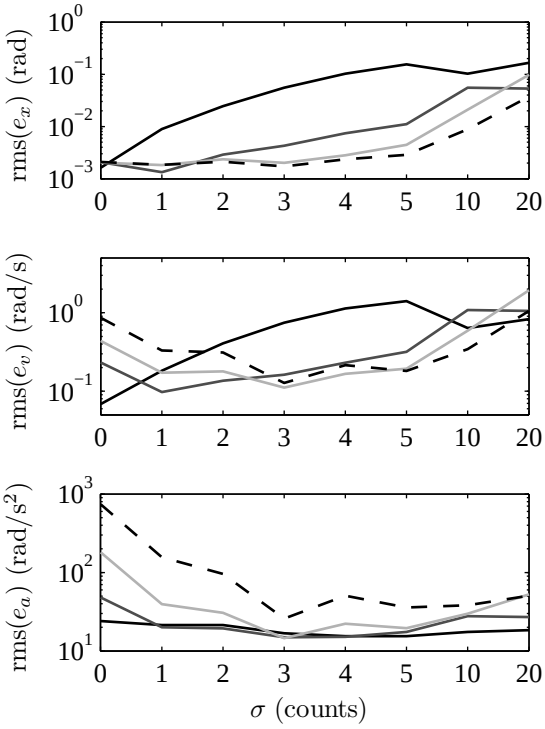

Figure 8.10: Estimation errors with various skip values σ for sinusoidal reference with varying amplitude A, $\pi/16$ rad (black), $\pi/4$ rad (dark grey), $\pi/2$ rad (light grey) and π rad (dashed).

constant skip value. The optimal skip setting, i.e., the skip setting to obtain the smallest estimation error, is dependent on the amplitude. For increasing amplitude the optimal skip value also increases.

In case of a skip of $\sigma = 3$ counts, every fourth subsequent count is stored. For a movement in one direction this corresponds to storing the same event of the four quadrature signals of one encoder slit. As an additional advantage, a skip value of $\sigma = 3$ counts therefore eliminates all event errors that are caused by phase errors between the quadrature signals. The phase errors have the largest contributions at twice the period-time of the quadrature output pulse signals. For sinusoidal setpoints, the velocity changes in time and with this the period-time of the pulse signals. The amount of phase error reduction by the time-stamping concept with

$\sigma = 3$ counts cannot be quantified easily in either the time or the frequency domain due to the change in period-time and the existence of other encoder errors [132].

8.6 Conclusions

The position measurements of optical incremental encoders suffer from quantization errors. Velocity and acceleration estimations obtained by numerical differentiation of the quantized position measurements show large spikes. The time-stamping concept uses encoder events, consisting of the counter value and the corresponding time instant. Through the stored events a polynomial is fitted and extrapolated to the desired time instant. Differentiation of the fitted polynomial and extrapolation lead to velocity and acceleration estimations that are applicable for control purposes. As more and more general-purpose embedded processers have time-stamping capabilities, the opportunities for real-time implementation are highly feasible. This chapter shows that the concept of encoder time-stamping is really useful in control system design.

Encoder imperfections and the limited resolution with which the encoder events are captured lead to errors in the encoder events. These errors result in oscillations in the velocity and acceleration estimations. Increasing the time span covered by the stored encoder events reduces the oscillations in the estimations. However, the amount of events to be stored is limited. Therefore, a skip option is proposed to discard a fixed number of events in between stored events. The skip option increases the covered time span without the need for additional events. The skip option performs a spatial low-pass filtering on the encoder counts.

Experiments show the improvement of the velocity and acceleration estimations with a skip of three events in comparison with differentiation of the quantized position measurement and in comparison with the time-stamping concept without skip. Compared to time-stamping without skip, the velocity estimation is improved by 54% and the acceleration estimation by 92%. The optimal skip value is for sinusoidal references independent on the frequency since a change in the frequency does not change the position information stored in the register. However, it is dependent on the amplitude of oscillation.

Future research includes the derivation of explicit conditions for the optimal number of events, the optimal fit order and the optimal skip value for various operating conditions.

Chapter 9

Optimal higher-order encoder time-stamping

Abstract - Optical incremental encoders are often used to measure the position of motion control systems. The accuracy of the position measurement is determined and bounded by the number of slits on the encoder. The position measurement is affected by quantization errors and encoder imperfections. In this chapter, a higher-order time-stamping (HOTS) method is proposed that uses stored events, consisting of the encoder counts and their time instants, captured at a high-resolution clock. Through the stored events a polynomial is fitted and extrapolated to the controller sampling times. The encoder imperfections are actively compensated using a look-up table. The HOTS method is extended with skip and delay options in order to obtain a good HOTS estimate even for a very limited number of stored events, as desired in many embedded control applications. The skip and delay options perform a spatial and time-based filtering of the stored events without introducing additional delay in the estimates. The optimal HOTS settings are obtained using a measured system response to a band-limited white noise signal and a mixed integer optimization. Real-time experiments on a motion system show that the proposed HOTS method significantly improves the position, velocity and acceleration estimates.

This chapter is based on: R.J.E. Merry, M.J.G. van de Molengraft and M. Steinbuch. Optimal higher-order encoder time-stamping. Submitted, 2009.

9.1 Introduction

Optical incremental encoders are commonly used for position measurements in motion control systems and are available in both rotational and linear form. They consist of three basic components: a slotted disk, a light source and a dual light detector, as shown in Fig. 9.1. The light source shines on the disk, which has a regularly spaced radial pattern of transmissive and reflective elements, called encoder increments. The quadrature light detector measures the amount of light passed through the slotted disc and generates two quadrature output pulse signals, denoted by $\mathcal{A}$ and $\mathcal{B}$. The up and down changes of the pulse signals are counted as a measurement of the encoder position.

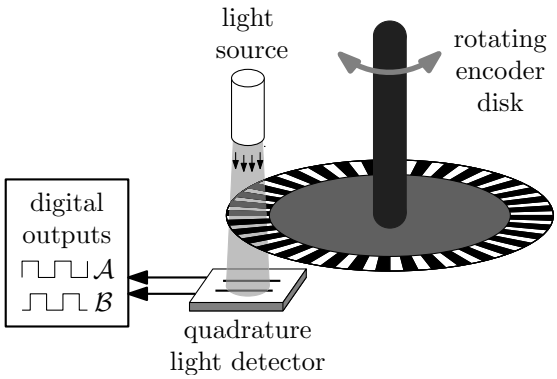

Figure 9.1: Schematic representation of an optical incremental encoder.

For the application of feedback control to motion systems with optical incremental encoders, the position is generally measured at a fixed sampling frequency. The measurement accuracy is limited by the quantization of the encoder, i.e., it is limited by the number of slits on the encoder disk. The velocity and acceleration information obtained by numerical differentiation will contain large spikes due to the quantization of the position signal. The quantization errors can be reduced by either using more expensive encoders with more increments or by using smart signal processing techniques. Furthermore, the position information of the encoders is distorted by several encoder imperfections, such as eccentricity and tilt of the disk, misalignment of the light detector/source, a non-equidistant slit distribution, etc. The quantization and encoder imperfections are the performance limiting factors (PLFs) in optical incremental encoders.

In literature, several signal processing techniques using the measured encoder information are proposed to improve the position, velocity and acceleration infor-

mation obtained from optical incremental encoders. The methods can be divided into two categories [14]: fixed-time methods, which measure the traveled encoder counts over a fixed period-time, and fixed-position methods, which measure the time necessary to travel over a fixed amount of encoder counts.

Fixed-position methods, as proposed in [120,139] and the hybrid algorithm of [41], which switches between fixed-time and fixed-position measurements, are not applicable for control purposes where the controller is evaluated at fixed-time intervals. Although the recent work in event driven control [168] looks promising, today fixed interval timing is still the standard framework for real-time control. Also algorithms that adjust the sampling interval based on the momentary velocity [120], or that switch between sensors with different sampling frequencies based on a velocity threshold [163] do not directly fit into this framework.

The fixed-time methods can be divided into three groups: predictive postfiltering techniques, observer based techniques and indirect measurements. Predictive postfiltering techniques perform a filtering on differentiated position signals to obtain velocity and/or acceleration estimates. The Euler-based methods [115, 223], the discrete-time adaptive windowing velocity estimation [88] and the polynomial delayless predictive differentiators [202] only use the position information of the encoder, thus disregarding the variable rate of occurrence of the encoder events. The transition based logic algorithm [110] assumes the sampling frequency to be much higher than the rate of the encoder events, which does not hold in most motion systems.

Observer based techniques perform a model-based postprocessing on the quantized position measurement to derive more accurate position information. Examples of observer based techniques are Kalman filters [13, 14, 25], dual-sampling rate observers [100] and neural network [29] or fuzzy logic [221] based observers. The acceleration estimator of [107] assumes a high-resolution position signal to be available, which is often not the case. The angular speed and acceleration observer of [196] switches between two filters based on an estimation error, which is generally not available. Since the focus of this chapter is to remove the quantization effect from the measured encoder events, these techniques are not applicable for our purpose. However, combinations of the technique proposed in this chapter with the above observer based techniques might lead to interesting results in the future.

Indirect measurement techniques perform an analog or digital postprocessing of available position and/or velocity signals. In [15], a Taylor-series method and a least-squares method are compared. In [106], the velocity in low-speed regions is estimated using an auxiliary sampling period to measure the interval between the encoder event and the controller sampling time. The velocity is estimated

in [225] by combining the information of an encoder in the low frequency range with the information of an accelerometer in the high frequency range [225], i.e., two sensors are required for the estimation. Furthermore, at low frequencies the velocity of the encoder is obtained by numerical differentiation without taking time information of the encoder events into account. Both the encoder counts and their time instants are used in [23] to estimate the velocity. This method is referred to as the time-stamping concept and will be used as a starting point for the proposed method in this chapter.

Other methods that use the time-stamping concept have been proposed before in literature. The time-stamping concept in combination with an exact quadratic fit through three events is presented in [58] with application to a permanent-magnet motor drive. In [24,28], it is shown that the least squares fit estimators give better performance than Taylor series, FIR filters and backward difference expansion estimators in the presence of encoder imperfections.

The effects and compensation of different kinds of encoder imperfections have also been addressed in literature. The use of a Kalman filter [218] to reduce the effect of encoder measurement errors requires a model of the encoder errors to be available. The encoder errors are regarded to have a stochastic nature [115], are assumed negligible small [163] or are assumed to be repetitive over a small number of increments [24]. In [20], a learning algorithm is applied to generate a look-up table for the encoder slit errors only. A look-up table for the compensation of errors in analog (SinCos) encoders is presented in [193]. In [96], a method to generate a look-up table with the encoder errors for an absolute shaft encoder is described. A neural network is used in [192] to obtain a look-up table containing the encoder errors. In this chapter, we will adopt a data-based approach and combine encoder error compensation using a look-up table with the time-stamping concept.

The contributions of this chapter are threefold. Firstly, a method to estimate accurate position, velocity and acceleration signals based on the time-stamping concept is proposed. The method, referred to as higher-order time-stamping (HOTS), consists of capturing the encoder events in hardware, fitting a polynomial through a number of encoder evens and extrapolating this polynomial to the next controller sampling time. HOTS is an extension of [23,58] for encoder applications and with different polynomial orders fitted through more events in a least squares sense, as recommended in [24, 28]. Compared to Chapter 8, the time-stamping concept is extended with both a skip and delay option, which perform a filtering of the encoder events with a spatial and time-based low-pass filter, respectively. Secondly, a procedure for selecting the optimal HOTS setting such as fit order, number of events and skip or delay parameters is provided. The procedure uses a measured system response to a band-limited white noise signal in a mixed integer optimization. The number of events that can be stored and handled is very limited in most

embedded controllers due to limited memory and CPU resources, which raises the need for the skip and delay options. We show that based on the amount of events that can be captured in hardware, the skip and delay options can be applied to extend the time span covered by the stored events, which allows good position, velocity and acceleration estimates to be made with less stored events. Finally, experimental validation of optimal HOTS combined with active compensation of the encoder imperfections using a look-up table shows the real-time applicability of the proposed method.

This chapter is organized as follows. The higher-order time-stamping concept and the skip and delay options will be explained in more detail in Section 9.2. The optimization problem for the selection of the optimal HOTS settings will be discussed in Section 9.3. The different kind of encoder imperfections and their influence on the encoder events will be described in Section 9.4. The experimental setup will be treated in Section 9.5. The encoder calibration will be presented in Section 9.6. The experimental results of optimal HOTS will be shown in Section 9.7 for different lengths of the hardware register. Finally, conclusions will be drawn in Section 9.8.

9.2 Higher-order time-stamping

In most motion control applications that use optical incremental encoders, the position is measured by reading out the encoder counter value at the sampling times t_c of the controller, as shown in Fig. 9.2. For feedback control, the encoder counter values are generally read at a fixed sampling period T_c. This introduces even for ideal encoders a quantization error of maximally half the encoder resolution x_e.

Using the time-stamping concept [23], the accuracy of the position information using the same resolution encoder can be improved. The time-stamping concept consists of capturing and storing both the time instants t_k and the corresponding position values x_k of the encoder pulse transitions. The index k denotes the encoder event number. The pair (t_k, x_k) is called an encoder event.

If encoder events are used for feedback control, a fixed sampling frequency is not straightforward anymore since the stored encoder events have a non-equidistant distribution in time. To obtain a position estimation at the equidistant sampling times of the controller, a polynomial is fitted through n past encoder events. The fitted polynomial is extrapolated to the next controller sampling time t_c to obtain a fixed-time position estimation, which can be more accurate than the raw quantized measurement.

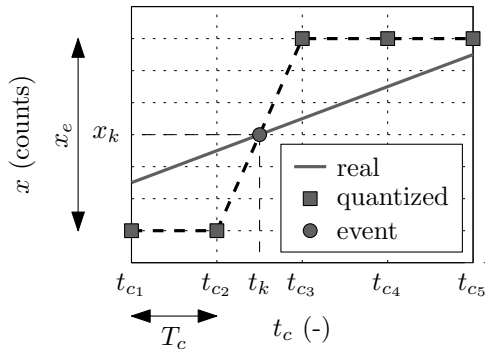

Figure 9.2: Time-stamping concept; the encoder transition x_k and time t_k are captured and stored as an event.

For the fit a polynomial function is chosen because of its wide applicability. However, the ideas and methods proposed in this chapter may also be used with other type of fit functions, e.g., parabolic functions or Fourier series.

The higher-order time-stamping (HOTS) concept consists of executing the following three steps at each controller sampling time:

1. read the hardware register containing stored encoder events at a high-resolution clock added to the encoder,
2. polynomial fitting through n past encoder events,
3. extrapolation of the polynomial to the next controller sampling time t_c.

The individual steps will be discussed in more detail next.

9.2.1 Event capturing and polynomial fit

The higher-order time-stamping concept fits a polynomial of order m through n past encoder events, as shown in Fig. 9.3 for an illustrative example.

The encoder events are captured in hardware at a high-resolution clock added to the encoder, with a sampling rate that is larger than the occurrence rate of the encoder events.

Let the polynomial coefficients to be estimated be denoted by $p_{0,\ldots,m}$. For the polynomial fit the last n events are used, i.e., the events with index numbers $K = [k, k-1, \ldots, k-n+1]$, where the most recent events has index k. The

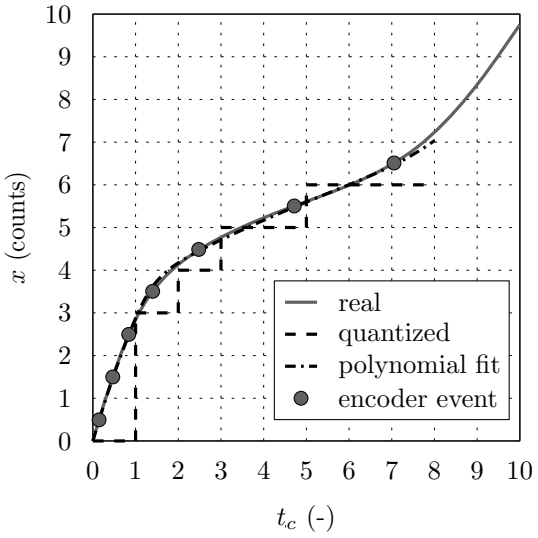

Figure 9.3: Example of the time-stamping concept and polynomial fit.

register contains the stored events $E_K = \begin{bmatrix} t_K & x_K \end{bmatrix}^T$. Now define the matrices $A \in \mathbb{R}^{n \times m+1}$, $P \in \mathbb{R}^{m+1}$ and $B \in \mathbb{R}^n$ as

$$A = \begin{bmatrix} t_{k-n+1}^m & t_{k-n+1}^{m-1} & \cdots & 1 \\ \vdots & \vdots & & \vdots \\ t_{k-1}^m & t_{k-1}^{m-1} & \cdots & 1 \\ t_k^m & t_k^{m-1} & \cdots & 1 \end{bmatrix}, \tag{9.1}$$

$$P = \begin{bmatrix} p_m & p_{m-1} & \cdots & p_0 \end{bmatrix}^T, \tag{9.2}$$

$$B = \begin{bmatrix} x_{k-n+1} & \cdots & x_{k-1} & x_k \end{bmatrix}^T. \tag{9.3}$$

For a least squares fit, the number of events $n > m$. The over-determined system of linear equations to be solved for the polynomial fit equals

$$AP = B.$$

The polynomial coefficients P are obtained in a least squared manner as

$$P = (A^T A)^{-1} A^T B. \tag{9.4}$$

To calculate the coefficients P of (9.4) in real-time, LU factorization without pivoting is used.

9.2.2 Polynomial extrapolation

The HOTS method is to be used in real-time control. Therefore, the estimates for the position, velocity and acceleration are obtained in a fixed-time manner by extrapolating the fitted polynomial to the desired controller sampling time t_c. The estimated position $\hat{x}$, velocity $\hat{\dot{x}}$ and acceleration $\hat{\ddot{x}}$ equal

$$\hat{x}(t_c) = p_m t_c^m + p_{m-1} t_c^{m-1} + \ldots + p_0, \tag{9.5}$$

$$\hat{\dot{x}}(t_c) = m p_m t_c^{m-1} + (m-1) p_{m-1} t_c^{m-2} + \ldots + p_1, \tag{9.6}$$

$$\hat{\ddot{x}}(t_c) = m(m-1) p_m t_c^{m-2} + (m-1)(m-2) p_{m-1} t_c^{m-3} + \ldots + p_2. \tag{9.7}$$

Since the estimates for the position, velocity and acceleration are predicted towards every controller sampling time, no phase lag is introduced in the signals in comparison with for example numerical differentiation of the position signal.

The estimated position can only be an improvement if it is within one encoder increment of the last quantized measurement. If the deviation is larger than one count, the estimation is replaced by the quantized measurement. This results in an adjusted estimated position $\hat{x}^*(t)$ as

$$\hat{x}^*(t) = \begin{cases} \hat{x}(t), & \text{if } |\hat{x}(t) - \bar{x}(t)| \leq 1 \\ \bar{x}(t), & \text{else,} \end{cases}$$

where $\bar{x}(t)$ (counts) denotes the quantized position measurement.

The stored encoder events used for the polynomial fit contain several error sources, such as encoder imperfections, quantization effects of the high but finite resolution clock, electric noise, and external disturbances influencing the encoder position. In Fig. 9.4, an illustrative example of the quantization effects of the high-resolution clock is shown. A linear fit through the last two stored events does not resemble the real signal and is clearly affected by the error in the captured events. If the time in between captured events that are used for the polynomial fit is increased, the effect of the clock errors can be reduced, as shown by the different fits in Fig. 9.4. Moreover, in most embedded hardware, memory and CPU resources seriously limit the practically allowed number of events to be stored, which in turn strongly affects the length of history that can be taken into account. To increase the time span in between stored events, two different options are proposed, referred to as skip and delay. Since these options affect only the stored past encoder events, they do not introduce a phase lag in the polynomial fit and extrapolation procedure. The skip and delay options are introduced in the next sections.

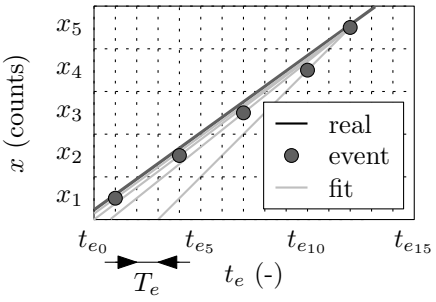

Figure 9.4: Stored events at a high-resolution clock with period-time T_e.

9.2.3 Skip

The skip option skips a fixed number of events in between two stored events. The skip option changes the stored encoder events based on the position information.

In Fig. 9.6(a), the skip option is visualized for a skip value of $\sigma = 2$ counts. The events that are stored in the register are indicated by the dark grey circles, the skipped events by the light grey circles. The arrows in Fig. 9.6(a) show that the skip option performs a filtering on the stored events with a constant position interval.

For a given event k the index numbers of the events to be stored in case of a skip factor of σ (counts) can be calculated as

$$k_\sigma(k,i) = k - \mathrm{mod}(k-1, \sigma+1) - (i-1)(\sigma+1), \tag{9.8}$$

where $i \in [1,\ldots,n]$ and the modulus after division is defined as

$$\mathrm{mod}(x,y) = x - y\lfloor x/y \rfloor, \tag{9.9}$$

in which $\lfloor q \rfloor = \max\{p \in \mathbb{Z} \mid p \leq q\}$ denotes the floor function. Despite the skip option, we choose to always store the most recent encoder even k. This results in the set $K_\sigma \in \mathbb{R}^n$ with the index number of the events to be stored in the register for a skip option of σ (counts) as

$$K_\sigma(k) = \begin{cases} [k \quad k_\sigma(k,1) \quad k_\sigma(k,2) \quad \ldots \quad k_\sigma(k,n-1)], & \text{if } k \neq k_\sigma(k,1), \\ [k_\sigma(k,1) \quad k_\sigma(k,2) \quad \ldots \quad k_\sigma(k,n)], & \text{if } k = k_\sigma(k,1). \end{cases} \tag{9.10}$$

In Fig. 9.5 the selection of K_σ is shown for an illustrative example with $n = 3$ and $\sigma = 1$. For the polynomial fit in case of skip, the events E_{K_σ} are used in the matrices A and B of (9.1) and (9.3), respectively.

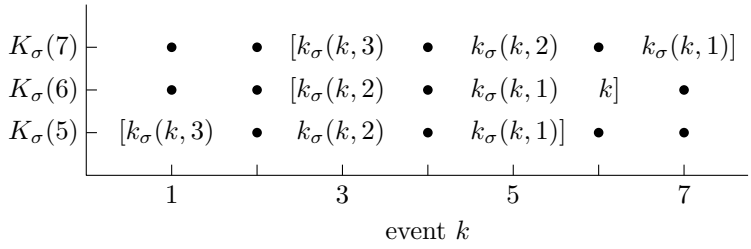

Figure 9.5: Selection of the stored events $K_\sigma(k)$ for skip with $n = 3$ and $\sigma = 1$.

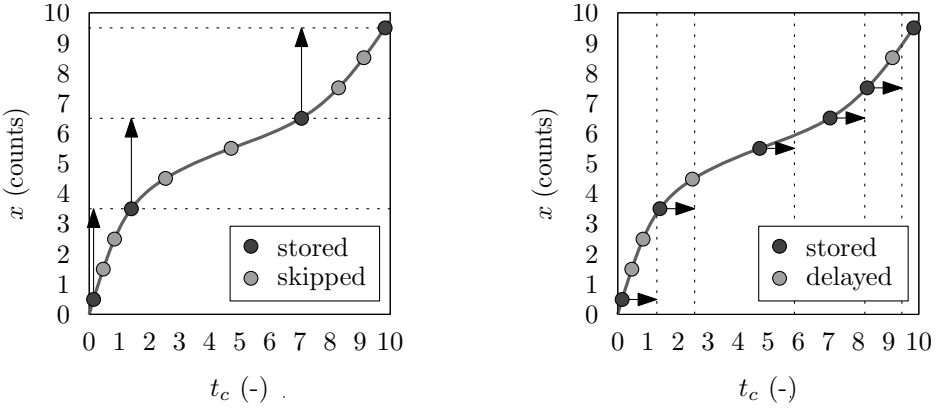

(a) Skip option for $\sigma = 2$ counts.

(b) Delay option for $\delta = 1.2T_c$.

Figure 9.6: Visualization of the skip and delay options.

9.2.4 Delay

The delay option guarantees a fixed minimal time interval of δ (s) in between two stored events. The delay option changes the stored encoder events based on the time information. Since the delay is only applied to the stored encoder events and the estimates are still obtained every controller sampling time, no delay is added to the estimated position, velocity and acceleration signals.

The delay option is visualized in Fig. 9.6(b) for a delay of $\delta = 1.2T_c$. Although the delay is chosen as $\delta > T_c$ for this illustrative example, this is not necessary.

For a delay of δ (s), the index numbers of the events to be stored in the register equal

$$k_\delta(k,i) = \{k^* \mid k^* \leq k,\ t_k^* - t_{k_\delta(k,i-1)} > \delta\}, \tag{9.11}$$

where $i \in [1, \ldots, n]$. According to (9.11), the minimal delay between stored events equals δ (s). So, the delay option can also omit the most recent events from the register. As was the case for the skip option, the most recent event is always required to be stored in the register, leading to the set $K_\delta \in \mathbb{R}^n$ with the index number of the stored events in case of a delay of δ (s) as

$$K_\delta(k) = \begin{cases} [k \quad k_\delta(k,1) \quad k_\delta(k,2) \quad \ldots \quad k_\delta(k,n-1)], & \text{if } k \neq k_\delta(k,1), \\ [k_\delta(k,1) \quad k_\delta(k,2) \quad \ldots \quad k_\delta(k,n)], & \text{if } k = k_\delta(k,1). \end{cases} \tag{9.12}$$

When using the delay option, the events E_{K_δ} are used for the polynomial fit of (9.1) and (9.3).

9.2.5 Scaling

Both the absolute time values and the time span of the stored encoder events $E_K = \begin{bmatrix} t_K & x_K \end{bmatrix}^T$ can be very small, even in the order of the sampling period of the high-resolution clock. This can introduce numerical problems in the polynomial fit and/or conditioning problems in the A matrix. To prevent numerical problems with the higher-order terms in (9.1), the time variable of the oldest event in the register, i.e., the event with time t_{k-n+1}, is redefined to be zero every controller sampling time t_c, i.e., $t_{k-n+1} := t_{k-n+1} - t_c$. Furthermore, to avoid ill-conditioning of the A matrix, the time span Δt_K of the stored events is scaled to one for the polynomial fit (see also [136]). The scaling of the time values of the stored events is done as follows

$$\alpha = \frac{1}{\Delta t_K},$$
$$t_K^* = \alpha t_K,$$

where α (s^{-1}) is the scaling factor and t_K^* (s) are the scaled time instants of the stored events. The scaling factor α also needs to be taken into account in the polynomial extrapolation by redefining the desired polynomial extrapolation time in Eq. (9.5) - (9.7) as $t_c := \alpha t_c$.

9.3 Optimal parameter settings

The performance of the HOTS method depends on the chosen settings for the fit order m, the number of events n and the chosen skip σ or delay δ values. In this section an optimization procedure is presented, which determines the optimal settings for a given system based on experimental data.

For the optimization, the system is excited with a band-limited white noise of which the upper bound is equal to the desired bandwidth of the system since this is generally the frequency up to which the signals have to be accurately tracked. For the optimization, the quantized position measurement and a high accuracy reference signal are required.

The optimization parameters are the settings of HOTS, i.e., $\xi = [m, n, \sigma, \delta]$. The parameters m, n and σ are integer variables, whereas δ is a continuous variable. Since the time-stamping concept is used to estimate the position, velocity and acceleration signals, they are all included in the objective function. The parameters in ξ are optimized such that the root-mean-square (rms) errors between the estimations and the reference signals are minimal. The bounded values of the optimization parameters and the constraint $n > m$ lead to the following bounded mixed-integer optimization problem

$$\begin{aligned} \min_{\xi} f &= \alpha \operatorname{rms}(\hat{e}_x(\xi)) + \beta \operatorname{rms}(\hat{e}_v(\xi)) + \gamma \operatorname{rms}(\hat{e}_a(\xi)), \\ \text{subject to} \quad & 2 \leq m \leq m_{\max}, \\ & 2 \leq n \leq n_{\max}, \\ & 0 \leq \sigma \leq \sigma_{\max}, \\ & 0 \leq \delta \leq \delta_{\max}, \\ & m - n < 0, \end{aligned} \tag{9.13}$$

where the position errors $e_x = x - \hat{x}(\xi)$, the velocity error $e_v = \dot{x} - \hat{\dot{x}}(\xi)$ and the acceleration error $e_a = \ddot{x} - \hat{\ddot{x}}(\xi)$. The scaling parameters α, β and γ are chosen such that the different terms in the objective function f are weighted equally. If the acceleration signal is to be estimated, the fit order m has a minimal value of $m = 2$ and since $n \geq m$, the minimal number of events equals $n = 2$. Furthermore, the skip and delay options are optimized independently, i.e., $\delta = 0$ if $\sigma \neq 0$ and vice versa.

In literature, several methods to solve mixed-integer optimization problems have been proposed, e.g., using evolutionary algorithms [46, 114]. However, in (9.13) the maximum allowable ranges of the integer parameters are not very large, which results in a limited number of possible parameter settings. The optimization of the real parameter δ has only to be done if no skip option is used, i.e., only if $\sigma = 0$. The optimization problem (9.13) is therefore solved by evaluating the objective function for all possible combinations of the integer parameters and by performing a bounded single-variable optimization using the golden section search [21, 150] and parabolic interpolation to obtain the optimal delay δ for all possibilities of (m, n) and $\sigma = 0$. Based on this bounded number of function evaluations and the single-variable optimization, the optimal parameter settings for the selected parameter ranges are obtained.

9.4 Encoder errors

Optical encoders incorporate both mechanical and electrical errors in their output signals, such as [45]:

1. quantization errors,
2. assembly errors (eccentricity, etc.),
3. coupling error (backlash, loose fit, etc.),
4. structural limitations (deformation due to loading),
5. manufacturing tolerances (slit distribution, etc.),
6. ambient effects (temperature, vibrations, dirt, etc.).

These error sources affect the position measurement, the encoder events and thus the quality of the position, velocity and acceleration estimates. The effect of the error sources can be reduced to some extend using the skip and delay options. However, deterministic reproducible errors in the position measurement can be identified.

The encoder imperfections lead to errors in the measured signals. They can be specified as phase shifts, in electrical degrees °e, of the rising or falling edges from the quadrature pulses $\mathcal{A}$ and $\mathcal{B}$ of the encoder output signal (see also Fig. 9.1). The errors can be related to the cycle C, defined as the amount of rotation between two rising edges of channel $\mathcal{A}$. One complete cycle corresponds to 360°e.

In this chapter, we will focus on the calibration of the assembly and manufacturing encoder imperfections. For these types of imperfections, the main error sources in the measured encoder signals are the following

Cycle error
: Indicates the cycle uniformity: the difference between an observed shaft angle which gives rise to one electrical cycle and the nominal angular increment. The cycle error causes the rising edge of the time-stamps of channel $\mathcal{A}$ to be shifted.

Pulse width error
: The deviation of the pulse width from its ideal value of 180°e. The pulse width error introduces a time shift between the time-stamps of the rising edge and falling edge of an equal channel.

Phase error
: The deviation of the phase between channel $\mathcal{A}$ and $\mathcal{B}$ from its ideal value of 90°e caused by the misalignment of the two light sensors. The phase error introduces a time shift between the edges of channel $\mathcal{A}$ with respect to the edges of channel $\mathcal{B}$.

Table 9.1: Errors for the HEDS-5540 encoder [1].

Description	Error (°e)	
	Typical	Maximum
Cycle error	3	5.5
Pulse width error	5	35
Phase error	2	15
Eccentricity	0.04 mm	
Electrical characteristics at 25°C	Rise time: 180 ns	
	Fall time: 40 ns	

Eccentricity
: Eccentricity of the code-wheel introduces a time shift to all edges. The amount of shifting describes a sinusoid with a period of one revolution.

For the experiments presented in this chapter, a HEDS-5540 encoder is used. Table 9.1 contains the encoder imperfections as specified on the data sheet of the encoder [1]. The captured time-stamps also contain information about the encoder imperfections. One method to identify above errors is by driving the encoder at a constant velocity and comparing the measured encoder positions to a high-resolution reference signal. The identified footprint of the encoder errors can be used to adjust the events according to their index number, also for different setpoints than constant velocities. The calibration of the encoder errors makes it possible to compensate for the imperfections, as will be presented in Section 9.6.

9.5 The experimental setup

The experimental setup consists of the motion system, an amplifier, a TUeDACs Microgiant data-acquisition device [205] and a computer, as shown in the block diagram of Fig. 9.7.

The motion system, shown in Fig. 9.8 consists of a DC motor, which is connected to a rotating mass. On the DC motor, a HEDS-5540 encoder [1] with a resolution of 100 slits per revolution is mounted. On the opposite side, a Heidenhain ROD-426 encoder with 5000 slits per revolution is connected to the rotating mass. The HOTS concept is applied to the low-resolution HEDS-5540 encoder. The output of the Heidenhain encoder is used as a reference to determine the improvement of the higher-order time-stamping concept.

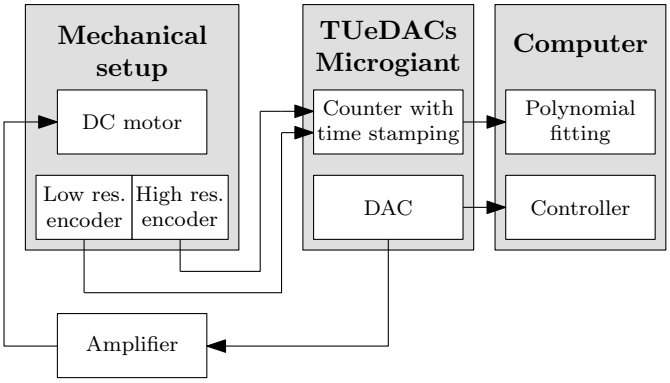

Figure 9.7: Schematic overview of the experimental configuration.

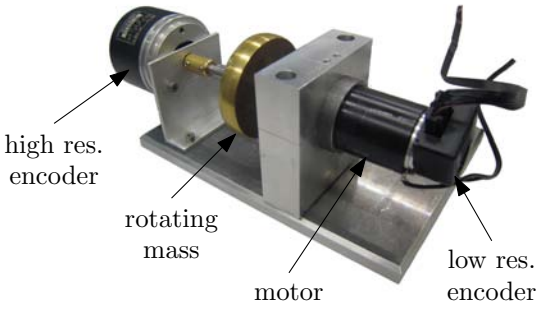

Figure 9.8: The mechanical setup.

The data-acquisition device is equipped with 32-bit quadrature counters with a maximum count frequency of 20 MHz and can generate and store encoder events with a time resolution of 50 ns [205]. Up to 30 past events can be stored inside the register contained in the data-acquisition device. The stored encoder events are transferred to the computer via a USB 2.0 connection at the fixed sampling period t_c of the controller.

A fully preemptive Linux kernel hosts the real-time application at a fixed sampling rate of 1 kHz. The computer reads the stored encoder events of the Microgiant for the polynomial fitting and generates the control signal to the system in order to track a reference profile.

9.6 Calibration results

In this section, calibration of the encoder imperfections of the HEDS-5540 encoder in the setup of Fig. 9.8 is presented. For the experiments, the system is feedback controlled using the output of the high-resolution reference encoder at a closed loop bandwidth of 10 Hz.

The reproducible error sources of the low-resolution encoder can be calibrated using the high-resolution encoder as a reference. The calibration of the encoder imperfections and the validation of the derived look-up table are discussed in the remainder of this section.

9.6.1 Look-up table

Using the measured low- and high-resolution encoder outputs for an experiment with a constant velocity of 0.5 rad/s, a look-up table is constructed by matching each increment of the low-resolution encoder with the output of the high-resolution encoder and averaging over a number of revolutions.

The look-up table, depicted in Fig. 9.9, can be used to adjust the encoder events according to their pulse index. The look-up table shows that the encoder imperfections contain a large low frequent harmonic content with a period of one revolution. This error is probably caused by a combination of the eccentricity and tilt of the code-wheel. Other error sources, such as the non-equidistant distribution of the slits on the code-wheel, are also present in the look-up table.

The derived look-up table of Fig. 9.9 contains high-frequent oscillations. These oscillations are partially due to the encoder imperfections of the individual slits, but also due to the limited resolution of the high-resolution clock at which the events are captured and due to the quantization of the high-resolution reference encoder. Because of the latter two disturbances, the encoder events and quantized position measurements will be compensated for encoder imperfections using a low-pass filtered version of the determined look-up table, as shown in Fig. 9.9 by the solid black line. The low-pass filtered version is obtained by anti-causal filtering with a sixth order low-pass filter with a cut-off frequency of 15 Hz.

9.6.2 Validation

For the validation of the look-up table, an experiment with and without the compensation of the encoder imperfections using the look-up table is performed. For

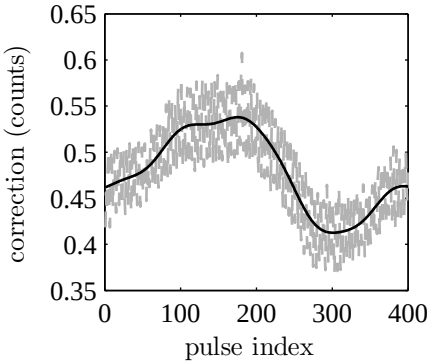

Figure 9.9: Look-up table of the encoder imperfections (grey, dashed) and a zero-phase low-pass filtered version (black, solid).

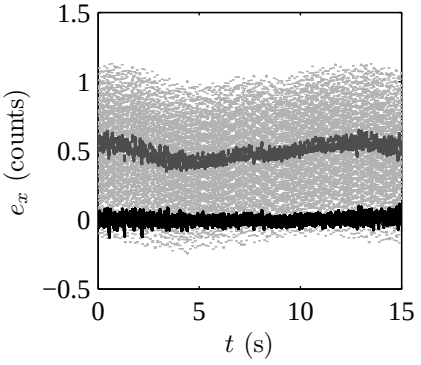

Figure 9.10: Position errors of the low-resolution encoder (light grey, dotted) and of HOTS without look-up table (dark grey, dashed) and with look-up table (black, solid).

this experiment, the higher-order time-stamping concept is applied with settings $\{n, m, \sigma, \delta\} = \{5, 1, 0, 0\}$. The quantized error $\bar{e}_x$ and the estimated error $\hat{e}_x$ with and without application of the look-up table are shown in Fig. 9.10.

The quantized error $\bar{e}_x$ clearly shows the influence of the encoder imperfections on the position measurement by the sinusoidal shape. Although the time-stamping concept reduces the position error, still the influence of the encoder imperfections is clearly visible by the offset and the low-frequent oscillation. The obtained position error of the HOTS concept with adjusted encoder events using the look-up table of Fig. 9.9 is centered around zero and does not contain a distinct harmonic content anymore, as shown by the solid black line in Fig. 9.10.

Since application of the look-up table clearly improves the position estimate, it will be applied to the quantized measurement and stored encoder events of the low-resolution encoder during all experiments for the remainder of this chapter.

9.7 HOTS results

In this section, first the optimal HOTS settings are determined for the large dedicated register length of 30 events. Subsequently, the HOTS optimization is performed for various lengths of the hardware register, where the skip and delay options are considered separately. Finally, the overall optimal HOTS settings and the HOTS

settings for a limited register length of 5 events are experimentally validated for a point-to-point movement, as typically encountered in high-tech mechatronic systems. Besides the position, also the velocity and acceleration signals are estimated.

At the beginning of each experiment, a homing procedure towards the index pulse of the low-resolution HEDS-5540 encoder is performed to obtain reproducible initial conditions. The feedback over the high-resolution encoder is only used for the tests in this chapter to compare different types of setpoints and to evaluate the performance of the HOTS concept. In real-life applications the HOTS estimates themselves are likely to serve as the feedback signals.

The calculation time of the polynomial fit and the extrapolation of the polynomial is in the order of microseconds, which is much smaller than the controller sampling time $t_c = 0.001$ s. Therefore, the higher-order time-stamping can be performed in real-time.

The high-resolution reference encoder also contains quantization effects, although of a much smaller order than the HEDS-5540 encoder. In order to obtain smooth reference position, velocity and acceleration signals, anti-causal filtering of the output of the high-resolution encoder is performed off-line with a fifth order low-pass filter $L(s)$ with a cut-off frequency $f_L = 50$ Hz, which is chosen a factor 5 above the bandwidth of the feedback controlled system. The filtered reference wil be named x_r and its first two derivatives $\dot{x}_r$ and $\ddot{x}_r$, respectively.

The velocity and acceleration estimations obtained by differentiation of the low-resolution encoder contain large spikes, which makes these signals not applicable for control purposes. Therefore, often a low-pass filtered version of the differentiated encoder position is used. The results of the HOTS concept will be compared to a low-pass filtered differentiated version of the low-resolution encoder position. The choice of the cut-off frequency f_c (Hz) of the first order low-pass filter $L_{\text{enc,lr}}(s) = (s/(2\pi f_c) + 1)^{-1}$ is a trade-off between the amount of noise that remains in the signals (high f_c) and the phase delay that is introduced by the filter (low f_c). For the results shown in this chapter, the cut-off frequency equals $f_c = 25$ Hz. The velocity and acceleration signals obtained by low-pass filtering of the differentiated low-resolution encoder signals are denoted by $\dot{\hat{x}}$ and $\ddot{\hat{x}}$, respectively.

The estimation errors are defined as $\hat{e}_x = x_r - \hat{x}$, $\hat{e}_v = \dot{x}_r - \dot{\hat{x}}$, $\hat{e}_a = \ddot{x}_r - \ddot{\hat{x}}$. The error of the quantized position measurement is defined as $\bar{e}_x = x_r - \bar{x}$, where $\bar{x}$ is the quantized low-resolution encoder measurement. The errors of the low-resolution low-pass filtered encoder outputs equal $\bar{e}_v = \dot{x}_r - \dot{\bar{x}}$ and $\bar{e}_a = \ddot{x}_r - \ddot{\bar{x}}$.

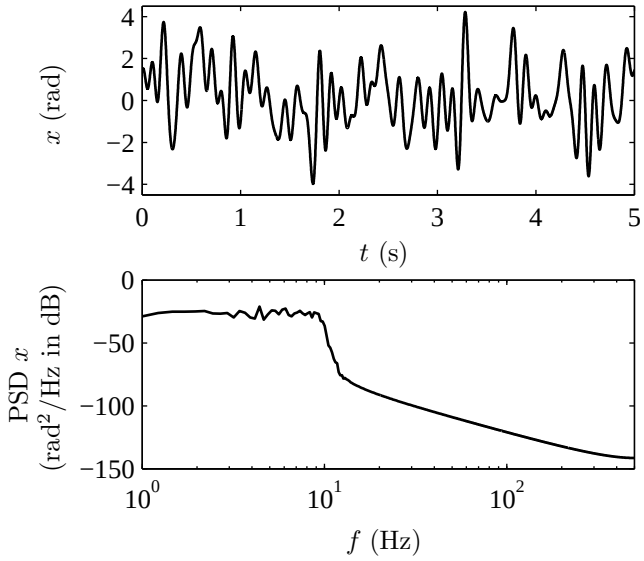

Figure 9.11: Band-limited white noise reference signal and PSD of the signal.

9.7.1 Optimal settings

The optimal HOTS settings for the system of Fig. 9.8 are determined using the optimization (9.13). For this purpose, the system is excited with a band-limited white noise reference signal up to 10 Hz, as shown in Fig. 9.11 together with its power spectral density (PSD).

The upper bounds of the optimization parameters are chosen as $m_{\max} = 5$, $n_{\max} = 30$ (depends on hardware register), $\sigma_{\max} = 10$ (can be chosen arbitrarily) and $\delta_{\max} = 0.01$ (s) (chosen as max 10 controller samples). With these upper bounds, since $m > 2$, $n \geq m$ and no skip and delay can be applied simultaneously, the total number of possibilities equals 1224. Using the optimization procedure as described in Section 9.3, a hardware register of 30 events and scaling factors $\alpha = 1$, $\beta = 1 \cdot 10^{-3}$ and $\gamma = 1 \cdot 10^{-5}$, the optimal HOTS settings for the system of Fig. 9.8 are determined as $\{m, n, \sigma, \delta\} = \{2, 8, 0, 0\}$. This means that the best overall performance is obtained with a second order fit through eight events without skip and delay. The optimal fit order and number of events are a trade-off between under- and overfitting of the data with respect to the bias and variance of the estimated signal [116].

The position errors and the cumulative power spectral densities (CPSDs) of the quantized measurement and the HOTS concept with the optimal settings are

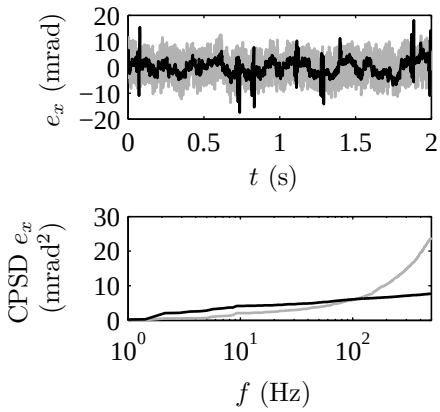

(a) Position error and CPSD.

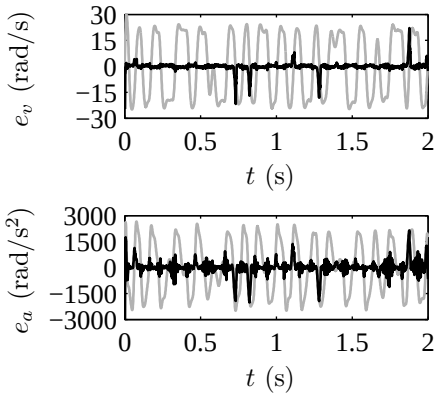

(b) Velocity and acceleration errors.

Figure 9.12: Position error with CPSD and velocity and acceleration errors for the band-limited white noise signal of Fig. 9.11 and time-stamping settings $\{m, n, \sigma, \delta\} = \{2, 8, 0, 0\}$: quantized low-resolution position and low-pass filtered derivatives (grey) and HOTS (black).

shown in Fig. 9.12(a) for the band-limited white noise signal of Fig. 9.11. It can be seen that the variation in the position error with HOTS is smaller than the quantized position error. The CPSDs show the reduction in errors by the HOTS concept. For $f \to \infty$ the CPSDs converge to the squared rms value of the errors, $\text{rms}(\bar{e}_x) = 4.89$ mrad for the quantized measurement and $\text{rms}(\hat{e}_x) = 2.78$ mrad for HOTS. In both cases the encoder imperfections are compensated for using the look-up table of Fig. 9.9. At lower frequencies the position error is larger with HOTS compared to the quantized position due to the deteriorated estimation quality at the time instants where the event rate is low, i.e., at the instants where the velocity of is small. At high frequencies no increase in error is visible since the HOTS concept does not suffer from the quantization errors that are present in the quantized position.

The velocity and acceleration errors of the HOTS concept and the low-pass filtered differentiations of the quantized measurement of the low-resolution encoder are shown in Fig. 9.12(b). The HOTS concept reduces the velocity error by a factor 7.6 from $\text{rms}(\bar{e}_v) = 17.69$ rad/s to $\text{rms}(\hat{e}_v) = 2.33$ rad/s. The acceleration error is reduced from $\text{rms}(\bar{e}_a) = 1487.17$ rad/s^2 for the low-pass filtered differentiated signal to $\text{rms}(\hat{e}_a) = 371.61$ rad/s^2 for the HOTS concept, which is an improvement of a factor 4.0. The spikes in the velocity and acceleration errors obtained with HOTS are caused by the limited estimation accuracy at the time instants where the velocity is low, i.e., where the event rate is small.

For the application of the optimal HOTS settings a hardware register of $n = 8$ events is required. However, this register size may be too large to be incorporated in embedded systems. In Table 9.2, the optimization results for register lengths $n \in [2, 7]$ are given. The optimizations are performed for the skip and delay options separately. In both cases, the possibility of $\sigma = 0$, respectively $\delta = 0$, is also included. It can be seen that for smaller lengths of the hardware register, skip and delay options are required to obtain the optimal results according to (9.13).

For register lengths $n \in [4, 7]$ a skip factor of $\sigma = 1$ events results in the optimal estimation results. The skip option extends the time span covered by the stored events scaled by the instantaneous velocity. The different estimation errors are somewhat larger than for the overall optimal settings, but are still a significant improvement compared to the original quantization errors. A register length of $n = 4$ events with a skip of $\sigma = 1$ resembles the optimal settings the most for all register lengths. These settings also result in smaller errors than with $n \in \{2, 3, 5, 6, 7\}$. For a register length of $n = 3$ events the optimal skip factor is increased to $\sigma = 3$ events, because in that case the time span of the history contained in the register resembles the optimal settings the best. Finally, for $n = 2$ again a skip of $\sigma = 1$ is optimal. Note however that for $n = 2$ and $m = 2$ only an exact fit through the stored events is possible.

The optimizations with delay for register lengths $n \in [1, 7]$ all result in non-zero delays. It can be seen that for a decreasing register length, the optimal delay value increases. This only does not hold for a register $n = 2$, in which an exact fit is made. The estimation errors of the optimizations with skip and delay are comparable. In general, better estimation results are obtained if longer registers can be used. However, for all cases a significant improvement compared to the quantized measurements is obtained. As expected, the skip and delay options are especially useful to increase the time span covered by the stored events in applications where the length of the register is limited.

In the next section, the overall optimal HOTS settings will be compared to the settings for $n = 5$ for a point-to-point movement.

9.7.2 Point-to-point movement

The HOTS concept is applied to a point-to-point movement over 2 rad, described by a third-order setpoint. Fig. 9.13 shows the measured and estimated position signals for the overall optimal settings $\{m, n, \sigma, \delta\} = \{2, 8, 0, 0\}$ and for the optimal settings for a buffer length of $n = 5$ events with skip, i.e., $\{m, n, \sigma, \delta\} = \{2, 5, 1, 0\}$. The estimated position signals of HOTS are available after n events are captured and are therefore not available at the start of each experiment. The application of

Table 9.2: Optimal time-stamping settings optimized with several maximum register lengths n for both skip and delay options and the corresponding rms values of the position, velocity and acceleration errors, compared to the quantized results and the overall optimal results for $n \leq 30$ events.

register n	m_{opt}	σ_{opt}	δ_{opt} (ms)	rms(e_x) (mrad)	rms(e_v) (rad/s)	rms(e_a) (rad/s^2)
quantized				4.89	17.69	1487.17
8	2	0	0	2.78	2.33	371.61
7	3	1	–	4.01	2.62	441.39
6	2	1	–	3.89	3.39	433.56
5	2	1	–	3.94	3.15	500.87
4	2	1	–	3.81	2.73	380.98
3	2	3	–	3.97	3.85	449.32
2	2	1	–	4.64	3.79	922.66
7	2	–	0.82	3.42	2.30	387.92
6	2	–	0.66	3.26	2.09	373.22
5	2	–	1.46	3.53	2.08	390.90
4	2	–	1.67	3.92	1.96	393.20
3	2	–	3.61	4.70	2.61	472.33
2	2	–	0.94	4.36	2.88	922.16

the optimal HOTS settings improves the position estimation by a factor 3.3 from rms($\bar{e}_x$) = 4.92 mrad to rms($\hat{e}_x$) = 1.51 mrad. With the register of $n = 5$ events still an improvement of a factor 2.4 to rms($\hat{e}_x$) = 2.07 mrad is obtained. The CPSDs of the error signals in Fig. 9.13 show the error reduction of both HOTS experiments compared to the quantized measurement. The HOTS results obtained with the smaller hardware register show a small increase in error compared to the overall optimal HOTS. However, for $f \to \infty$ both CPSDs obtained with HOTS converge to a much smaller value than the CPSD of the quantized error.

The velocities, errors and CPSDs of the velocity errors for the point-to-point movement over 2 rad are shown in Fig. 9.14. The optimal HOTS settings improve the velocity from a quantized error of rms($\bar{e}_v$) = 0.13 rad/s to rms($\hat{e}_v$) = 0.025 rad/s, which is an improvement of a factor 5.3. The estimated velocity with the register of $n = 5$ events is a bit more noisy, but still the error is reduced by a factor 4.0 to rms($\hat{e}_v$) = 0.033 rad/s. The CPSDs of both errors obtained with HOTS are located below the CPSD of the quantized error for the complete frequency range. Also the slight increase in error by the limited register length is clearly visible.

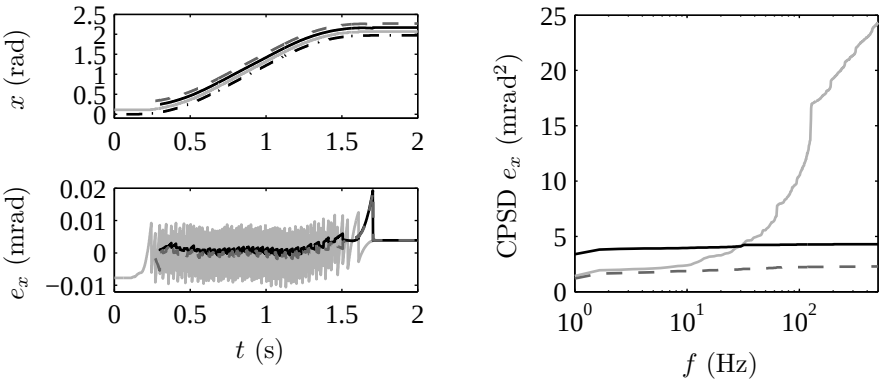

Figure 9.13: Positions, errors e_x and CPSDs of e_x for the point-to-point movement: reference (dashed-dotted, black), quantized measurement (solid, light-grey, added offset = 0.1 rad), HOTS with $\{m, n, \sigma, \delta\} = \{2, 5, 1, 0\}$ (solid, black, added offset = 0.2 rad) and with $\{m, n, \sigma, \delta\} = \{2, 8, 0, 0\}$ (dashed, dark-grey, added offset = 0.3 rad).

The estimated velocities at the end of the movement keep on increasing in time because the estimated velocity with the last stored encoder events is not equal to zero. Since no new events are obtained, the estimated velocity will not change and thus the position will also keep on increasing. This can easily be corrected for by resetting the estimated velocity if no new events occurred during some specified time interval, i.e., if the last estimation becomes too old. Another possible correction method would be to add a weighting to the least squares fit of (9.4). In this way, the most recent events could be weighted more heavily, which could improve the estimation at very low event rates.

The acceleration signals obtained through filtered differentiation and by the HOTS concept for register lengths $n = 8$ and $n = 5$ are shown in Fig. 9.15. Although the estimated acceleration of HOTS shows significant disturbances, the general trend resembles the reference acceleration signal. Furthermore, with the optimal settings, HOTS outperforms the acceleration signal obtained by differentiation and low-pass filtering of the low-resolution quantized measurement by a factor 10.4 with an error reduction from $\text{rms}(\bar{e}_a) = 10.93$ rad/s^2 to $\text{rms}(\hat{e}_a) = 1.06$ rad/s^2. Only a slightly deteriorated acceleration estimation is obtained for reduction of the register length to $n = 5$ with a skip of $\sigma = 1$, the acceleration estimation is still improved by a factor 8.5 to $\text{rms}(\hat{e}_a) = 1.29$ rad/s^2.

All estimates deteriorate when the event rate is low. For the experiments presented in this section, the settings are fixed during the experiment. Adapting the

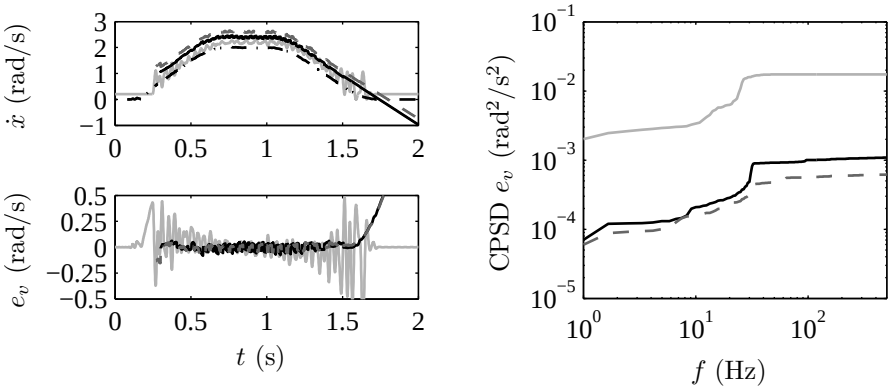

Figure 9.14: Velocities, errors e_v and CPSDs of e_v for the point-to-point movement: reference (dashed-dotted, black), quantized measurement (solid, light-grey, added offset = 0.2 rad/s), HOTS with $\{m, n, \sigma, \delta\} = \{2, 5, 1, 0\}$ (solid, black, added offset = 0.4 rad/s) and with $\{m, n, \sigma, \delta\} = \{2, 8, 0, 0\}$ (dashed, dark-grey, added offset = 0.6 rad/s).

settings based on the momentary event rate of the signal might further improve the estimation quality. This requires an online change of the parameters and a smooth transition between estimates using different settings, which will be subject of future research.

9.8 Conclusions

The position measurements of optical incremental encoders suffer from quantization errors, which are largely amplified in the velocity and acceleration signals obtained by numerical differentiation. To reduce the quantization errors, we proposed a higher-order time-stamping (HOTS) concept to estimate accurate position, velocity and acceleration signals. The HOTS concept extrapolates a least-squares polynomial fit through a number of past encoder events, consisting of the counter value and their time instants.

The HOTS concept is extended with skip and delay options, which perform a spatial and time-based filtering on the stored past encoder events, respectively. The skip and delay options make it possible to extend the time span covered by the stored events. In case of a limited length of the hardware register, the skip and delay options can be used to improve the estimates of the position, velocity and acceleration signals.

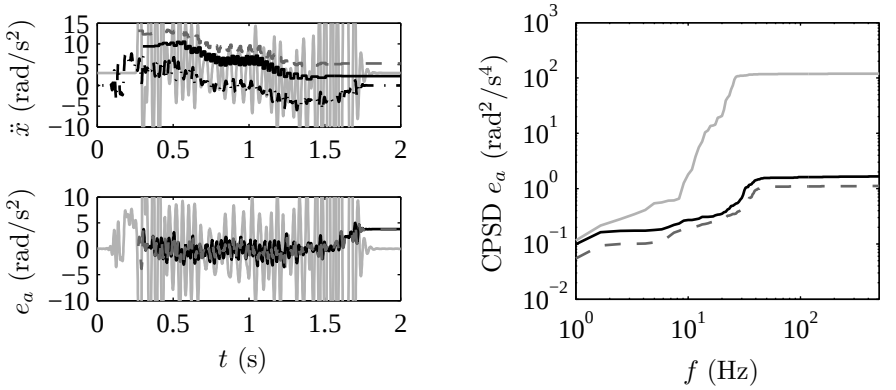

Figure 9.15: Accelerations, errors e_a and CPSDs of e_a for the point-to-point movement: reference (dashed-dotted, black), quantized measurement (solid, light-grey, added offset = 3 rad/s^2), HOTS with $\{m, n, \sigma, \delta\} = \{2, 5, 1, 0\}$ (solid, black, added offset = 6 rad/s^2) and with $\{m, n, \sigma, \delta\} = \{2, 8, 0, 0\}$ (dashed, dark-grey, added offset = 9 rad/s^2).

To reduce the effects of encoder imperfections, the HOTS concept is combined with an encoder error calibration using a look-up table containing a footprint of the encoder imperfections. The application of the look-up table significantly improves the position estimation.

The optimal HOTS settings are obtained by solving a mixed-integer optimization problem using the response of the system to a band-limited white noise input. For optimizations where the register length is limited, skip and delay factors are required to obtain the optimal estimates.

The application of HOTS to motion systems requires a high-resolution clock and a hardware register in the data-acquisition to capture and store the encoder events. Experiments show that HOTS with the overall optimal settings significantly improves the position, velocity and acceleration estimates. If the size of the hardware register is limited, the estimation quality reduces somewhat, but still a large improvement compared to the quantized and low-pass filtered differentiated quantized measurements is obtained using skip and delay, even for a very limited number of stored events.

Future research involves extending the HOTS concept to adjust the settings online based on the momentary event rate of the signal to be estimated.

Part V

Closing

Chapter 10

Conclusions and recommendations

Abstract - The performance of three representative cases of nano-motion systems has been improved by developing dedicated actuator driver software, sensor signal processing and control algorithms. The selected performance limiting factors for nano-motion systems have been modeled and suitable compensation algorithms have been derived. Experimental validation shows the obtained performance improvement. In this chapter, the main conclusions of the different developed models and control algorithms for the three nano-motion systems are given and grouped according to the research objectives. Also, the main contributions of this thesis are summarized. Finally, recommendations for future research are given.

10.1 Concluding remarks

In this thesis, the performance-driven control of nano-motion systems with piezo actuators and/or encoder sensors has been considered. Nano-motion systems are defined as the class of high-precision motion systems that require a movement with velocities ranging from nanometers per second to millimeters per second with (sub)nanometer resolution. To improve the performance of nano-motion systems, state-of-the-art theoretical developments can be translated into useful technologies. For this translation, we adopted a procedure consisting of modeling and compensation of a selected performance limiting factor (PLF) at a component level, followed

by an experimental validation of the obtained performance improvement on a system level.

The design freedom for the compensation methods as considered in this thesis are the actuator driver software, the sensor signal processing and control algorithms. To illustrate the applicability of the adopted PLF procedure, three illustrative cases are selected. The first case is a long-stroke one degree-of-freedom (DOF) nano-motion stage driven by a walking piezo actuator. The second case is a metrological AFM, which contains a short-stroke 3-DOF stage driven by piezo stack actuators through a flexure mechanism. The third case is a rotating encoder system. The different cases exhibit different PLFs to which the adopted systematic approach has been applied successfully, resulting in a performance improvement of the different systems. The specific conclusions of the different developed models, actuator driver software, sensor signal processing and control algorithms are mentioned next in relation with the formulated research objectives.

10.1.1 Nano-motion piezo actuation

The long-stroke nano-motion stage is driven by a walking piezo actuator, which is an elliptical stepping piezo actuator that employs four bimorph piezo legs. A dynamic electro-mechanical model of the piezo legs has been derived, which shows that the resonance frequencies of the legs are located at frequencies $f > 215$ kHz. Although the dynamics of the considered model are irrelevant for control design, the derived model structure could be used to predict the behavior of differently dimensioned bimorph piezo actuators. A static linearization of the model gives a physical interpretation of the bending and extension coefficients of the piezo legs. Experimental validation shows that the static linearized model describes different tip trajectories with an accuracy between 77% and 90%.

A model of the nano-motion stage with the walking piezo actuator is derived, including the alternating drive principle of the piezo legs, the contact dynamics and the stick-slip behavior between the legs and the stage. The friction is modeled using a set-valued force law. For the model, formulated in terms of a differential inclusion, a dedicated time-stepping solver has been developed. The model describes the experimental data in the driving x-direction with an accuracy of 93% and in the perpendicular y-direction with an accuracy of 80% for various electric drive waveforms to the piezo legs.

The short-stroke 3-DOF stage in the metrological AFM is driven by piezo stack actuators in combination with a flexure mechanism. A non-parametric MIMO identification of the 3-DOF stage is used to investigate the coupling beween the

axes through the relative gain array (RGA). The RGA shows that for feedback controller design the axes of the metrological AFM can be considered to be decoupled up to a frequency of 100 Hz. The hysteresis present in the piezo stack actuators of the 3-DOF stage shows an asymmetry between the trace and retrace directions and an offset that is dependent on the applied voltage range. An extended Coleman-Hodgdon model is developed to describe the asymmetric hysteresis with an accuracy of 97% over all voltage ranges.

10.1.2 Piezo driver software design

The use of sinusoidal input waveforms to the piezo legs of the walking piezo actuator results in elliptical tip trajectories with a take-over point between the driving pair of legs at a theoretical zero velocity in the drive direction. New asymmetric waveforms are proposed resulting in overlapping tip trajectories with a take-over point at a non-zero velocity in drive direction, which results in a smoother stage movement at the cost of a somewhat reduced attainable velocity of the motor. The asymmetric waveforms reduce the tracking error between 50% and 92%, depending on the reference velocity.

Using the derived model of the long-stroke 1-DOF nano-motion stage with the walking piezo actuator, a waveform optimization is performed to derive optimal leg orbits for the piezo legs in order to improve the driving properties of the actuator at constant velocity. The model-based waveforms improve the driving properties of the piezo actuator for constant velocities by 24% compared to the asymmetric waveforms. The limited accuracy of the obtained velocity from the model limits the results of the experiments with the model-based waveforms. Therefore, a data-based waveform optimization is performed using the measured stage velocity. The data-based waveforms further improve the driving properties of the piezo legs for constant velocity by 47% compared to the asymmetric waveforms and by 30% compared to the model-based waveforms.

10.1.3 Control of nano-motion systems

The overshoot and settling time of the long-stroke nano-motion stage during point-to-point movements can be reduced significantly by continuously adjusting the step size of the walking piezo actuator dependent on the reference velocity. For this, a feedforward control method of the amplitude and phase of the waveforms to the piezo legs combined with gain scheduling is derived, which reduces the overshoot of a step response by 96% and the settling time by up to 67% compared to feedback control only.

The periodic walking movement of the piezo actuator in the long-stroke nanomotion stage introduces repetitive disturbances in the system. The disturbances are fully repetitive with respect to the angular orientation of the piezo legs, but have a time-varying period-time. A delay-varying repetitive control (DVRC) method is developed, which uses knowledge of the repetitive variable of the system to determine and adjust the time-varying repetitive delay accordingly. A new $\mathcal{H}_\infty$ norm based stability criterion is derived, which gives a sufficient condition for stability using the variation in the repetitive delay, while still allowing the design of the learning filters using frequency domain techniques as is common in repetitive control (RC). DVRC reduces the tracking error by 85% compared to standard RC. Furthermore, DVRC can also be applied for references that have a varying velocity, i.e., which have an inherent time-varying repetitive delay.

Using the derived extended Coleman-Hodgdon hysteresis model for the short-stroke 3-DOF stage of the metrological AFM a model-inversion based feedforward is designed. The feedforward contains separate models for the trace and retrace directions. The switch between the models is performed at standstill of the stage. The application of the hysteresis feedforward improves the tracking performance by 89% compared to using only feedback control and by 43% compared to using feedback control and a position feedforward.

The coupling effects between the axes of the AFM affect the performance of the metrological AFM. Using a low-order system model, a MIMO $\mathcal{H}_\infty$ controller is derived. The MIMO controller is compared to a high-gain decentralized controller that has comparable cross-over frequencies of the diagonal loop gains. Despite the small amount of coupling present in the system, the output sensitivity is shown to have a better disturbance suppression using the MIMO controller compared to the decentralized controller.

The orientation of the sample under the metrological AFM is not necessarily aligned with the direction of actuation, which causes the repetitive disturbances introduced by the sample topography of the transfer samples to become non-repetitive. To compensate for this time-varying character a directional repetitive control (DRC) scheme is developed that aligns the actuation axes with the sample orientation under the microscope. The required coordinate transformation is obtained from a scan over a couple of lines. DRC is shown to reduce the tracking error by 44% compared to standard RC for a rotated sample over 0.22 rad.

10.1.4 Signal processing for incremental encoders

The position measurements of optical incremental encoders suffer from quantization errors and encoder imperfections. An encoder signal processing technique is

developed based on the time-stamping concept, which uses stored past encoder events consisting of the counter value and the corresponding time instant. The method, referred to as higher-order time-stamping (HOTS), consists of storing captured encoder events in a hardware register, polynomial fitting through a number of encoder events and a subsequent extrapolation to the desired controller sampling time. The polynomial fit makes it possible to derive also accurate velocity and acceleration information from the encoder.

HOTS is extended with skip and delay options, which perform a spatial and time-based filtering on the stored past encoder events, respectively. In case of a limited hardware register, the skip and delay options can be used to improve the position, velocity and acceleration estimates. The optimal number of events, order of the polynomial fit and skip or delay are determined by a mixed-integer optimization using the response of the system to a band-limited white noise input.

To reduce the effects of encoder imperfections, HOTS is combined with an encoder error calibration using a look-up table, which significantly improves the position estimation. HOTS combined with the encoder error compensation makes it possible to estimate position, velocity and acceleration signals which are, respectively, 43%, 87% and 75% more accurate than the quantized position measurement and its low-pass filtered derivatives for a point-to-point movements over 2 rad.

10.1.5 Experimental implementation

The derived actuator driver software, sensor signal processing and control algorithms for the three cases have been implemented and validated experimentally.

The long-stroke nano-motion stage is able to track constant velocity profiles ranging from nanometers per second to millimeters per second with tracking errors of nanometers to micrometers using the derived waveforms for the walking piezo actuator and the developed DVRC method. Using the feedforward control method with gain scheduling to adjust the step size, point-to-point movements over a distance of nanometers to the complete stroke of the stage are possible with a significantly reduced overshoot and settling time.

The metrological AFM with the short-stroke 3-DOF piezo stage can perform scanning movements and obtain sample images within the sensor bound of the interferometers using the derived hysteresis feedforward in combination with the feedback controller and the DRC method.

The effects of quantization in optimal incremental encoders can be reduced significantly using HOTS in combination with a look-up table to compensate the encoder

imperfections, resulting in a more accurate position estimate. Furthermore, HOTS makes it possible to derive accurate velocity and acceleration estimates, which are suitable for control purposes.

10.1.6 Thesis contributions

The major contributions of this thesis can be summarized as follows:

- *The derivation of a feedforward control method combined with gain scheduling to adjust the step size of a walking piezo actuator.* The overshoot and settling time of a nano-motion stage driven by a walking piezo actuator can be reduced significantly by continuously adjusting the step size of the actuator dependent on the reference velocity during point-to-point movements.

- *The modeling and waveform optimization for a long-stroke nano-motion stage with a walking piezo actuator.* A model of a long-stroke nano-motion stage with a walking piezo actuator containing the alternating drive principle and contact dynamics and stick-slip effects between the motor and drive surface of the stage is derived, which enables a model-based optimization of the electric waveforms to the piezo legs for a desired stage performance.

- *A repetitive control scheme for systems containing repetitive disturbances that are repetitive with respect to another variable than time.* The periodic walking movement of stepping piezo actuators introduces repetitive disturbances that are fully repetitive with respect to the angular orientation of the piezo legs, but not with respect to time. For systems that exhibit repetitive disturbances that are repetitive with respect to another variable than time, a new repetitive control scheme is derived that adjusts the repetitive delay using the knowledge of the repetitive variable. A new $\mathcal{H}_\infty$ norm based criterion is derived to guarantee stability of the repetitive control scheme for a certain variation in the repetitive delay.

- *A hysteresis feedforward for short-stroke piezo stack driven stages with asymmetric hysteresis and an input voltage range dependent offset.* An extended Coleman-Hodgdon model is derived to model hysteresis effects with an asymmetry between the trace and retrace directions and an offset that is dependent on input voltage range. A corresponding model-inversion based feedforward controller is developed to compensate for the hysteresis.

- *A repetitive control scheme for multi-DOF stages subject to repetitive disturbances in a rotated coordinate frame.* For multi-DOF nano-motion stages

that encounter repetitive disturbances caused by an external source with a rotated coordinate frame, as for example encountered in microscopes or planar stages with repetitive samples, a novel repetitive control scheme is derived that aligns the coordinate axes to render the disturbance fully repetitive.

- *Signal processing algorithm and error compensation method for optical incremental encoders.* To reduce the quantization effects in optical incremental encoders a higher-order time-stamping method is developed, which enables accurate position, velocity and acceleration information to be derived from a number of stored past encoder events.

10.2 Recommendations for future development

Based on the various derived models and compensation methods and performed experiments with the three different cases considered in this thesis, the following recommendations for future development can be given.

10.2.1 The walking piezo actuator

Experiments with the long-stroke nano-motion stage driven by the walking piezo actuator reveal the presence of hysteresis effects, which appear to be located in the separate piezo stacks of the different piezo legs. Modeling of the hysteresis effects enables a feedforward control method to be derived to compensate for the hysteresis in the piezo legs. By a proper adjustment of the input voltages to the different stacks, the hysteresis effects of the legs in both the driving x-direction and the perpendicular y-direction can be compensated for simultaneously, which is expected to further improve the performance of the long-stroke nano-motion stage driven by the walking piezo actuator.

Furthermore, the varying system dynamics, caused by the changing contribution of the legs in the drive direction over one drive cycle as prescribed by the waveforms, can be incorporated in the synthesis of a feedback controller, which could further improve the performance. Available control techniques that can explicitly take the operation-point dependent system dynamics into account are $\mathcal{H}_\infty$ control or linear-parameter-varying (LPV) control.

The actuation of nano-motion systems by elliptical stepping piezo actuators is influenced by several microscopic effects, such as the contact dynamics between

the piezo actuator, roughness of the drive surface, nano-stiffness and friction of the bearings, etc. In this thesis, the effects of stick-slip and contact dynamics are taken into account using elementary models, which give a course approximation. More research into and modeling of these microscopic effects allows even more accurate actuator driver software and control algorithms to be designed, which ultimately improve the performance of the nano-motion stages driven by stepping piezo actuators.

10.2.2 The metrological AFM

The obtained reduction of the coupling effects between the different axes in the metrological AFM is not explicitly specified in the controller synthesis step since only diagonal weighting filters are used. The use of non-diagonal weighting filters to prescribe the desired coupling reduction between the different axes could further improve the performance of the metrological AFM. Specification of the MIMO performance by non-diagonal weighting filters is however non-trivial and is recommended as a direction for future research. Also, the derivation of a low-order control-relevant MIMO model appeared to be a crucial step for a successful control synthesis. For the reduction of dynamic coupling effects, model identification techniques should be developed that derive accurate control oriented models, especially also of the non-diagonal terms in case of a large dynamic range between the different terms in the system FRF.

The derived control algorithms for the metrological AFM enable movements of the 3-DOF stage within the sensor noise bound. However, the desired accuracy of one nanometer in all axes is not achieved due to the large noise bounds on the different axes. To meet the performance specification, the source of the external disturbances should be located and appropriate modifications to the hardware design or control algorithms to suppress the external disturbances are recommended as a future development to improve the performance of the metrological AFM.

10.2.3 The encoder setup

The derived encoder higher-order time-stamping (HOTS) method uses a fixed (optimal) settings for the number of events, the polynomial fit order and the skip or delay options. An extension of the HOTS method to continuously adjust the settings based on the momentary event rate of the signal to be estimated could possibly improve the estimated position, velocity and acceleration signals even further, thus further improving the applicability of incremental encoders for use in nano-motion systems.

Bibliography

[1] Quick assembly two and three channel optical encoders, technical data HEDS-554x. March 2004. http://www.avagotech.com.

[2] D. Y. Abramovitch, S. B. Andersson, L. Y. Pao, and G. Schitter. A tutorial on the mechanisms, dynamics, and control of atomic force microscopes. *American Control Conference*, pages 3488–3502, July 2007.

[3] V. Acary and B. Brogliato. *Numerical Methods for Nonsmooth Dynamical Systems, Applications in Mechanics and Electronics*, volume 35 of *Lecture Notes in Applied and Computational Mechanics*. 2008. ISBN 978-3-540-75391-9.

[4] R. A. Adams. *Calculus*. Addison-Wesley, 4 edition, 1999. ISBN 0-201-39607-6.

[5] H. J. M. T. S. Adriaens, W. L. De Koning, and R. Banning. Modeling piezoelectric actuators. *IEEE/ASME Transactions on Mechatronics*, 5(4):331–341, 2000.

[6] M. Al Janaideh, J. Mao, S. Rakheja, W. Xie, and C. Su. Generalized Prandtl-Ishlinskii hysteresis model: Hysteresis modeling and its inverse for compensation in smart actuators. *IEEE Conference on Decision and Control*, pages 5182–5187, December 2008.

[7] A. Amthor, T. Hausotte, Ch. Ament, P. Li, and G. Jaeger. Friction identification and compensation on nanometer scale. *IFAC World Congress*, pages 2014–2019, July 2008.

[8] T. Ando, N. Kodera, E. Takai, D. Maruyama, K. Saito, and A. Toda. A high-speed atomic force microscope for studying biological macromolecules. *Proceedings of the National Academy of Sciences*, 98(22):12468–12472, October 2001.

[9] M. Aoyagi, S. P. Beeby, and N. M. White. A novel multi-degree-of-freedom thick-film ultrasonic motor. *IEEE Transactions on Ultrasonics, Ferroelectrics and Frequency Control*, 49(2):151–158, February 2002.

[10] APEX Microtechnology. *Data sheet Power Operational Amplifier PB51*, 2005. http://www.apexmicrotech.com/.

[11] S. C. Ashley, U. Aridogan, R. Riddle, and K. Leang. Hysteresis inverse iterative learning control of piezoactuators in AFM. *IFAC World Congress*, pages 8269–8274, July 2008.

[12] M. Ataka, A. Omodaka, N. Takeshima, and H. Fujita. Fabrication and operation of polyimide bimorph actuators for a ciliary motion system. *Journal of Microelectromechanical Systems*, 2(4):146–150, December 1993.

[13] P. R. Bélanger. Estimation of angular velocity and acceleration from shaft encoder measurements. *IEEE Conference on Robotics and Automation*, pages 585–592, May 1992.

[14] P. R. Bélanger, P. Dobrovolny, A. Helmy, and X. Zhang. Estimation of angular velocity and acceleration from shaft-encoder measurements. *The International Journal of Robotics Research*, 17(11):1225–1233, November 1998.

[15] M. F. Benkhoris and M. Aït-Ahmed. Discrete speed estimation from a position encoder for motor drives. *IEEE Conference on Power Electronics and Variable Speed Drives*, pages 283–287, September 1996.

[16] B. Bhushan. *Modern Tribology Handbook*, volume 1. CRC Press, 2001. ISBN 0-8493-8403-6.

[17] G. Binning, C. F. Quate, and Ch. Gerber. Atomic force microscope. *Physical Review Letters*, 56(9):930–933, 1986.

[18] M. L. G. Boerlage. *Rejection of disturbances in multivariable motion systems.* Phd thesis, Eindhoven University of Technology, September 2008. ISBN 978-90-386-1375-8.

[19] M. L. G. Boerlage, A. G. De Jager, and M. Steinbuch. Control relevant blind identification of disturbances. *IEEE Transactions on Control Systems Technology*, 2009.

[20] N. K. Boggarpu and R. C. Kavanagh. New learning algorithm for high-quality velocity measurement from low-cost optical encoders. *IEEE Instrumentation and Measruement Technology Conference*, pages 1908–1913, May 2008.

[21] R. P. Brent. *Algorithms for Minimization Without Derivatives*. Prentice-Hall, 1973. ISBN 0-13-022335-2.

[22] E. Bristol. On a new measure of interaction for multivariable process control. *IEEE Transactions on Automatic Control*, 11(1):133–134, 1966.

[23] R. H. Brown and S. C. Schneider. Velocity observations from discrete position encoders. *IEEE Conference of the Industrial Electronics Society*, pages 1111–1118, November 1987.

[24] R. H. Brown, S. C. Schneider, and M. G. Mulligan. Analysis of algorithms for velocity estimation from discrete position versus time data. *IEEE Transactions on Industrial Electronics*, 39(1):11–19, 1992.

[25] Y. Buchnik and R. Rabinovici. Speed and position estimation of brushless DC motor in very low speeds. *IEEE Convention of Electrical and Electronics Engineers*, pages 317–320, September 2004.

[26] J. A. Butterworth, L. Y. Pao, and D. Y. Abramovich. Architectures for tracking control in atomic force microscopes. *IFAC World Congress*, pages 8236–8250, July 2008.

[27] Z. Cao and G. F. Ledwich. Adaptive repetitive control to track variable periodic signals with fixed sampling rate. *IEEE/ASME Transactions on Mechatronics*, 7(3):378–384, 2002.

[28] P. S. Carpenter, R. H. Brown, J. A. Heinen, and S. C. Schneider. On algorithms for velocity estimation using discrete position encoders. *IEEE Conference on Industrial Electronics, Control, and Instrumentation*, 2:844–849, November 1995.

[29] S. P. Chan. Velocity estimation for robot manipulators using neural network. *Journal of Intelligent and Robotic Systems*, 23(2-4):147–163, 1998.

[30] K. Chang, I. Shim, and G. Park. Adaptive repetitive control for an eccentricity compensation of optical disk drivers. *IEEE Transactions on Consumer Electronics*, 52(2):445–450, 2006.

[31] S. H. Chang, C. K. Tseng, and H. C. Chien. An ultra-precision XYθ_z piezo-micropositioner. Part I: Design and analysis. *IEEE Transactions on Ultrasonics, Ferroelectrics and Frequency Control*, 46(4):897–905, 1999.

[32] W. S. Chang, I. H. Suh, and T. W. Kim. Analysis and design of two types of digital repetitive control systems. *Automatica*, 31(5):741–746, 1995.

[33] C. Chen and G. T. C. Chiu. Compensating for spatially repetitive disturbance with linear parameter varying repetitive control. *IEEE Conference on Control Applications*, pages 736–741, September 2004.

[34] K. K. Chew and M. Tomizuka. Digital control of repetitive errors in disk drive systems. *IEEE Control Systems Magazine*, 10(1):16–20, 1990.

[35] N. Chuang and I. R. Petersen. Robust H^{∞} control of hysteresis in a piezoelectric stack actuator. *IFAC World Congress*, pages 1996–2001, July 2008.

[36] M. Clerc. The swarm and the queen: towards a deterministic and adaptive particle swarm optimization. *Congress on Evolutionary Computation*, pages 1951–1957, July 1999.

[37] B. D. Coleman and M. L. Hodgdon. A constitutive relation for rate-independent hysteresis in ferromagnetically soft materials. *International Journal of Engineering Science*, 24(6):897–919, 1986.

[38] F. Côté, P. Masson, N. Mrad, and V. Cotoni. Dynamic and static modelling of piezoelectric composite structures using a thermal analogy with MSC/-MASTRAN. *Composite Structures*, 65:471–484, 2004.

[39] J. Daafouz, P. Riedinger, and C. Iung. Stability analysis and control synthesis for switched systems: a switched Lyapunov function approach. *IEEE Transactions on Automatic Control*, 47(11):1883–1887, 2002.

[40] A. Daniele, S. Salapaka, M. V. Salapaka, and M. Dahleh. Piezoelectric scanners for atomic force microscopes: design of lateral sensors, identification and control. *American Control Conference*, pages 253–257, June 1999.

[41] S. D'Arco, L. Piegari, and R. Rizzo. An optimised algorithm for velocity estimation method for motor drives. *IEEE Symposium on Diagnostics for Electric Machines*, pages 76–80, August 2003.

[42] F. De Ambroggi, L. Fortuna, and G. Muscato. PLIF: piezo light intelligent flea-new micro-robots controlled by self-learning techniques. *IEEE Conference on Robotics and Automation*, 2:1767–1772, April 1997.

[43] B. De Kraker and D. H. Van Campen. *Mechanical Vibrations*. Shaker Publishing BV, 2001. ISBN 90-423-0165-1.

[44] D. De Roover, O. H. Bosgra, and M. Steinbuch. Internal model based design of repetitive and iterative learning controllers for linear multivariable systems. *International Journal of Control*, 73(10):914–929, 2000.

[45] C. W. De Silva. *Sensors and Actuators, Control System Instrumentation*. CRC Press, 2007. ISBN 1-4200-4483-4.

[46] K. Deep, K. P. Singh, M. L. Kansal, and C. Mohan. A real coded genetic algorithm for solving integer and mixed integer optimization problems. *Applied Mathematics and Computation*, 212(2):505–518, 2009.

[47] S. Devasia, E. Eleftheriou, and S. O. R. Moheimani. A survey of control issues in nanopositioning. *IEEE Transactions on Control Systems Technology*, 15(5):802–823, 2007.

[48] D. L. Devoe and A. P. Pisano. Modeling and optimal design of piezoelectric cantilever microactuators. *Journal of Microelectromechanical Systems*, 6(3):266–270, September 1997.

[49] K. Dirscherl. *Online correction of scanning probe microscopes with pixel accuracy*. Phd thesis, Technical University of Denmark, August 2000.

[50] K. Dirscherl, J. Garnæs, L. Nielsen, J. Jøgensen, and M. Sørensen. Modeling the hysteresis of a scanning probe microscope. *Journal of Vacuum Science and Technology B*, 18(2):621–625, March 2000.

[51] J. Dong, S. M. Salapaka, and P. M. Ferreira. Robust MIMO control of a parallel kinematics nano-positioner for high resolution high bandwidth tracking and repetitive tasks. *IEEE Conference on Decision and Control*, pages 4495–4500, December 2007.

[52] X. Dong and G. Meng. Dynamic analysis of structures with piezoelectric actuators based on thermal analogy method. *International Journal of Advanced Manufacturing Technology*, 27:841–844, 2006.

[53] H. G. M. Dotsch, H. T. Smakman, P. M. J. Van den Hof, and M. Steinbuch. Adaptive repetitive control of a compact disc mechanism. *IEEE Conference on Decision and Control*, pages 1720–1725, December 1995.

[54] J. Doyle, A. Packard, and K. Zhou. Review of LFTs, LMIs, and μ. *IEEE Conference on Decision and Control*, pages 1227–1232, December 1991.

[55] Y. Egashira, K. Kosaka, S. Takada, T. Iwabuchi, T. Baba, S. Moriyama, T. Harada, K. Nagamoto, A. Nakada, H. Kubota, and T. Ohmi. 0.69 nm resolution ultrasonic motor for large stroke precision stage. *IEEE Conference on Nanotechnology*, pages 397–402, October 2001.

[56] E. Elbeltagi, T. Hegazy, and D. Grierson. Comparison among five evolutionary-based optimization algorithms. *Advanced Engineering Informatics*, 19(1):43–53, 2005.

[57] E. Elka, D. Elata, and H. Abramovich. The electromechanical response of multilayered piezoelectric structures. *Journal of Microelectromechanical Systems*, 13(2):332–341, 2004.

[58] Z. Feng and P. P. Acarnley. Extrapolation technique for improving the effective resolution of position encoders in permanent-magnet motor drives. *IEEE/ASME Transactions on Mechatronics*, 13(4):410–415, August 2008.

[59] A. Ferreira and J. G. Fontaine. Coarse/fine motion control of a teleoperated autonomous piezoelectric nanopositioner operating under a microscope. *IEEE/ASME Conference on Advanced Intelligent Mechatronics*, 2:1313–1318, July 2001.

[60] R. H. B. Fey, D. H. Van Campen, and A. De Kraker. Long term structural dynamics of mechanical systems with local nonlinearities. *Journal of Vibration and Acoustics*, 118(2):147–153, 1996.

[61] A. J. Fleming and A. G. Wills. Optimal input signals for bandlimited scanning systems. *IFAC World Congress*, pages 11805–11810, July 2008.

[62] B. A. Francis and W. M. Wonham. The internal model principle of control theory. *Automatica*, 12(5):457–465, 1976.

[63] G. F. Franklin, J. D. Powell, and A. Emami-Naeini. *Feedback Control of Dynamic Systems*. Prentice Hall, 5 edition, 2005. ISBN 0-131-49930-0.

[64] J. Friend, A. Umeshima, T. Ishii, K. Nakamura, and S. Ueha. A piezoelectric linear actuator formed form a multitude of bimorphs. *Sensors and Actuators A*, 109:242–251, 2004.

[65] R. Fukui, A. Torii, and A. Ueda. Micro robot actuated by rapid deformation of piezoelectric elements. *International Symposium on Micromechatronics and Human Science*, pages 117–122, September 2001.

[66] K. Furutaniy, M. Urushibata, and N. Mohri. Displacement control of piezoelectric element by feedback of induced charge. *Nanotechnology*, 9(2):93–98, June 1998.

[67] P. Gahinet and P. Apkarian. A linear matrix inequality approach to H_∞ control. *International Journal of Robust and Nonlinear Control*, 4(4):421–448, 1994.

[68] H. Gao, J. Lam, C. Wang, and Y. Wang. Delay-dependent output-feedback stabilisation of discrete-time systems with time-varying state delay. *IEEE Control Theory and Applications*, 151(6):691–698, 2004.

[69] P. J. Gawthrop, B. Bhikkaji, and S. O. R. Moheimani. Physical-model-based control of a piezoelectric tube scanner. *IFAC World Congress*, pages 11811–11816, July 2008.

[70] Ping Ge and Musa Jouaneh. Modeling hysteresis in piezoceramic actuators. *Precision Engineering*, 17(3):211–221, 1995.

[71] C. Glocker. *Set-Valued Force Laws, Dynamics of Non-Smooth Systems*, volume 1 of *Lecture Notes in Applied and Computational Mechanics*. Springer, 2001. ISBN 978-3-540-41436-0.

[72] M. Goldfarb and N. Celanovic. Modeling piezoelectric stack actuators for control of micromanipulation. *IEEE Control Systems Magazine*, 17(3):69–79, 1997.

[73] P. Grosdidier and M. Morari. Interaction measures for systems under decentralized control. *Automatica*, 22(3):309–319, 1986.

[74] N. W. Hagood and A. J. McFarland. Modeling of a piezoelectric rotary ultrasonic motor. *IEEE Transactions on Ultrasonics, Ferroelectrics and Frequency Control*, 42(2):210–224, 1995.

[75] E. Hairer and G. Wanner. *Solving Ordinary Differential Equations II: Stiff and Differential-Algebraic Problems*, volume 14 of *Springer Series in Computational Mathematics*. Springer, Berlin, 2002. ISBN 3-540-60452-9.

[76] L. Hamm, B. Brorsen, and M. Hagan. Comparison of stochastic global optimization methods to estimate neural network weights. *Neural Processing Letters*, 26(3):145–158, 2007.

[77] S. Hara, Y. Yamamoto, T. Omata, and M. Nakano. Repetitive control system: a new type servo system for periodic exogenous signals. *IEEE Transactions on Automatic Control*, 33(7):659–668, 1988.

[78] Heidenhain. *Exposed linear encoders*, 2003. http://www.heidenhain.com.

[79] L. Hetel, J. Daafouz, and C. Iung. Equivalence between the Lyapunov-Krasovskii functionals approach for discrete delay systems and that of the stability conditions for switched systems. *Nonlinear analysis: Hybrid systems*, 2(3):697–705, 2008.

[80] J. H. Holland. *Adaptation in Natural and Artificial Systems: An Introductory Analysis with Applications to Biology, Control, and Artificial Intelligence*. MIT Press, 1992. ISBN 0-262-58111-6.

[81] J. Hu. Variable structure digital repetitive controller. *American Control Conference*, pages 2686–2690, June 1992.

[82] Y. Huang and C. Cheng. Robust tracking control of a novel piezodriven monolithic flexure-hinge stage. *IEEE Conference on Control Applications*, 2:977–982, September 2004.

[83] Y. Huang and D. Lin. Tracking control of a piezoelectric actuator based on experiment hysteretic modeling. *IEEE/ASME Conference on Advanced Intelligent Mechatronics*, pages 308–313, July 2003.

[84] A. Humphris, M. Miles, and J. Hobbs. A mechanical microscope: High-speed atomic force microscopy. *Applied physics letters*, 86(3):034106, 2005.

[85] L. Ingber and B. Rosen. Genetic algorithms and very fast simulated reannealing: a comparison. *Mathematical and Computer Modelling*, 16(11):87–100, 1992.

[86] Embedded Systems Institute. *Boderc: Model-based design of high-tech systems.* Embedded Systems Institute, Eindhoven, The Netherlands, 2006. ISBN 978-90-78679-01-1.

[87] L. Jabben. *Mechatronic design of a magnetically suspended rotating platform.* Phd thesis, Technische Universiteit Delft, December 2007. ISBN 978-90-9022523-4.

[88] F. Janabi-Sharifi, V. Hayward, and C. S. J. Chen. Discrete-time adaptive windowing for velocity estimation. *IEEE Transactions on Control Systems Technology*, 8(6):1003–1009, 2000.

[89] M. Jang, C. Chen, and J. Lee. Modeling and control of a piezoelectric actuator driven system with asymmetric hysteresis. *IEEE International Conference on Systems & Signals*, pages 676–681, April 2005.

[90] T. Y. Jiang, T. Y. Ng, and K. Y. Lam. Optimization of a piezoelectric ceramic actuator. *Sensors and Actuators A*, 84(1-2):81–94, 2000.

[91] Z. Jiang and Y. Wang. Input-to-state stability for discrete-time nonlinear systems. 37(6):857–869, 2001.

[92] S. Johansson, M. Bexell, and A. Jansson. Fine control of electromechanical motors, 2004. patent 6,798,117.

[93] L. Juhas, A. Vujanic, N. Adamovic, L. Nagy, and B. Borovac. Development of platform for micro-positioning actuated by piezo-legs. *IEEE Conference on Robotics and Automation*, 4(April):3647–3653, 2000.

[94] A. H. Kadhim, T. K. M. Babu, and D. O'Kelly. Measurement of steady-state and transient load-angle, angular velocity, and acceleration using an optical encoder. *IEEE Transactions on Instrumentation and Measurement*, 41(4):486–489, 1992.

[95] C. Kao and B. Lincoln. Simple stability criteria for systems with time-varying delays. *Automatica*, 40(8):1429–1434, 2004.

[96] S. K. Kaul, R. Koul, C. L. Bhat, I. K. Kaul, and A. K. Tickoo. Use of a 'look-up' table improves the accuracy of a low-cost resolver-based absolute shaft encoder. *Measurement Science and Technology*, 8:329–331, 1997.

[97] J. Kennedy and R. Eberhart. Particle swarm optimization. *IEEE International Conference on Neural Networks*, pages 1942–1948, November 1995.

[98] S. Kim and S. H. Kim. A precision linear actuator using piezoelectrically driven friction force. *Mechatronics*, 11(8):969–985, 2001.

[99] J. H. Kindt, G. E. Fantner, J. A. Cutroni, and P. K. Hansma. Rigid design of fast scanning probe microscopes using finite element analysis. *Ultramicroscopy*, 100(3-4):259–265, 2004.

[100] L. Kovudhikulrungsri and T. Koseki. Precise speed estimation from a low-resolution encoder by dual-sampling-rate observer. *IEEE/ASME Transactions on Mechatronics*, 11(6):661–670, 2006. 1083-4435.

[101] T. Kusakawa, A. Torii, K. Doki, and A. Ueda. Control waveforms applied to piezo elements used in a miniature robot. *International Symposium on Micro-Nanomechatronics and Human Science*, pages 307–312, October 2004.

[102] N. M. Kwok, Q. P. Ha, M. T. Nguyen, J. Li, and B. Samali. Bouc-Wen model parameter identification for a MR fluid damper using computationally efficient GA. *ISA Transactions*, 46(2):167–179, 2007.

[103] D.C. Lay. *Linear Algebra and its application.* Pearson Education, Inc., 2003. ISBN 0-321-14992-0.

[104] M. Lazar, D. Muñoz de la Peña, W. P. M. H. Heemels, and T. Alamo. On the stability of min-max nonlinear model predictive control. *Systems & Control Letters*, 57(1):39–48, 2008.

[105] K. K. Leang and S. Devasia. Design of hysteresis-compensating iterative learning control for piezo-positioners: Application to atomic force microscopes. *Mechatronics*, 16(3-4):141–158, April 2006.

[106] S. Lee, T. A. Lasky, and S. A. Velinsky. Improved velocity estimation for low-speed and transient regimes using low-resolution encoders. *IEEE/ASME Transactions on Mechatronics*, 9(3):553–560, September 2004.

[107] S. Lee and J. Song. Acceleration estimator for low-velocity and low-acceleration regions based on encoder position data. *IEEE/ASME Transactions on Mechatronics*, 6(1):58–64, 2001.

[108] R. I. Leine and H. Nijmeijer. *Dynamics and Bifurcations of Non-Smooth Mechanical Systems*, volume 18 of *Lecture Notes in Applied and Computational Mechanics.* Springer, 2004. ISBN 978-3-540-21987-3.

[109] D. J. Leith and W. E. Leithead. Survey of gain scheduling analysis and design. *International Journal of Control*, 73(11):1001–1025, July 2000.

[110] M. Lemkin, P. H. Yang, A. C. Huang, J. Jones, and D. M. Auslander. Velocity estimation from widely spaced encoder pulses. *American Control Conference*, 1:998–1002, June 1995.

[111] J. Li and T. Tsao. Robust performance repetitive control systems. *Journal of Dynamic Systems, Measurement, and Control*, 123(3):330–337, 2001.

[112] H. C. Liaw and B. Shirinzadeh. Study of neural network motion control of piezoelectric actuation systems for micro/nano manipulation. *International Conference on Control, Automation, Robotics and Vision*, pages 1103–1108, December 2008.

[113] C. Lin and S. Yang. Precise positioning of piezo-actuated stages using hysteresis-observer based control. *Mechatronics*, 16(7):417–426, 2006.

[114] Y. Lin, F. Wang, and K. Hwang. A hybrid method of evolutionary algorithms for mixed-integer nonlinear optimization problems. *Congress on Evolutionary Computation*, 3:2159–2166, July 1999.

[115] G. Liu. On velocity estimation using position measurements. *American Control Conference*, 2:1115–1120 vol.2, May 2002.

[116] L. Ljung. *System Identification: theory for the user*. Prentice Hall, 2 edition, 1999. ISBN 0-13-656695-2.

[117] R. W. Longman. Iterative learning control and repetitive control for engineering practice. *International Journal of Control*, 73(10):930–954, 2000.

[118] J. Lopez-Sanchez, P. Miribel-Catala, E. Montane, M. Puig-Vidal, S. A. Bota, J. Samitier, U. Simu, and S. Johansson. High accuracy piezoelectric-based microrobot for biomedical applications. *IEEE Conference on Emerging Technologies and Factory Automation*, pages 603–609, October 2001.

[119] T. S. Low and W. Guo. Modeling of a three-layer piezoelectric bimorph beam with hysteresis. *Journal of Microelectromechanical Systems*, 4(4):230–237, 1995.

[120] J. N. Lygouras. Accurate velocity evaluation using adaptive sampling interval. *Microprocessors and Microsystems*, 24(5):269–275, 2000.

[121] MatWeb. Material property data, piezo kinetics 556, PZT. www.matweb.com, February 2009.

[122] P. Mendes and D. B. Kell. Non-linear optimization of biochemical pathways: applications to metabolic engineering and parameter estimation. *Bioinformatics*, 14(10):869–883, 1998.

[123] R. J. E. Merry, N. C. T. De Kleijn, M. J. G. Van de Molengraft, and M. Steinbuch. Control of a high precision stage using a walking piezo actuator. *IEEE Conference on Control Applications*, pages 1285–1290, October 2007.

[124] R. J. E. Merry, N. C. T. De Kleijn, M. J. G. Van de Molengraft, and M. Steinbuch. Using a walking piezo actuator to drive and control a high precision stage. *IEEE/ASME Transactions on Mechatronics*, 14(1):21–31, February 2009.

[125] R. J. E. Merry, D. J. Kessels, M. J. G. Van de Molengraft, W. P. M. H. Heemels, and M. Steinbuch. Delay-varying repetitive control applied to a walking piezo actuator. Submitted, 2009.

[126] R. J. E. Merry, D. J. Kessels, M. J. G. Van de Molengraft, and M. Steinbuch. Repetitive control applied to a walking piezo actuator. *International Conference on Control & Automation*, December 2009.

[127] R. J. E. Merry, M. G. J. M. Maassen, M. J. G. Van de Molengraft, N. Van de Wouw, and M. Steinbuch. Modeling and waveform optimization of a nano-motion piezo stage. Submitted, 2009.

[128] R. J. E. Merry, M. J. C. Ronde, M. J. G. Van de Molengraft, K. R. Koops, and M. Steinbuch. MIMO H_∞ and directional repetitive control of a metrological AFM. Submitted, 2009.

[129] R. J. E. Merry, M. Uyanik, K. R. Koops, M. J. G. Van de Molengraft, M. Van Veghel, and M. Steinbuch. Modeling, identification and control of a metrological atomic force microscope with a 3 DOF stage. *American Control Conference*, pages 2716–2721, June 2008.

[130] R. J. E. Merry, M. Uyanik, M. J. G. Van de Molengraft, K. R. Koops, and M. Steinbuch. Identification, control and hysteresis compensation of a 3 DOF metrological AFM. *Asian Journal of Control*, 11(2):130–143, 2009.

[131] R. J. E. Merry, M. Uyanik, M. J. G. Van de Molengraft, M. Steinbuch, K. R. Koops, and M. Van Veghel. Modeling and compensation of asymmetric hysteresis in a piezo actuated metrological AFM. *American Control Conference*, pages 967–972, June 2009.

[132] R. J. E. Merry, M. J. G. Van de Molengraft, and M. Steinbuch. Error modeling and improved position estimation for optical incremental encoders by means of time stamping. *American Control Conference*, pages 3570–3575, July 2007.

[133] R. J. E. Merry, M. J. G. Van de Molengraft, and M. Steinbuch. Iterative learning control with wavelet filtering. *International Journal of Robust and Nonlinear Control*, 18:1052–1071, 2008.

[134] R. J. E. Merry, M. J. G. Van de Molengraft, and M. Steinbuch. Velocity and acceleration estimation for optical incremental encoders. *IFAC World Congress*, pages 7570–7575, July 2008.

[135] R. J. E. Merry, M. J. G. Van de Molengraft, and M. Steinbuch. Modeling of a walking piezo actuator. *International Conference on Control & Automation*, December 2009.

[136] R. J. E. Merry, M. J. G. Van de Molengraft, and M. Steinbuch. Velocity and acceleration estimation for optical incremental encoders. *Mechatronics*, accepted, 2009.

[137] R. J. E. Merry, M. J. G. Van de Molengraft, and M. Steinbuch. Modeling of a walking piezo actuator. Submitted, 2009.

[138] R. J. E. Merry, M. J. G. Van de Molengraft, and M. Steinbuch. Optimal higher-order encoder time-stamping. Submitted, 2009.

[139] M. Mizuochi, T. Tsuji, and K. Ohnishi. Multirate sampling method for acceleration control system. *IEEE International Symposium on Industrial Electronics*, 4:1629–1634, June 2005.

[140] S. O. R. Moheimani and A. J. Fleming. *Piezoelectric Transducers for Vibration Control and Damping*. Advances in Industrial Control. Springer, London, 2006. ISBN 1-84628-331-0.

[141] C. G. Moles, P. Mendes, and J. R. Banga. Parameter estimation in biochemical pathways: A comparison of global optimization methods. *Genome Research*, 13(11):2467–2474, November 2003.

[142] K. L. Moore. *Iterative Learning Control for Deterministic Systems*. Springer: Berlin, 1993. ISBN 0-387-19707-9.

[143] J. J. Moreau. *Unilateral contact and dry friction in finite freedom dynamics*, volume 302 of *Non Smooth Mechanics and Applications, CISM Courses and Lectures*. Springer-Verslag, 1988.

[144] G. Muller. *CAFCR: A Multi-view Method for Embedded Systems Architecting; Balancing Genericity and Specificity*. Phd thesis, Technische Universiteit Delft, June 2004. ISBN 90-5639-120-2.

[145] B. N. Norden. On the compression of a cylinder in contact with a plane surface. Technical Report NBSIR 73-243, Institute for Basic Standards, National Bureau of Standards, Washington D.C., USA, July 1973.

[146] P. W. J. M. Nuij, M. Steinbuch, and O. Bosgra. Experimental characterization of the stick/sliding transition in a precision mechanical system using the third order sinusoidal input describing function. *Mechatronics*, 18(2):100–110, 2008.

[147] T. A. E. Oomen and O. H. Bosgra. Robust-control-relevant coprime factor identification: A numerically reliable frequency domain approach. *American Control Conference*, s:625–631, June 2008.

[148] T. A. E. Oomen, R. M. A. Van Herpen, and O. H. Bosgra. Robust-control-relevant coprime factor identification with application to model validation of a wafer stage. *IFAC Symposium on System Identification*, pages 1044–1049, July 2009.

[149] L. Y. Pao, A. Butterworth, and D. Y. Abramovich. Combined feedforward/feedback control of atomic force microscopes. *American Control Conference*, pages 3509–3515, July 2007.

[150] P. Papalambros and D. Wilde. *Principles of Optimal Design, Modeling and Computation*. Cambridge University PRess, 2 edition, 2000. ISBN 0-521-62727-3.

[151] P. M. Pardalos and H. E. Romeijn. *Handbook of Global Optimization*, volume 2. 2002. ISBN 1-4020-0632-2.

[152] N. Petit, M. B. Milam, and R. M. Murray. Inversion based constrained trajectory optimization. *IFAC Symposium on Nonlinear Control Systems*, July 2001.

[153] F. Pfeiffer and C. Glocker. *Multibody Dynamics with Unilateral Contacts*. Wiley, 1996. ISBN 978-0-471-15565-2.

[154] PI. *P-517, P-527 Multi-Axis, Piezo Nanopositioning / Scanning Stages with Parallel Metrology*, 2005. www.physikinstrumente.com.

[155] Piezomotor AB. *PiezoLEGS motor*, 2004. www.piezomotor.com.

[156] F. Pigache, F. Giraud, and B. Lemaire-Semail. Modelling and identification of a planar standing wave ultrasonic motor. *European Physical Journal, Applied Physics*, 34:55–65, 2006.

[157] G. Pipeleers, B. Demeulenaere, J. De Schutter, and J. Swevers. Robust high-order repetitive control: Optimal performance trade-offs. *Automatica*, 44(10):2628–2634, 2008.

[158] A. Preumont. *Mechatronics Dynamics of Electromechanical and Piezoelectric Systems*, volume 136 of *Solid Mechanics and its Applications*. Springer, 2006. ISBN 1-4020-4695-2.

[159] H. Richter, E. A. Misawa, D. A. Lucca, and H. Lu. Modeling nonlinear behavior in a piezoelectric actuator. *Precision Engineering*, 25:128–137, 2001.

[160] M. J. C. Ronde, R. J. E. Merry, M. J. G. Van de Molengraft, K. R. Koops, and M. Steinbuch. Multivariable control of a metrological atomic force microscope. *European Control Conference*, pages 2265–2270, August 2009.

[161] D. Ruffieux, M. A. Dubois, and N. F. De Rooij. An AlN piezoelectric microactuator array. *Conference on Micro Electro Mechanical Systems*, pages 662–667, January 2000.

[162] W. J. Rugh and J. S. Shamma. Research on gain scheduling. *Automatica*, 36(10):1401–1425, October 2000.

[163] J. Rull, A. Sudria, J. Bergas, and S. Galceran. Programmable logic design for an encoder-based velocity sensor in a DSP-controlled motion system. *IEEE Conference on Emerging Technologies and Factory Automation*, 2:1243–1247 vol.2, October 1999.

[164] K. Saito, K. Kamiyama, T. Ohmae, and T. Matsuda. A microprocessor-controlled speed regulator with instantaneous speed estimation for motor drives. *IEEE Transactions on Industrial Electronics*, 35(1):95–99, 1988.

[165] S. Salapaka, A. Sebastian, J. P. Cleveland, and M. V. Salapaka. Design, identification and control of a fast nanopositioning device. *American Control Conference*, 3:1966–1971, May 2002.

[166] S. Salapaka, A. Sebastian, J. P. Cleveland, and M. V. Salapaka. High bandwidth nano-positioner: a robust control approach. *Review of Scientific Instruments*, 73(9):3232–3241, 2002.

[167] S. P. Salisbury, D. F. Waechter, R. B. Mrad, S. E. Prasad, R. G. Blacow, and Y. Bin. Closed-loop control of a complementary clamp piezoworm actuator. *IEEE/ASME Transactions on Mechatronics*, 12(6):590–598, December 2007.

[168] J. H. Sandee. *Event-driven control in theory and practice: trade-offs in software and control performance*. Phd thesis, Eindhoven University of Technology, December 2006. ISBN 978-90-386-1933-0.

[169] T. Sashida and T. Kenjo. *An Introduction to Ultrasonic Motors*, volume 28 of *Monographs in Electrical and Electronic Engineering*. Clarendon Press, Oxford, 1993. ISBN 0-19-856395-7.

[170] P. Schellekens, N. Rosielle, H. Vermeulen, M. Vermeulen, S. Wetzels, and W. Pril. Design for precision: Current status and trends. *Annals of the CIRP*, 47(2):557–586, 1998.

[171] G. Schitter. Advanced mechanical design and control methods for atomic force microscopy in real-time. *American Control Conference*, pages 3503–3508, July 2007.

[172] G. Schitter, G. E. Fanter, P. J. Thurner, J. Adams, and P. K. Hansma. Design and characterization of a novel scanner for high-speed atomic force microscopy. *IFAC Mechatronics Conference*, pages 819–824, September 2006.

[173] G. Schitter, P. Menold, H. F. Knapp, F. Allgöwer, and A. Stemmer. High performance feedback for fast scanning atomic force microscopes. *Review of Scientific Instruments*, 72(8):3320–3327, 2001.

[174] G. Schitter, R. W. Stark, and A. Stemmer. Fast contact-mode atomic force microscopy on biological specimen by model-based control. *Ultramicroscopy*, 100(3-4):253–257, 2004.

[175] G. Schitter, A. Stemmer, and F. Allgöwer. Robust 2 DOF-control of a piezoelectric tube scanner for high speed atomic force microscopy. *American Control Conference*, 5:3720–3725, June 2003.

[176] A. Sebastian and S. M. Salapaka. Design methodologies for robust nano-positioning. *IEEE Transactions on Control Systems Technology*, 13(6):868–876, 2005.

[177] R. S. Sexton, R. E. Dorsey, and J. D. Johnson. Optimization of neural networks: A comparative analysis of the genetic algorithm and simulated annealing. *Eurpoean journal of Operational Research*, 114(3):589–601, 1999.

[178] E. Shamoto and T. Moriwaki. Development of a "walking drive" ultraprecision positioner. *Precision Engineering*, 20(2):85–92, March 1997.

[179] S. Skogestad and I. Postlethwaite. *Multivariable Feedback Control, analysis and design*. John Wiley & Sons, 2 edition, 2005. ISBN 0-470-01168-8.

[180] R.C. Smith, M. Salapaka, and L. Cherveny. A Preisach model for quantifying hysteresis in an atomic force microscope. *SPIE Smart Structures and Materials*, page 7, March 2002.

[181] D. Song and C. J. Li. Modeling of piezo actuator's nonlinear and frequency dependent dynamics. *Mechatronics*, pages 391–410, 1999.

[182] J Song and A. der Kiureghian. Generalized Bouc–Wen model for highly asymmetric hysteresis. *Journal of Engineering Mechanics*, 132(6):610–618, 2006.

[183] S. Song, J. Kim, C. Yim, and H. Kim. H_∞ control of discrete-time linear systems with time-varying delays in state. *Automatica*, 35(9):1587–1591, 1999.

[184] E. D. Sontag. Smooth stabilization implies coprime factorization. *IEEE Transactions on Automatic Control*, 34(4):435–443, 1989.

[185] M. Steinbuch. Repetitive control for systems with uncertain period-time. *Automatica*, 38:2103–2109, 2002.

[186] M. Steinbuch and M. L. Norg. Advanced motion control: An industrial perspective. *European Journal of Control*, 4(4):278–293, 1998.

[187] M. Steinbuch, S. Weiland, and T. Singh. Design of noise and period-time robust high-order repetitive control, with application to optical storage. *Automatica*, 43(12):2086–2095, 2007.

[188] M. Steinbuch, S. Weiland, J. Van den Eerenbeemt, and T. Singh. On noise- and period-time sensitivity in high order repetitive control. *IEEE Conference on Decision and Control*, pages 1295–1300, December 2004.

[189] A. Stemmer, G. Schitter, J. M. Rieber, and F. Allgöwer. Control strategies towards faster quantative imaging in atomic force microscopy. *European Journal of Control*, 11(4-5):384–395, 2005.

[190] Y. Stepanenko and S. Chun-Yi. Intelligent control of piezoelectric actuators. *IEEE Conference on Decision and Control*, pages 4234–4239, December 1998.

[191] Z. Sun. Tracking or rejecting rotational-angle dependent signals using time varying repetitive control. *American Control Conference*, pages 144–149, June 2004.

[192] K. K. Tan and K. Z. Tang. Adaptive online correction and interpolation of quadrature encoder signals using radial basis functions. *IEEE Transactions on Control Systems Technology*, 13(3):370–377, 2005.

[193] K. K. Tan, H. X. Zhou, and T. H. Lee. New interpolation method for quadrature encoder signals. *IEEE Transactions on Instrumentation and Measurement*, 51(5):1073–1079, 2002.

[194] P. E. Tenzer and R. B. Mrad. A systematic procedure for the design of piezoelectric inchworm precision positioners. *IEEE/ASME Transactions on Mechatronics*, 9(2):427–435, June 2004.

[195] S. Tien, Q. Zou, and S. Devasia. Iterative control of dynamics-coupling-caused errors in piezoscanners during high-speed AFM operation. *IEEE Transactions on Control Systems Technology*, 13(6):921–931, 2005.

[196] A. Tilli and M. Montanari. A low-noise estimator of angular speed and acceleration from shaft encoder measurements. *Automatika*, 42(3-4):169–176, 2001.

[197] M. Tomizuka. Zero phase error tracking algorithm for digital control. *Journal of Dynamic Systems, Measurement, and Control*, 109:65–68, 1987.

[198] I. C. Trelea. The particle swarm optimization algorithm: convergence analysis and parameter selection. *Information Processing Letters*, 85(6):317–325, 2003.

[199] T. Tsao, Y. Qian, and M. Nemani. Repetitive control for asymptotic tracking of periodic signals with an unknown period. *Journal of Dynamic Systems, Measurement, and Control*, 122(2):364–369, June 2000.

[200] K. Uchino and J. R. Giniewicz. *Micromechatronics*, volume 22 of *Materials Engineering*. Marcel Dekker, Inc., New York, 2003. ISBN 0-8247-4109-9.

[201] S. Ueha and Y. Tomikawa. *Ultrasonic Motors: Theory and Applications*. Monographs in Electrical and Electronic Engineering. Clarendon Press, Oxford, 1994. ISBN 0-19-859376-7.

[202] S. Väliviita and O. Vainio. Delayless differentiation algorithm and its efficient implementation for motion control applications. *IEEE Transactions on Instrumentation and Measurement*, 48(5):967–971, 1999.

[203] H. Van Brussel, D. Reynaerts, P. Vanherck, M. Versteyhe, and S. Devos. A nanometre-precision, ultra-stiff piezostepper stage for ELID-grinding. *CIRP Annals - Manufacturing Technology*, 52(1):317–322, 2003.

[204] J. C. L. Van de Griendt and F. C. Van Nijmweegen. *User manual TUeDACS/1 Advanced Quadrature / analog / digital Interface (AQI)*. Eindhoven University of Technology, April 2005. http://www.tuedacs.nl/Products/AQI/AQI.html.

[205] J. C. L. Van de Griendt and F. C. Van Nijmweegen. *Usermanual TUeDACS/1 USB MicroGiant*. Eindhoven University of Technology, January 2006. http://www.tuedacs.nl/Products/MicroGiant/MicroGiant.html.

[206] M. Van de Wal, G. Van Baars, F. Sperling, and O. Bosgra. Multivariable $\mathcal{H}_\infty/\mu$ feedback control design for high-precision wafer stage motion. *Control Engineering Practice*, 10(7):739–755, 2002.

[207] P. M. J. Van den Hof. Closed-loop issues in system identification. *Annual Reviews in Control*, 22:173–186, November 1998.

[208] P. Van Overschee and B. De Moor. N4SID: Subspace algorithms for the identification of combined deterministic stochastic systems. *Automatica*, 30(1):75–93, 1994.

[209] M. Versteyhe, D. Reynaerts, and H. Van Brussel. Hybrid force-position control of clamping with a piezo-stepper. *IEEE Control Systems Magazine*, 19(2):31–39, April 1999.

[210] M. Viberg. Subspace-based methods for the identification of linear time-invariant systems. *Automatica*, 31(12):1835–1851, 1995.

[211] J. Wallaschek. Contact mechanics of piezoelectric ultrasonic motors. *Smart Materials and Structures*, 7:369–381, 1998.

[212] M. S. Weinberg. Working equations for piezoelectric actuators and sensors. *Journal of Microelectromechanical Systems*, 8(4):529–533, December 1999.

[213] G. Weiss, Q. Zhong, T. C. Green, and J. Liang. H^{∞} repetitive control of DC-AC converters in microgrids. *IEEE Transactions on Power Electronics*, 19(1):219–230, 2004.

[214] Y. Wu and Q. Zou. Iterative control approach to compensate for the hysteresis and the vibrational dynamics effects of piezo actuators. *American Control Conference*, pages 424–429, June 2006.

[215] Y. Wu, Q. Zou, and C. Su. A current cycle feedback iterative learning control approach for AFM imaging. *IEEE Transactions on Nanotechnology*, 8(4):515–527, 2009.

[216] K. Yamada, T. Arakawa, H. Hoshi, and T. Okuyama. Two-step design method for robust repetitive control systems. *JSME international journal Series C, Mechanical Systems, Machine Elements and Manufacturing*, 46(3):1068–1074, 2003.

[217] Q. Yang, C. Ftaclas, M. Chun, and D. Toomey. Hysteresis correction in the curvature adaptive optics system. *Journal of the Optical Society of America A*, 22(1):142–147, January 2005.

[218] Y. Yang, N. Rees, and T. Chuter. Reduction of encoder measurement errors in UKIRT telescope control system using a Kalman filter. *IEEE Transactions on Control Systems Technology*, 10(1):149–157, 2002.

[219] J. Yi, S. H. Chang, K. Moon, and Y. Shi. Dynamic modeling of an L-shape PMN-PT piezo-based manipulator. *American Control Conference*, pages 3755–3760, June 2008.

[220] W. Ying and Z. Qingze. Iterative control approach to compensate for both the hysteresis and the dynamics effects of piezo actuators. *IEEE Transactions on Control Systems Technology*, 15(5):936–944, 2007.

[221] F. Yusivar, D. Hamada, K. Uchida, S. Wakao, and T. Onuki. A new method of motor speed estimation using fuzzy logic algorithm. *International Conference on Electric Machines and Drives*, pages 278–280, May 1999.

[222] B. Zhang and Z. Zhu. Developing a linear piezomotor with nanometer resolution and high stiffness. *IEEE/ASME Transactions on Mechatronics*, 2(1):22–29, March 1997.

[223] Y. Zhang, G. Liu, and A. A. Goldenberg. Friction compensation with estimated velocity. *IEEE Conference on Robotics and Automation*, 3:2650–2655, May 2002.

[224] K. Zhou, J. C. Doyle, and K. Glover. *Robust and Optimal Control*. Prentice Hall, Inc., 1996. ISBN 0-13-456567-3.

[225] W. Zhu and T. Lamarche. Position tracking control with velocity from accelerometer and encoder. *IFAC World Congress*, pages 14828–14833, July 2008.

[226] Q. Zou and S. Devasia. Preview-based optimal inversion for output tracking: application to scanning tunneling microscopy. *IEEE Transactions on Control Systems Technology*, 12(3):375–386, 2004.

Appendix A

Position-dependent dynamics of the walking piezo motor

Abstract - This appendix describes the varying dynamics of the nano-motion stage driven by the walking piezo actuator. The system dynamics vary due to the changing contribution of the legs in the drive direction over one drive cycle as prescribed by the waveforms. To identify this variation, frequency response function (FRF) measurements are performed for a grid of leg angles over one walking period. The excitation level is chosen such that no slip is present. The series of FRF measurements shows a clear variation of the static gain as function of the leg orientation.

A.1 FRF measurements

To drive the nano-motion stage using the walking piezo actuator, the input voltages to the different piezo stacks are described by periodic waveforms. Different waveforms result in different tip trajectories and driving properties of the motor. For a given choice of the waveforms, the contributions of the piezo legs in the drive direction vary as function of the momentary orientation of the piezo legs α in each drive cycle.

The derived model of the individual piezo legs in Chapter 3 shows that the dynamics vary with the angular orientation α (rad) resulting from the momentary

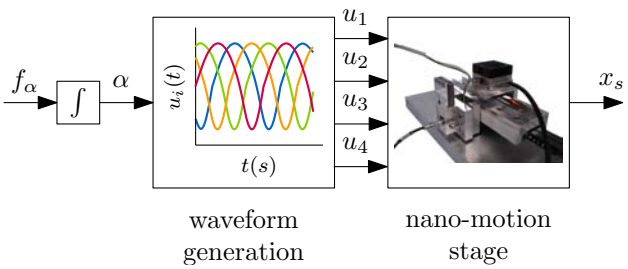

Figure A.1: Schematic representation of the piezo-driven nano-motion stage from a control perspective.

input voltages. In this appendix the frequency response function (FRF) measurements of the system, consisting of the nano-motion stage (see Fig. 4.1) and the walking piezo actuator, are presented for different angular orientations α (rad) of the legs in each drive cycle as prescribed by the asymmetric waveforms, derived in Chapter 2.

A schematic representation of the system from a control perspective is shown in Fig. A.1. The input of the system is the drive frequency f_α (Hz) of the piezo legs, the output is the stage position x_s (m). Integration of the drive frequency gives the momentary leg angle α (rad) of the piezo legs as

$$\alpha(t) = 2\pi \int_0^t f_\alpha(\tau) d\tau.$$

The input voltages to the motor $u_i(t)$, $i \in \{1, 2, 3, 4\}$ are calculated for a chosen waveform shape using the angle α. For the asymmetric waveforms, derived in Chapter 2, the input voltages equal

$$u_{i,asym}(t) = \frac{A}{\bar{A}} a_0 + \frac{A}{\bar{A}} \sum_{k=1}^{4} \{a_k \cos[k\alpha(t) + k\psi_i] + b_k \sin[k\alpha(t) + k\psi_i]\}, \qquad \text{(A.1)}$$

where the maximum and input amplitudes $\bar{A} = A = 46$ V, the Fourier coefficients equal $a_0 = 28.80$, $a_1 = -10.78$, $b_1 = 18.73$, $a_2 = 2.387$, $b_2 = 4.097$, $a_3 = 1.985$, $b_3 = -0.007792$, $a_4 = 0.2298$ and $b_4 = -0.3901$, and the phases $[\psi_1, \psi_2, \psi_3, \psi_4] = [0, \frac{1}{2}\pi, \pi, \frac{3}{2}\pi]$ rad.

The walking piezo motor contains four piezo legs, which drive the nano-motion stage in pairs of two, i.e., the first pair p_1 is driven by input voltages $u_1(t)$ and $u_2(t)$ and the second pair p_2 by input voltages $u_3(t)$ and $u_4(t)$. Using the model derived in Chapter 3, the positions of the tips of the piezo legs in the driving

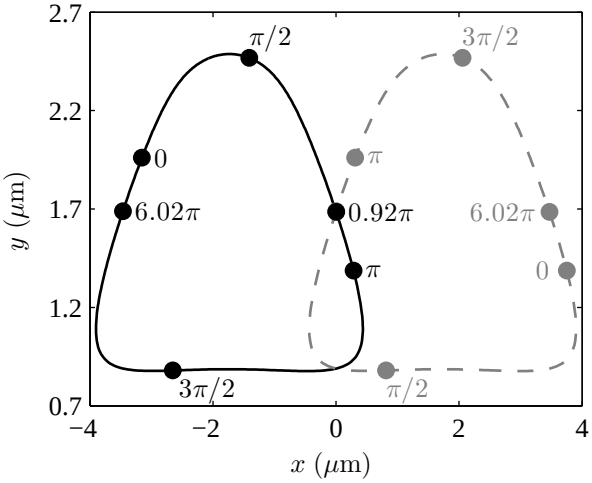

Figure A.2: Leg trajectories of pair p_1 (black, solid) and pair p_2 (grey, dashed) for the asymmetric waveforms (A.1), the marked points indicate the angular orientation α (rad) of the legs in one drive cycle.

x-direction and perpendicular y-direction equal

$$\begin{aligned} x_{p_1} &= c_x(u_1(t) - u_2(t)), \\ y_{p_1} &= c_y(u_1(t) + u_2(t)), \\ x_{p_2} &= c_x(u_3(t) - u_4(t)), \\ y_{p_2} &= c_y(u_3(t) + u_4(t)), \end{aligned} \tag{A.2}$$

with bending coefficient $c_x = 64.5$ nm/V and extension coefficient $c_y = 29.8$ nm/V. The theoretical tip trajectories of the piezo legs with the asymmetric waveforms (A.1) for $\alpha \in [0,\ 2\pi]$ are shown in Fig. A.2. Since (A.2) only describes relative positions, the trajectory of pair p_2 is shifted over 1.73 nm such that the two curves intersect at the theoretical take-over moment between the driving pair of legs at $\alpha = 0.92\pi$ rad. Fig. A.2 shows that a variation in α over a fixed angle results in displacements with different contributions in the driving x-direction, i.e., in a different gain between the input α and output x_s.

To measure the different FRFs as function of the orientation α, the integrator in Fig. A.1 is omitted for the moment, making α the input variable of the system. The FRFs are measured by exciting the system with a white noise signal for small angles $\tilde{\alpha}$ around a nominal angle α_0. The occurrence of stick-slip between the legs and the drive strip of the nano-motion stage would affect the FRF measurements and the locations of the measured (anti-)resonances [146]. Therefore, the amplitude of

the noise should be chosen such that slip between the legs and the drive strip of the nano-motion stage is avoided. To determine the maximum allowable amplitude of $\tilde{u}$, the waveforms u_i, $i \in \{1, 2, 3, 4\}$ are linearized at each nominal angle α_0 as

$$\tilde{u}_i(t) = u_i(\alpha_0) + \frac{\delta u_i}{\delta \alpha}(\alpha_0)\tilde{\alpha}, \tag{A.3}$$

where the input $\tilde{\alpha}$ is a white noise signal with frequencies $\tilde{f}$ up to the Nyquist frequency, i.e., $\tilde{f} \in [0, 2]$ kHz for a sampling frequency $f_s = 4$ kHz. The amplitude of the white noise signal $\tilde{A}$ (rad) should be chosen such that the resulting leg inertia term $m\ddot{x}_{p_{1,2}}$ (N) is less than the friction force F_w (N) in the contact between the legs and the stage, with m (kg) the lumped mass of stage and the legs in x-direction. The maximum allowable amplitude $\tilde{A}$ of the noise on the angular orientation $\tilde{\alpha}$ is determined as $\tilde{A}_{\max} = 0.03$ rad using the leg acceleration calculated with (A.2) for the linearized waveforms (A.3), the mass $m = 0.428$ kg and a static friction force $F_w = 13$ N.

The measured FRFs $H(f)$ from the angle α to the position of the stage x_s are shown in Fig. A.3 for various nominal leg angles $\alpha_0 \in [0, 2\pi]$. A clear fluctuation in the gain of the FRFs at low frequencies can be seen, with magnitudes of $|H(f)|_{f<200\text{ Hz}} \in \{-143.0, -121.6\}$ dB. The first resonance frequency at $f = 543$ Hz and anti-resonance frequency at $f = 575$ Hz show no significant changes for varying α, indicating that the corresponding modes of the system are not affected by the angular orientation of the legs in the drive cycle. The resonances at frequencies $f > 600$ Hz are affected by the momentary angular orientation of the piezo legs in a drive cycle.

For feedback control purposes, the variation in system dynamics should be incorporated in the control synthesis to guarantee stability of the closed-loop system. The variation of the low-frequent gain shows a structure over a complete drive cycle $\alpha \in [0, 2\pi]$, which will be discussed in the next section.

A.2 Gain variations

The gain of the different FRFs at 100 Hz is plotted in Fig. A.4 as function of the leg angle α. Two clear maxima can be observed at angles $\alpha = 2.79$ rad and $\alpha = 5.93$ rad. From Fig. A.2 follows that at these angles the legs are located near the theoretical take-over point, at which both leg pairs are in contact with the stage and move both in positive x-direction. The minima are located at angles where the driving pair of legs has only a small component in the driving x-direction and the other pair of legs is located in the bottom corners of the leg trajectories.

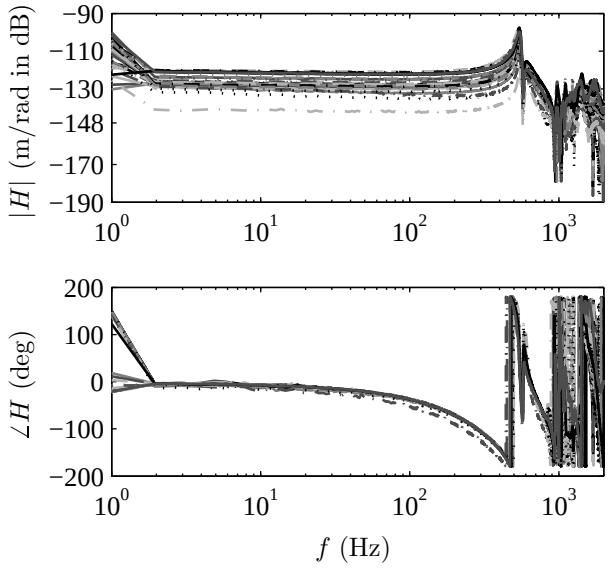

Figure A.3: FRFs of $H(f)$ for different angles α of the piezo legs.

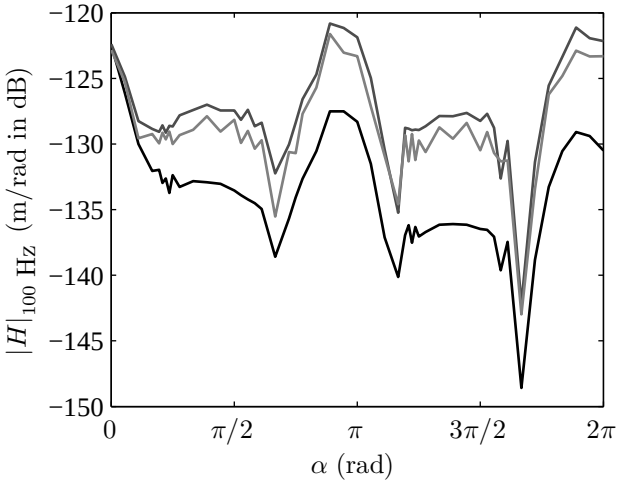

Figure A.4: Gain $|H(f)|_{100\ \mathrm{Hz}}$ as a function of the angle α (rad).

The sequence of FRF measurements is repeated several times to test the reproducibility, as shown by the different lines in Fig. A.4. The two grey lines are obtained by measurements at the same day, whereas the black line results from measurements at a different day. The measurements performed at the same day show a large correspondence. The measurement of the different day shows an offset over the complete angle α. Possible explanations for the variation can be temperature effects, contamination of the piezo legs or different contact properties at the used parts of the drive strip during the different measurements.

Modeling of the gain variation and incorporating it in the controller synthesis, e.g., using $\mathcal{H}_\infty$ control, gain scheduling or linear parameter varying (LPV) control, could possibly further improve the performance of the piezo-driven nano-motion stage, which is subject of future research.

Appendix B

List of symbols

Roman uppercase

Symbol	Description	Unit
A	amplitude	
	area	m^2
	system matrix	
	matrix with encoder event times	
$\mathcal{A}$	pulse signal	V
B	input matrix	
	vector with encoder event positions	
$\mathcal{B}$	pulse signal	V
C	controller transfer function	
	capacitance	F
	output matrix	
	set of admissible friction forces	
	cycle	
D	electric displacement	C/m^2
$\underline{D}$	damping matrix	
E	electric field	V/m
	Young's modulus	Pa

E	output multiplicative perturbation	
	matrix with encoder events	
F	force	N
F_d	damping force	N
F_h	holding force	N
F_p	preload force	N
F_N	normal force	N
$\mathcal{F}_l$	lower fractional transform	
G	system transfer function	
H	model matrix	
	system transfer function	
I	identity matrix	
J	inertia	kgm^2
K	gain	
	index numbers of stored events	
K_a	stiffness	N/m
K_A	gain scheduling term	
K_ϕ	gain scheduling term	
L	length	m
	learning filter transfer function	
	loop gain transfer function	
	low-pass filter transfer function	
M	mass	kg
	moment	Nm
	maximum delay	-
$\underline{M}$	mass matrix	
M_p	overshoot	m
M_s	modifying sensitivity transfer function	
N	number of samples	-
	closed-loop transfer function	
P	system transfer function	
	parameter set	
	vector with polynomial coefficients	
P_α	repetitive period	s
Q	electric charge	C
	robustness filter transfer function	

Q^{nc}	nonconservative generalized forces	N
R	radius	m
	rotation matrix	-
$\mathcal{R}$	correlation	-
S	sensitivity transfer function	
	matrix with generalized force directions	
	strain	
S_P	process sensitivity transfer function	
T	period time	s
	stress	N/m^2
	kinetic energy	J
	complementary sensitivity transfer function	
T_s	sampling time	s
V	potential energy	J
	Lyapunov function	
	voltage	V
V_R	voltage range	V
W	weighing filter	
$\underline{W}$	output matrix	

Roman lowercase

Symbol	Description	Unit
a	Fourier series coefficient	
b	damping	Ns/m
	Fourier series coefficient	
b_s	width	m
c	motor constant	
	width	m
c_x	bending coefficient	m/V
c_y	extension coefficient	m/V
d	damping	Ns/m
	disturbance	
d_{31}	piezoelectric constant	m/V

d_{33}	piezoelectric constant	m/V
d_s	depth	m
e	error	m, rad
e_{31}	piezoelectric constant	N/(Vm)
f	frequency	Hz
	force	N
	objective function	
f_s	sampling frequency	Hz
f_t	total force	N
f_α	drive frequency	Hz
g	gravitational constant	m/s^2
	output function	
i	current	A
k	stiffness	N/m
	electro-mechanical coupling factor	-
	discrete time sample index	-
	gain	
	iteration number	
l	delay L filter	-
m	mass	kg
	minimum delay	-
	fit order	
n	number of layers	-
n	number of events	-
n_F	number of forces	-
n_M	number of moments	-
p	leg pair	-
	polynomial coefficient	
q	generalized coordinate	
	overlap	
	delay Q filter	-
r	reference	
	position vector	
	convergence parameter	
	model output	
s	Laplace variable ($s = j\omega$)	rad/s

s^E	compliance	m^2/V
t	time	s
t_s	settling time	s
u	voltage	V
	input	
v	velocity	m/s
	vector with measured variables	
w	external input signal	
	waveform number	
x	Cartesian coordinate	m
x	state variable	
y	Cartesian coordinate	m
y	output	
z	Cartesian coordinate	m
z	z-transform variable ($z = e^{j\omega}$)	
z	vector with control variables	
z	sample height	m

Greek

Symbol	Description	Unit
α	angle	rad
	repetitive variable	
	gain	
β	angle	rad
	dimensionless damping coefficient	-
	gain	
γ	friction coefficient	-
	gain	
	optimization argument	
δ	delay	
	distance	
Δ	displacement	m
ϵ	accuracy	
	offset	V

ϵ^T	dielectric constant	$\mathrm{N/V^2}$
θ	rotation around z-axis	rad
λ	friction force	N
	characteristic loci	
μ	friction coefficient	-
	structured singular value	
	mean value	
ν	Poisson's ratio	-
ξ	optimization parameters	
ρ	density	$\mathrm{kg/m^3}$
σ	singular value	
	variance	
	skip factor	
τ	rotation around x-axis	rad
	input	
	phase shift	
ϕ	phase	rad
	rotational position vector	
φ	rotation around y-axis	rad
ψ	phase	rad
Ω	angular velocity	rad/s
ω	frequency	rad/s

Subscripts, superscripts and indices

Symbol	Description
$_0$	initial
$_a$	acceleration
	actuation
$_A$	amplitude
	start of time step
$_{\mathrm{BW}}$	bandwidth

b	bearing
CM	center of mass
c	contact
	controller
d	diagonal
	decentralized
E	end of time step
e	equilibrium
	experiment
	event
h	motor housing
i	index
k	index
K	stored encoder events
LP	low-pass
l	leg
	small perturbations
m	model
	motor
max	maximum
nd	non-diagonal
nr	non-repetitive
o	original
	output
opt	optimal
p	leg pair
	pole
r	reference
	repetitive
	retrace
	rotated
RC	repetitive control
res	resonance
s	stage
	simulation
t	total

$_t$	tip
	trace
$_v$	velocity
$_x$	Cartesian coordinate
$_y$	Cartesian coordinate
$_z$	Cartesian coordinate
$_\delta$	delay
$_\sigma$	skip
$_\phi$	phase

Special symbols and operations

Symbol	Description
j	imaginary number
$\mathrm{Re}(a)$	real part
$\mathrm{Im}(a)$	imaginary part
a^T	transpose
$\lvert a \rvert$	absolute value
	complex modulus (magnitude)
$\lfloor a \rfloor$	floor function
$\angle a$	phase angle
$\dot{a}$	time derivative
$\bar{a}$	model
	quantized
	normalized
	maximum value
	average value
$\tilde{a}$	model
	linear perturbation
$\hat{a}$	model
	estimated
Δa	finite difference
$\mathbb{E}(a)$	expected value

Acronyms and initialisms

Abbreviation	Description
AFM	atomic force microscope
AQI	advanced quadrature interface
BIBO	bounded-input bounded-output
CM	center of mass
CPSD	cumulative power spectral density
CPU	central processing unit
DAC	digital-to-analog converter
DAE	differential-algebraic equation
DC	direct current
DMMS	distributed micro-motion systems
DOF	degree-of-freedom
DRC	directional repetitive control
DVRC	delay-varying repetitive control
FB	feedback
FEM	finite element modeling
FF	feedforward
FIR	finite impulse response
FRF	frequency response function
GA	genetic algorithms
HOTS	higher-order time-stamping
ILC	iterative learning control
ISS	input-to-state stability
LFK	Lyapunov-Krasovskii functional
LFT	lower fractional transformation
LMI	linear matrix inequality
LPV	linear parameter-varying
LU	lower-upper
MIMO	multiple-input multiple-output
PI	proportional-integral
PLF	performance limiting factor
PSD	power spectral density
PSO	particle swarm optimization

PZT	lead zirconate titanate
RC	repetitive control
RGA	relative gain array
rms	root-mean-square
SA	simulated annealing
SISO	single-input single-output
SPM	scanning probe microscope
TTL	transistor-transistor logic
USB	universal serial bus
ZPETC	zero-phase-error-tracking-control

Summary

Performance-driven control of nano-motion systems

The performance of high-precision mechatronic systems is subject to ever increasing demands regarding speed and accuracy. To meet these demands, new actuator drivers, sensor signal processing and control algorithms have to be derived. The state-of-the-art scientific developments in these research directions can significantly improve the performance of high-precision systems. However, translation of the scientific developments to usable technology is often non-trivial.

To improve the performance of high-precision systems and to bridge the gap between science and technology, a performance-driven control approach has been developed. First, the main performance limiting factor (PLF) is identified. Then, a model-based compensation method is developed for the identified PLF. Experimental validation shows the performance improvement and reveals the next PLF to which the same procedure is applied. The compensation method can relate to the actuator driver, the sensor system or the control algorithm.

In this thesis, the focus is on nano-motion systems that are driven by piezo actuators and/or use encoder sensors. Nano-motion systems are defined as the class of systems that require velocities ranging from nanometers per second to millimeters per second with a (sub)nanometer resolution. The main PLFs of such systems are the actuator driver, hysteresis, stick-slip effects, repetitive disturbances, coupling between degrees-of-freedom (DOFs), geometric nonlinearities and quantization errors.

The developed approach is applied to three illustrative experimental cases that exhibit the above mentioned PLFs. The cases include a nano-motion stage driven by a walking piezo actuator, a metrological AFM and an encoder system.

The contributions of this thesis relate to modeling, actuation driver development,

control synthesis and encoder sensor signal processing. In particular, dynamic models are derived of the bimorph piezo legs of the walking piezo actuator and of the nano-motion stage with the walking piezo actuator containing the switching actuation principle, stick-slip effects and contact dynamics. Subsequently, a model-based optimization is performed to obtain optimal drive waveforms for a constant stage velocity. Both the walking piezo actuator and the AFM case exhibit repetitive disturbances with a non-constant period-time, for which dedicated repetitive control methods are developed. Furthermore, control algorithms have been developed to cope with the present coupling between and hysteresis in the different axes of the AFM. Finally, sensor signal processing algorithms have been developed to cope with the quantization effects and encoder imperfections in optical incremental encoders.

The application of the performance-driven control approach to the different cases shows that the different identified PLFs can be successfully modeled and compensated for. The experiments show that the performance-driven control approach can largely improve the performance of nano-motion systems with piezo actuators and/or encoder sensors.

Samenvatting

De markt voor ultra-precisie mechatronische systemen stelt steeds hogere eisen aan de snelheid en nauwkeurigheid van machines. Om aan deze eisen te voldoen dienen nieuwe methoden voor motorsturing, sensorverwerking en regelaarontwerp ontwikkeld te worden. Recente wetenschappelijke resultaten op deze gebieden bieden een goed perspectief om de prestaties van ultra-precisie mechatronische systemen te verbeteren. De vertaling van nieuwe kennis naar bruikbare en toepasbare technologie is hierbij echter niet triviaal.

Om de afstand tussen de wetenschappelijke resultaten en de technologie te verkleinen, is een prestatiegedreven regeltechnische methodiek ontwikkeld. De eerste stap is de identificatie van de dominante prestatie-limiterende factor (PLF) in het systeem. Vervolgens wordt een modelgebaseerd compensatie-algoritme voor de betreffende PLF ontworpen. Implementatie en experimentele validatie van het compensatie-algoritme tonen de behaalde verbetering en openbaren de volgende PLF voor het systeem, waarop vervolgens dezelfde methodiek kan worden toegepast. Compensatie-algoritmes kunnen deel uitmaken van zowel de motorsturing, de sensorverwerking als het regelaarontwerp.

In dit proefschrift wordt gefocussed op nano-bewegingssystemen die aangedreven worden door piezo-motoren en/of gebruik maken van optische incrementele encoders als positiesensor. De nano-bewegingssystemen zijn de klasse van systemen met snelheden variërend van nanometers per seconde tot millimeters per seconde bij een (sub)nanometer resolutie in de positioneernauwkeurigheid. De belangrijkste PLFs voor dergelijke systemen zijn de gebruikte motorsturing, de aanwezige hysterese, het stick-slip gedrag, de aanwezige repeterende verstoringen, de koppeling tussen de vrijheidsgraden van het systeem, de geometrische niet-lineariteiten en de kwantisatiefouten in de encoders.

De ontwikkelde PLF-methodiek is toegepast op drie representatieve bewegingssystemen die bovengenoemde PLFs bevatten: 1) een ultra-precisie platform dat

wordt aangedreven door een wandelende piezo-motor, 2) een atomic force microscoop (AFM), en 3) een roterend massasysteem met een positie-encoder.

De bijdragen van dit proefschrift bestaan uit een aantal technieken voor piezomotorsturing, encoderverwerking en regelaarontwerp. Als eerste bijdrage noemen we het model van de wandelende piezo-motor in het ultra-precisie platform dat zowel de overname van de aandrijvende pootjes als het stick-slip gedrag en de dynamische verschijnselen in het contact tussen motor en platform beschrijft. Met behulp van dit model zijn optimale aanstuurspanningen voor de motor bepaald. Zowel het ultra-precisie platform als de atomic force microscoop zijn onderhevig aan repeterende verstoringen, waarvoor twee verschillende modelgebaseerde lerende regelaars zijn ontwikkeld. De koppeling tussen en de hysterese in de verschillende assen van de microscoop zijn gemodelleerd en vervolgens gereduceerd met een modelgebaseerd regelaarontwerp. Tenslotte is een gecombineerde model/datagebaseerde techniek ontwikkeld om de kwantisatiefouten en imperfecties in optische incrementele encoders te reduceren.

De behaalde resultaten met de verschillende systemen tonen aan dat de prestatiegedreven regeltechnische methodiek met succes kan worden toegepast om de geïdentificeerde PLF's achtereenvolgens te modelleren en te compenseren. De experimenten laten zien dat de toepassing van de PLF-methodiek significante verbeteringen in de prestaties van nano-bewegingssystemen met piezo-motoren en positie-encoders kan opleveren.

Dankwoord

Nu ik dit dankwoord schrijf, besef ik me pas echt dat het einde van vier geweldige jaren promoveren met rasse schreden nadert. Met een smile op mijn gezicht denk ik terug aan een promotieonderzoek in een groep met een unieke sfeer, waarbij de vele gezellige koffie- en borrelmomenten, de conferentiebezoeken, het jaar Hora Est bestuur en Tech United slechts enkele dingen zijn die aan dit gevoel bijdragen. Zoals velen al weten, zie ik een promotie als iets waarin je buiten de wetenschappelijke diepgang ook jezelf in de breedte kunt ontwikkelen. Graag wil ik op deze plaats dan ook enkele mensen bedanken die mij in deze exploratie geholpen hebben.

Allereerst wil ik Maarten Steinbuch bedanken voor de geboden kans om dit promotieonderzoek te starten. Jouw coaching en de inspirerende en motiverende gesprekken tijdens de verschillende IWO's en daarbuiten, hebben mij enorm geholpen dit onderzoek vorm te geven en maken de werksfeer bijzonder aangenaam. Hierbij mag jouw oprechte interesse, ook op persoonlijk vlak, zeker erg bijzonder en prijzenswaardig genoemd worden. Verder ben ik je erg dankbaar voor de mogelijkheden die ik gekregen heb om meer te ontwikkelen dan alleen de wetenschappelijke vaardigheden.

René van de Molengraft wil ik graag bedanken voor de dagelijkse coaching. Jouw capaciteit om de verbanden te zien en telkens weer de juiste kritische vragen te stellen, heeft veel bijgedragen aan de kwaliteit van dit proefschrift. Jouw vermogen om dingen in perspectief te plaatsen, maken de verschillende obstakels, die je gedurende een promotie tegenkomt, makkelijker te trotseren. Verder wil ik je bedanken de kans gekregen te hebben om deel uit te maken van Tech United Eindhoven, het middle-size RoboCup team van de TU/e, en enkele jaren de teamleider te mogen zijn geweest. Deze al snel verslavende nevenactiviteit heeft menig uurtje gekost, maar ik had deze unieke ervaring voor geen goud willen missen.

De verschillende afstudeerders die ik heb mogen begeleiden ben ik ook zeer erkentelijk. Niels, Mustafa, Michel, Mike, Dirk, Martijn, Michael, Shiqian en Joep, jullie

hebben allen op een eigen manier een bijdrage geleverd aan de totstandkoming van dit proefschrift.

Een woord van dank gaat uit naar Kees-Jan Leliveld van Bosch Rexroth voor de organisatie van het Micro- & Nano Motion project. Graag wil ik Edwin Verschueren bedanken voor de verschillende gesprekken, waarin jouw kennis over en ervaring met nano-bewegingssystemen mij telkens weer inspireerden. Ook Richard Koops en Marijn van Veghel van het NMi wil ik bedanken voor het mogelijk maken van de verschillende experimenteersessies op de atomic force microscoop.

Alle collega's van de DCT sectie wil ik bedanken voor de gezelligheid tijdens de koffiepauzes, uitjes, borrels en de verschillende conferentiebezoeken. Met name wil ik mijn kamergenoten bedanken, Tom, Gert en in het bijzonder Jeroen, voor de vele discussies, al dan niet over werkgerelateerde onderwerpen. Jeroen, altijd kon ik bij jou een luisterend oor vinden, super bedankt hiervoor. Petra en Lia wil ik bedanken voor de soms broodnodige praatjes tussen het harde werken door. Elke ochtend begon met koffie en een praatje in de DCT kantine, Harrie, Peter, Rob, Sjef, Pieter, Hennie, ik zal deze aangename start van de dag zeker gaan missen.

In dit lijstje mag zeker ook het RoboCup team, Tech United Eindhoven, niet ontbreken. Het samen nastreven van één doel in zo'n geweldig team is een unieke ervaring. Vooral de toernooien zijn altijd erg intensief, maar de sfeer en spirit blijven onverstoorbaar goed. Super bedankt voor de onvergetelijke teamavonden, demonstraties en toernooien.

Graag wil ik mijn familie bedanken voor de interesse die ze gedurende de jaren getoond hebben. Audrey, je bent echt een geweldig zussie. Dank je wel dat ik met werkelijk alles bij je aan kan kloppen. Pap en mam, dank jullie wel voor jullie onvoorwaardelijke steun en vertrouwen. Woorden kunnen niet beschrijven hoezeer ik waardeer wat jullie allemaal voor mij gedaan hebben, zonder jullie was dit resultaat nooit mogelijk geweest.

Tenslotte, maar zeker niet op de laatste plaats, wil ik Louise bedanken. Samen hebben we de mooie momenten mogen delen en de tegenslagen getrotseerd. Super bedankt voor alle steun, liefde en alles wat je voor me gedaan hebt tijdens het soms erg drukke promotietraject. Schat, ik hoop nog vele jaren samen met jou tegemoet te gaan.

Roel Merry
Oktober, 2009

Curriculum Vitae

Roel Merry was born on August 20, 1980 in Sittard, the Netherlands. After finishing his secondary education at the College Sittard in 1998, he started his study Mechanical Engineering at the Eindhoven University of Technology (TU/e). He received the Master's degree (cum laude) in 2005. During his traineeship at Philips Automotive Playback Modules in Wetzlar, Germany, he worked on the "Startup of a DVD/CD player under vibration". The topic of his graduation project was "Iterative learning control with wavelet filtering". In 2006, he started as a PhD student in the Control Systems Technology group at the department of Mechanical Engineering of the TU/e on the topic of "Performance-driven control of nano-motion systems", resulting in this thesis.